UAM

Facultad de Ciencias
Departamento de Física Teórica

Jet production in charged current deep inelastic scattering at HERA

Submitted in partial fullfilment of the requirements
for the degree "Doctor en Ciencias Físicas" by

Mónica Luisa Vázquez Acosta

Director : Juan Terrón Cuadrado

16/12/2002

Facultad de Ciencias
Departamento de Física Teórica

Producción de chorros hadrónicos en interacciones débiles cargadas en HERA

Memoria presentada para la obtención del
título de Doctor en Ciencias Físicas por

Mónica Luisa Vázquez Acosta

Director : Juan Terrón Cuadrado

16/12/2002

A mis padres

que siempre me han animado a
perseguir mis suenõs. Su con-
tinua dedicación y sacrificio lo
han hecho posible. A pesar de
la distancia siempre han estado
muy próximos ...

*" De poco sirve el conocimiento sin sabiduría, no hay sabiduría
sin espiritualidad y la verdadera espiritualidad incluye siem-
pre el servicio a los demás ... "*. Isabel Allende

Introduction

Jet production in charged-current (CC) deep inelastic e^+p scattering (DIS) provides a testing ground for QCD as well as for the electroweak sector of the Standard Model (SM). In addition, searches for new physics rely crucially on accurate determinations of event rates and cross sections from SM processes. Up to leading order in the strong coupling constant α_s, jet production in CC DIS proceeds via the quark-parton model ($Wq \to q$), the QCD-Compton ($Wq \to qg$) and W-gluon fusion ($Wg \to q\overline{q}$) processes. Differential jet cross sections are sensitive to α_s and the mass of the propagator M_W, which are fundamental parameters of the SM.

The final state jets in CC DIS also have an internal structure, a useful representation of which is the subjet multiplicity [Ca92]. The lowest-order non-trivial contribution to the subjet multiplicity is of order α_s, so that measurements of the subjet multiplicity provide a test of QCD.

Measurements of the CC DIS cross section at HERA [Ah94, De95, Ai95, Ai96, De96, Br00, Ad01c, Ch02] at high virtuality of the exchanged boson, Q^2, demonstrate the presence of a space-like propagator with a finite mass, consistent with that of the W boson. At HERA, multijet structure has been observed in CC DIS [De96, Ad01] at large Q^2 and the jet substructure has been studied using the differential and integrated jet shapes [Br99].

This manuscript reports a detailed study of the hadronic final state in CC DIS. Differential cross sections for inclusive jet and dijet production are presented. The jets were identified in the laboratory frame using the longitudinally invariant k_T cluster algorithm [Ca93].

The inclusive jet cross sections are presented as a function of the jet transverse energy, E_T^{jet}, jet pseudorapidity, η^{jet}, and the virtuality of the exchanged boson, Q^2. The dependence of the dijet cross sections on Q^2 and the invariant mass of the two highest E_T jets, m_{12}, are given. The mean subjet multiplicity, $\langle n_{sbj} \rangle$, was measured as a function of the resolution scale, y_{cut}, η^{jet} and E_T^{jet} using the inclusive jet sample. The measurements of $\langle n_{sbj} \rangle$ are compared to the results in neutral current DIS [ZE01b]. Parton shower Monte Carlo calculations and next-to-leading-order QCD predictions are compared to the measurements.

The results of this manuscript (see chapter 7), have been presented by the author in the Photon'2001 conference in Ascona. Furthermore, they have been published by ZEUS as a contributed paper to the International Eurephysics Conference on High Energy Physics, Budapest, Hungary (2001) [ZE01] and the 31st International Conference on High Energy Physics,Amsterdam, Holland (2002) [ZE02].

Introducción

La producción de chorros colimados de hadrones ("jets") en colisiones e^+p profundamente inelásticas (DIS) mediadas por interacciones débiles cargadas (CC), permite verificar no sólo la teoría de QCD sino también el sector electrodébil del modelo estándar (SM). La búsqueda de nuevos procesos físicos depende de la determinación precisa de secciones eficaces de procesos dentro del marco del SM. A primer orden en la constante de acoplo fuerte α_s, la producción de "jets" en procesos CC DIS ocurre mediante los procesos del modelo partónico de quarks ($Wq \rightarrow q^{'}$), QCD-Compton ($Wq \rightarrow q^{'}g$) y fusión W-gluón ($Wg \rightarrow q\overline{q}^{'}$) Las secciones eficaces de producción de "jets" son sensibles a α_s y a la masa del propagador M_W, que son parámetros fundamentales del SM.

El estado hadrónico final en CC posee una estructura interna, que se puede estudiar mediante la multiplicidad de "subjets" [Ca92]. La contribución no trivial de orden más bajo a la multiplicidad de "subjets" es de orden α_s, por lo que las medidas de la multiplicidad de "subjets" proprocionan un test de QCD.

Las medidas de secciones eficaces de procesos CC en HERA [Ah94, De95, Ai95, Ai96, De96, Br00, Ad01c, Ch02] con grandes momentos transferidos, Q^2, demostraron la presencia de un propagador con una masa finita, consistente con la masa del bosón W. Los procesos CC con "jets" han sido observados [Ah94, De95, Ai95, Ai96, De96, Br00, Ad01c, Ch02] y la estructura de los "jets" ha sido estudiada en términos de los jet shapes [Br99].

Esta memoria presenta un estudio detallado del estado hadrónico final en procesos CC DIS. Las medidas de secciones eficaces diferenciales de producción inclusiva de "jets" y la producción de dos o más "jets" son presentadas. Los "jets" han sido identificados en el sistema de referencia del laboratorio usando el algoritmo k_T [Ca93] que es invariante ante traslaciones longitudinales.

Se presentan las medidas de secciones eficaces inclusiva de "jets" en CC en función de la energía transversa de los "jets", E_T^{jet}, la pseudorapidez, η^{jet}, y Q^2. La dependencia de la producción de dos o más "jets" con Q^2 y la masa invariante de los dos "jets" con mayor energía transversa también se presenta. La multiplicidad media de "subjets", $\langle n_{sbj} \rangle$, es medida en función de la escala de resolución y_{cut}, η^{jet} y E_T^{jet} usando la muestra de "jets" inclusiva. Las medidas de $\langle n_{sbj} \rangle$ han sido comparadas con resultados similares en interacciones débiles neutras [ZE01b]. Las predicciones teóricas a segundo orden en α_s han sido comparadas con las medidas.

Los resultados de esta memoria (ver el capítulo 7), han sido presentados por el autor en la conferencia Photon'2001 en Ascona. Además han sido publicados por ZEUS como un artículo en la Conferencia Internacional de Física Europea de Altas Energías, Budapest, Hungría (2001) [ZE01] y la XXXI Conferencia Internacional de Altas Energías, Amsterdam, Holanda (2002) [ZE02].

Contents

List of Figures

ix

List of Tables

Chapter 1

Theoretical introduction

1.1   The Standard Model

Particle physics studies particles and their interactions. The elementary constituents of matter are quarks and leptons, which are fermions of spin[1] $1/2$. There are six leptons and six quarks. The leptons are: electron (e), muon (μ), tau (τ), electron neutrino (ν_e), muon neutrino (ν_μ) and tau neutrino (ν_τ). The quarks are: up quark (u), down quark (d), charm quark (c), strange quark (s), top quark (t) and bottom quark (b). For each particle, there exists a corresponding anti-particle with the same mass but opposite quantum numbers (see table 1.1).

There are four known fundamental interactions in nature. In quantum field theory these forces are mediated by gauge bosons. The four known interactions are:

1. Electromagnetic Interaction
   The Electromagnetic Force is the interaction occurring between particles which carry *electrical charge*, i.e. *charged* particles. The gauge boson that mediates the electromagnetic force is the photon (γ). Photons are massless and electrically neutral.

2. Weak Interaction
   The Weak Force acts between fermions and is mediated by the $W^\pm$ and Z^0 gauge bosons. These gauge bosons are massive[2].

3. Strong Interaction
   The Strong Force couples particles having *strong colour-charge*, i.e. *colour*. In this case the gauge bosons are the *gluons*. Gluons themselves are massless but carry colour-charges and are subject to the strong interaction.

4. Gravitational Interaction
   The Gravitational Force acts between all particles. In quantum theories of gravity, the gravitational field is mediated by a spin-two ($s = 2$) boson which is called a *Graviton*. This interaction is the weakest of the four interactions.

---

[1]Spin is the intrinsic angular momentum of particles and is given in units of $\hbar = 6.58 \cdot 10^{-25}\,\text{s} \cdot \text{GeV}$
[2]The W-boson has a mass of 80.422 ± 0.047 GeV and the Z^0 boson 91.1876 ± 0.0021 GeV.

The Strong and the Weak Force are short-range and play a role only at sub-nuclear distances, in contrast to the long-range electromagnetic and gravitational forces. Due to the weakness of the gravitational force, it can be neglected at the energies presently available in high energy physics (HEP) experiments.

Families			electric charge	Forces			
				str	em	weak	grav
Quarks	u	c	t	$2/3$	$\times$	$\times$	$\times$	$\times$
	d	s	b	$-1/3$	$\times$	$\times$	$\times$	$\times$
Leptons	ν_e	ν_μ	ν_τ	0	-	-	$\times$	$\times$
	e	μ	τ	-1	-	$\times$	$\times$	$\times$

Masses of Quarks (MeV)					
d	u	s	c	b	t
< 100	< 100	~ 400	~ 1500	~ 5000	~ 175000

Table 1.1 - Generations of fermions in the Standard Model, showing The electric charge of the particles and their interactions. The symbol $\times$ means that the particles are subject to the specific force, whereas $-$ indicates that the particles do not interact via that force. The second table gives estimates of the masses of the quarks.

Quantum Electrodynamics (QED) is the theory of electromagnetic interactions. The results of QED can be calculated using a perturbative expansion since the electromagnetic coupling constant $\alpha \simeq 1/137$ is much smaller than unity. At larger distances the effective charges are smaller than the real ones. This is due to screening effects (charges emit and absorb virtual photons which, in turn, fluctuate in electron-positron pairs). Therefore, at small distances (large energy scales) the electromagnetic coupling constant increases. For the present energy scales in HEP experiments α is small enough so that the perturbative approach can be applied.

Strong interactions are described by Quantum Chromodynamics (QCD). The mediators of the strong interaction, the gluons, carry colour. Colour plays for the strong interaction the role of the charge in the electromagnetics interactions. Gluons interact between themselves strongly as opposed to the field quanta of the electromagnetic interactions (photons). Due to this fact the strong coupling constant α_s decreases as the energy scale increases. Calculation of results in QCD using perturbative methods is not always possible. In fact perturbative QCD (pQCD) cannot be always applied and its use depends also on the particular process for which the calculations are made.

A plausible property of QCD is *confinement*, which keeps quarks bound into colourless hadrons. This prevents the observation of free quarks. The colour degree of freedom and confinement explain why observed hadrons are made of either $q\bar{q}$ (mesons) or triple-quark states (baryons). These combinations ensure that the hadrons are colourless and have integer electrical charges.

The electromagnetic and weak interactions are unified within the electroweak (EW) theory of Glashow, Salam and Weinberg [Gl61]. The combination of the Electroweak

Theory with QCD constitutes the *Standard Model* (SM). In the context of this model, the 12 elementary fermions (quarks and leptons) are classified in three families (generations). The masses of the particles (see table 1.1) vary between families, but the way the particles interact remains the same.

QED, QCD and the electroweak theory are quantum field gauge theories[3] and can be derived from symmetry principles. For the strong interaction, the basic symmetry is $SU(3)_C$, where the "3" refers to the three colour-charges, while for the electroweak interaction the basic symmetry is $SU(2)_L \otimes U(1)_Y$. Experimental evidence from a large number of high energy experiments has shown an overwhelming success for the Standard Model. Fundamental tests of its correctness have been made and precise determinations of its free parameters have been done. Some more aspects of QCD and EW theory are described in this chapter. In spite of these successes, there are still many open questions concerning the Standard Model. Some of the problems and still unresolved questions are listed below :

- The Standard Model does not predict the masses of quarks and leptons.

- The existence of exactly three families of quarks and leptons is not predicted by the Standard Model.

- The scale of Quantum Gravity is not yet understood. The Standard Model cannot predict why this scale is so different from that of the electroweak scale.

- One of the main still unsolved questions in the Standard Model and High Energy Physics is the existence of the Higgs Boson. Its existence is related to the generation of elementary particle masses. Gauge bosons and fermions obtain their masses by interacting with the Higgs field. Associated with this mechanism is the existence of massive scalar particles called Higgs bosons. The proof for the Higgs mechanism would come directly from the observation of the Higgs particle. A clear experimental observation of the Higgs bosons has not yet been made. The LEP experiments at CERN[4] have observed a number of collisions compatible with the production of a Higgs particle with a mass of around 115 GeV. However, these events were also compatible with other known processes [LE00].

- The Standard Model failes to account for the solar, atmospheric and reactor neutrino data which strongly indicate the need for neutrino transformations, as would arise from neutrino-mass-induced oscillations [Ah00, Fu98, Ka02].

  Neutrino Masses : for a long time it was assumed that the neutrinos have no mass. Even a small mass would allow for the transformation of the neutrino from one species to the other (e.g. $\nu_\tau \leftrightarrow \nu_e$).

---

[3]The equations of the interactions are invariant under a gauge transformation
[4]CERN - **C**onseil **E**uropéen pour la **R**echerche **N**ucléaire - Switzerland.
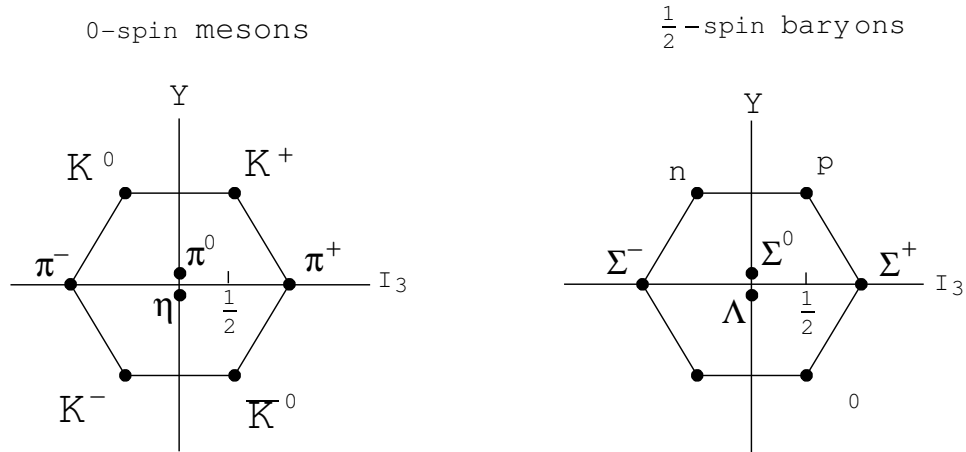
Figure 1.1 - Examples of particle octets of $SU(3)$.

1.1.1   The Quark Model

In the study of nuclear interactions the quantum number of *isospin*, I, was introduced. The nucleon has an internal degree of freedom with two allowed states, the proton and the neutron, which the nuclear interaction does not distinguish. The isospin symmetry is based on the $SU(2)$ group and the proton and the neutron form a isospin doublet. The proton and the neutron are not degenerate and therefore the isospin symmetry is not an exact symmetry of the strong interactions. Since the mass difference of the nucleons is small, the $SU(2)$ isospin symmetry is an approximate symmetry of the strong interactions.

In 1947 the pion was discovered and the nucleon lost its unique role in particle physics. Subsequently, many more strong interacting particles (hadrons) were identified. The discovery of Λ^0 and K^0 particles lead to the proposal of a new additive quantum number the *strangeness*, S, which is conserved by the strong interactions but violated by the weak interaction.

In 1953 Gell-Mann [Ge53] and independently Nishijima and Nakano [Ni53], by stuying the properties of the hadrons, noted a linear relation among the three additive quantum numbers of strangeness S, electromagnetic charge Q and the third com-
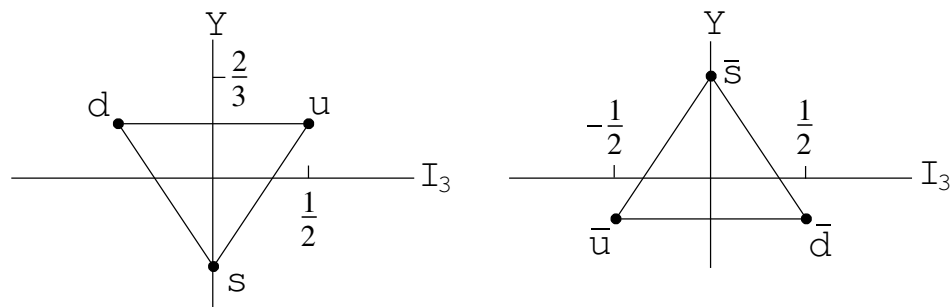
Figure 1.2 - Quark and antiquark multiplets of $SU(3)$.

ponent of the strong isospin T_3:

$$Q = T_3 + \frac{Y}{2}, \tag{1.1}$$

where the hypercharge Y, the baryon number B and the strangeness S are related by $Y = B + S$. The existence of the new conserved quantum number S suggested a larger symmetry for the strong interactions than $SU(2)$. In 1961 Gell-Mann and Ne'eman proposed the group $SU(3)$ which contains $SU(2)$. They established that all mesons and baryons with the same spin and parity can be grouped into irreducible representations of $SU(3)$. Each particle is labelled by its (T_3, Y) quantum numbers and fits into one of the elements in this representation. This classification of hadrons was named "The Eightfold-Way", as the first hadrons studied fitted into a representation of dimension eight. Two examples are shown in Fig. 1.1.

In 1964 Gell-Mann and Zweig[Ge64] noted that the lowest dimensional irreducible representation of $SU(3)$ was not occupied by any of the known hadrons. They proposed the existence of new particles named *quarks* which fitted into the fundamental representation and by making appropiate compositions with them could build up the whole spectra of hadrons. This idea led to the prediction of the three lightest quarks u, d and s, with baryon number 1/3 and charge 2/3, -1/3 and -1/3, respectively (see figure 1.2). The proton (neutron) are now seen as a uud (udd) bound state.

The description of hadrons by means of the irreducible representations of $SU(3)$ is called the *Quark Model*. The mesons (B=0) are composite states of a quark and an antiquark and the baryons (B=1) are composite states of three quarks. The mass differences between the quarks (hadrons) in the same multiplet indicates that $SU(3)$ is not an exact symmetry of the strong interactions.

The Quark Model failed with the discovery of the Δ^{++} particle. The quantum numbers of the Δ^{++} were explained with a bound state of three identical u fermions. This gave a completely symmetric ground state which contradicts Fermi statistics. Gell-Mann solved this problem by introducing a new quantum number, color. Each quark can have one of three different colours and the hadrons are in the singlet representations of the colour group $SU(3)_C$. As the singlet representation is antisymmetric, the colour wave function of the Δ^{++} is antisymmetric.

1.1.2   QCD

Quantum Chromodynamics (QCD) is the gauge theory of the strong interactions. The interactions of quarks and gluons are described in QCD, a non-Abelian gauge theory based on the $SU(3)_C$ colour symmetry group. The gluons, which are electrically neutral but form a colour charge octet, are the gauge boson particles associated with this gauge symmetry.

The Lagrangian which describes the interactions of quarks and gluons is [Ha84]

$$\mathcal{L}_{\text{QCD}} = \sum_q \overline{\psi}_q^i \left[i\, \gamma^\mu \left(D_\mu \right)_{ij} - m_q \right] \psi_q^j - \frac{1}{4} F_{\mu\nu}^a F_a^{\mu\nu} \tag{1.2}$$

$$F_{\mu\nu}^a = \partial_\mu A_\nu^a - \partial_\nu A_\mu^a - g_s f_{abc} A_\mu^b A_\nu^c$$

$$(D_\mu)_{ij} \quad = \quad \delta_{ij} \, \partial_\mu \; + \; i \, g_s \sum_a \frac{\lambda_{i,j}^a}{2} \, A_\mu^a,$$

where g_s ($g_s = \alpha_s/4\pi$) is the QCD coupling constant and $\psi_q^i(x)$ are the Dirac spinors associated which each quark field of colour i and flavour q. γ_μ are the Dirac Matrices which satisfy $\{\gamma^\mu, \gamma^\nu\} = 2g^{\mu\nu}$ ($\mu, \nu = 0, 1, 2, 3$), where $g^{\mu\nu}$ is the space-time metric. $A_\mu^a(x)$ are the Yang-Mills gluon fields. $\lambda_\alpha/2$ are the generators of the group $SU(3)$ which satisfy

$$\left[\frac{\lambda_\alpha}{2} , \frac{\lambda_\beta}{2} \right] = i \, f_{\alpha\beta\gamma} \, \frac{\lambda_\gamma}{2}, \tag{1.3}$$

where the tensor $f_{\alpha\beta\gamma}$ is totally antisymmetric and its elements are the *structure constants* of $SU(3)$.

QCD has properties which make it much more difficult to work with theoretically than electroweak theory. The strong coupling constant α_s becomes large at large distances. This makes the use of perturbation theory very difficult.

The dependence of the effective strong coupling constant α_s with energy, is given by the *renormalisation group equation* and the β *function*

$$\mu^2 \frac{d\alpha_s}{d\mu^2} \quad = \quad \beta(\alpha_s) = -b \, \alpha_s^2 \, (1 + b_1 \alpha_s + ...), \tag{1.4}$$

where

$$\begin{aligned} b \quad &= \quad \frac{33 - 2n_f}{12\pi}, \\ b_1 \quad &= \quad \frac{153 - 19n_f}{2\pi(33 - 2n_f)}, \end{aligned} \tag{1.5}$$

and n_f is the number of active quark flavours, that is, the number of quarks whose mass is smaller than the energy scale μ. α_s decreases with increasing energy scale as long as $n_f < 17$. The known number of flavours is 6.

The solution of equation 1.4 to first order in an expansion in α_s is

$$\alpha_s(\mu) = \frac{\alpha_s(Q)}{1 + 2b \, \alpha_s(Q) \ln\left[\frac{\mu}{Q}\right]}. \tag{1.6}$$

At large μ, α_s is small and the quarks are quasi-free. In this region of *asymptotic freedom*, perturbative QCD (pQCD) is applicable and predictions can be made.

The renormalisation group equation gives the dependence of the coupling constant on the scale, but not the absolute value which has to be obtained from experiment. The value of α_s at a given reference scale Q, which is large enough to be in the perturbative domain, can be chosen as a fundamental parameter of the theory. The common choice for the reference scale is the mass of the Z^0 boson. The value at any other scale is then completely defined by the evolution of the coupling constant with the scale (Eq. 1.6).

Another approach is to introduce a dimensional parameter which is considered the fundamental parameter of QCD, Λ_{QCD}. This parameter is the energy scale at which

α_s becomes large and the perturbative approach is no longer valid. Λ_{QCD} is defined by the following relation

$$\ln \frac{\mu}{\Lambda_{QCD}} = -\frac{1}{2} \int_{\alpha_s(\mu)}^{\infty} \frac{dx}{\beta(x)} = \int_{\alpha_s(\mu)}^{\infty} \frac{dx}{2bx^2 (1 + b_1 x + ...)}. \qquad (1.7)$$

The introduction of Λ_{QCD} allows to write the asymptotic solution of the renormalisation group equation in terms of this parameter. In leading order the integration yields:

$$\alpha_s(\mu) = \frac{1}{2b \ln \left[\frac{\mu}{\Lambda_{QCD}} \right]} = \frac{12\pi}{2(33 - 2n_f) \ln \left[\frac{\mu}{\Lambda_{QCD}} \right]}, \qquad (1.8)$$

which agrees with the expression in Equation 1.6 for large scales.

Including the next-to-leading order contribution the definition of Λ_{QCD} leads to an implicit equation for α_s

$$\frac{1}{\alpha_s(\mu)} + b_1 \ln \left[\frac{b_1 \alpha_s(\mu)}{1 + b_1 \alpha_s(\mu)} \right] = 2b \ln \left[\frac{\mu}{\Lambda_{QCD}} \right]. \qquad (1.9)$$

This equation can be solved numerically to obtain $\alpha_s(\mu)$ for a given value of Λ_{QCD}. An approximate solution can be obtained in terms of an expansion in inverse powers of $\ln(\mu/\Lambda_{QCD})$

$$\alpha_s(\mu) = \frac{1}{2b \ln(\mu/\Lambda_{QCD})} \left[1 - \frac{b_1}{b} \frac{\ln[2 \ln(\mu/\Lambda_{QCD})]}{2 \ln(\mu/\Lambda_{QCD})} \right]. \qquad (1.10)$$

Figure 1.3 shows the dependence of the strong coupling constant on the scale μ for a value of $\alpha_s(M_Z) = 0.118$. The coupling constant decreases with increasing
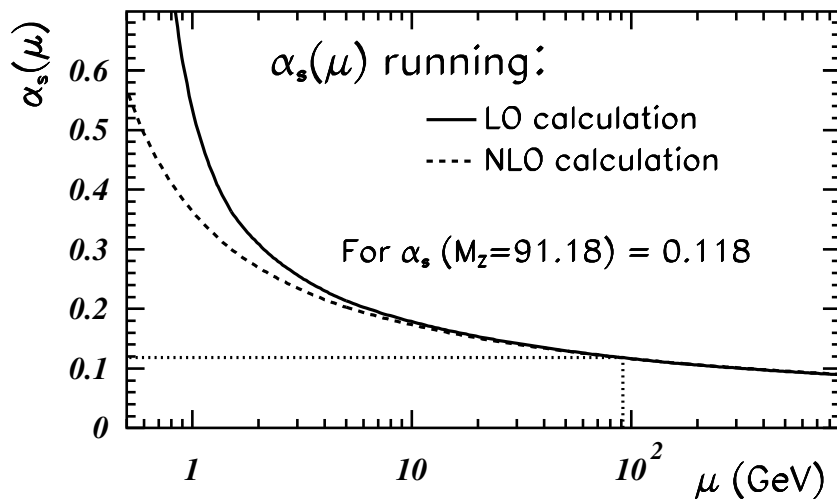
Figure 1.3 - Running of the strong coupling constant calculated at leading and next-to-leading order of the perturbative QCD expansion. The absolute value of the coupling constant was set to $\alpha_s(M_Z) = 0.118$.

scale (asymptotic freedom) and increases rapidly for $\mu \sim 1$ GeV, which suggests the presence of confinement.

The use of Λ_{QCD} as a fundamental parameter of QCD presents several difficulties

- Λ_{QCD} depends on the renormalisation scheme;

- Λ_{QCD} depends on the number of active flavours.

The world average has been determined to be $\Lambda_{\mathrm{QCD}}^{(5)}(\overline{\mathrm{MS}}) = 216^{+25}_{-24}$ MeV (Particle Data Group [Ha02]) for five active flavours in the $\overline{\mathrm{MS}}$ renormalisation scheme (see Section 1.3.1).

1.1.3 The standard electroweak model

The standard electroweak model is the gauge theory for the electroweak interactions based on the gauge group $SU(2)_L \bigotimes U(1)_Y$, where $SU(2)_L$ is the weak isospin group which acts only on the left-handed fermions and $U(1)_Y$ is the weak hypercharge group. There are four gauge bosons in the theory: the three weak bosons, W_μ^i $i = 1, 2, 3$, of $SU(2)_L$ and the hypercharge boson B_μ of $U(1)_Y$. The corresponding gauge coupling constants are g and g'. The generators of $SU(2)_L$, $T_i = \frac{\sigma_i}{2}$, and $U(1)_Y$, $Y/2$, satisfy

$$[\, T_i \, , \, T_j \,] \; = \; i \, \epsilon_{ijk} \, T_k \; ; \; [\, T_i \, , \, Y \,] \; = \; 0 \; ; \; i, j, k = 1, 2, 3. \tag{1.11}$$

The left-handed fermion fields ψ_i of the i-th fermion family, $\begin{pmatrix} \nu_i \\ l_i \end{pmatrix}_L$ and $\begin{pmatrix} u_i \\ d'_i \end{pmatrix}_L$, transform as doublets under $SU(2)_L$, where $d'_i \equiv \sum_j V_{ij} d_j$ and V is the Cabibbo-Kobayashi-Maskawa [Ca63, Ko73] mixing matrix. The right-handed fields are $SU(2)$ singlets. The left-handed and right-handed fields are defined by means of the chirality operator, γ_5: $e_L^- = \frac{1}{2}(1 - \gamma_5)e^-$; $e_R^- = \frac{1}{2}(1 + \gamma_5)e^-$.

The Lagrangian for the fermion fields can be written as [He98]:

$$\mathcal{L}_F \;\; = \;\; i \sum_{i=l,q} \overline{\psi_i} \, \gamma^\mu D_\mu \, \psi_i \; - \; \frac{1}{4} W_{\mu\nu}^i W_i^{\mu\nu} \; - \; \frac{1}{4} B_{\mu\nu} B^{\mu\nu} \; + \; \mathcal{L}_{\mathrm{SBS}} \; + \; \mathcal{L}_{\mathrm{YW}} \tag{1.12}$$

$$W_{\mu\nu}^i \;\; = \;\; \partial_\mu W_\nu^i \; - \; \partial_\nu W_\mu^i \; + \; g \, \epsilon^{ijk} W_\mu^j W_\nu^k$$

$$B_{\mu\nu} \;\; = \;\; \partial_\mu B_\nu \; - \; \partial_\nu B_\mu.$$

The last two terms are the Symmetry Breaking Sector (SBS) and the Yukawa (YW) lagrangians which are needed in order to provide the desired M_W and M_Z gauge boson masses and m_f fermion masses. The physical gauge bosons of the massive charged and neutral current weak boson fields $W_\mu^\pm$, Z_μ, respectively, and the massless photon field A_μ are given by [He98]

$$W_\mu^\pm \;\; = \;\; \frac{1}{\sqrt{2}} \left(W_\mu^1 \mp i \, W_\mu^2 \right) \tag{1.13}$$

$$Z_\mu \;\; = \;\; \cos\theta_w \, W_\mu^3 \; - \; \sin\theta_w \, B_\mu \tag{1.14}$$

$$A_\mu \;\; = \;\; \sin\theta_w \, W_\mu^3 \; + \; \cos\theta_w \, B_\mu, \tag{1.15}$$

where θ_w defines the rotation in the neutral sector. The relation between the couplings are $g = \frac{e}{\sin\theta_w}$ and $g' = \frac{e}{\cos\theta_w}$, where e is the electromagnetic coupling.

The terms $M_W^2 W_\mu W^\mu$, $M_Z^2 Z_\mu Z^\mu$ and $m_f \bar{f} f$ are forbidden by the $SU(2)_L \otimes U(1)_Y$ gauge invariance. The spontaneous breaking of the $SU(2)_L \otimes U(1)_Y$ symmetry by the Higgs Mechanism provides the masses of the gauge bosons and fermions in a gauge invariant way.

1.1.3.1 Spontaneous symmetry breaking and the Higgs Mechanism

A physical system has a symmetry that is spontaneously broken if the Lagrangian describing the dynamics of the system is invariant under certain symmetry transformations, but the vacuum of the theory is not. The Goldstone Theorem [Na60] establishes that if a theory has a global symmetry of the Lagrangian which is not a symmetry of the vacuum then there must exist one massless boson, scalar or pseudoscalar, associated with each generator, which does not annihilate the vacuum and has its same quantum numbers. These modes are referred to as Nambu-Goldstone bosons or simply as *Goldstone bosons*.

In the case that the spontaneous symmetry breaking occurs in a gauge theory the Higgs Mechanism [Hi53] operates:

"The would-be Goldstone bosons associated to the global symmetry breaking do not manifest explicitly in the physical spectrum but instead they combine with the massless gauge bosons and as result, once the spectrum of the theory is built up on the asymmetrical vacuum, there appear massive vector particles. The number of vector bosons that acquire a mass is equal to the number of would-be-Goldstone bosons".

The spontaneous breaking of the $SU(2)_L \otimes U(1)_Y$ symmetry via the Higgs Mechanism requires the introduction of an additional field Φ whose self-interactions produce the symmetry breaking $SU(2)_L \otimes U(1)_Y \rightarrow U(1)_{em}$.

The choice of the system Φ which provides the symmetry breaking is not unique. Φ must fulfil the following conditions:

1. it must be a scalar field so that the symmetry breaking preserves Lorentz invariance;

2. it must be a complex field so that the Hamiltonian is hermitian;

3. it must have non-vanishing weak isospin and hypercharge in order to break $SU(2)_L$ and $U(1)_Y$. The assignment of quantum numbers and the choice of Φ can be done in many ways. Some possibilities are

   • choice of a non-linear representation: Φ transforms non-linearly under $SU(2)_L \otimes U(1)_Y$;

   • choice of a linear representation: Φ transforms linearly under $SU(2)_L \otimes U(1)_Y$. The simplest linear representation is a complex doublet which gives the minimal model. Alternative choices are complex triplets, more than on

doublet, etc. In particular, one may choose two complex doublets H_1 and H_2 as in the Minimal Supersymmetric SM.

4. only the neutral components of Φ are allowed to acquire a non-vanishing vacuum expectation values in order to preserve the $U(1)_{em}$ symmetry of the vacuum;

5. the interactions of Φ with the gauge and fermionic sectors must be introduced in a gauge invariant way;

6. the self-interactions of Φ given by the potential $V(\Phi)$ must produce the wanted breaking which is characterized in this case by $< 0|\phi|0 > \neq 0$;

7. to make predictions both at low and high energies the interactions in $V(\Phi)$ must be renormalizable.

Taking the previous requirements into account the simplest choice for the system Φ and the SBS Lagrangian is [He98]

$$\Phi = \begin{pmatrix} \phi^+ \\ \phi^0 \end{pmatrix} \tag{1.16}$$

$$\mathcal{L}_{SBS} = (D_\mu \Phi)^\dagger (D^\mu \Phi) - V(\Phi) \tag{1.17}$$

$$V(\Phi) = -\mu^2 \Phi^\dagger \Phi + \lambda (\Phi^\dagger \Phi)^2 \; ; \; \lambda > 0,$$

where $D_\mu \Phi = (\partial_\mu - \frac{1}{2} ig\vec{\sigma} \cdot \vec{W}_\mu - \frac{1}{2} ig' B_\mu)\Phi$.

In the case $-\mu^2 > 0$ the minimum of the potential $V(\Phi)$ occurs at $< 0|\Phi|0 >= 0$, i.e. the vacuum is $SU(2)_L \bigotimes U(1)_Y$ symmetric and no symmetry breaking occurs.

On the other hand, if $-\mu^2 < 0$ the minimum is at $| < 0|\Phi|0 > | = \begin{pmatrix} 0 \\ \frac{v}{\sqrt{2}} \end{pmatrix}$, with arbitrary $\arg \Phi$ and $v \equiv \sqrt{\frac{\mu^2}{\lambda}}$. There are infinite degenerate vacua corresponding to the infinite values of $\arg \Phi$. Either of the these vacua is $SU(2)_L \bigotimes U(1)_Y$ non-symmetric and $U(1)_{em}$ symmetric. The symmetry breaking occurs once a particular vacuum is chosen. Three of the real components of Φ are the would-be Goldstone bosons and the fourth one is introduced to complete the complex doublet. After the symmetry breaking, this extra degree translates into the appearance in the spectrum of an extra massive scalar particle, the Higgs boson particle H.

In order to get the fermion particle spectra and masses the Yukawa Lagrangian is introduced [He98]

$$\mathcal{L}_{YW} = \lambda_e \bar{l}_L \Phi e_R + \lambda_u \bar{q}_L \widetilde{\Phi} u_R + \lambda_d \bar{q}_L \widetilde{\Phi} d_R + h.c. + 2^{nd} \text{ and } 3^{rd} \text{ families,} \tag{1.18}$$

where $l_L = \begin{pmatrix} \nu_L \\ e_L \end{pmatrix}$, $q_L = \begin{pmatrix} u_L \\ d_L \end{pmatrix}$ and $\widetilde{\Phi} = i \begin{pmatrix} \Phi_0^\star \\ -\Phi^- \end{pmatrix}$.

After spontaneous symmetry breaking the Lagrangian for the fermion fields in the minimal model is [Ha84]

$$\mathcal{L}_F = \sum_i \overline{\psi}_i \left[i\gamma^\mu D_\mu - m_i - \frac{gm_iH}{2M_W} \right] \psi_i$$

$$- \frac{g}{2\sqrt{2}} \sum_i \overline{\psi}_i \, \gamma^\mu \, (1 - \gamma_5) \, (T^+ W^+_\mu \; + \; T^- W^-_\mu) \, \psi_i$$

$$- e \sum_i q_i \, \overline{\psi}_i \, \gamma^\mu \, \psi_i \, A_\mu$$

$$- \frac{g}{\cos\theta_w} \sum_i \overline{\psi}_i \gamma^\mu \, (g^i_V - g^i_A \gamma^5) \, \psi_i Z_\mu. \tag{1.19}$$

The vector and axial couplings are $g^i_V \equiv t_{3L}(i) - 2q_i \sin^2\theta_w$ and $g^i_A \equiv t_{3L}(i)$, where $t_{3L}(i)$ is the weak isospin of fermion i and q_i is the electrical charge of ψ_i in units of e. H is the physical neutral Higgs scalar which is the only remaining part of Φ after the spontaneous symmetry breaking. In non-minimal models there are additional charged and neutral scalar Higgs particles.

The second term in $\mathcal{L}_F$ represents the charged-current weak interaction. For example, the coupling of a W to an electron and a neutrino is [Ha84]

$$- \frac{e}{2\sqrt{2}\sin\theta_w} \left[\, W^-_\mu \, \overline{e} \, \gamma^\mu (1 - \gamma^5) \, \nu + W^+_\mu \, \overline{\nu} \, \gamma^\mu \, (1 - \gamma^5) \, e \, \right]. \tag{1.20}$$

For momenta small compared to M_W, this term gives rise to the effective four-fermion interaction with the Fermi constant given by $G_F/\sqrt{2} = g^2/8M^2_W$.

1.2   Deep Inelastic Scattering

Many aspects of the Standard Model have been discovered in deep inelastic lepton-hadron scattering (DIS). The first experimental evidence for the structure of the proton came from such experiments performed at the High Energy Physics Laboratory at Stanford University in the early 1950s [Ho53]. In the following section the kinematics of ep scattering is described in detail.

1.2.1   Kinematic Variables for Lepton Nucleon Scattering

The scattering of positrons (electrons) off protons proceeds through the exchange of a gauge boson : γ^* or Z^0 in the case of neutral current (NC) interactions and $W^\pm$ in the case of charged current (CC) interactions (in this case the incoming positron is converted into an anti-neutrino). In this section the kinematic variables are defined. The ep collision can be viewed as a $\gamma^* p$ ($Z^0 p$, $W^\pm p$) collision with the lepton emitting the gauge photon. A Feynman diagram for the single gauge-boson exchange process is depicted in figure 1.4.

The four momenta for the incoming positron (electron) and proton in the laboratory frame, are given by:

$$\begin{aligned} k &= (E_e, 0, 0, -E_e) \\ p &= (E_p, 0, 0, E_p). \end{aligned}$$

The coordinate system is defined such that the incoming protons move in the positive z-direction. Some important (Lorentz invariant) variables for the description of the kinematics of ep scattering are:
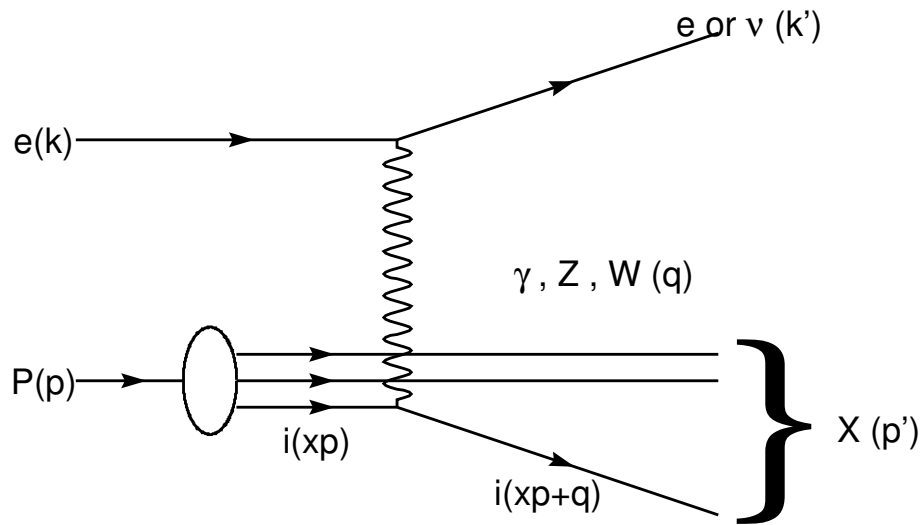
Figure 1.4 - Kinematics of ep scattering - the scattering proceeds through the exchange of a gauge boson $(\gamma^*, Z^0$ or $W^\pm)$. The lowest-order Feynman diagram for DIS is shown. The four-momenta of the particles are given in brackets.

- the center-of-mass energy squared of the ep system:

$$s = (p + k)^2 \simeq 4E_e E_p, \tag{1.21}$$

where the approximation of neglecting the rest masses of the particles has been used.

- the virtuality (negative of the invariant mass squared) of the exchanged boson $(\gamma^*, Z^0$ or $W^\pm)$:

$$Q^2 = -q^2 = -(k - k')^2. \tag{1.22}$$

The upper limit of Q^2 is s: $Q^2 \leq s$;

- the Bjorken variable x, which is, in the Quark Parton Model, the fraction of the proton's momentum carried by the struck quark:

$$x = \frac{Q^2}{2p \cdot q}; \tag{1.23}$$

- the inelasticity y, which is the relative energy transfer from the positron to the proton in the proton's rest frame:

$$y = \frac{p \cdot q}{p \cdot k}; \tag{1.24}$$

- the center of mass energy squared of the photon-proton system:

$$W^2 = (q + p)^2 \simeq sy - Q^2; \tag{1.25}$$

- the (absolute) energy transfer from the positron to the proton in the protons rest frame:

$$\nu = \frac{p \cdot q}{M} \simeq \frac{Q^2}{2Mx},$$ (1.26)

where M is the proton mass.

The variables Q^2, x, and y are not independent. They are related through the following formula:

$$Q^2 = s \cdot x \cdot y.$$ (1.27)

1.2.2 Reconstruction of Kinematics

A precise reconstruction of the kinematics (x, Q^2) is vital for the description of DIS events. In DIS the reconstruction is based on measurements of the final state of the event with the detector.

1.2.2.1 The Jacquet - Blondel Method

The kinematics of CC DIS events are determined from the hadrons since the neutrino in the final state escapes without being detected. Jacquet and Blondel proposed the following reconstruction method of the kinematics [Ja79]

$$
\begin{aligned}
y_{JB} &= \frac{E - P_z}{2E_e}, \\
Q^2_{JB} &= \frac{\not{p}_t^2}{1 - y_{JB}}, \\
x_{JB} &= \frac{\not{p}_t^2}{s \cdot y_{JB}(1 - y_{JB})} = \frac{Q^2_{JB}}{s \cdot y_{JB}},
\end{aligned}
$$ (1.28)

where the total four-momentum of the hadrons in the event is given as $P = (E, P_x, P_y, P_z)$.

The $\not{p}_t$ is the absolute value of the missing transverse momentum $\vec{\not{p}_t}$:

$$
\begin{aligned}
\vec{\not{p}_t} &\equiv (-P_x, -P_y) \\
\not{p}_t &\equiv |\vec{\not{p}_t}| = \sqrt{P_x^2 + P_y^2}.
\end{aligned}
$$ (1.29)

The total transverse energy of the event, E_t, is defined as

$$E_t \equiv \sum_i \sqrt{(P_x^i)^2 + (P_y^i)^2},$$ (1.30)

where i runs over all the final-state hadrons. An advantage of this method is that the particles which escape through the forward beam pipe contribute little to $E - P_z$ and $\not{p}_t$, and hence to the reconstructed kinematic variables.

The angle (γ_h) and energy (E_q) of the hadronic system are defined as

$$\cos\gamma_h \equiv \frac{\not{p}_t^2 - (E - p_z)^2}{\not{p}_t^2 + (E - p_z)^2}, \tag{1.31}$$

$$E_q \equiv \frac{\not{p}_t}{\sin\gamma_h}, \tag{1.32}$$

respectively. In the naive Quark Parton Model (see section 1.3), γ_h and E_q are equivalent to the scattering angle and energy of the struck quark, respectively.

1.2.3 Cross Sections and Proton Structure Functions

In DIS ep experiments the exchanged high Q^2 virtual gauge bosons are used to probe the proton structure. The momentum transfer (squared) can be related to the wavelength of the virtual boson through Heisenberg's uncertainty principle:

$$\lambda \simeq \frac{\hbar}{\sqrt{Q^2}}. \tag{1.33}$$

The wavelenth of the virtual boson is inversely proportional to $\sqrt{Q^2}$, implying that with increasing Q^2 the virtual boson probes smaller distances.

The *Deep Inelastic Scattering* regime is that where Q^2 is much larger than the mass squared of the proton. In this regime, the proton can be viewed as a group of quasi-free constituents, one of which interacts with the boson while the rest (proton remnant) move unperturbed. At a given center-of-mass energy $\sqrt{s}$ the kinematics of inclusive DIS scattering is completely described by two Lorentz-invariant quantities, e.g. x and Q^2.

In the single boson-exchange approximation the cross section for deep inelastic ep scattering can be factorised into a leptonic tensor $L_{\mu\nu}$, associated to the leptonic vertex, and a hadronic tensor $W^{\mu\nu}$, which describes the structure of the hadron:

$$d\sigma \sim L_{\mu\nu} W^{\mu\nu}. \tag{1.34}$$

The leptonic tensor, which is symmetric in μ and ν, can be calculated exactly using the Electroweak theory. For the charged-current DIS process in electron- proton collisions, $L_{\mu\nu}$ can be written as [Ha84]

$$L_{\mu\nu}(e^-p \to \nu X) \equiv \left[\overline{\nu_e}(k')\,\gamma_\mu\left(\frac{1-\gamma_5}{2}\right)e(k)\right]\left[\overline{\nu_e}(k')\,\gamma_\nu\left(\frac{1-\gamma_5}{2}\right)e(k)\right]^*$$

$$L_{\mu\nu}(e^+p \to \overline{\nu} X) \equiv \left[\overline{e}(k)\,\gamma_\mu\left(\frac{1-\gamma_5}{2}\right)\nu_e(k')\right]\left[\overline{e}(k)\,\gamma_\nu\left(\frac{1-\gamma_5}{2}\right)\nu_e(k')\right]^*$$

$$L_{\mu\nu} = 2\left[k_\mu k'_\nu + k'_\mu k_\nu - g_{\mu\nu}k\cdot k' \pm i\varepsilon_{\mu\nu\alpha\beta}k^\alpha k'_\beta\right], \tag{1.35}$$

where the upper and lower signs are for an electron and positron beam, respectively, and the incoming-lepton mass has been neglected.

The structure of the proton and, hence, the details of the interaction at the hadronic vertex are parametrised in the hadronic tensor $W^{\mu\nu}$. The most general form of the tensor $W^{\mu\nu}$ which can be constructed with Lorentz invariant terms using the metric tensor $g^{\mu\nu}$ and the independent variables p and q is [Ha84]

$$W_{\mu\nu} = -W_1 g^{\mu\nu} + \frac{W_2}{M^2} p^\mu p^\nu + i\varepsilon^{\mu\nu\rho\sigma} p_\rho q_\sigma W_3 + \frac{W_4}{M^2} q^\mu q^\nu + \frac{W_5}{M^2}(p^\mu q^\nu + q^\mu p^\nu). \quad (1.36)$$

The conservation of the four-vector current yields

$$W_5 = -\frac{p \cdot q}{q^2} W_2 \qquad \text{and} \qquad W_4 = \left(\frac{p \cdot q}{q^2}\right)^2 W_2 + \frac{M^2}{q^2} W_1. \quad (1.37)$$

The three remaining functions W_1, W_2 and W_3 depend on two independent Lorentz-invariant scalar variables, traditionally chosen to be ν and Q^2.

Nowadays a slightly different notation is used:

$$\begin{aligned}
F_1(x, Q^2) &= M \cdot W_1(\nu, Q^2) \\
F_2(x, Q^2) &= \nu \cdot W_2(\nu, Q^2) \\
F_3(x, Q^2) &= \nu \cdot W_3(\nu, Q^2).
\end{aligned} \quad (1.38)$$

The functions F_i are called *proton structure functions* and can be interpreted in terms of the parton density functions in the proton.

The Born cross section for *charged current* DIS, $ep \to \nu X$, can be written in terms of the structure functions of the proton F_i as follows [Ha84]:

$$\begin{aligned}
\frac{d^2 \sigma(e^\pm p)}{dx \, dQ^2} &= \frac{G_F^2}{4\pi x} \left(\frac{M_W^2}{M_W^2 + Q^2}\right)^2 \left[y^2 x \, F_1^{CC} + (1-y) \, F_2^{CC} \mp \left(y - \frac{y^2}{2}\right) x \, F_3^{CC} \right] \\
&= \frac{G_F^2}{4\pi x} \left(\frac{M_W^2}{M_W^2 + Q^2}\right)^2 \left[Y_+ \cdot F_2^{CC} - y^2 \cdot F_L^{CC} \mp Y_- \cdot x \, F_3^{CC} \right], \quad (1.39)
\end{aligned}$$

where M_W is the mass of the W boson and G_F is the Fermi coupling constant. The kinematic factor $Y_\pm$ is defined as $Y_\pm = 1 \pm (1-y)^2$ and the longitudinal structure function F_L is given by

$$F_L = F_2 - 2x F_1. \quad (1.40)$$

$F_3(x, Q^2)$ describes the parity violating contribution due to the weak interaction and is only relevant in the high Q^2 region ($Q^2 \gtrsim M_W^2$).

Similarly, the cross section for *neutral current* DIS, $ep \to eX$, can be written as:

$$\frac{d^2 \sigma(e^\pm p)}{dx \, dQ^2} = \left(\frac{2\pi\alpha^2}{xQ^4}\right) \left[Y_+ \cdot F_2^{NC} - y^2 \cdot F_L^{NC} \mp Y_- \cdot x F_3^{NC} \right]. \quad (1.41)$$

The parity violating contribution arises from Z^0 exchange and is important when $Q^2 \gtrsim M_Z^2$.

Within the single-photon approximation, the ep cross section can be written as a product of the photon flux with the (virtual) photon-proton cross section, $\sigma_{\text{tot}}^{\gamma^* p}$, provided the virtual photon lifetime is longer than its interaction time with the proton. Virtual photons can be transversely or longitudinally polarised. The cross section can therefore be written as a sum of two parts - longitudinal and transverse:

$$\sigma_{\text{tot}} = \sigma_{\text{L}} + \sigma_{\text{T}}. \tag{1.42}$$

The structure functions F_i can be related to these transverse and longitudinal cross sections as follows:

$$F_1 = \frac{Q^2}{8x\pi^2\alpha} \cdot \sigma_{\text{T}} \; ; \;\; F_2 = \frac{Q^2}{4\pi^2\alpha} \cdot (\sigma_{\text{T}} + \sigma_{\text{L}}) \; ; \;\; F_{\text{L}} = \frac{Q^2}{4\pi^2\alpha} \cdot \sigma_{\text{L}}, \tag{1.43}$$

where the structure functions are defined with respect to the Born cross section given by equation 1.41.

1.3 The Quark Parton Model

Two models were developed to describe the proton structure and that of other hadrons, the *Parton Model* from Feynman [Fe69] and the *Quark Model* (section 1.1.1) by Gell-Mann and Zweig [Ge64]. In the parton model the proton is considered to consist of (quasi) free point-like objects, called partons. Each parton i carries a fraction of the total momentum of the proton: $p_i = \xi_i \cdot p$, where p is the total momentum of the proton, p_i is the momentum of parton i, and $0 \leq \xi_i \leq 1$. Therefore, the ep interaction is viewed as an incoherent sum of scatterings of the electron with the quasi-free partons in the proton.

Since in the Parton Model the partons are pointlike, an increase in the momentum transfer Q^2 will not make any new detail visible. As a consequence the structure functions are expected to be independent of Q^2. This effect is called *scale invariance*, i.e. *scaling*, which was predicted (1968) by Bjorken. In the high energy limit $Q^2 \to \infty$ but $x = Q^2/2pq$ finite, the structure functions depend only on the dimensionless scaling variable x:

$$F_1(x, Q^2) \longrightarrow F_1(x)$$
$$F_2(x, Q^2) \longrightarrow F_2(x). \tag{1.44}$$

In the frame in which the proton carries infinite momentum, all the transverse momenta are negligible. In this frame the scaling variable x can be interpreted as the fractional longitudinal momentum ξ carried by the struck parton. After scattering with the positron, the momentum of the struck parton is given by $q' = \xi \cdot p + q$. Neglecting the parton and proton masses it follows that

$$0 \simeq m^2 = (\xi p + q)^2 = \xi^2 p^2 + q^2 + 2\xi qp = \xi^2 p^2 - Q^2 + 2\xi qp \Rightarrow$$

$$\xi = \frac{Q^2}{2pq} = x. \tag{1.45}$$

Bjorken and Paschos suggested (1969) that the fermions which made up the proton according to the two models (partons and quarks) were one and the same thing. Thus the model was called the *Quark Parton Model*. Scaling behaviour was confirmed at SLAC measurements [Bl69].

In the proton infinite momentum frame, the rate at which partons interact with one another is slowed down, due to Lorentz contraction and relativistic time dilatation. During the time the virtual exchanged boson interacts with the quark, the quark itself is essentially a free particle, not interacting with the other quarks in the proton. In other words, the parton distributions during the ep collision are effectively "frozen", so that only one parton takes part in the interaction. The probability for an additional parton to take part in the interaction is suppressed as $1/(\pi r_p^2 Q^2)$, where r_p is the radius of the proton. Therefore the inelastic ep amplitude of the cross section is then given as the incoherent sum of amplitudes of elastic electron-parton scattering:

$$\frac{d^2 \sigma}{dx \, dQ^2} = \sum_i e_i^2 \, f_i(x, Q^2) \left(\frac{d^2 \sigma_i}{dx \, dQ^2} \right), \qquad (1.46)$$

where e_i is the charge of parton i and $f_i(x, Q^2)$ is the probability of finding a parton i with momentum fraction between x and $x + dx$ in the proton. In the QPM the structure functions F_1 and F_2 are related to the parton distributions functions of the proton. The structure function F_2 is the charge-square-weighted sum of the parton distribution functions:

$$F_2(x) = \sum_i e_i^2 \, x \, f_i(x). \qquad (1.47)$$

The charges e_i are given in units of the proton charge e. The QPM relates also the structure functions F_1 and F_2 to one another:

$$F_1(x) = \frac{1}{2x} \, F_2(x). \qquad (1.48)$$

The above relation is known as the Callan-Gross relation [Ca69]. It implies that the structure function F_L is zero. This can also be proved using general considerations. By applying helicity conservation [Ha84], it follows that the quarks in the QPM can only couple to transversely polarised photons. Therefore, $\sigma_L = 0 \Rightarrow F_L = 0$.

The QPM was very succesful in explaining many results obtained in DIS experiments. This model is though not perfect and some problems became apparent. One of them is the prediction that all the parton momentum is carried by quarks. The experimental data proved this prediction to be wrong. In fact, from experimental measurements it was obtained that less than 50% of the proton's momentum is carried by the charged valence quarks:

$$\sum_i \int_0^1 dx \, x f_i(x) \simeq 0.5. \qquad (1.49)$$

That is, half of the momentum of the proton is carried by neutral particles. In addition, the fact that no free quarks were observed experimentally could not be explained by

the QPM. Both these problems were solved by Quantum Chromodynamics (QCD). In the limit $Q^2 \to \infty$, QCD reproduces the QPM. In the QCD improved parton model, the proton no longer consists merely of quasifree quarks, but also of a sea of gluons and virtual quark-antiquark pairs.

1.3.1 Factorization

Hadron-hadron and lepton-hadron interactions are described in QCD as an incoherent sum of the interaction of the constituent partons (quarks, gluons) from one hadron with those of the other hadron or with the lepton[5]. The distributions of partons in hadrons cannot be calculated, at present, from first principles.
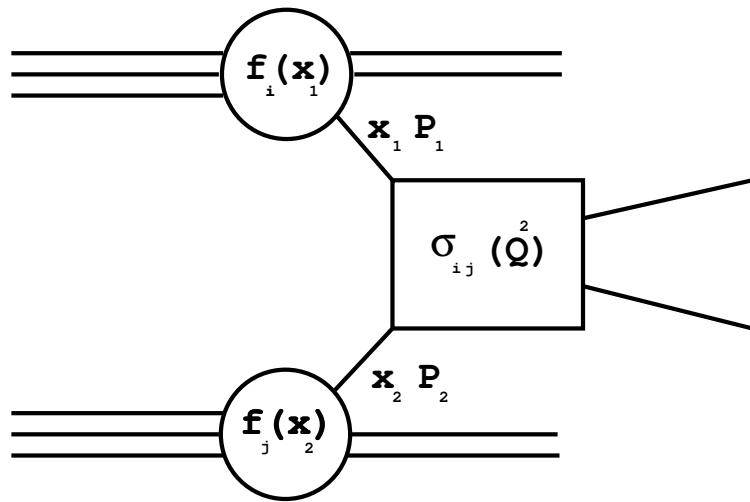
Figure 1.5 - Factorization: separation of the short-ranged and long-ranged physics. The parton distributions in the hadrons cannot be perturbatively calculated (long-ranged physics). The hard cross section $\sigma_{ij}(Q^2)$ is perturbatively calculable (short-ranged physics).

A separation of the short-ranged (hard processes) and long-ranged (soft-processes) physics is introduced. This separation is called *factorization*. The QCD factorization theorem [Co85] states that for hard scattering reactions the cross section can be decomposed into the flux of incoming particles and the cross section for the hard process (see figure 1.5):

$$\sigma = f_{i/1}(x_1) \otimes \sigma_{i,j}(Q^2) \otimes f_{j/2}(x_2), \tag{1.50}$$

where $f_{i/1}(x_1)$ and $f_{j/2}(x_2)$ are the fluxes of the incoming particles. $\sigma_{i,j}(Q^2)$ is the cross section (matrix element) for the hard scattering of the two partons i and j.

The flux of incoming particles depends on the parton distribution functions, i.e. on the probability to find a particular parton having a momentum fraction in the range

---

[5]The total amplitude of the interaction is an incoherent sum of the amplitudes of the interactions of the constituents.

$(x, x + dx)$. So $f_{i/1}(x_1) \cdot dx_1$ is the probability to find the parton i in the first hadron carrying a fraction x_1 of its momentum.

Generally, parton distribution functions give the probability to find partons (quarks and gluons) in a hadron as a function of the fraction x of the hadron's momentum they carry.

In order to perform the factorization, a hard scale μ_F - the factorization scale - has to be introduced. The long-ranged (non perturbative) processes are absorbed into the parton distribution functions (PDFs). These parton distribution functions are assumed to be universal, i.e. process independent. At present it is not possible to calculate them in QCD and their values are determined from experimental results.

On the other hand, the cross section for the hard process is a short-ranged process and can be perturbatively calculated.

In addition, pQCD introduces another scale μ_R - the renormalization scale. By introducing the renormalization scale the divergences coming from the calculation of virtual corrections (which yield divergent integrals) are absorbed into the definition of the parameters of the theory. Several renormalization schemes are used, the most important being the *minimal subtraction scheme* - $\overline{MS}$ and the *deep inelastic scattering scheme* - DIS.

1.3.2   QCD evolution equations

The Q^2 dependence of the parton distribution functions can be calculated within pQCD. The main origin of this dependence is that a quark seen at a certain scale Q_0^2 as carrying a certain fractional momentum of the hadron x_0 can be resolved into more quarks and gluons if it is probed at a higher scale Q^2. The resolved quarks and gluons carry a smaller fractional momentum of the hadron ($x < x_0$). The change of the structure function F_2 with increasing scale is schematically shown in figure 1.6. Thus, when all QCD effects are included, the structure function F_2 is expected to rise at low x. This is because the low x region is populated by gluons and sea quarks and the quark density is large. The resulting logarithmic dependence of F_2 on Q^2 at fixed x is known as *scaling violation*.

At HERA, the structure function F_2 has been measured in a very wide range of Q^2 and x and the scaling violation at low x has been demonstrated. This is shown in figure 1.7.

The DGLAP (Dokshitzer-Gribov-Lipatov-Altarelli-Parisi [Al77]) equations are a set of $(2n_f + 1)$ coupled integro-differential equations. They can be used to determine the quark and gluon distribution functions for any value of Q^2 provided they are known at a particular value Q_0^2 within the range of applicability of perturbative QCD. These equations are derived by requiring that the structure functions F_1 and F_2 be independent of the choice of the factorization scale μ_F, that is:

$$\mu_F^2 \left(\frac{dF_i(x, Q^2)}{d\mu_F^2} \right) = 0 \qquad ; \qquad i = 1, 2. \qquad (1.51)$$

In a first step, the DGLAP equations were derived in the *leading logarithm approximation* - LLA. The terms which give the dominant contributions at large x and Q^2
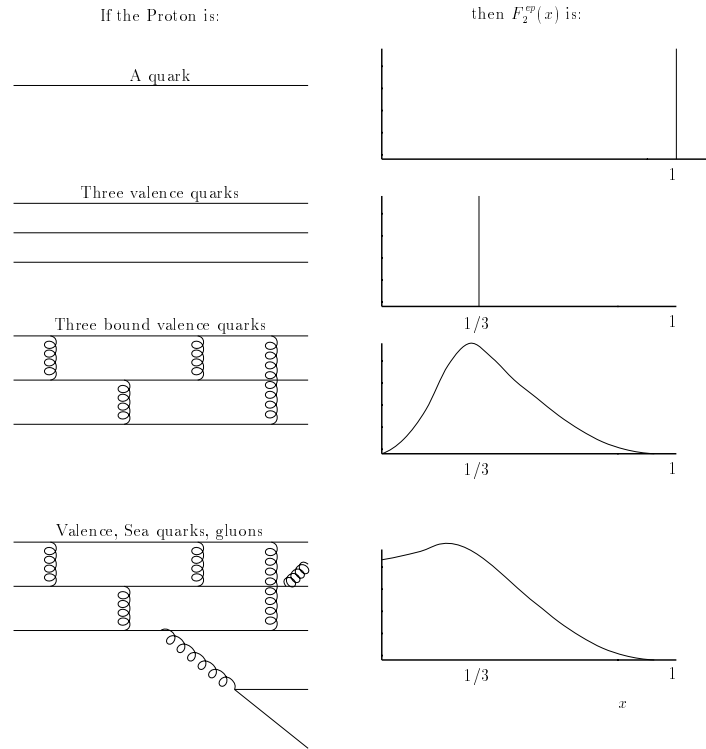
Figure 1.6 - The proton structure function F_2 pictured assuming different compositions for the proton. The two top pictures show the case of QPM. The two bottom pictures show the modifications induced by QCD effects.

were summed to all orders. All other terms were neglected.

In a compact form the DGLAP equations can then be written as:

$$\frac{\partial}{\partial \ln Q^2} \begin{pmatrix} q \\ g \end{pmatrix} = \frac{\alpha_s(Q^2)}{2\pi} \begin{bmatrix} P_{qq} & P_{qg} \\ P_{gq} & P_{gg} \end{bmatrix} \otimes \begin{pmatrix} q \\ g \end{pmatrix}, \qquad (1.52)$$

where $q(x, Q^2)$ ($g(x, Q^2)$) are the quark (gluon) distributions, and $P_{ij}(x)$ are the splitting functions. The latter describe the probability to find a parton of type i with given fractional momentum originating from the parton of type j, where i, j can be a quark or a gluon.

Given a specific factorization and renormalization schemes, the splitting functions are obtained in pQCD as expansion series in α_s:

$$\frac{\alpha_s}{2\pi} P_{ij}(x, Q^2) = \frac{\alpha_s}{2\pi} P_{ij}^{(1)}(x) + (\frac{\alpha_s}{2\pi})^2 P_{ij}^{(2)}(x) + ... \qquad (1.53)$$

The truncation after the first two terms in the series defines the next-to-leading order (NLO) DGLAP evolution equations.

The DGLAP equations are valid as long as the impact of the neglected terms is small. At very low x this is not true anymore. In this region another approach is used and the calculations lead to the BFKL (Balitsky-Fadin-Kuraev-Lipatov [Ku76]) equations. DGLAP deals with Q^2 evolution and is inadequate at very low x. BFKL deals with the $\frac{1}{x}$ evolution and is inadequate at large Q^2.
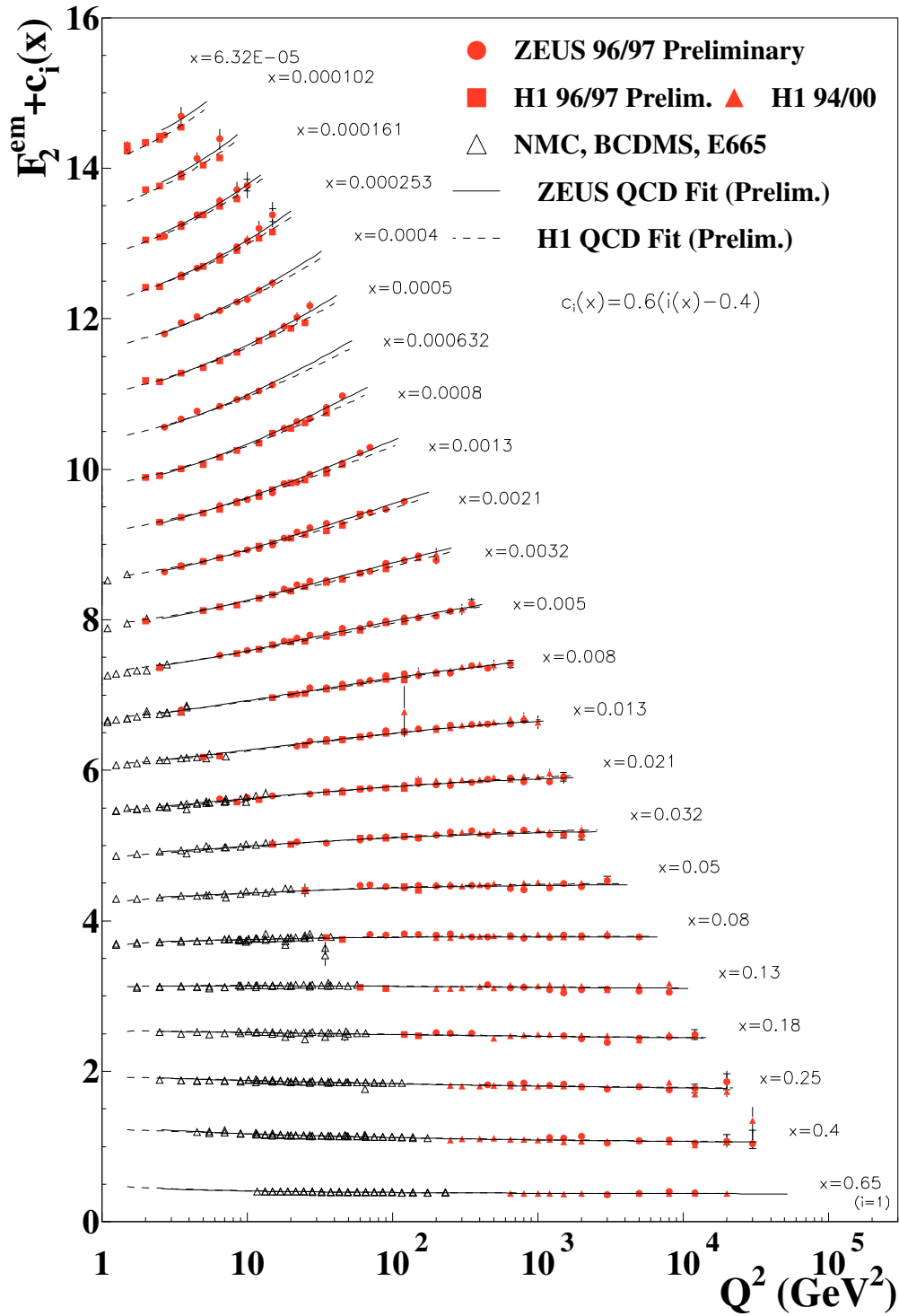
Figure 1.7 - Measurement of the structure function F_2 as a function of Q^2 for different values of x. The F_2 measurements at different values of x have been scaled by constant factors for display purposes. The evolution of the structure functions through the DGLAP equations are also shown.

The inclusive measurement of F_2 at HERA has shown that the evolution of structure functions through the DGLAP equations is in good agreement with the experimental results (figure 1.7). Until now no experimental evidence for BFKL effects has been observed.

Attempts have been made to achieve a unified description embodying both DGLAP- and BFKL-type of evolution. Evolution equations which allow an evolution in Q^2 as well as in x are included in the CCFM (Ciafaloni-Catani-Fiorani-Marchesini [Ci88]) evolution equations.

1.4   Photoproduction

The kinematical regime where Q^2 is very small ($Q^2 \simeq 0$) is called *Photoproduction*. In photoproduction events the scattered electron has a very small angle with respect to the incoming one. Therefore, most of the time it goes undetected through the rear beam pipe[6]. The exchanged photon is quasi-real.

In photoproduction the hard scale of the interaction cannot be identified with Q^2 but with the transverse energy of the (hard) outgoing partons. The situation now is reversed and the proton is not anymore being probed by the photon. In fact, both the proton and photon are probed by the exchanged virtual partons.

---

[6]At HERA, in some cases the very-low-angle scattered electron can be detected in the luminosity monitor.

Chapter 2

The HERA collider and the ZEUS detector

2.1   The Hadron Electron Ring Accelerator

Figure 2.1 - View of DESY.

The HERA (Hadron Elektron Ring Anlage) collider is located at DESY in Hamburg, Germany. It offers unique opportunities to explore the structure of the proton as it is the first ep collider in the world. Figure 2.1 shows an aerial view of DESY and the
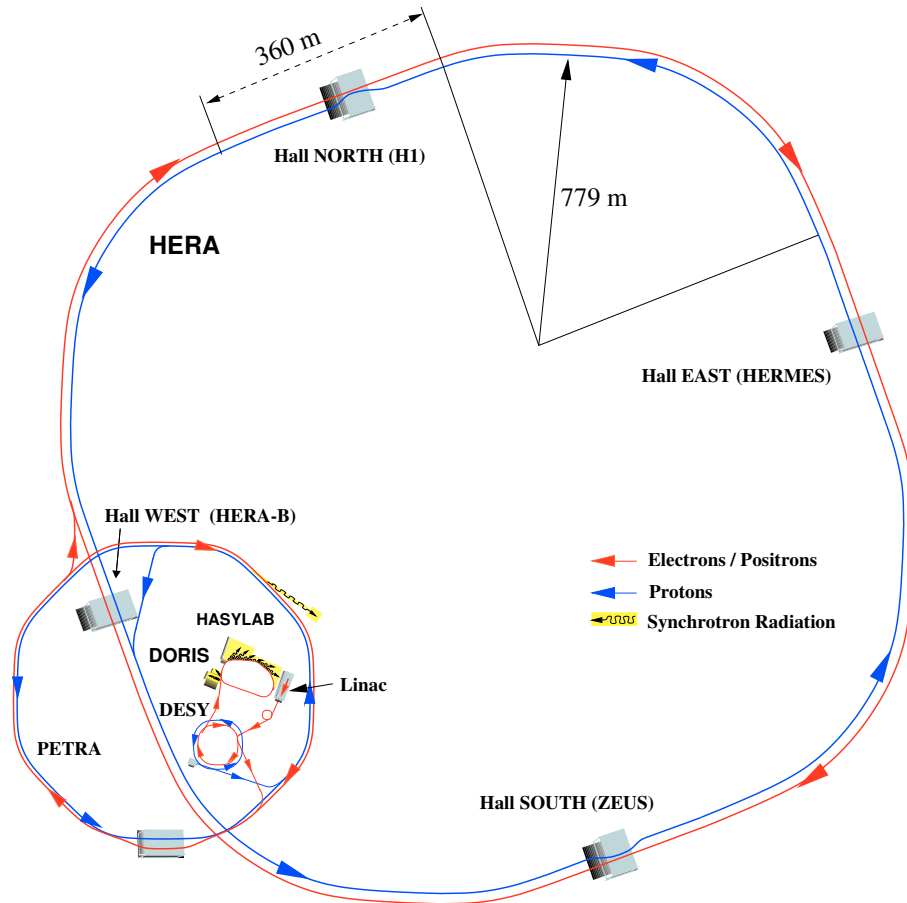
Figure 2.2 - The HERA accelerator complex. Four experiments are located in the experimental halls : South (ZEUS), West (HERA-B), North (H1), and East (HERMES).

surrounding area including the location of the two largest accelerators HERA and PETRA.

HERA was approved in 1984 and first collisions were observed in 1991. Operations for physics started in 1992. HERA consists of one storage ring for protons and one for electrons. The design energy is 30 GeV for electrons and 820 GeV for protons. Each storage ring consists of four $90°$ arcs connected by 360 m long straight sections and is located (10–25) m below ground. Superconducting magnets are used for the proton storage ring. Four experimental halls (North, South, East, West) are situated in the middle of the straight sections. The two collider experiments, H1 and ZEUS, are located in the northern and southern experimental halls, respectively. In both interaction regions electrons and protons collide head-on at zero crossing angle. Two fixed-target experiments, HERMES and HERA-B, have been installed in the eastern and western experimental halls, respectively. They make use of only the HERA electron (HERMES) and proton (HERA-B) beams, respectively. HERMES [HE93] is investigating the spin structure of the nucleon and HERA-B [HB94] aims to study the $\mathcal{CP}$-violation in the $B^0\overline{B^0}$-system. Figure 2.2 shows the layout of the HERA collider, the four experimental halls and the system of pre-accelerators used at DESY. In a first step electrons and protons are accelerated using linear accelerators. A small

HERA parameters	Design Values		Values of 1997	
	$e^{\pm}$	p	e^{+}	p
Circumference (m)	6336			
Energy (GeV)	30	820	27.6	821.2
Center-of-mass energy (GeV)	314		301	
Injection energy (GeV)	14	40	12	40
Energy loss per turn (MeV)	127	$1.4 \cdot 10^{-10}$	127	$1.4 \cdot 10^{-10}$
Current (mA)	58	160	36	78
Magnetic field (T)	0.165	4.65	0.165	4.65
Number of bunches	210	210	174+15	174+6
Bunch crossing time (ns)	96			
Horizontal beam size (mm)	0.301	0.276	0.200	0.200
Vertical beam size (mm)	0.067	0.087	0.054	0.054
Longitudinal beam size (mm)	0.8	11	0.8	11
Specific luminosity ($cm^{-2}s^{-1}mA^{-2}$)	$3.6 \cdot 10^{29}$		$5.0 \cdot 10^{29}$	
Instantaneous luminosity ($cm^{-2}s^{-1}$)	$1.6 \cdot 10^{31}$		$1.45 \cdot 10^{31}$	
Integrated luminosity per year (pb^{-1}/a)	35		36.5	

Table 2.1 - HERA parameters. In 1997 HERA operated with 174 colliding bunches, 15 positron-pilot bunches and 6 proton-pilot bunches.

storage ring PIA (Positron-Intensity-Accumulator) is used in between the linear accelerator and DESY II to accumulate electrons until sufficient intensity is reached. In a next step the particles are injected into DESY II (electrons) and DESY III (protons). After injection into PETRA and further acceleration, electrons and protons are injected into HERA. From 1995 to 1997 positrons were used instead of electrons because severe lifetime problems of the electron beam were observed. The reason is most likely the capturing of positively-charged dust which originates from ion getter pumps from the HERA electron vacuum system by the electron beam [DE94]. With the installation of new pumps in the winter shutdown 1997/1998 the problem has been significantly reduced and HERA switched back to electrons in 1998. Several HERA parameters from the 1997 runing period and the corresponding design values are given in table 2.1.

2.2 The ZEUS Detector

The ZEUS detector is a general purpose magnetic detector designed to study various aspects of electron-proton scattering. It has been in operation since 1992 [ZE93] and consists of various sub-components to measure the hadrons and leptons in the final-state and, therefore, to characterize the final-state in terms of energy, direction, and type of the produced particles.

The coordinate system of the ZEUS detector is a Cartesian right-handed coordinate system. The origin $((X, Y, Z) = (0, 0, 0))$ is located at the nominal interaction point. The Z-axis points in the proton beam direction, the Y-axis upwards, and the X-axis horizontally towards the center of HERA. The polar (azimuthal) angle θ (ϕ) is de-
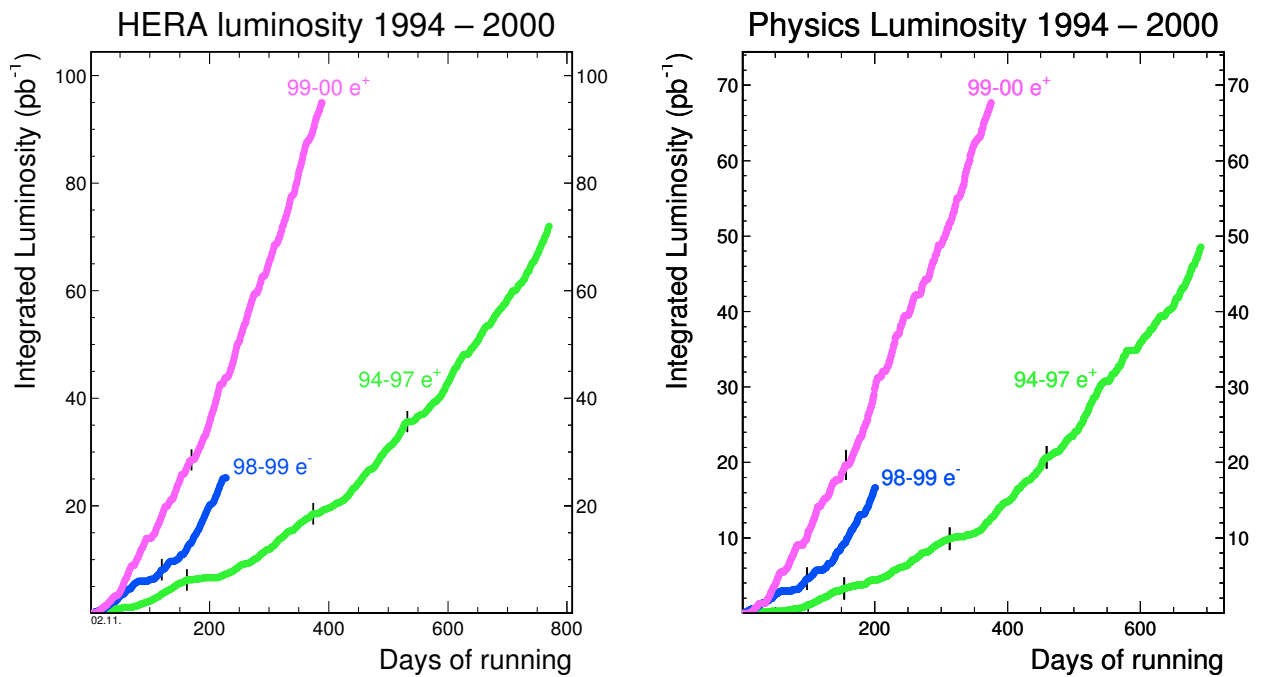
Figure 2.3 - Integrated luminosity delivered by HERA in the different running periods (left plot) and the one taken with the ZEUS detector (right plot). The latter is used for physics analysis.
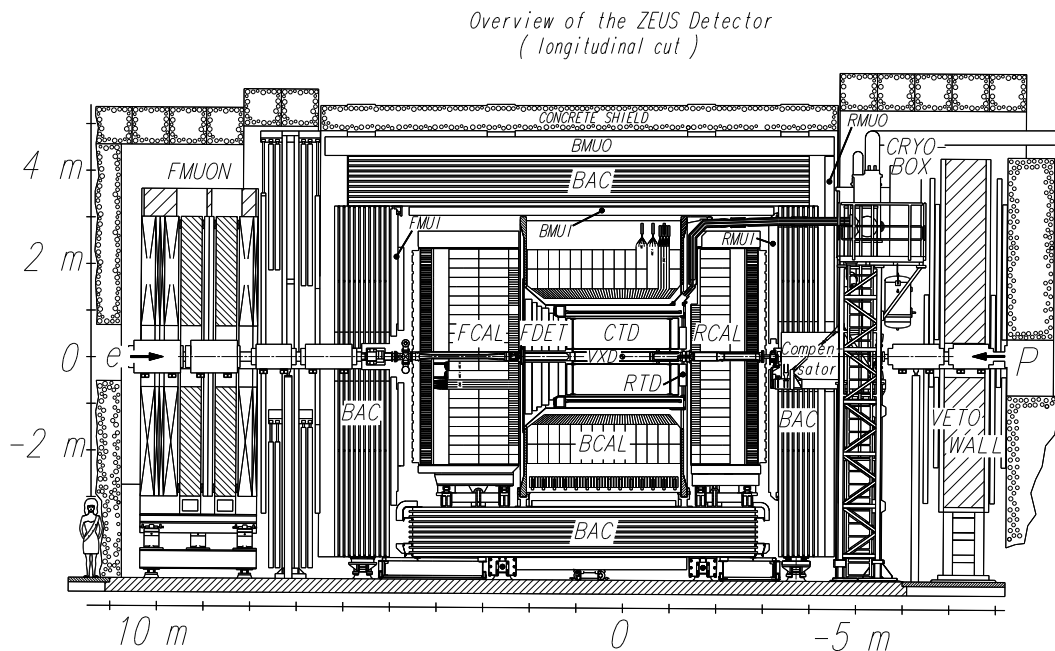
Figure 2.4 - View of the ZEUS detector along the beam direction.
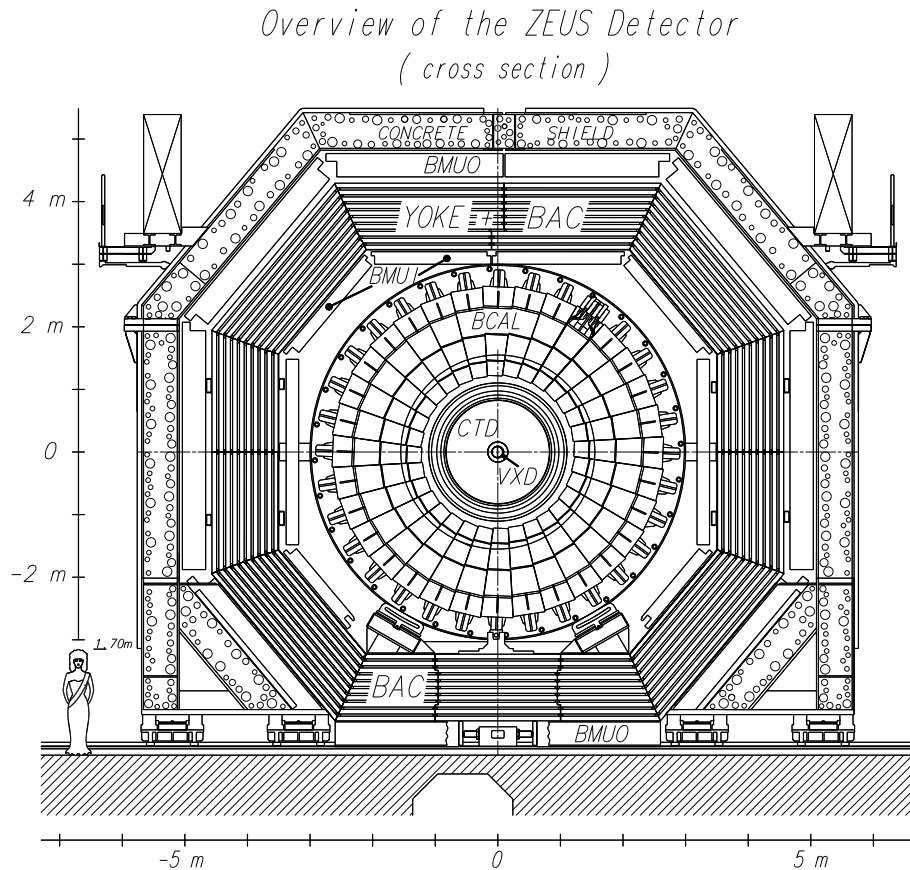
Figure 2.5 - View of the ZEUS detector perpendicular to the beam direction. See text for a description of the components.

termined relative to the positive Z-axis (X-axis). With this definition the polar angle of the incoming electron beam is $180°$ and that of the incoming proton beam is $0°$. The +Z-direction is referred as the *forward*, and the −Z-direction as the *backward* direction.

The ZEUS detector consists of the main detector located around the nominal interaction point and several small detectors positioned along the beam line in both positive and negative Z-directions. The main detector is shown in figures 2.4 and 2.5 along and perpendicular to the beam direction, respectively. The design is asymmetric with respect to the Z-axis because of the large forward-backward asymmetry of the final-state system. The difference in the energy of the electron beam (27.5 GeV) and proton beam (820 GeV) results in a center-of-mass system which is moving in the direction of the proton beam relative to the laboratory frame.

The inner part of the main detector consists of the tracking system enclosed by a superconducting solenoid which produces an axial magnetic field of $1.43\,\mathrm{T}$. The CTD, a cylindrical drift chamber, surrounds the beam pipe at the interaction point. In order to provide additional means of track reconstruction in the forward (backward) direction, the CTD was supplemented by the FTD (RTD). The FTD consists of three sets of planar drift chambers with transition radiation detectors (TRD) in between. The RTD is one planar drift chamber with three layers. The vertex detector VXD measures the event vertex and possibly secondary vertices and improves the momentum and

angular resolution of charged particles as determined with the CTD alone. In 1994 high voltage problems and damage due to synchrotron radiation caused part of the VXD to be off and it was removed.

The high resolution uranium calorimeter (UCAL) encloses the tracking detectors. It is subdivided into the forward (FCAL), barrel (BCAL), and rear (RCAL) parts.

The UCAL in turn is surrounded by an iron yoke made of 7.3 cm thick iron plates. The yoke serves two purposes: it provides a return path for the solenoid magnetic field flux and, in addition, is instrumented with proportional chambers. The latter design feature makes it possible to measure energy leakage out of the UCAL. The yoke is therefore referred to as the backing calorimeter (BAC). As the yoke is magnetized to 1.6 T by copper coils it is used to deflect muons. In order to detect and measure the momentum of muons, limited streamer tubes are mounted surrounding the iron yoke in the barrel (BMUI, BMUO) and the rear (RMUI, RMUO) regions. As the particle density and the muon momentum in the forward direction is higher than in the barrel and rear directions due to the energy difference of the electron and proton beam, the muon chambers in the forward direction are designed differently. Limited streamer tubes mounted on the inside of the iron yoke (FMUI) and drift chambers and limited streamer tubes mounted outside the iron yoke (FMUO) are used for this purpose. Two iron toroids provide a toroidal magnetic field of 1.7 T. In the backward direction at $Z = -7.3$ m, a veto wall outside the detector composed of iron and scintillation counters is used to reject background events dominated by proton-beam-gas reactions.

2.2.1   The Central Tracking Detector

The tracking system of the ZEUS detector consists of the forward, central and rear tracking devices, which operate under a high magnetic field of 1.43 T to achieve a high resolution for high momentum tracks. All the tracking quantities used in this analysis are provided by the Central-Tracking Detector (CTD) [Fo93]. The CTD is a cylindrical drift chamber which provides a high precision measurement of the direction and transverse momentum of charged particles and of the event vertex. The position resolution in $r - \phi$ is about 230 μm and the transverse momentum resolution is

$$\frac{\sigma(p_t)}{p_t} = 0.0058 \cdot p_t(\text{GeV}) \oplus 0.0065 \oplus \frac{0.0014}{p_t} , \qquad (2.1)$$

where the first term corresponds to the resolution of the hit positions, the second term to smearing from multiple scattering within the CTD and the last term to multiple scattering before the CTD. The position of the interaction point in X and Y is measured with a resolution of 0.1 cm and in Z with a resolution of 0.4 cm.

The CTD is filled with a mixture of argon, CO_2, and ethane. Particle identification is possible by measurements of the mean energy loss dE/dx of charged particles within the tracking detector. The CTD covers a polar angle of $15° < \theta < 164°$ and the full range of the azimuthal angle ϕ. Its active volume has a length of 205 cm, an inner radius of 18.2 cm, and an outer radius of 79.4 cm.

The CTD is designed as a multi-cell superlayer chamber and subdivided into eight
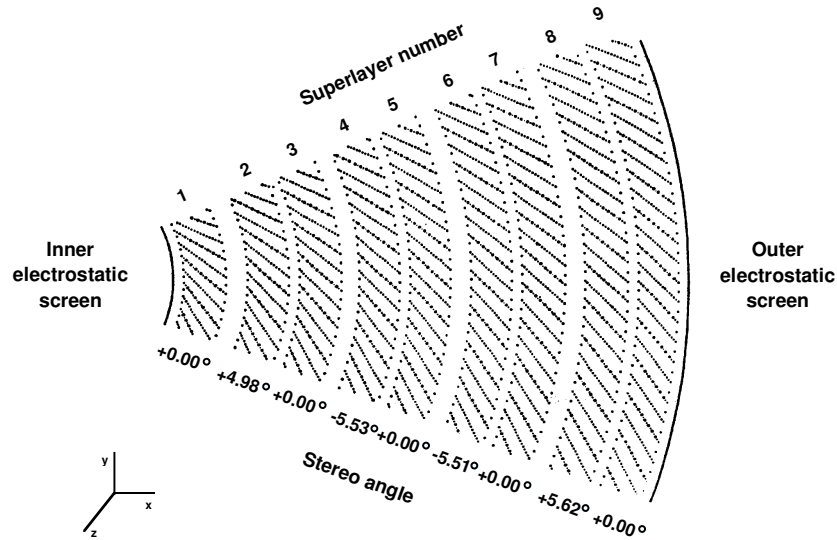
Figure 2.6 - Layout of a CTD octant. Each octant has nine superlayers with the even numbered ones declined with respect to the beam axis ('Stereo angle').

sections and nine superlayers. One octant is shown in figure 2.6. The CTD consists of 576 cells with each cell being equipped with eight sense wires. The number of cells increases from 32 in the innermost superlayer to 96 cells for the outermost superlayer. Every other superlayer has its sense wires rotated by a certain angle with respect to the beam axis. The angles for each superlayer are given in figure 2.6. With this configuration the Z position of a track can be reconstructed with an accuracy of aproximately 2 mm.

2.2.2   The Uranium-Scintillator Calorimeter (UCAL)

Calorimeters in particle physics measure the energy of particles by their absorption in a medium that becomes ionised or excited through shower processes. The ZEUS calorimeter (UCAL) has been designed as a sampling calorimeter, where absorber layers alternate with scintillator layers, which are the optical readout. The calorimeter is required to be hermetic with a nearly full solid-angle coverage and to have a good hadronic energy resolution by achieving an equal response to electromagnetic and hadronic particles.

The UCAL is divided into three parts, which cover different polar angles [De91]. All parts of the calorimeter, FCAL ($2.2° < \theta < 39.9°$), BCAL ($36.7° < \theta < 128.1°$), and RCAL ($128.1° < \theta < 176.5°$) are built of alternating layers of 3.3 mm thick depleted uranium and 2.6 mm thick plastic scintillator plates (SCSN38). The natural radioactivity of ^{238}U is used as a reference signal to calibrate the readout channels to a precision of $< 0.2\%$.

Uranium is an advantageous absorber for hadron calorimetry, since it provides a high yield of spallation neutrons which impart the energy to the hydrogen nuclei of the scintillator. Together with an additional contribution of photons from neutron cap-

C - leg

tension strap

back beam

4.6m

PARTICLES

photomultiplier

HAC tower

silicon detector

scintillator plate

DU - plate

wave length shifter

EMC tower

2m

12t
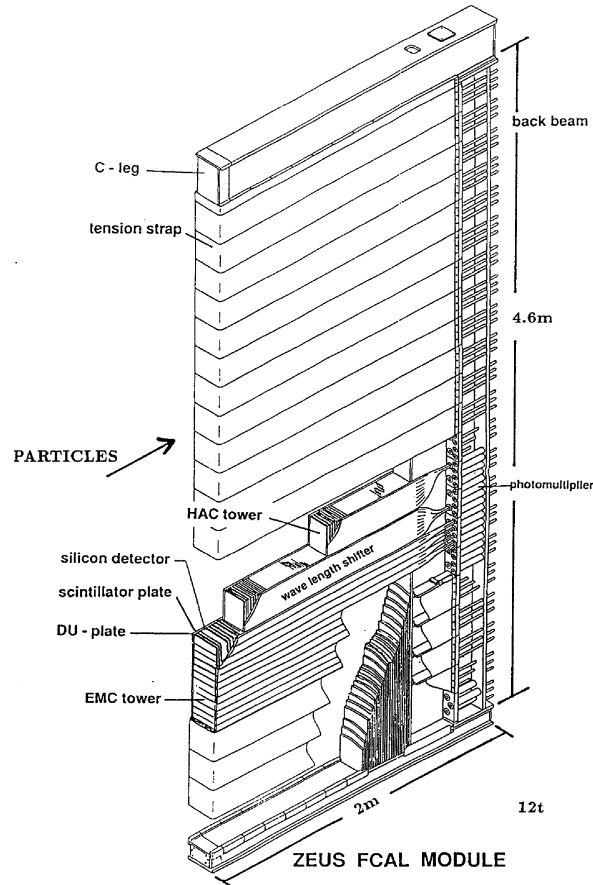
ZEUS FCAL MODULE

Figure 2.7 - Layout of a FCAL module. The UCAL modules are subdivided into one electromagnetic (EMC) and two hadronic (HAC1,HAC2) sections, which in turn are divided into cells. A cell is read out on two opposite sides by one wavelength shifter each.

ture of the uranium, this helps to compensate the signal loss of hadrons arising from the loss of binding energy, nuclear fission fragments and from undetected decay products. Electrons and photons do not suffer such losses as they interact predominantly with the atomic electrons and not with the nuclei. The ratio between the pulse heights of electrons and hadrons, e/h, which has been achieved is

$$e/h \; = \; 1.00 \; \pm 0.03 \tag{2.2}$$

The three calorimeter parts are subdivided into modules. The modules are transversally separated into towers and the towers in turn longitudinally into electromagnetic (EMC) and hadronic sections (HAC). The design of an FCAL module is shown in figure 2.7. The FCAL and RCAL modules are planar and perpendicular with respect to the beam axis (see figure 2.4), while the BCAL modules are wedge-shaped and projective in the polar angle. The calorimeter modules are further segmented into cells. The design of the three calorimeter parts takes into account the different particle densities and energies due to the asymmetric electron and proton beam energies. Each EMC section is segmented transversally into four cells (two in RCAL), while a HAC tower is not divided transversally. They are instead longitudinally subdivided

Figure 2.8 - Location of ZEUS detectors in negative Z-direction. Shown are the gamma (LUMIG) and electron detectors (LUMIE) used for the luminosity measurement.

into two (one in RCAL) hadronic cells (HAC1, HAC2). Each cell is read out on two opposite sides. This is done on each side by a wavelength shifter coupled to one photomultiplier tube. The information of both photomultiplier tubes is used to provide a limited reconstruction of the position of the measured particle and to check the uniformity of the readout.

The single particle energy resolution for electrons and hadrons was determined in test-beam experiments to be $\sigma_E/E = 0.18/\sqrt{E}$ and $\sigma_E/E = 0.35/\sqrt{E}$ respectively, where E is mesured in GeV.

2.3 The Luminosity measurement

The luminosity, $\mathcal{L} \equiv N/\sigma$, relates the number of events N with the cross section σ. A precise determination of the luminosity is essential for any cross section measurement in a high energy physics experiment. The luminosity of ep-collisions at HERA is measured by observing the rate of hard bremsstrahlung photons from the Bethe-Heitler process $ep \to e\gamma p$ [Be34]. As the theoretical cross section is known to an accuracy of 0.5% from QED calculations, a precise measurement of the photon rate permits a precise determination of the ep-luminosity at HERA.

Figure 2.8 shows the layout of the HERA magnet system and the ZEUS luminosity detectors in the backward (–Z)-direction. In the case of ZEUS this is done by two lead/scintillator electromagnetic calorimeters at $Z = -34$ m (LUMIE) and $Z = -107$ m (LUMIG). Photons with $\theta_\gamma < 0.5$ mrad originating from the Bethe-Heitler process $ep \to e\gamma p$ are detected by the LUMIG detector [An92]. The energy resolution of the LUMIG detector was measured under test-beam conditions to be $18\%/\sqrt{E}$. It was also determined that the carbon/lead filter placed in front of the detector to shield it against synchrotron radiation degrades the resolution to $23\%/\sqrt{E}$. The impact position of incoming photons can be determined with a resolution of 0.2 cm in X and

Y, because at a depth of $7X_0$ 1 cm wide scintillator strips are installed within the LUMIG detector. The LUMIG detector is also used to determine the electron beam tilt and to measure photons from initial-state radiation.

The LUMIE calorimeter [An92] at $Z = -35$ m detects electrons in the limited energy range from 7 to 20 GeV which are produced under polar angles of less than 5 mrad with respect to the electron beam direction. These electrons are deflected by the HERA magnet system and leave the beam pipe at $Z = -27$ m through an exit window similar to the one in front of the LUMIG detector. The LUMIE detector has an energy resolution of $18\%/\sqrt{E}$ under test-beam conditions. It was initially designed to measure the electrons of the Bethe-Heitler process $ep \rightarrow e\gamma p$ at the same time as the photons of this process are measured in the LUMIG detector. It was found that this was not necessary to have a precise measurement of the luminosity.

2.4   The ZEUS trigger and data acquisition systems

The short bunch crossing time at HERA of 96 ns, equivalent to a rate of of about 10^7 crossings per second , is a technical challenge and puts stringent requirements on the ZEUS trigger and data acquisition systems. The total interaction rate, which is dominated by background from upstream interactions of the proton beam with residual gas in the beampipe, is of the order 10 - 100 kilo-events per second (10 - 100 kHz) while the rate of ep physics events in the ZEUS detector is of the order of a few Hz [Sm84, Yo92]. Other background sources are electron beam gas collisions, beam halo and cosmic events.

ZEUS employs a sophisticated three-level trigger system in order to select ep physics events efficiently while reducing the rate to a few Hz. A schematic diagram of the ZEUS trigger system is shown in figure 2.9.

The First Level trigger (FLT) is a hardware trigger, designed to reduce the input rate below 1 kHz. Each detector component has its own FLT, which stores the data in a pipeline, and makes a trigger decision within 2 µs after the bunch crossing. The decision from the local FLTs are passed to the Global First Level Trigger (GFLT), which decides whether to accept or reject the event, and returns this decision readout within 4.4 µs. The typical information available at FLT are CAL activity (total transverse energy, missing transverse momentum,...), CTD tracks (number of tracks,...), hits in the muon chambers, etc.

If the event is accepted, the data is fully digitalised and transferred to the Second Level Trigger (SLT). The trigger signals at the SLT have a better resolution than those at the FLT. Moreover, some information is first available at the SLT like CAL timings, which are useful in rejecting non-ep background events. The SLT is designed to reduce the rates to the order of 50-100Hz. Each detector component has its own SLT, which passes a trigger decision to the Global Second trigger (GSLT) [Ui92].

If the event is accepted by the GSLT, all detector components send their data to the Event Builder (EVB), which combines all the data of an event into a single record of ADAMO [Fi93] database tables. This is the data structure on which the Third Level Trigger (TLT) code runs. The TLT is software based and runs part of the offline
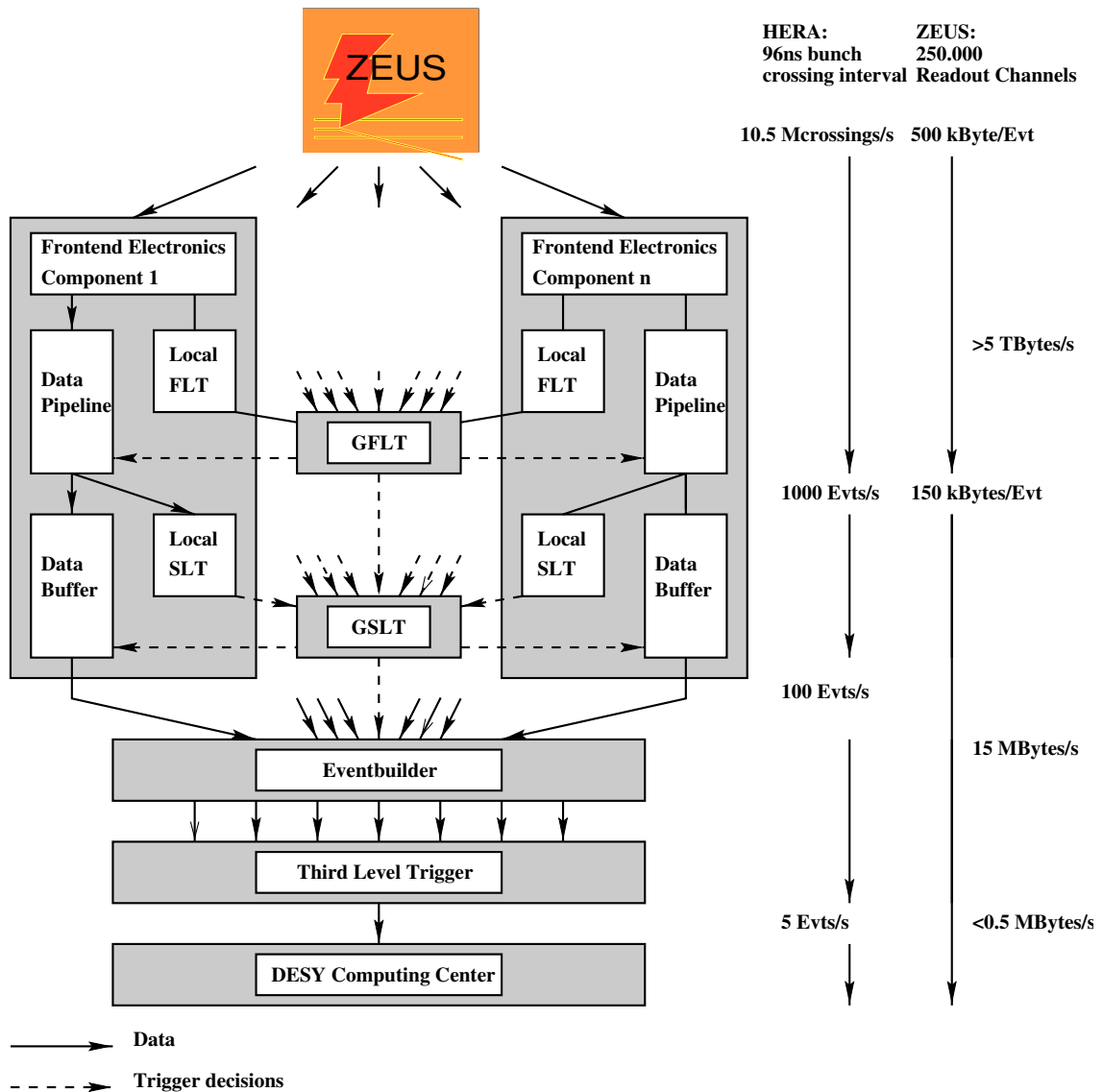
Figure 2.9 - Schematic diagram of the ZEUS trigger and data acquisition systems.

reconstruction code. It is designed to reduce the rate to a few Hz.

2.5 Event reconstruction and analysis

The scheme of the ZEUS offline and Monte Carlo (MC) simulation programs is shown in figure 2.10. Events from the real detector or simulated events are reconstructed by the program ZEPHYR, where the signals of the different calorimeter components are calibrated and highly complex tasks like tracking reconstruction are performed. After reprocessing the raw data, the user has access to the raw and reconstructed quantities via the program EAZE. In the framework of EAZE, the user writes his own analysis program in either Fortran or C. It is used to reconstruct relevant quantities and perform selection cuts. Subsets of the data or MC simulated
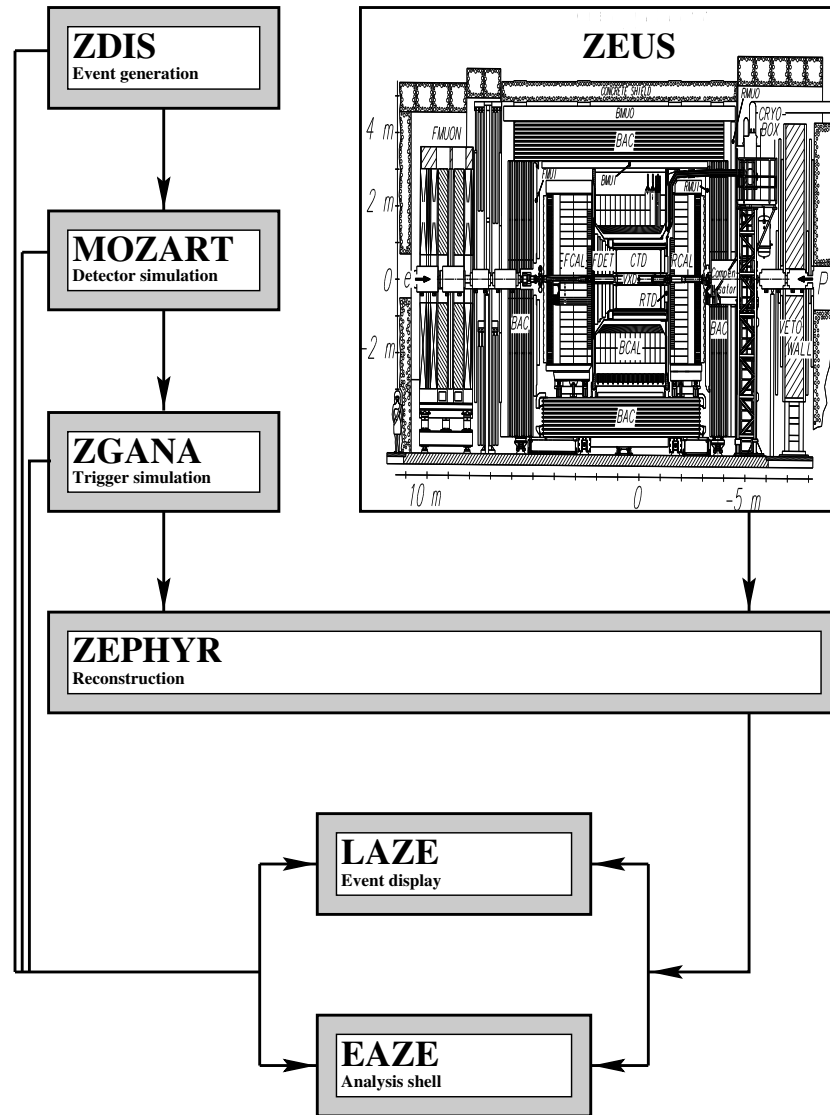
Figure 2.10 - Interrelationship of the ZEUS offline and Monte Carlo (MC) simulation programs.

events can be saved for further analysis. The program LAZE is an event display program which allows graphical viewing of various aspects of an event including the tracks of charged particles in the CTD, energy depositions in the CAL, and other component-related quantities. To allow fast access to specific types of events during reconstruction it is checked wether each event meets one of the conditions designed by the ZEUS analysis groups. If a specific condition is met, a flag called a DSTBIT is set. Before analyzing detailed component information in the user's EAZE program, the events can be preselected by requiring certain DSTBITS. This allows a faster loop over the whole data sets since only those events are processed further.

MC events are generated using the program ZDIS which contains a shell environment to steer a number of MC generator programs. The output data is stored in the same (ADAMO) format as the data from the real detector and passed to the ZEUS detector simulation program MOZART, based on the CERN GEANT program [Br87].

A simulation of the ZEUS trigger chain is done by the program ZGANA. Interfaces between the programs used for MC generation and the programs EAZE and LAZE provide specific MC information such as generated kinematic quantities, vertices and particles to the user. An overview of the physics analysis environment of the ZEUS experiment can be found in [Ba95].

Chapter 3

Jets

3.1 Jets in QCD

In HEP reactions partons are produced in the final state as a result of the hard under-
lying process. Because of color confinement it is not possible to observe quarks and
gluons as final-state particles of the reactions. The partons will radiate other par-
tons (parton shower) and will finally recombine to form color-singlet states (hadrons).
This last process is called hadronization.

The resulting hadrons will form a collimated "stream" of particles around the direction
of the original parton. This collimation of the final-state particles around the direction
of the initial partons has to do with the fact that the transverse energies involved in
the hadronization process are of the order of 300 MeV while the hard scatterings are
of the order of several GeV. These collimated flows of particles are called *jets*. Jets
are correlated with the primary partons, but one should not think that by measuring
jets we are measuring a primary parton. The jet is merely an event property that is
largely determined by the primary parton [Se95].

During a HEP reaction, low-transverse-momentum particles are also generated from
the extra hadronic activity in the event (not directly related to the hard scattering) and
form the *soft underlying event*. The soft underlying event overlaps with the jet formed
by the hard scattering. This is one of the difficulties in assigning final state jets to
original partons. The hadronization effects are theoretically not understood from first
principles and are estimated using phenomenological models.

3.2 Jet Finders

A jet algorithm assigns partons or hadrons to jets and calculates the physical quan-
tities (transverse energy, pseudorapidity, etc.) related to these new objects (jets).
There are different ways of defining jets. A jet should be well defined and easy to
measure from the hadronic final state, easy to calculate order-by-order in pQCD,
and it should have a close correspondence to the outgoing partons. For quantitative
measurements, jets are defined by using jet finding algorithms which are based on

Parton(s) $\xrightarrow[\text{shower}]{\text{parton}}$ Many partons $\xrightarrow[\text{models}]{\text{Monte Carlo}}$ Hadrons $\xrightarrow[\text{response}]{\text{detector}}$ Detector

jet definition

JETS $\xleftarrow[\text{correction}]{\text{showering}}$ JETS $\xrightarrow[\text{correction}]{\text{hadronization}}$ JETS $\xleftarrow[\text{correction}]{\text{detector}}$ JETS
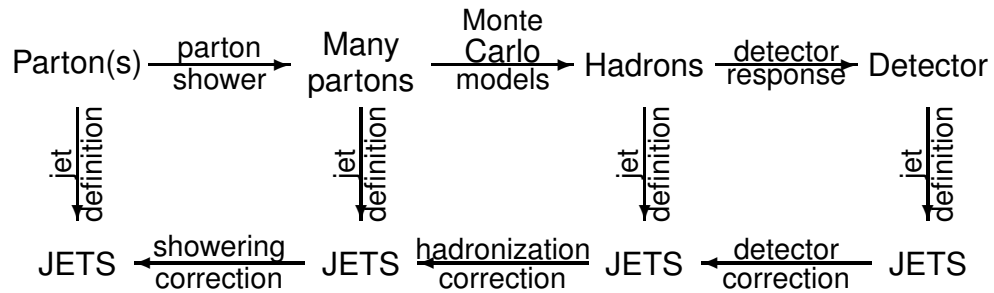
Figure 3.1 - Schematic diagram of a typical analysis using jets [Se95]. In the upper line the partons are produced from the hard scattering process and then radiate other partons (parton shower). Color-singlet states (hadrons) are produced through the process of hadronization. The hadrons deposit energy in the detector. At each stage the jet finding can be applied. From the measured data by the detector one can correct backwards, in principle, down to the parton level.

the assumption that the final state particles belonging to a jet are close to each other in space.

There are two main types of jet-finders (algorithms) commonly used: the cone algorithms, used mainly in $p\bar{p}$ experiments, and the clustering algorithms, used mainly in e^+e^- experiments. The cone algorithms define a direction that maximizes the energy flowing into a cone drawn around it. The clustering algorithms are based on iterative clustering procedures in which particles are merged together into pseudoparticles, which are the output jets.

From the theoretical and from the experimental points of view, a jet finding algorithm should fulfill the following two requirements:

1. **collinear safe**: the jet finding should treat a collinear pair of particles identically to a single particle with their combined momentum. From the theoretical point of view this means that the jet finding is independent of a particle splitting into two parallel travelling partons. Such a dependence would cause divergencies in the theoretical calculations, which are called *collinear divergencies*.

   From the experimental point of view, such a property means that the jet finding is largely independent of the granularity of the detector. Particles which go in the same calorimeter cell cannot be resolved anyway.

2. **infrared safe**: the jet finding should be insensitive to the emission of low energy particles. Theoretically, this property avoids the soft divergencies in perturbative calculations. Experimentally, cuts to suppress the detector noise are applied to make the jet finding as independent as possible of low energy deposits.

A schematic diagram of an analysis using jets is shown in figure 3.1. The jet finding can be done on: 1. detector objects (for example calorimeter cells), 2. hadrons or 3. partons. The comparison with the theory in this analysis is done at the hadron level.

3.2.1 The Snowmass Convention

Jet finding algorithms are applied to objects in the final state. These can be calorimeter cells or hadrons (partons) in the final state of real events or Monte Carlo simulated events. Below it is explained the way these objects are assigned to jets. After the jets are defined, the transverse energy and the coordinates (angles) of the jet are calculated from the energies and coordinates (angles) of the objects which form that jet. The quantities used in this analysis to characterize jets, namely the transverse energy, E_T^{jet}, the pseudorapidity [1], η^{jet}, and the azimuthal angle, ϕ^{jet}, are calculated using the *Snowmass Convention* [Hu90]:

$$
\begin{aligned}
E_T^{jet} &= \sum_i E_T^i \,, \\
\eta^{jet} &= \frac{1}{E_T^{jet}} \sum_i E_T^i \cdot \eta^i \,, \\
\phi^{jet} &= \frac{1}{E_T^{jet}} \sum_i E_T^i \cdot \phi^i \,,
\end{aligned}
\tag{3.1}
$$

where the sums in the above expressions run over all the objects assigned to the given jet.

3.2.2 Cone Algorithm

There are different cone algorithms generally used. They all associate hadrons within a cone of radius R in the $\eta - \phi$ space with the same jet. Here we discuss shortly the cone algorithm which was traditionally used in ZEUS(EUCELL).

At the beginning clusters are determined using a grid in the $\eta - \phi$ space. All the objects with transverse energy larger than a certain value (at ZEUS this is 300 MeV) are selected as seed "cells" for beginning the jet finding.

A cone of radius R is then placed around the seed with highest transverse energy and all objects within this cone, that is all objects fulfilling the condition

$$
(\phi_{object} - \phi_{seed})^2 + (\eta_{object} - \eta_{seed})^2 < R^2
\tag{3.2}
$$

are assigned to a jet and this jet (the objects belonging to it) is removed from further consideration. This procedure is repeated until no seed above the threshold is found. Typical values for the cone radius are $R = 1$ and $R = 0.7$.

Such an algorithm can be run with an upper pseudorapidity (η) cut on the found jets, so that very little, if any, proton remnant is included in the jets found. Cone algorithms are collinear safe but not infrared safe at higher orders. Low energy radiation between two jets could lead to a change of the seed position and, consequently, the found jets can be completely different.

---

[1] The pseudorapidity η is defined as $\eta = -\ln\left(\tan\frac{\theta}{2}\right)$, where θ is the polar angle with respect to the proton beam direction

The cone algorithms are usually faster to implement than clustering algorithms and, for this reason, it was used at the TLT. The main problem of cone algorithms is the issue of overlapping of jets: these algorithms are not able to unambiguosly separate jets which overlap. In addition, there is a bias arising from the choice of seeds.

3.2.3 Clustering Algorithms

The clustering jet finding algorithms have some advantages in comparison to the cone algorithms. The clustering algorithms have no overlapping jets since they unambiguously assign every object to a single jet. Furthermore, there is no seed choice dependence. The clustering algorithms are collinear and infrared safe.

Here we describe shortly the longitudinally invariant k_T cluster algorithm [Ca93, El93]. The k_T algorithm is applied in the following steps:

1. for every object i its distance to the beam is calculated as $d_i = E_{Ti}^2$

2. for every pair of objects the distance between them is calculated in the following way: $d_{ij} = min\left[E_{Ti}^2, E_{Tj}^2\right] \cdot \left((\eta_i - \eta_j)^2 + (\phi_i - \phi_j)^2\right)$

3. If the smallest of all the d_i and d_{ij} quantities is a d_{ij}, the objects i and j are recombined into a new object k following the p_T recombination scheme:

$$
\begin{aligned}
E_{Tk} &= E_{Ti} + E_{Tj}; \\
\eta_k &= \frac{E_{Ti} \cdot \eta_i + E_{Tj} \cdot \eta_j}{E_{Ti} + E_{Tj}}; \\
\phi_k &= \frac{E_{Ti} \cdot \phi_i + E_{Tj} \cdot \phi_j}{E_{Ti} + E_{Tj}}.
\end{aligned}
$$

4. If the smallest of all d_i and d_{ij} quantities is a d_i the object i is defined as a protojet and is no longer merged. This protojet is removed from further clustering.

5. the procedure is repeated for the remaining particles until none is left.

Jets are all the protojets with transverse energy above a certain (analysis defined) threshold E_T^{cut}.

3.3 Jet Internal Structure

A large fraction of the hadronic final states in hadron-hadron, electron-hadron and electron-positron collisions consists of high-energy jets. These jets have an extended structure in phase space which can be studied both experimentally and theoretically. Measurements of the internal structure of jets are very interesting because both the hard and soft part of QCD are probed. Possible measurements of such structure are subjets, which are defined in section 3.3.1.
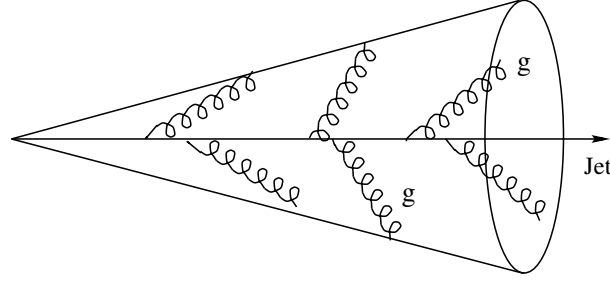
Figure 3.2 - Gluon radiation within a jet.

The internal structure of a jet is expected to depend mainly on the type of primary parton, quark or gluon, and to lesser extent on the particular hard scattering process. In QCD there are three fundamental vertices representing the three- and four-gluon coupling, and the coupling of a quark current to a gluon. Neglecting the four gluon coupling, which is $\mathcal{O}(\alpha_S^2)$, three fundamental processes are described by these vertices: radiation of a gluon by a quark ($q \rightarrow qg$) or by another gluon ($g \rightarrow gg$) and the splitting of a gluon into quark-antiquark pair ($g \rightarrow q\overline{q}$). The probabilities of these processes are given by the splitting amplitudes and are proportional to the colour factors C_F, C_A and T_F, respectively (which are the structure constants of the SU(3) colour symmetry group of QCD). As the main contribution to particle production in hadronic events is due to radiation of gluons, the internal structure of jets is mostly sensitive to C_A and C_F.

Calculations of multiplicity distributions in QCD [El96] predict that the average multiplicity of any type of object in a gluon jet should asymptotically become C_A/C_F times larger than in quark-initiated jets:

$$\langle\, N_g\,\rangle \sim \frac{C_A}{C_F}\,\langle\, N_q(Q^2)\,\rangle \tag{3.3}$$

The multiplicity distribution should also become wider for a gluon jet by a factor $\sqrt{C_A/C_F}$

$$\sigma_{N_q} \sim \left(1 + \frac{C_F}{3C_A}\right) N_q^2 \;\; ; \;\; \sigma_{N_g} \sim \frac{4}{3}\, N_g^2\,, \tag{3.4}$$

where σ_{N_q} (σ_{N_g}) are the second multiplicity moments for quark (gluon) jets. At sufficiently high transverse energy of the jet, the internal structure of jets is expected to be driven mainly by gluon emission of the primary parton (figure 3.2). The differences between quark and gluon jets arise from the larger strength of the gluon-gluon coupling ($\sim C_F$) with respect to that of the quark-gluon coupling ($\sim C_A$). As a consequence, QCD predicts gluon jets to be broader than quark jets.

3.3.1 Subjets

"Subjets" are jet-like structures within a jet. To define such structures the k_T clustering algorithm is re-applied to all the particles assigned to a given jet until the distances between every pair of particles satisfy

$$d_{ij} > y_{cut}\, (\, E_T^{jet}\,)^2 \tag{3.5}$$
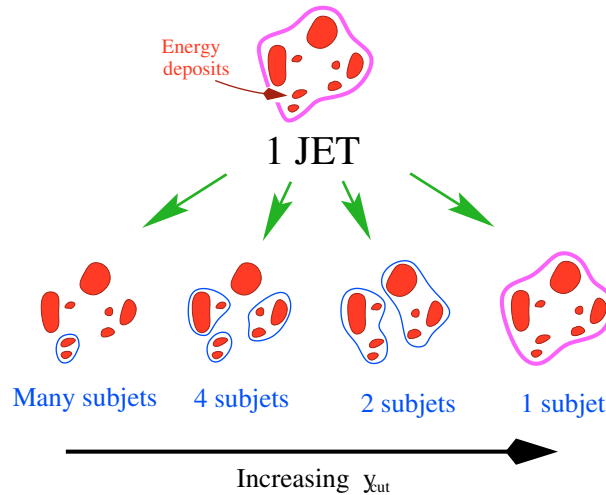
Figure 3.3 - The internal structure of jets can be studied by resolving jet-like structures ("subjets"). As the resolution scale y_{cut} decreases an increasing number of "subjets" is resolved.

for a given resolution scale (y_{cut}). At each y_{cut} the resulting objects found inside a jet are called *"subjets"*. The mean number of subjets inside a jet ($< n_{sbj} >$) or "mean subjet multiplicity" is an observable which can be measured and compared with pQCD predictions.

The number of "subjets" inside a jet increases as the resolution scale decreases (see figure 3.3). For very small values of y_{cut} the hadrons inside the jet are resolved.

If the transverse energy of the jet is of the order of $E_T^{jet} \sim 10$ GeV, to be able to resolve subjets of transverse energy of $E_{T_i} \sim 1$ GeV the resolution scale must be of the order of $y_{cut} \sim 10^{-2}$. In this case, for resolution scales smaller than $y_{cut} \sim 10^{-2}$ pQCD cannot be applied. As the transverse energy of the jet increases, pQCD calculations can be performed for smaller values of the resolution scale.

3.4   Jet production in DIS at HERA

Jet production in DIS is the manifestation of QCD effects and, therefore, a sensitive probe of colour dynamics. Studies of jets in DIS provide a testing ground for understanding perturbative and non-perturbative aspects of QCD.

At HERA, clean jet structures can develop thanks to the large available center-of-mass energy. In the identification of jets from the hard subprocess, it is preferred to have as little contamination as possible from the remnant of the proton. Therefore, the jet finders must have some feature which reduces this contamination. The most suitable algorithm for jet studies at HERA is the K_T algorithm. In the K_T algorithm the clustering of particles is weighted with the transverse energy, which implicitly suppresses the contribution from the proton remnant (E_T[proton remnant]~ 0).

Jet production in CC DIS ($e^+p \rightarrow \overline{\nu_e} + \text{jet(s)} + X$) is described in the SM at lowest order in perturbation theory by the Born process (see figure 3.4), i.e. the scattering
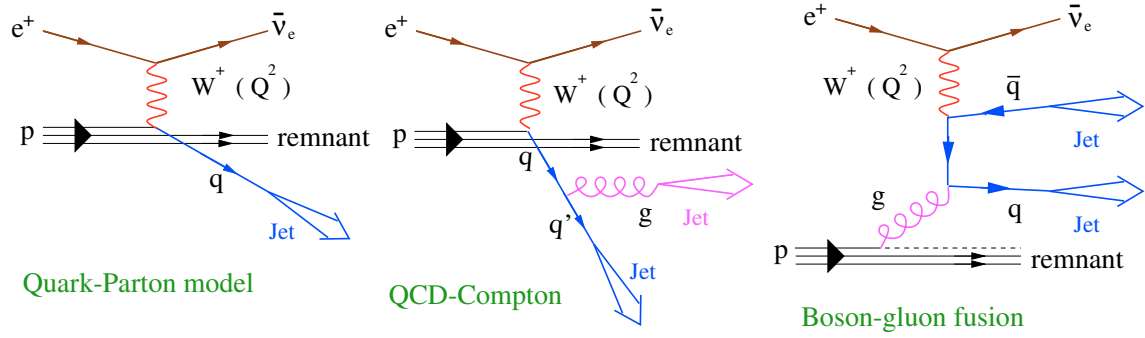
Figure 3.4 - Feynman diagrams of different processes in Charged Current interactions at HERA: i) Born, ii) QCD-Compton and c) boson-gluon fusion processes.

of the lepton off a quark in the proton via the exchange of a virtual W boson. Multi-jet production is described up to order $\mathcal{O}(\alpha_s)$ by the QCD Compton (QCDC) and boson-gluon fusion (BGF) processes (see figure 3.4). Due to the latter contribution multi-jet cross sections are directly sensitive to the gluon density of the proton and to α_s.

Chapter 4

Data Selection

In this chapter the selection criteria for the charged current event sample is presented. The data used for the present analysis was collected with the ZEUS detector at HERA during the 1995-1997 and 1999-2000 periods and correspond to an integrated luminosity of 110.5 pb^{-1}. During the running periods 1995-1997 (1999-2000) HERA operated with protons of energy $E_p = 820$ GeV (920 GeV) and positrons of energy $E_e = 27.5$ GeV, yielding a centre-of-mass energy of 300 GeV (318 GeV).

4.1 The $\not{p}_t$ threshold and background events

CC DIS events can be distinguished from events originating from NC DIS processes by the presence of a large missing transverse momentum ($\not{p}_t$) due to the undetected outgoing neutrino or the absence of the scattered positron. The $\not{p}_t$ value is related to the event kinematics (see equation 1.28). In figure 4.1 lines of constant $\not{p}_t$ in the (x, Q^2) plane are shown. In order to obtain events in the lower Q^2 and higher y regions, it is preferable to keep the $\not{p}_t$ threshold as low as possible. In this analysis a threshold of $\not{p}_t > 11$ GeV is used.

However, the low $\not{p}_t$ threshold allows for more background events from other ep processes. Possible sources of background are photoproduction and NC DIS events with large transverse energy. This type of events can display relatively large values of $\not{p}_t$ due to the limited resolution of the CAL or due to the presence of muons resulting from the decay of heavy quarks. Although the probability for these configurations is very low, the contamination from these processes is important since they have much larger cross sections than that of CC DIS. The most effective criterion to reduce this contamination is to require a large value of $\not{p}_t/E_t$ since the $\not{p}_t$ in such background events is likely to be caused by a fluctuation in the measurement of a large tranverse energy deposit.

Furthermore, there are considerable amount of events with a large $\not{p}_t$ originating from non-ep interactions. Cosmic-ray muons falling on the top part of the detector (called "*cosmic ray*" events) and beam-halo muons passing through the detector along the z-direction (called "*halo-muon*" events) can give rise to a large and localized energy deposit in the CAL, which results in a large value of $\not{p}_t$. Another
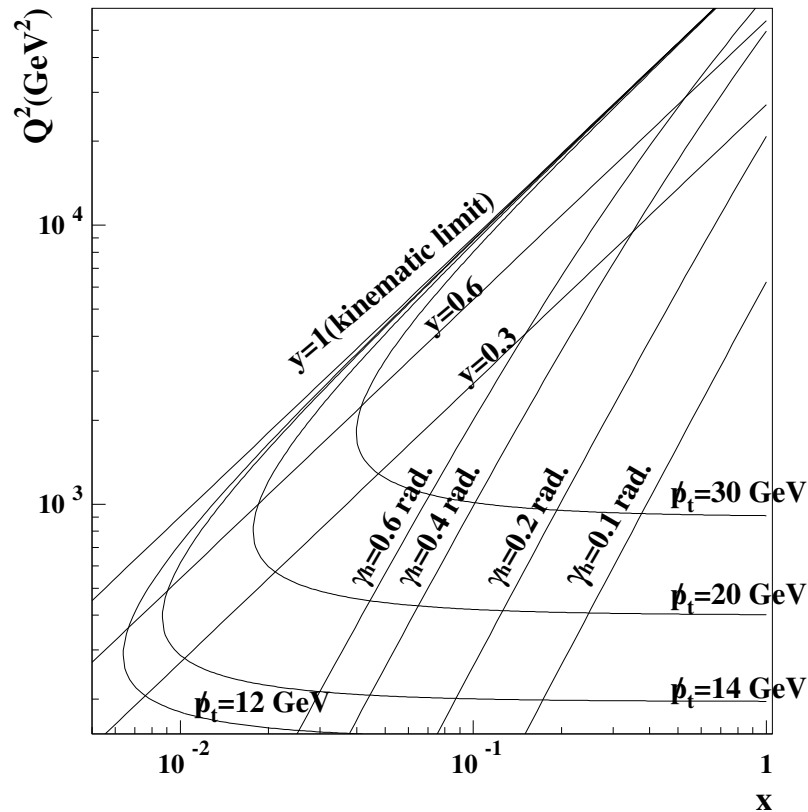
Figure 4.1 - Lines of constant $\not{p}_{\mathrm{t}}$, γ_{h} and y in the $(\mathrm{x}, \mathrm{Q}^2)$ kinematic plane.

important source of background is the p-gas process (called "*beam-gas*" events). In these events, large energy deposits are detected close to the forward beam pipe, mostly in the innermost ring of the FCAL. To remove this type of events the value of $\not{p}_{\mathrm{t}}$ excluding the FCAL first ring, $\not{p}_{\mathrm{t}}^{-1\mathrm{r}}$, is calculated and it is required to be above a certain threshold.

The CC data sample was selected by applying both online and offline cuts. The details of the selection procedure are presented in the forthcoming sections.

4.2 Online Event Selection - Trigger Logic

The CC sample was selected online with the ZEUS three level trigger system. The cuts applied by the first, second and third level trigger constitute the online selection. The particular trigger algorithms used in this analysis select events with missing transverse momentum measured from the main calorimeter. These events are good candidates for charged-current interactions.

4.2.1 First Level Trigger

The First Level Trigger requires a certain minimum amount of energy to be detected in the main calorimeter (CAL). At least one of the following conditions must be fulfilled for the event to pass the first level trigger:

- the missing transverse momentum ($\not{p}_t$) and the transverse energy excluding the innermost and second innermost FCAL rings (E_t^{-2r}) have to be greater than 5 GeV and the presence of at least one *good track* [1] is required in the event.

- the missing transverse momentum must be greater than 8 GeV and either the energy in the FCAL must be greater than 10 GeV or the event must contain at least one CTD track.

To increase the trigger efficiency for CC DIS events, other subtriggers based on calorimeter energies are also used. If the event satisfies at least one of the requirements listed below it is also selected:

- the transverse energy in the calorimeter greater than 30 GeV;

- at least one *good track* and at least one of the following conditions fullfilled:

  - the total energy in the calorimeter greater than 15 GeV;

  - the transverse energy greater than 11.5 GeV;

  - the total calorimeter energy deposited in the EMC cells greater than 10 GeV;

  - the total energy deposited in the EMC cells of the BCAL greater than 3.4 GeV;

  - the total energy deposited in the EMC cells of the RCAL greater than 2 GeV;

- the total energy deposited in the EMC cells of the BCAL (RCAL) greater than 4.8 GeV (3.4 GeV).

4.2.2 Second Level Trigger

The Second Level Trigger has a larger latency than the first level trigger, but has access to the entire calorimeter event information (pulse times of the photomultipliers and a preliminary vertex from the central tracking detector). Therefore, more precise selection algorithms are applied at this stage.

One of the following conditions has to be fulfilled for the event to be accepted by the SLT:

- $\not{p}_t^{SLT} > 6$ GeV , $E_t^{-2r} > 6$ GeV and at least one *good track*;

---

[1] A good track at FLT is defined as a CTD track with the hits aligned in the z-direction so that they point to the nominal interaction point

- $\not{p}_t^{SLT} > 9$ GeV , $E_t^{-1r} > 8$ GeV and $E_{FCAL} > 20$ GeV,

where E_t^{-1r} (E_t^{-2r}) is the transverse energy in the calorimeter calculated excluding the first (first and second) ring of the FCAL.

All the readout systems of the ZEUS sub-components are synchronous to the HERA clock. Their calibration is such that an ep collision occuring at the ZEUS nominal interaction point results in a measured event time equal to zero. An interaction occurring outside the interaction region will produce time shifts in one direction or the other. Cuts are applied to the times measured by different components in order to reject events coming from outside the interaction region. The second level trigger rejects more precisely beam-gas events and other non-ep background events.

In the case of the trigger designed for selection of CC events, the accepted events must verify that:

- the average CAL timing, t_{global}, must be less than 7 ns in absolute value.

4.2.3   Third Level Trigger

The time the third level trigger has available for making a decision is about $100ms$. This is much larger than the corresponding times at the first level trigger, $6.4\mu s$, and the second level trigger, $20ms$. The full event information from the different components of the ZEUS detector is available at the third level, allowing more stringent and finer cuts to be applied. At this level a complete tracking reconstruction is performed. In comparison to the offline level the tracking is not as refined due to time limits.

One of the following conditions has to be fulfilled for the event to be accepted by the TLT:

- $\not{p}_t^{TLT} > 8$ GeV and either $E_{FCAL}^{TLT} > 10$ GeV or the event has at least one TLT *good track* [2];

- $\not{p}_t^{FLT} > 6$ GeV and at least one *good track*.

Non-ep background contributions are further reduced by requiring all the following conditions:

- A vertex cut is applied, $|z_{vertex}| < 60$ cm. The ep interactions occur around the region $z_{vertex} = 0$. Beam-gas events can occur anywhere and the restriction on the vertex will cut out much more background than ep events. If no information on the CTD vertex exists, the vertex is set to zero (all three coordinates);

- $t_{BCAL}^{top} - t_{BCAL}^{bottom} > -10$ ns, which rejects events due to cosmic muons leaving energy in the calorimeter and moving from top to bottom. The event times are calculated using energy-weighted means of calorimeter channels above a threshold of 200 MeV.

---

[2]A good track at TLT is defined as a CTD track with $p_t > 0.5$ GeV, the distance of closest approach (DCA) of the extrapolated track to the beam z-axis is less than 1.5 cm and the DCA to the IP in the z-direction must be less than 60 cm.

4.3   Offline Event Selection

Detailed calibration of the detectors, noise studies and the full reconstruction can only be made offline. Therefore, the offline selection cuts are more accurate than the ones at the trigger level and increase the purity of the sample.

4.3.1   General Selection

The event sample selected with online cuts is further required to verify the following conditions:

- $\not{p}_t > 11$ GeV. The trigger simulation shows that this cut is sufficiently far above the 9 GeV trigger threshold to ensure high efficiency;

- the event has to have a fitted tracking vertex, determined from at least one track compatible with intersecting the beam line. The vertex position must verify $|Z_{vertex}| < 50$ cm. This cut eliminates a large fraction of non-ep background;

- $\dfrac{\not{p}_t^{-1r}}{\not{p}_t} > 0.8$. This cut rejects beam-gas events and p-beampipe collisions, in which the $\not{p}_t$ is concentrated in the first ring around the forward beampipe;

- the ratio of the number of tracks associated with the fitted vertex, $N_{track}(vertex)$, and the total number of tracks in the event, $N_{track}(total)$, is required to satisfy $N_{track}(vertex)/N_{track}(total) > 0.2$. This requirement rejects beam-gas events and p-beampipe collisions;

- at least one *good track* [3] is required. This requirement removes cosmic-ray events and beam-gas interactions with spurious vertices caused by low-energy secondary interactions in the beampipe;

- $|\Delta\phi| < 1$ rad, where $\Delta\phi$ is the difference between the azimuthal angle of the net momentum calculated with *good tracks* and the azimuthal angle measured by the calorimeter. This requirement removes events resulting from the overlay of a cosmic ray and an ep interaction;

- $\not{p}_t^{\,good\ tracks}/\not{p}_t > 0.1$, where $\not{p}_t^{\,good\ tracks}$ and $\not{p}_t$ are the transverse momentum calculated with *good tracks* and the calorimeter, respectively. This cut removes non-ep related energy deposits in the calorimeter and is complementary to the previous requirement;

- if the cell with maximal transverse energy in the CAL, E_t^{max}, has more than 70% of the total transverse energy in the CAL, the event is removed from the sample. This criterium is used to exclude events in which a cosmic muon or a spark produces large values of $\not{p}_t$ (see section 4.3.4);

---

[3]A *good track* is defined as a reconstructed CTD track originated from the vertex with a polar angle between $15°$ and $164°$ and a transverse momentum exceeding 0.2 GeV.

- A pattern recognition algorithm, MUFFIN [Kr98], based on the topology of the calorimeter energy distribution and the signals detected in the muon chambers is applied to reject cosmic-rays and halo-muons.

Simulations of ep background due to NC DIS show that some of these events still pass the above cuts so that additional cuts must be applied to remove them.

4.3.2 Rejection of NC DIS events

The rejection of NC DIS events is based on the fact that in this type of event there is a positron in the final state. To reject NC DIS events the electron finder Sinistra95 [Ab95] is used. This algorithm searches for positron candidates in the main calorimeter. Sinistra analyses clusters ("islands" of $3x3$ calorimeter cells around the highest energy cell) of energy depositions in the calorimeter and information such as the ratio of energy deposited in the electromagnetic part to the total energy deposited, the shower profile, tracking information, etc. A neural network is used to optimize the electron identification.

The event is removed from the sample if one of the following conditions is satisfied:

- $20° < \theta_{e^+} < 140°$

  - there is a positron candidate with energy larger than 10 GeV, which is *isolated* and the energy distribution is *narrow*;

- $\theta_{e^+} > 140°$

  - there is a positron candidate with energy larger than 10 GeV and transverse momentum $p_t^{e^+} > 11$ GeV;

  - $y_{e^+} < 0.7$ and the Sinistra probability for the positron candidate is larger than 0.95.

An e^+ candidate is said to be *isolated* if the ratio of the energy of the CAL not associated with the candidate inside a cone of radius $R = 0.7$ around the candidate divided by the energy of the positron is smaller than 0.1.

An e^+ candidate is said to be *narrow* if at least 90% of the energy of the positron is contained in a cone of radius $R = 0.3$ around the positron direction.

4.3.3 Rejection of photoproduction events

To reject photoproduction background events, a requirement is made on azimuthal collimated energy flow. One-jet events are required to have $\not{p}_t/E_t > 0.5$. In the case of dijet production in photoproduction the events are characterised by back-to-back jet configurations. To remove photoproduction background in dijet production, the selected events are required to satisfy the following conditions:

- $\displaystyle{\not}p_t/E_T > 0.3$.

- the difference of the azimuths of the net missing transverse momentum of the event and the closest jet must be greater than 1 radian.

4.3.4 Uranium-noise and spark suppression

As the calorimeter uses depleted uranium as an absorber, the radioactivity of the uranium produces background noise. An energy cut of 60 (100) MeV was applied to the EMC (HAC) cells. This threshold was raised to 100 (150) MeV for isolated EMC (HAC) cells. These thresholds were determined in a study using randomly triggered events [Sa98].

The Zeus photomultiplier bases sometimes suffer a high voltage discharge ("spark"), which results in a fake energy deposit in the calorimeter. This effect can be avoided by removing cells which have a large energy imbalance between the pulse-heights measured by the two photomultipliers of the cell. All cells with measured energy greater than 1.5 GeV that satisfy the following condition are removed:

$$\frac{|E_L - E_R|}{E_L + E_R} > 0.9, \tag{4.1}$$

where E_L and E_R are the energies measured by the left and right side photomultipliers, respectively. The threshold was also determined from a study based on randomly triggered events.

4.4 Jet selection

Jets are found using the k_T jet finding algorithm applied to the UCAL cells in the laboratory frame. In the laboratory frame the final state is boosted in the positive Z-direction due to the large difference between the proton and positron beam energies. With a Lorentz boost to other systems of reference this effects can be removed. As the neutrino escapes detection in charged current events, the kinematics is poorly reconstructed and the quantities reconstructed in other frames suffer a large degradation. To avoid the large resolution loss in the reconstruction of jet quantities, the analysis has been carried out in the laboratory frame.

Events with one or more jets in the final state are selected. The jets are ordered according to transverse energy. The jet selection is then done in the following way:

- in the laboratory frame

  * $-1 < \left(\eta^{jet}\right)_i < 2$
  * $\left(E_T^{jet}\right)_i > 14$ GeV.

Dijet production has been studied by selecting events with at least two jets with $-1 < \eta^{jet} < 2$, $E_T^{jet,1} > 14$ GeV and $E_T^{jet,2} > 5$ GeV, where $E_T^{jet,1}$ ($E_T^{jet,2}$) is the

transverse energy of the jet with the highest (second-highest) transverse energy in the event.

4.5 Kinematic cuts

The analysis is restricted to the kinematic region:

$$Q^2 > 200 \text{ GeV}^2 \text{ and } y < 0.9. \tag{4.2}$$

The cut on y is needed since the x and Q^2 resolutions degrade at high y. From equation 1.28, the Q^2 resolution is expressed as

$$\frac{\Delta Q^2}{Q^2} = \sqrt{4 \left(\frac{\Delta \not{p}_t}{\not{p}_t} \right)^2 + \left(\frac{\Delta y}{1 - y} \right)^2}, \tag{4.3}$$

which degrades at $y \approx 1$. In addition, for a NC DIS event without any initial-state QED radiation, the value of $E - P_z$ is conserved since the particles which escape through the forward beampipe carry little $E - P_z$. Hence, $E - P_z$ peaks at $2 \cdot E_e = 55$ GeV for NC DIS events, where the e^+ energy has been included in the hadronic system. From equation 1.28 it can be inferred that $y_{JB} \sim 1$ for NC DIS events. Therefore, the cut $y < 0.9$ reduces the NC DIS background.

4.6 Charged Current event sample

After applying the above selection criteria to the data collected with the ZEUS detector during the years 1995-1997 (1999-2000), 862 (1349) charged current candidates were selected (see table 4.1). After applying the jet selection criteria an inclusive jet sample of 723 (1142) events remained; 105 (177) of the events have two or more jets in the final state.

	Events passing selection cuts	
	95-97 e^+p ($\mathcal{L} = 45.0$ pb^{-1})	**99-00** e^+p ($\mathcal{L} = 65.5$ pb^{-1})
CC selection	862	1349
Kinematic cuts	827	1287
Inclusive Jet cuts	723	1142
Dijet cuts	105	177

Table 4.1 - Number of events passing the cuts for the CC sample. The total luminosity for this sample is 110.5 pb^{-1}.
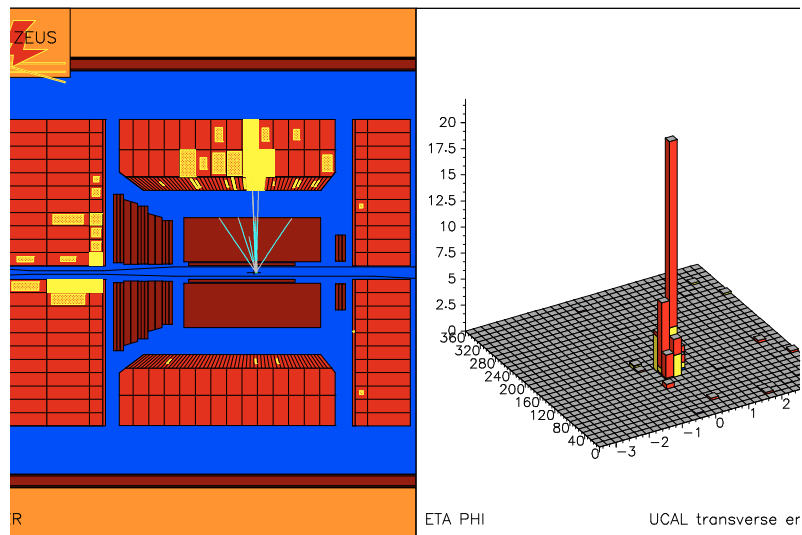
Figure 4.2 - Example of a charged current one-jet event registered with the ZEUS detector.

An example of a charged current event with one jet as seen in the ZEUS detector is shown in figure 4.2. The energy and position measurements of the uranium calorimeter and the central tracking chamber for the event are displayed on the left side of the plot, where the $r - Z$ projection is shown. The large energy deposit in the barrel region is associated with the jet. There is a clear vertex defined by the tracks close to the nominal interaction point and a large energy deposit around the forward beampipe, associated with the proton remnant. The transverse momentum in the calorimeter is not balanced. The right side of the figure shows the transverse energy deposits in the calorimeter as viewed in the $\eta - \phi$ plane. A clear hadronic jet is seen. An example of a charged current dijet event as seen in the ZEUS detector is shown in figure 4.3. Large energy deposits in the barrel and forward regions, associated with the two jets, are seen. There is a clear vertex defined by the tracks close to the nominal interaction point. The left side of the figure shows the transverse energy deposits in the calorimeter as viewed in the $\eta - \phi$ plane. Two clear jets are seen.
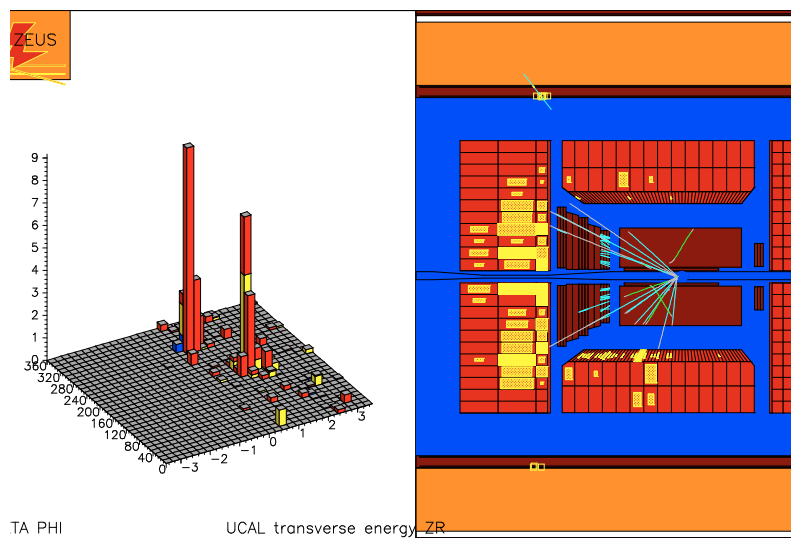

Figure 4.3 - Example of a charged current dijet event registered with the ZEUS detector.

Chapter 5

Event and Detector Simulation

The predictions to be compared with experimental measurements result from the convolution of hard-scattering processes with various detector effects. This gives rise to complex final states. Therefore, the relation of the measurements to the physical quantities is not straight forward: first, we do not always understand completely the physics of the hard-scattering processes; second, the detector effects cannot be described analytically. In order to extract the physical observables from the measured quantities one has to correct for all detector-related effects. This is usually done by using Monte Carlo methods.

Monte Carlo (MC) methods are an essential tool in experimental HEP. They are used to simulate complete events. The simulation is divided into *physics simulation* and *detector simulation*. The generated events (MC events) are used to correct the data for detector effects (acceptance, smearing, kinematic cuts, etc.) and for the extraction of physical quantities from the measurements. This can be done under the condition that the simulated final-state quantities agree well with those measured with the detector.

The physics simulation of ep collisions at HERA is divided into separate steps:

- **Hard Scattering**: the SM is used for calculating the cross section of the hard scattering at leading or higher orders.

- **Parton Showering**: simulation of the initial- and final-state QCD radiation.

- **Hadronization**: partons fragment into color-neutral hadrons. This process is called hadronization. Hadronization is a non-perturbative process and various models are used for its simulation.

The output of the physics simulation is a list containing the four-vectors of all particles (hadrons and leptons), which are fed into the detector simulation. The detector simluation is based on the GEANT package [Br87]. A detailed simulation of the geometry and materials of the detector is performed at this stage. In addition, the three-level trigger is simulated. The program used for detector simulation has been developed so as to give the best possible description of the response of the detector. The full GEANT simulation of the ZEUS detector is done using the program MOZART (Monte Carlo for Zeus Analysis, Reconstruction and Trigger). For every

particle MOZART simulates its interaction with the detector material, its possible decays, the signals produced in the different components (e.g. tracking, calorimeters) and the digitisation of the signals, including the various sources of noise. Finally, the information from the detector and trigger simulation of the events is written to tape in an identical format as the real data. This allows to pass the Monte Carlo events through the same reconstruction chain and selection as used for the data.

The stage after the parton showering is called *parton level*, the one after the hadronization *hadron level* and the final one *detector level*.

In this chapter the following topics are considered:

- the Monte Carlo models used for correcting the data;

- comparisons between data and MC generated events made in order to show the description of the data by the simulation.

5.1   Monte Carlo Models

In this analysis the DJANGOH 1.1 [Sc91] Monte Carlo package is used to correct the data. DJANGOH is an interface between HERACLES [Kw92] and LEPTO [In97] or ARIADNE [lö02].

The HERACLES program simulates the ep-DIS process including first-order EW radiative corrections. A hard scattering between an incoming parton and the virtual boson is simulated according to the SM EW cross-section formula and the proton PDFs. The lowest-order process is the Born process, $V^*q \rightarrow q'$, where V^* denotes generally a virtual vector boson, q denotes the incoming quark and q' denotes the scattered quark. There are many parametrizations of the proton PDFs compiled in the PDFLIB [Pl93] library. In this analysis the CTEQ4 [La97] set of proton PDFs is used.

The programs LEPTO or ARIADNE are used for the QCD corrections so that a complete simulation of the ep-DIS process is made. The first-order QCD effects can be simulated using the exact matrix elements. There are two such processes: the QCD Compton process (QCDC), $V^*q \rightarrow qg$, and the boson-gluon fusion process (BGF), $V^*g \rightarrow q\overline{q}$. For higher-order QCD corrections the two programs use different models:

- LEPTO uses the MEPS (Matrix Element plus Parton Shower) model. In this model, additional parton radiation is generated according to the DGLAP-splitting functions. This corresponds to a leading-log approximation of gluon emission.

- ARIADNE uses the colour dipole model (CDM). This model is based on the idea to treat gluon emission from a $q\overline{q}$ pair as radiation from the colour dipole between the q and the $\overline{q}$. This model incorporates BGF as an extra process, while the QCDC is already included in the colour-dipole radiation.

Finally the partons are simulated to fragment into a set of primary hadrons which subsequently may decay further. Both ARIADNE and LEPTO use the Lund String

model as implemented in the JETSET [Sj94] program for the simulation of hadronisation.

5.2   Description of Data by the Simulation

Comparisons of event distributions between data and Monte Carlo generated samples have been made. It is shown that the MC samples describe the data well enough to keep the systematic uncertainties smaller than the statistical uncertainties of the data. This agreement allows the application of a bin-by-bin correction, which will be discussed in the next chapter.

Particularly important is the Monte Carlo description of the data for the quantities used in the event selection and in the determination of the kinematics. Therefore, the MC simulation is compared to the calorimeter and tracking quantities.

Various data distributions are compared with the simulations in the following plots. The points (back dots) are the data measured with the ZEUS detector, the solid lines are the predictions of CDM and the dashed lines are the predictions of MEPS. The MC predictions have been normalised taking into account the luminosity of the data.

The distributions of the kinematic variables Q^2, x and y reconstructed with the Jacquet-Blondel method are shown in figure 5.1. The distribution of the missing transverse momentum ($\not{p}_t$) measured with the CAL is also shown. The agreement between data and both Monte Carlo samples is reasonable.

Distributions of calorimeter quantities are shown in figure 5.2: the ratio of the missing transverse momentum over the total transverse energy ($\not{p}_t/E_t$), the ratio of the missing transverse momentum excluding the first ring of the FCAL over the missing transverse momentum ($\not{p}_t^{-1r}/\not{p}_t$), and the ratio of the transverse energy of the calorimeter cell with highest transverse energy over the total transverse energy (E_t^{max}/E_t^{cal}). The distribution of $E - P_z$ is also shown. The measured tranverse energy flow measured by the calorimeter is well described by both Monte Carlo models.

The distributions of the tracking quantities measured with the CTD and used in the data selection are presented in figure 5.3 . The description of the tracking variables in the data by both MC samples is reasonably good.

The distributions of the transverse energy (E_T^{jet}) and pseudorapidity (η^{jet}) of the jets reconstructed with the calorimeter are shown in figure 5.4 . The description of the jet variables in the data by both MC samples is good.

It is concluded that for both CDM and MEPS, the agreement between data and MC is satisfactory. These MC samples are used to correct the data to the hadron level (see sections 6.2).
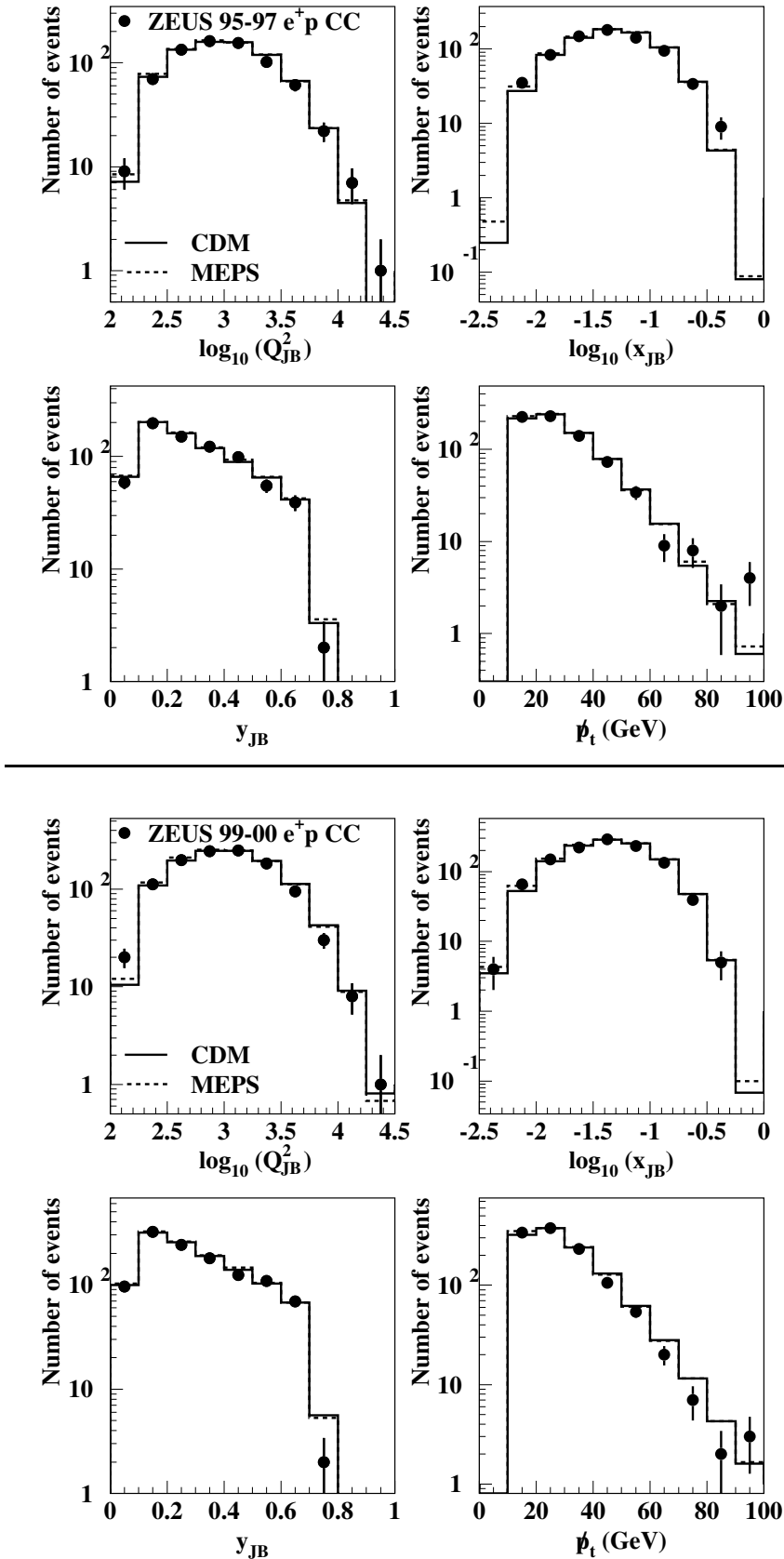
Figure 5.1 - Distributions of the kinematic variables Q^2, x and y reconstructed with the Jacquet-Blondel method. The distribution of the transverse momentum ($\not{p}_t$) measured with the CAL is also shown. The points represent the ZEUS data taken in the years 95-97 (upper plots) and 99-00 (lower plots). The solid (dashed) lines show the CDM (MEPS) Monte Carlo simulations.
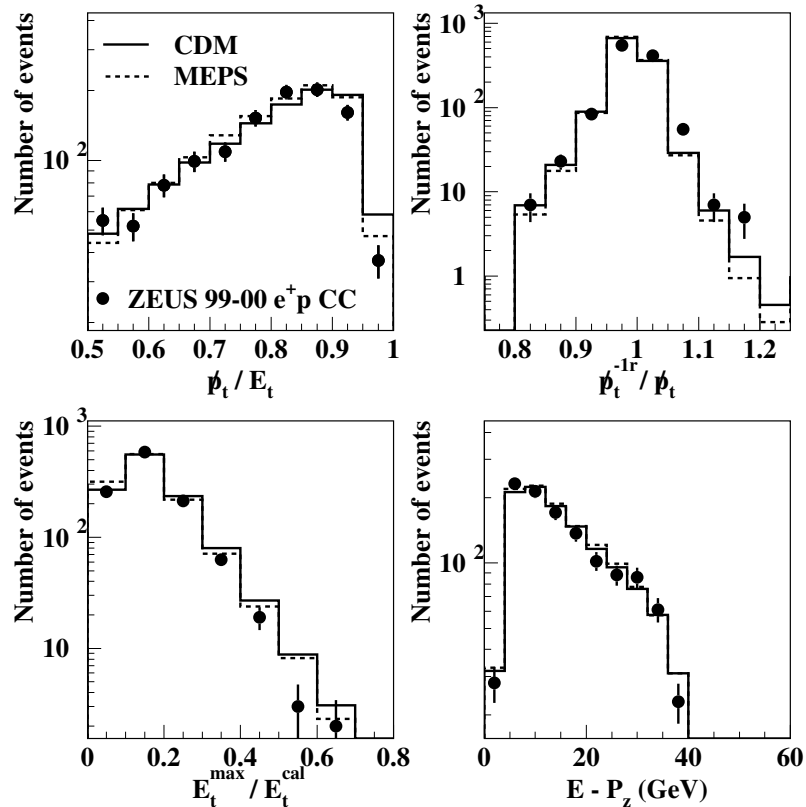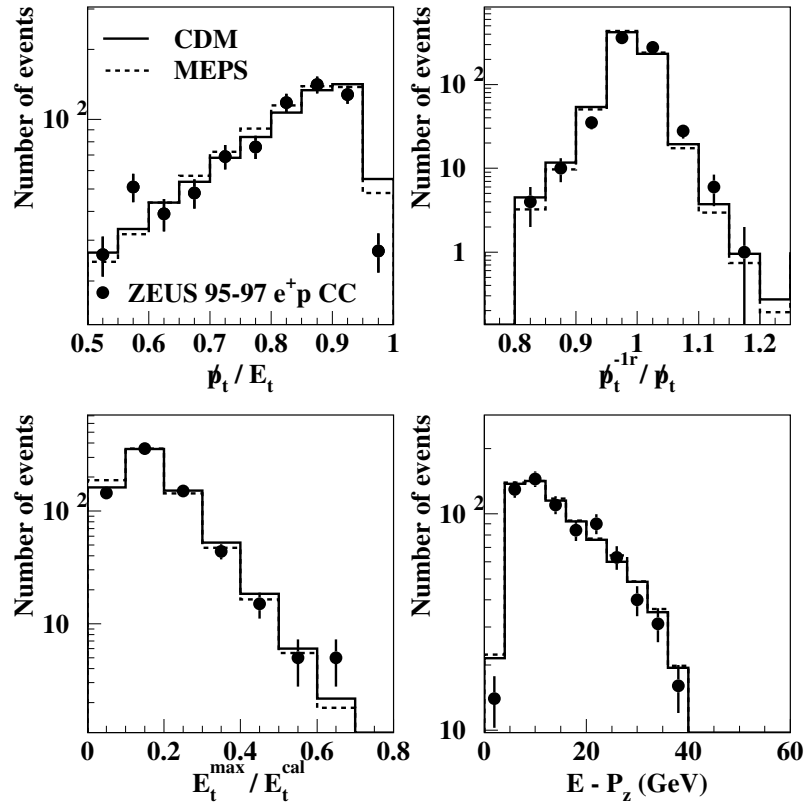
Figure 5.2 - Distributions of calorimeter quantities: the ratio of the total transverse momentum over the total transverse energy $(\not{p}_t/E_t)$, the ratio of the total transverse momentum excluding the first ring of the FCAL over the total transverse momentum $(\not{p}_t^{-1r}/\not{p}_t)$ and the ratio of the transverse energy of the calorimeter cell with highest transverse energy over the total transverse energy (E_t^{max}/E_t^{cal}). The distribution of the $E-P_z$ measured with the CAL is also shown.
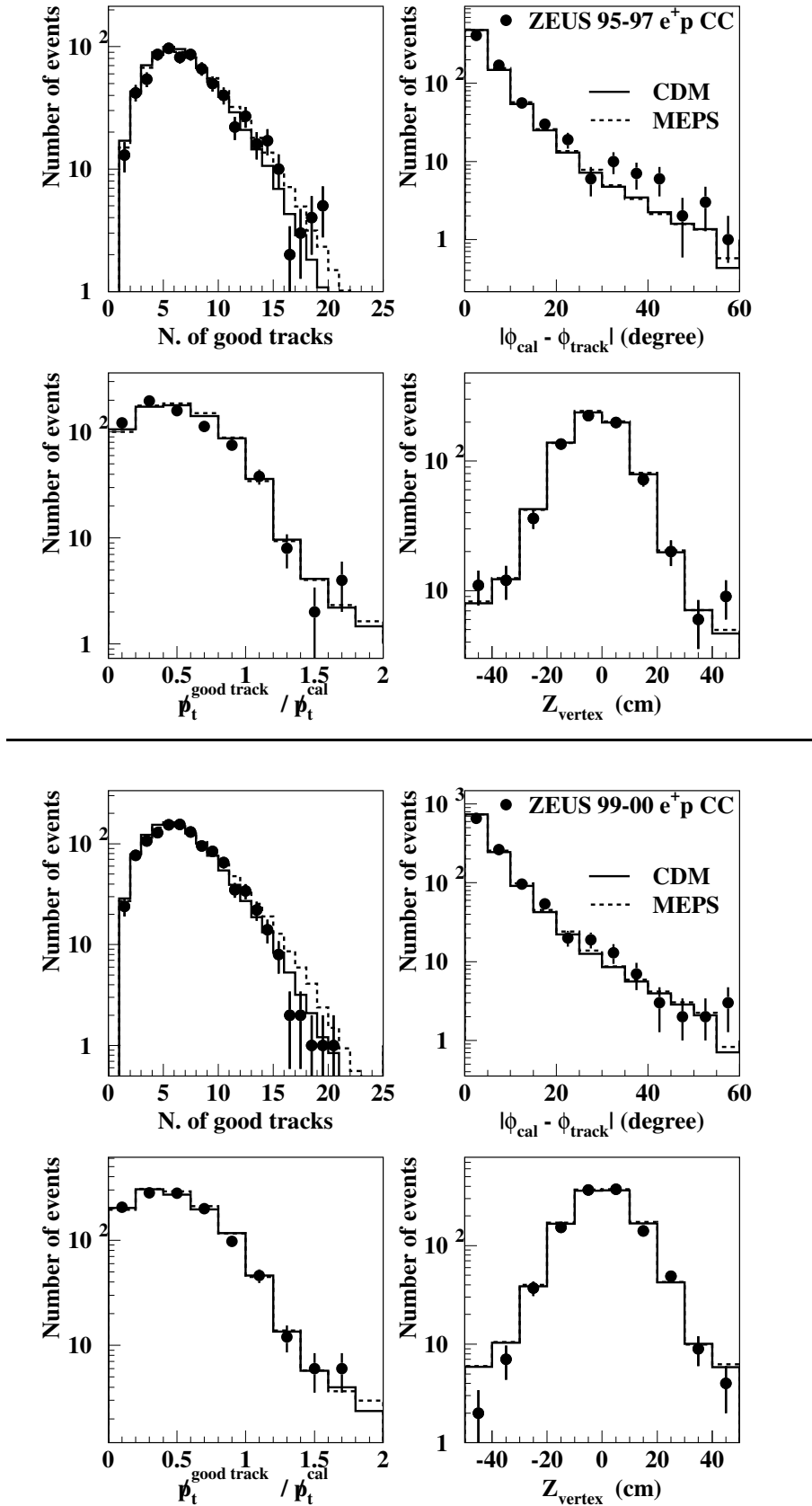
Figure 5.3 - Distributions of tracking quantities measured with the CTD: the number of *good tracks*, the absolute difference between the azimuthal angle of the net momentum calculated with *good tracks* and the azimuthal angle measured by the calorimeter $\left(|\phi_{cal}-\phi_{track}|\right)$, the ratio of the transverse momentum calculated with *good tracks* and the calorimeter $\left(\not{p}_t{}^{good\ tracks}/\not{p}_t{}^{cal}\right)$ and the Z_{vertex}.
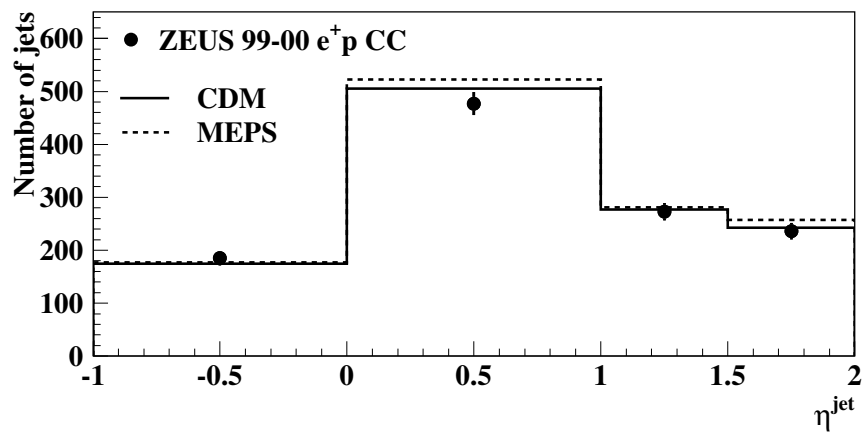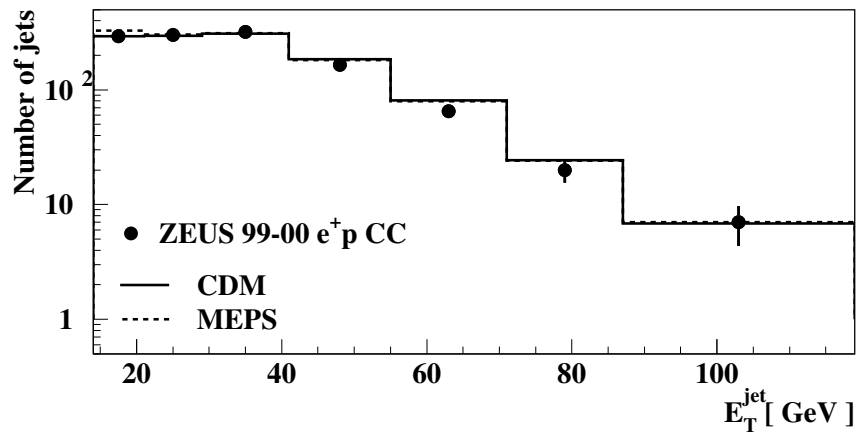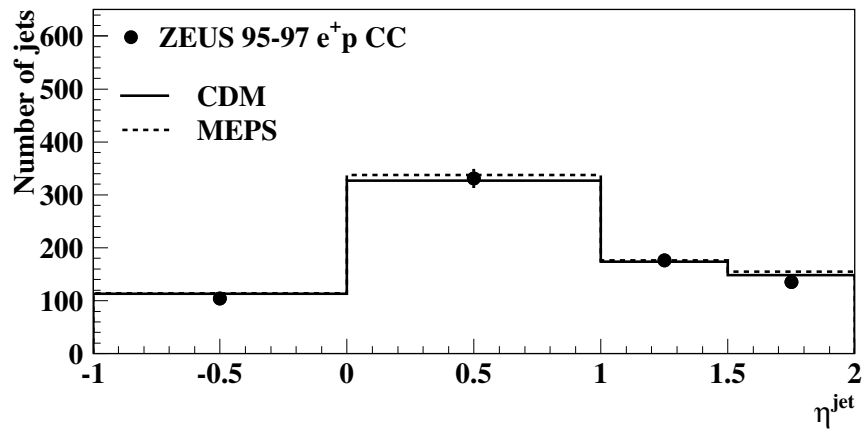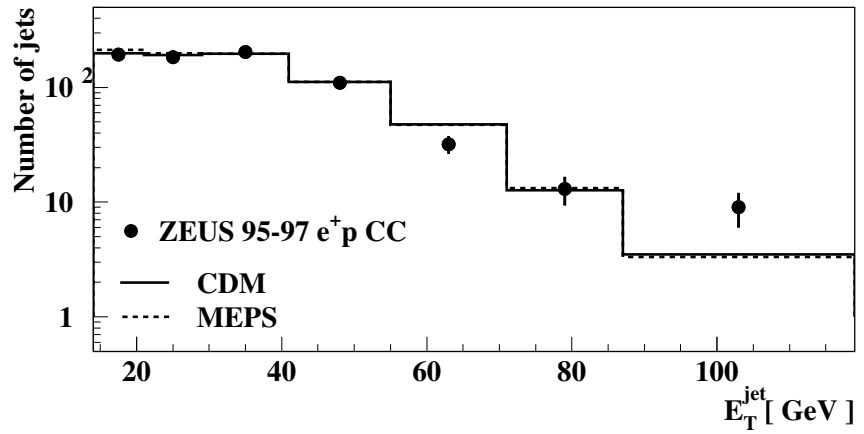
Figure 5.4 - Distributions of the transverse energy (E_T^{jet}) and pseudorapidity (η^{jet}) of the jets reconstructed with the calorimeter.

Chapter 6

Analysis Method

6.1 Resolution in the jet and kinematic variables

The data measured with the ZEUS detector are a convolution of the physical quantities with detector effects. In general, the distribution of the measured values displays a shift, called *bias*, and a spread with respect to the true value, called *resolution*. A good measurement should have both a small bias and a small resolution. The size of the systematic uncertainties assigned to the corrected data depends on the resolution of the measurement. The size of the bins of a measured distribution, for example a cross section, are chosen such that they are much larger than the resolution in order to keep the number of events that migrate outside the bin or into the bin low.

The determination of the resolution for a certain quantity X can be done using the Monte Carlo simulation since this quantity is known both at the generator level (the present case the hadron level) and at the detector level. In the case of a variable X with units, we define:

$$\delta_X = \frac{X^{\mathrm{GEN}} - X^{\mathrm{DET}}}{X^{\mathrm{GEN}}} \, , \tag{6.1}$$

where GEN and DET stand for generator level and detector level, respectively. The variable δ_X defined above has a certain distribution. Its mean value is the bias and the spread is the resolution. For a dimensionless variable, the following definition is more appropriate:

$$\delta_X = X^{\mathrm{GEN}} - X^{\mathrm{DET}} \, . \tag{6.2}$$

In both cases, the variable δ_X is dimensionless. The study of the resolution for some measured quantities is discussed in the next sections.

6.1.1 Jet Energy Correction

A jet measured in the calorimeter has a transverse energy that differs from that at the hadron level. A jet measured in the calorimeter usually has a smaller transverse energy $E_T^{cal}(jet)$ than the "true" value $E_T^{had}(jet)$ of the set of hadrons. This energy loss is due to dead material in front of the calorimeter and particles which do not

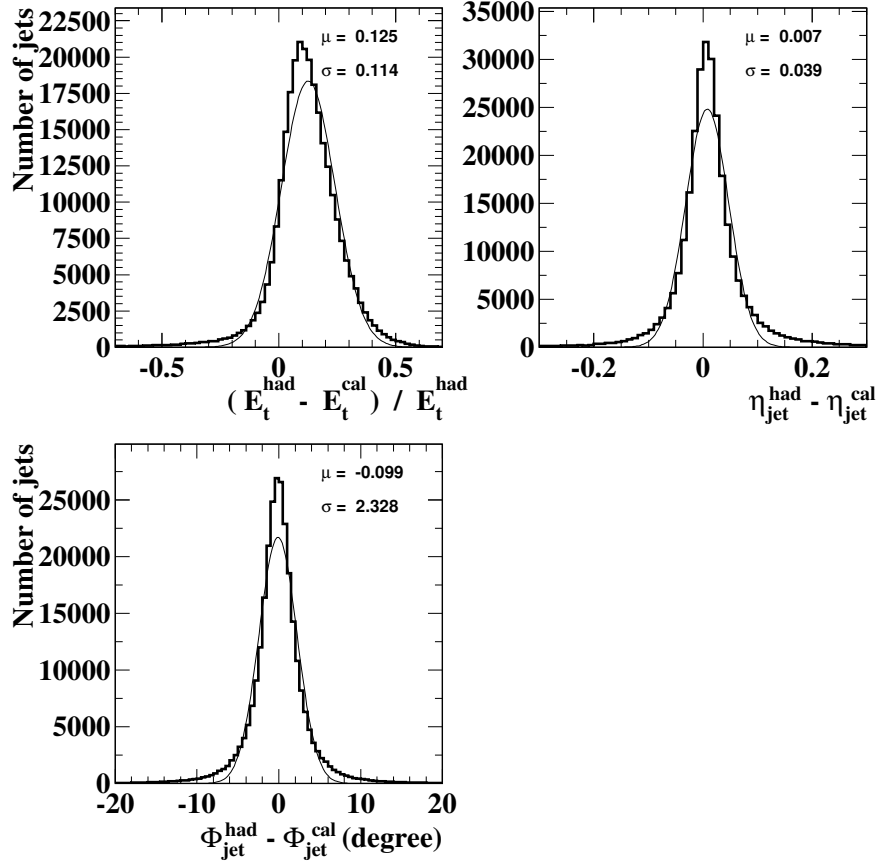**Figure 6.1 -** The distributions of $(E_T^{had} - E_T^{cal})/E_T^{cal}$, $\eta_{jet}^{had} - \eta_{jet}^{cal}$ and $\phi_{jet}^{had} - \phi_{jet}^{cal}$ using the CDM MC sample.

deposit a significant amount of energy in the main calorimeter, such as muons and neutrinos. The transverse jet energy as measured with the UCAL needs therefore to be corrected. By correcting for the bias an improvement of the purities and efficiencies (see section 6.2) is achieved. The CDM Monte Carlo sample was used for calculating the energy correction. In order to compare jets at the detector (cal) and hadron (had) level, definite ranges in η^{jet} and thresholds in E_t^{jet} have to be considered. The following ranges were used:

$$E_T^{cal} \, (jet) \; \geq \; 10 \, \text{GeV} \quad ; \quad -1 \; \leq \; \eta^{cal} \, (jet) \leq 2$$
$$E_T^{had} \, (jet) \; \geq \; 14 \, \text{GeV} \quad ; \quad -1 \; \leq \; \eta^{had} \, (jet) \leq 2$$

A matching of the hadron and calorimeter jets was done. For each hadron jet the distance in the $\eta - \phi$ plane between that jet and each calorimeter jet is computed as:

$$d(had - cal) = \sqrt{(\eta^{had} \, (jet) - \eta^{cal} \, (jet))^2 + (\phi^{had} \, (jet) - \phi^{cal} \, (jet))^2} \qquad (6.3)$$

The pair with the minimum $d(had - cal)$ is taken, provided this distance itself is smaller than 1 unit. The jet variables for this hadron-calorimeter pair of jets are then compared and used to estimate the biases and resolutions.
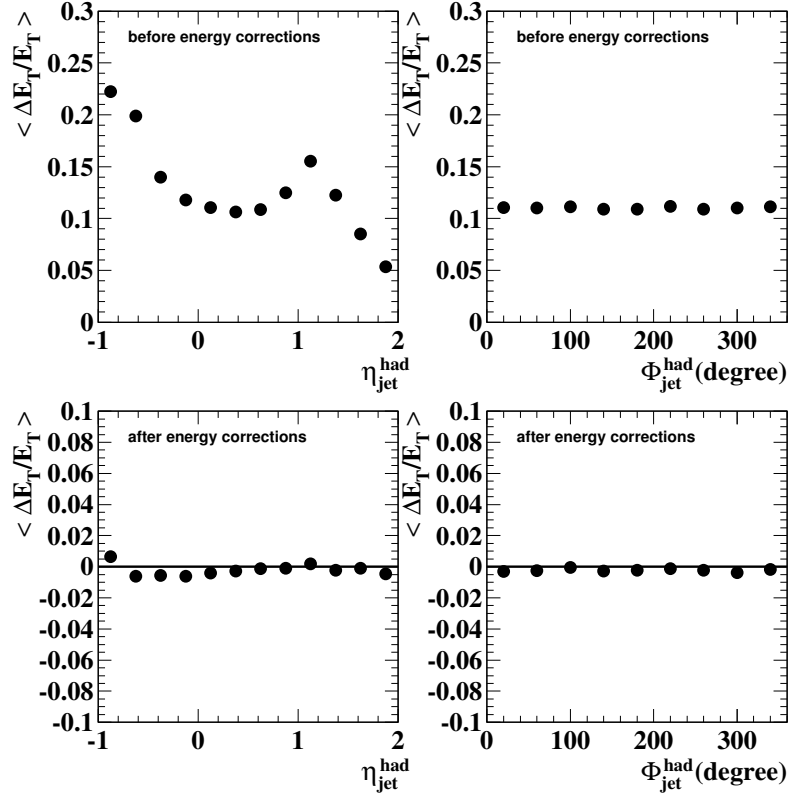
Figure 6.2 - The mean value $< (E_T^{had} - E_T^{cal})/E_T^{cal} >$ as a function of η_{jet} (left) and ϕ_{jet} (right) before (top) and after (bottom) jet transverse energy corrections are applied. The CDM MC sample has been used.

The distributions of $\delta_{E_T(jet)}$, $\delta_{\eta(jet)}$ and $\delta_{\phi(jet)}$ in the CDM MC sample are shown in figure 6.1. The resolution in E_T^{jet} is about 11% and the bias is 13%. For the η^{jet} and ϕ^{jet} variables there is no significant bias. The resolution in η^{jet} is about 0.04 units and in the case of ϕ^{jet} is 2.3 degrees.

The energy correction has been constructed as:

$$\left(E_T^{jet}\right)_{corrected} = C_1(E_T^{cal}, \eta_{jet}) + C_2(E_T^{cal}, \eta_{jet}) \cdot E_T^{cal} \qquad (6.4)$$

The mean transverse energy of the jets at CAL level, $< E_T^{cal}(jet) >$, as a function of the transverse energy at hadron level, $E_T^{had}(jet)$, has been obtained for 12 different bins in η^{jet}. The energy correction was determined by a linear fit of the form:

$$< E_T^{cal}(jet) > = P_0 + P_1 \cdot E_T^{had}(jet) . \qquad (6.5)$$

The parameters C_1 and C_2 of equation 6.4 are then determined in each η^{jet} bin as follows:

$$C_1 = -\frac{P_0}{P_1} , \quad C_2 = \frac{1}{P_1} \qquad (6.6)$$

The parameters depend on η_{jet}^{cal} due to the fact that the distribution of the dead material varies with pseudorapidity. This dependence of the correction factors on

η^{jet} is shown in figure 6.2: the mean value of $(E_T^{had}(jet) - E_T^{cal}(jet))/E_T^{cal}(jet)$ as a function of η_{jet} (upper-left) and ϕ_{jet} (upper-right) has been considered. The former shows two peaks, one at $\eta^{jet} \approx 1.1$ and another at $\eta^{jet} \approx -1$, which are understood in terms of the increase in dead material in front of the calorimeter in those two regions. The azimuthal angle ϕ^{jet} dependence is pretty much constant. For this reason the above parametrization was made η^{jet}-dependent only.

After applying the above correction to the jet transverse energy, the bias in $E_T^{corr}(jet)$ is reduced to less than 1%, as shown in figure 6.2.

In the case of dijets, the jet energy corrections were obtained with dijet Monte Carlo events using the same procedure that was applied to correct for the transverse energy of the inclusive jet sample. In order to compare jets at the detector (cal) and hadron (had) level, definite ranges in η^{jet} and thresholds in E_t^{jet} have to be considered. The following ranges were used:

$$E_T^{cal}(jet, 1) \geq 10 \text{ GeV}$$
$$E_T^{cal}(jet, 2) \geq 3.5 \text{ GeV}$$
$$E_T^{had}(jet, 1) \geq 14 \text{ GeV}$$
$$E_T^{had}(jet, 2) \geq 5.0 \text{ GeV}$$

where $E_T^{cal}(jet, 1)$ $(E_T^{cal}(jet, 1))$ is the transverse energy of the jet with highest (second-highest) E_T of each event. After the jet energy corrections the bias in the transverse energy of the two highest E_T-jets in the dijet sample was reduced to less than 1%.
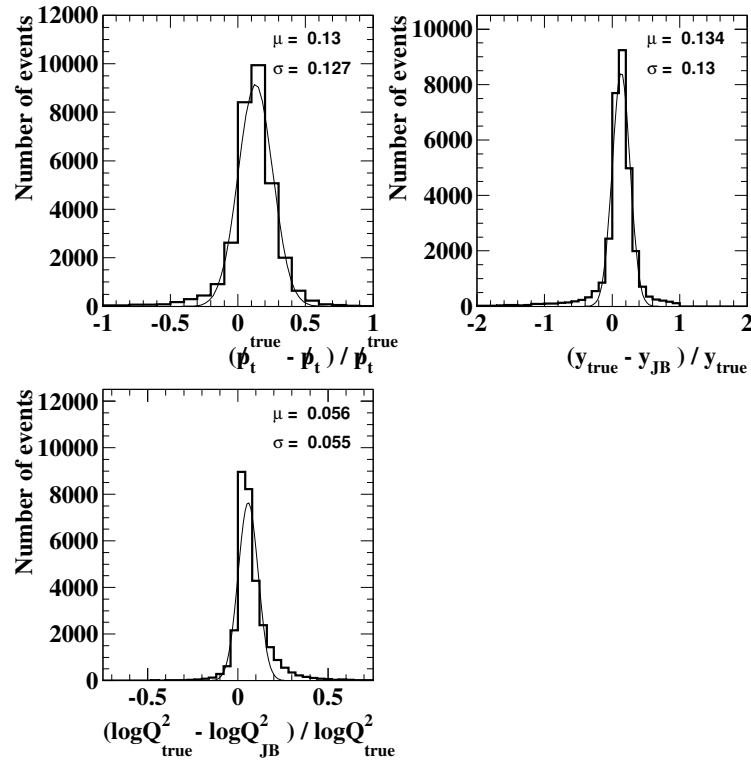

Figure 6.3 - The distribution of $(\not{p}_t^{true} - \not{p}_t)/\not{p}_t^{true}$, $(y_{true} - y_{JB})/y_{true}$ and $(\log Q_{true}^2 - \log Q_{JB}^2)/\log Q_{true}^2$ using the CDM MC sample.
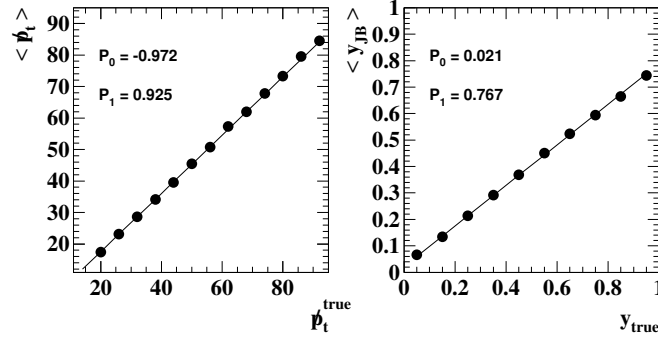
Figure 6.4 - Mean value of the reconstructed $\not{p}_t$ as a function of $\not{p}_t^{\text{true}}$ (left); mean value of y_{JB} as a function of y_{true} (right). The CDM MC sample was used.

6.1.2 Correction of the Kinematic Variables

Due to energy losses in front of the the calorimeter both $\not{p}_t$ and $E - P_z$ reconstructed with the UCAL underestimate the true values; these biases produce a shift in the measured value of Q_{JB}^2 and y_{JB} with respect to the true values (see Fig 6.3). The detector simulation was used to determine corrected values of the kinematic variables, $\not{p}_{t\text{corr}}$ and $(y)_{\text{corr}}$. The correction for the kinematic variables has been constructed as:

$$
\begin{aligned}
(\not{p}_t)_{\text{corr}} &= C_1 + C_2 \cdot \not{p}_t \\
(y)_{\text{corr}} &= C_1' + C_2' \cdot y_{\text{JB}}
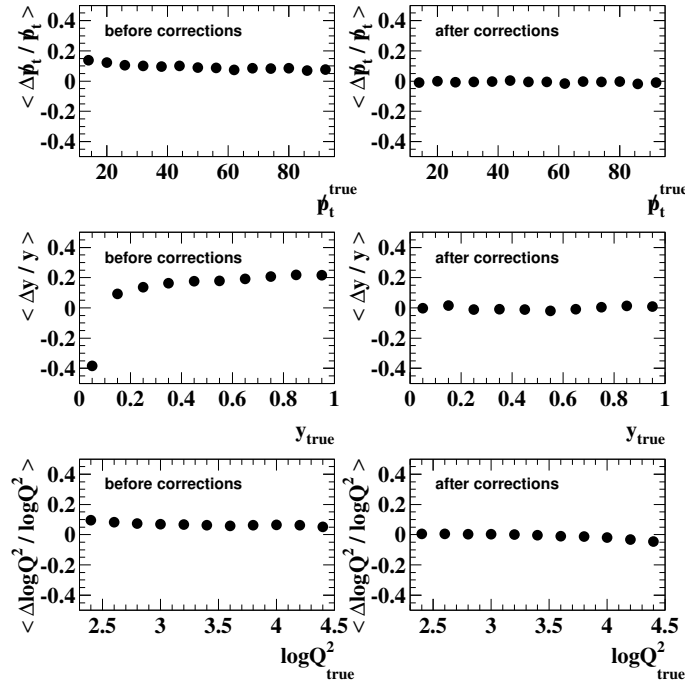\end{aligned}
\tag{6.7}
$$

Figure 6.5 - Mean values $\langle \frac{\Delta \not{p}_t}{\not{p}_t} \rangle$, $\langle \frac{\Delta y}{y} \rangle$ and $\langle \frac{\Delta \log Q^2}{\log Q^2} \rangle$ as a function of $\not{p}_t^{\text{true}}$, y_{true} and $\log Q_{\text{true}}^2$, respectively. The CDM MC sample was used.

The mean $\not{p}_t$ (y_{JB}) as a function of the true value $\not{p}_t^{\text{true}}$ (y_{true}) has been obtained.

The correction for the kinematic variables was determined by linear fits of the form:

$$
\begin{aligned}
< \not{p}_t > &= P_0 + P_1 \cdot p_t^{\text{true}} \\
< y_{JB} > &= P_0' + P_1' \cdot y_{\text{true}},
\end{aligned}
\tag{6.8}
$$

as shown in Fig. 6.4. The parameters C_1, C_2, C_1' and C_2' of equation 6.7 are obtained as follows:

$$
C_1 = -\frac{P_0}{P_1} \;,\;\; C_2 = \frac{1}{P_1} \;,\;\; C_1' = -\frac{P_0'}{P_1'} \;,\;\; C_2' = \frac{1}{P_1'}
\tag{6.9}
$$

The corrected value of Q^2, $(Q^2)_{\text{corr}}$, was calculated in terms of $(\not{p}_t)_{\text{cor}}$ and $(y)_{\text{cor}}$ using the relation given in equation 1.28. Figure 6.5 shows the mean values of $\langle\frac{\Delta\not{p}_t}{\not{p}_t}\rangle$, $\langle\frac{\Delta y}{y}\rangle$ and $\langle\frac{\Delta\log Q^2}{\log Q^2}\rangle$ before and after corrections. After corrections the bias in $(y)_{\text{corr}}$ and $(Q^2)_{\text{corr}}$ is reduced to less than 5%.

6.2 Correction of the measured distributions

The various observables measured in this analysis are obtained from the ZEUS data at the calorimeter level. The LO MC models give a good description of the data (see chapter 5). The hadron level results are determined by correcting the data for detector effects. The correction factors are calculated using the Monte Carlo simulations.

6.2.1 Determination of jet cross sections

A *bin-by-bin correction* method has been used in this analysis. In this method, the number of data events in each bin of a given distribution is counted (at the detector level) as well as the number of Monte Carlo events in that bin at both detector and hadron levels. The corrected value of the observable may depend on the particular Monte Carlo model used. If the Monte Carlo model considered does not describe the data, the bin-by-bin correction method becomes model dependent. In the present case it has been shown that the MC describes the data (see Chapter 5).

The efficiency in bin i, $\mathcal{E}_i$, is defined as:

$$
\mathcal{E}_i \equiv \frac{N_i^{\text{GEN\&DET}}}{N_i^{\text{GEN}}} \;,
\tag{6.10}
$$

where N_i^{GEN} is the number of generated events in that bin and $N_i^{\text{GEN\&DET}}$ is the number of events generated and reconstructed in that bin. The efficiency displays the fraction of the generated events that "remain" in the bin. Another important quantity is the purity in bin i, $\mathcal{P}_i$, which is defined by:

$$
\mathcal{P}_i \equiv \frac{N_i^{\text{GEN\&DET}}}{N_i^{\text{DET}}} \;,
\tag{6.11}
$$

where N_i^{DET} is the number of Monte Carlo events reconstructed in bin i. The purity is the fraction of events reconstructed in bin i that were indeed generated in that bin.

With the bining chosen in this analysis, the efficiency of the measured $d\sigma/E_T^{jet}$ $(d\sigma/\eta^{jet})$ in inclusive jet production in CC DIS is $\sim 60\%$ $(\sim 80\%)$. The purity of the measured $d\sigma/E_T^{jet}$ $(d\sigma/\eta^{jet})$ is $\sim 80\%$ $(\sim 90\%)$. The efficiency of the dijet cross section measurements is $\sim 40\%$ and the purity $\sim 60\%$.

The number of data events N_i^{DAT} in bin i of a given distribution is corrected to the hadron level by multiplying with a correction factor as follows:

$$N_i^{COR} = N_i^{DAT} \cdot C_i^{MC} \tag{6.12}$$

The correction factor C_i^{MC} is calculated from the MC samples as follows:

$$C_i^{MC} = \frac{\mathcal{P}_i}{\mathcal{E}_i} = \frac{N_i^{GEN}}{N_i^{DET}} \tag{6.13}$$

The correction factors, C_i^{MC}, given by CDM and MEPS for the inclusive jet cross section measurements as a function of η^{jet}, E_T^{jet} and Q^2 are shown in Fig. 6.6 for the detector simulation of the years 1995-1997 (left) and 1999-2000 (right). The detector correction of the inclusive jet cross sections are $\sim 30\%$. The corrections increase up to 50% for small jet transverse energies, and are reduced for higher E_T^{jet} bins which are further away from the phase space limits.

Figure 6.7 shows the correction factors for the dijet cross section measurements as a function of m_{12} and Q^2. The detector corrections for the dijet cross sections are $\sim 50\%$. Both CDM and MEPS give similar detector correction factors.

The selection cuts on the missing transverse momentum, $\not{p}_t$, and the virtuality of the event, Q^2, are the main contributions to the loss of CC jet events in some phase space regions. The cut on $\not{p}_t$ is crucial to separate the CC interaction from NC ep scattering processes and the Q^2 cut is necessary to select deep inelastic processes. Even though the loss of events is large both selection cuts cannot be avoided.

The cross section in each bin i is determined as

$$\sigma_i^{COR} = \frac{N_i^{COR}}{\mathcal{L} \cdot \Delta_i}, \tag{6.14}$$

where N_i^{COR} is the corrected number of events in bin i, $\mathcal{L}$ is the integrated luminosity and Δ_i is the bin width.

The statistical uncertainty of the corrected number of events is calculated using standard error propagation methods. The data and the correction factor C_i^{MC} are independent of each other. The statistical uncertainty of the data is calculated as the square root of the number of events:

$$\left(\frac{\sigma_i^{COR}}{N_i^{COR}}\right)^2 = \left(\frac{\sqrt{(N_i^{DAT})}}{N_i^{DAT}}\right)^2 + \left(\frac{\sigma_{C_i^{MC}}}{C_i^{MC}}\right)^2 \tag{6.15}$$

It is not possible to calculate the uncertainty of the correction factor directly from the formula 6.13 because the number of generated (N_i^{GEN}) and reconstructed (N_i^{DET})
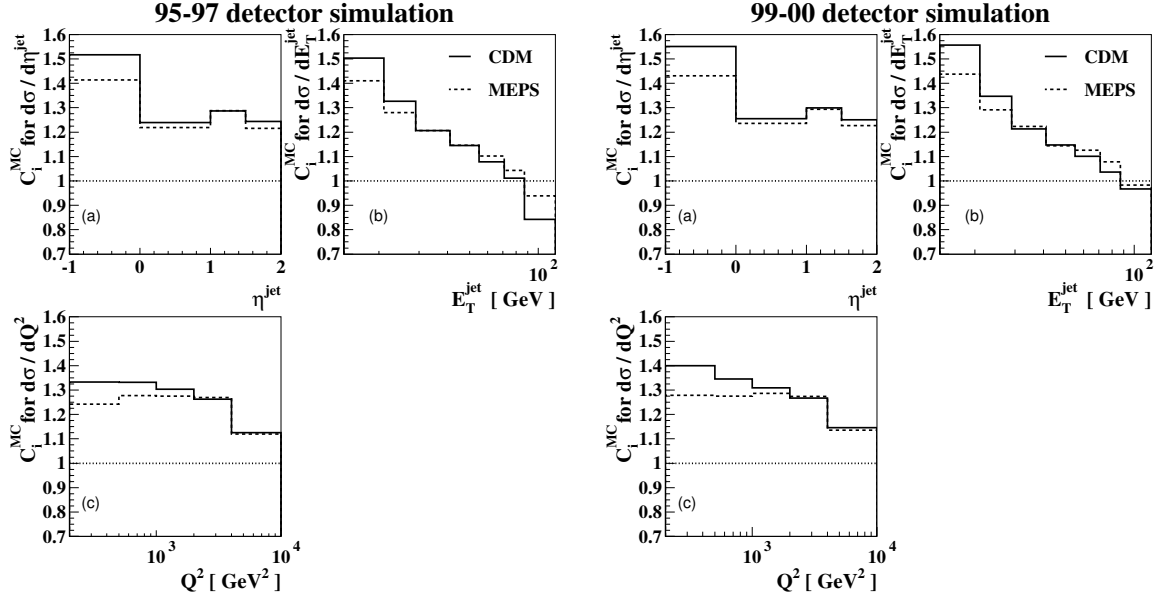
Figure 6.6 - Detector correction factors for the inclusive jet cross-section measurement as a function of (a) η^{jet}, (b) E_T^{jet} and (c) Q^2, given by the CDM and MEPS MC models for the simulation of the years 1995-1997 (left) and 1999-2000 (right).

events or jets are not independent[1]. To apply error propagation the following quantities are defined in each bin:

$$A1 = N(\text{GEN \& DET}) = N^{\text{GEN\&DET}}$$
$$A2 = N(\text{GEN \& }\overline{\text{DET}}) \qquad (6.16)$$
$$A3 = N(\overline{\text{GEN}}\text{ \& DET})$$

, where $N(\text{GEN\&DET})$ are the number of events generated and reconstructed in the bin, $N(\text{GEN\&}\overline{\text{DET}})$ are the number of events generated in the bin and reconstructed in another bin and $N(\overline{\text{GEN}}\text{\&DET})$ are the number of events reconstructed in the bin that were generated in another bin.

The three numbers above are independent of each other and, their respective statistical uncertainties can be calculated using Poisson statistics. The following relations hold:

$$N_i^{\text{GEN}} = A1_i + A2_i$$
$$N_i^{\text{DET}} = A1_i + A3_i$$
$$C_i^{\text{MC}} = \frac{A1_i + A2_i}{A1_i + A3_i} \qquad (6.17)$$

The statistical uncertainties of the correction can be calculated from the above relations using error propagation:

$$\left(\frac{\sigma_{C_i^{\text{MC}}}}{C_i^{\text{MC}}}\right)^2 = \left(\frac{\partial C_i^{\text{MC}}}{\partial A1_i} \cdot \frac{\sigma_{A1_i}}{A1_i}\right)^2 + \left(\frac{\partial C_i^{\text{MC}}}{\partial A2_i} \cdot \frac{\sigma_{A2_i}}{A2_i}\right)^2 + \left(\frac{\partial C_i^{\text{MC}}}{\partial A3_i} \cdot \frac{\sigma_{A3_i}}{A3_i}\right)^2 \qquad (6.18)$$

---

[1]In the case of an ideal detector these two sets of events would be exactly the same.

95-97 detector simulation **99-00 detector simulation**
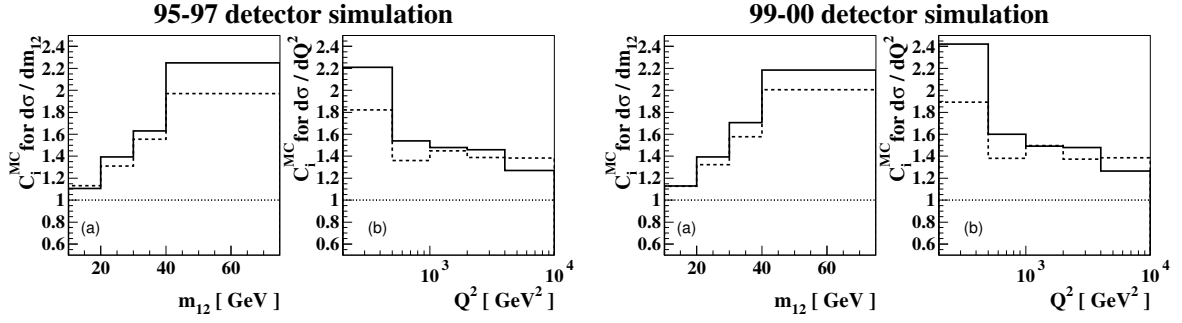
Figure 6.7 - Detector correction factors for the dijet cross-section measurement as a function of (a) m_{12} and (b) Q^2, given by the CDM and MEPS MC models for the simulation of the years 1995-1997 (left) and 1999-2000 (right).

The three partial derivatives and the statistical uncertainties of the quantities $A1$, $A2$, and $A3$ are:

$$\frac{\partial C_i^{MC}}{\partial A1_i} = \frac{A3_i - A2_i}{(A1_i + A3_i)^2} \quad , \quad \sigma_{A1_i} = \sqrt{A1_i}$$

$$\frac{\partial C_i^{MC}}{\partial A2_i} = \frac{1}{A1_i + A3_i} \quad , \quad \sigma_{A2_i} = \sqrt{A2_i} \qquad (6.19)$$

$$\frac{\partial C_i^{MC}}{\partial A3_i} = -\frac{A1_i + A2_i}{(A1_i + A3_i)^2} \quad , \quad \sigma_{A3_i} = \sqrt{A3_i}$$

By using the relations (6.15), (6.16), (6.18) and (6.19), the statistical uncertainty of the corrected number of events is calculated.

6.2.2 Determination of the jet internal structure

The jet internal structure can be studied in terms of many observables. In this analysis the mean subjet multiplicity is considered. The mean subjet multiplicity reconstructed with the calorimeter is corrected to hadron level using Monte Carlo techniques and with a *bin-by-bin correction* method in a similar way as for the cross sections. This procedure corrects for acceptance and smearing effects. The correction factors also take into account the efficiency of the trigger, the selection criteria, and the efficiency and purity of the jet reconstruction.

For the mean subjet multiplicity, $\langle n_{sbj} \rangle$, the corrected observable is obtained as follows:

$$\langle n_{sbj} \rangle_{corr} = C^{MC} \cdot \langle n_{sbj} \rangle_{cal} , \qquad (6.20)$$

where $\langle n_{sbj} \rangle_{cal}$ is the subjet multiplicity as reconstructed with the calorimeter and C^{MC} is the MC correction factor. C^{MC} is calculated as:

$$C^{MC} = \frac{\langle n_{sbj} \rangle_{had}^{MC}}{\langle n_{sbj} \rangle_{det}^{MC}} , \qquad (6.21)$$

where $\langle n_{sbj} \rangle_{had}^{MC}$ and $\langle n_{sbj} \rangle_{det}^{MC}$ are the values of the subjet multiplicity at hadron and detector level, respectively.
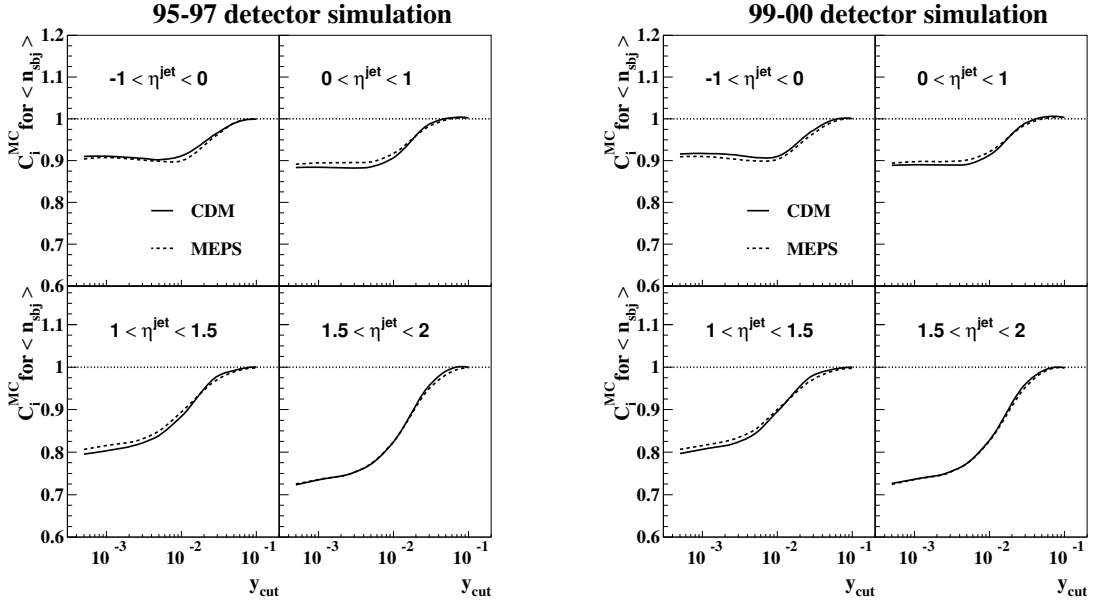
Figure 6.8 - Detector correction factors for the $\langle n_{sbj} \rangle$ as function of y_{cut} in different η^{jet} regions, given by the CDM and MEPS MC models for the simulation of the years 1995-1997 (left) and 1999-2000 (right).
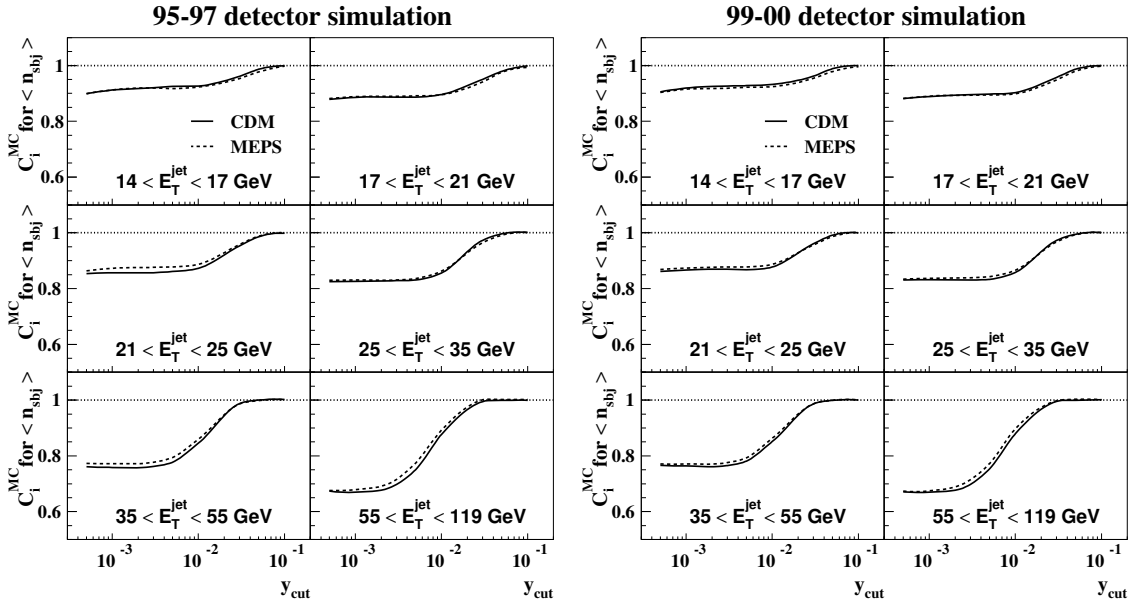

Figure 6.9 - Detector correction factors for $\langle n_{sbj} \rangle$ as a function of y_{cut} in different E_T^{jet} regions, given by the CDM and MEPS MC models for the simulation of the years 1995-1997 (left) and 1999-2000 (right).
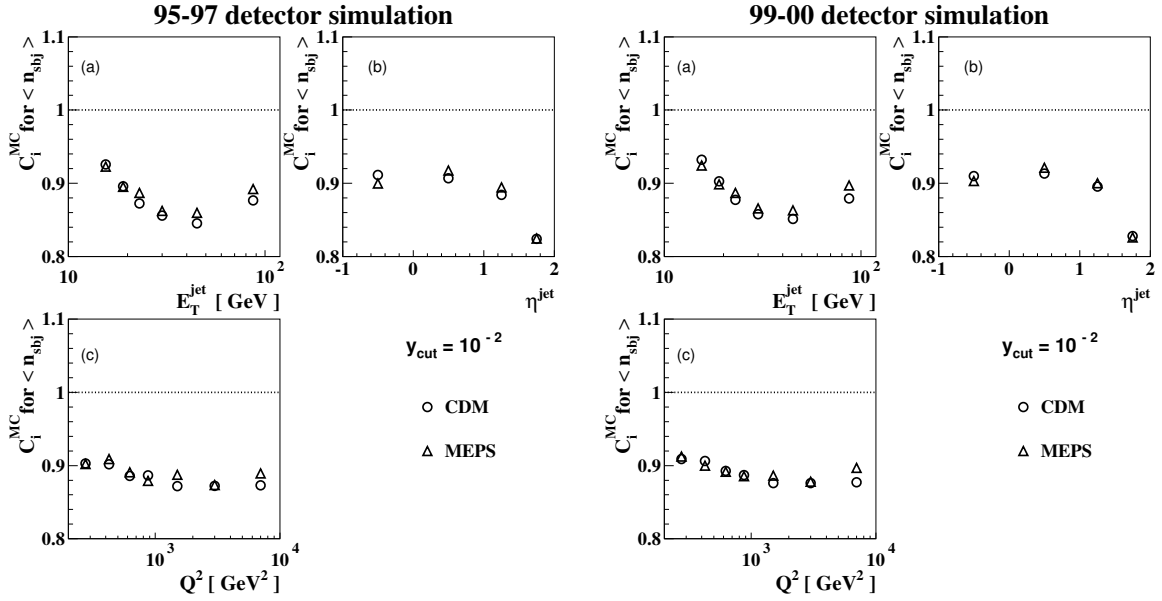
Figure 6.10 - Detector correction factors for the $\langle n_{sbj} \rangle$ as function of (a) E_T^{jet}, (b) η^{jet} and (c) Q^2 for fixed value of $y_{cut} = 10^{-2}$, given by the CDM and MEPS MC models for the simulation of the years 1995-1997 (left) and 1999-2000 (right).

The correction factor given by CDM and MEPS for the measurement of $\langle n_{sbj} \rangle$ as a function of y_{cut} for different η^{jet} and E_T^{jet} regions are shown in Fig. 6.8 and Fig. 6.9, respectively. The corrections increase as the resolution scale y_{cut} decreases. The corrections for $\langle n_{sbj} \rangle$ as a function of η^{jet}, E_T^{jet} and Q^2 for a fixed value of $y_{cut} = 0.01$ are shown in Fig. 6.10a, b and c, respectively. These corrections are $\sim 10\%$. Both CDM and MEPS give similar detector correction factors for $\langle n_{sbj} \rangle$.

6.2.3 Correction for QED effects

To compare the data with perturbative QCD calculations, the resuls have to be corrected for QED radiative effects, mainly due to radiation of photons in the initial state, which are not included in the NLO QCD calculations. To obtain the correction factors, MC samples of CDM and MEPS events were generated with and without QED effects. The predictions given by the different samples are used to compute the QED correction factor, C^{QED}, defined as the ratio between the predictions without QED effects and that with those effects included.

The correction factors given by CDM and MEPS for the inclusive jet cross section measurements as a function of η^{jet}, E_T^{jet} and Q^2 are shown in Fig. 6.11 for the MC simulation with center-of-mass energy $\sqrt{300}$ GeV (left) and $\sqrt{318}$ GeV (right). Figure 6.12 shows the correction factors for the dijet cross section measurements as a function of m_{12} and Q^2.

The QED correction factors for both the differential inclusive jet and dijet cross sections are approximately constant and $\sim 5\%$. For the inclusive cross section $d\sigma/dE_T^{jet}$,
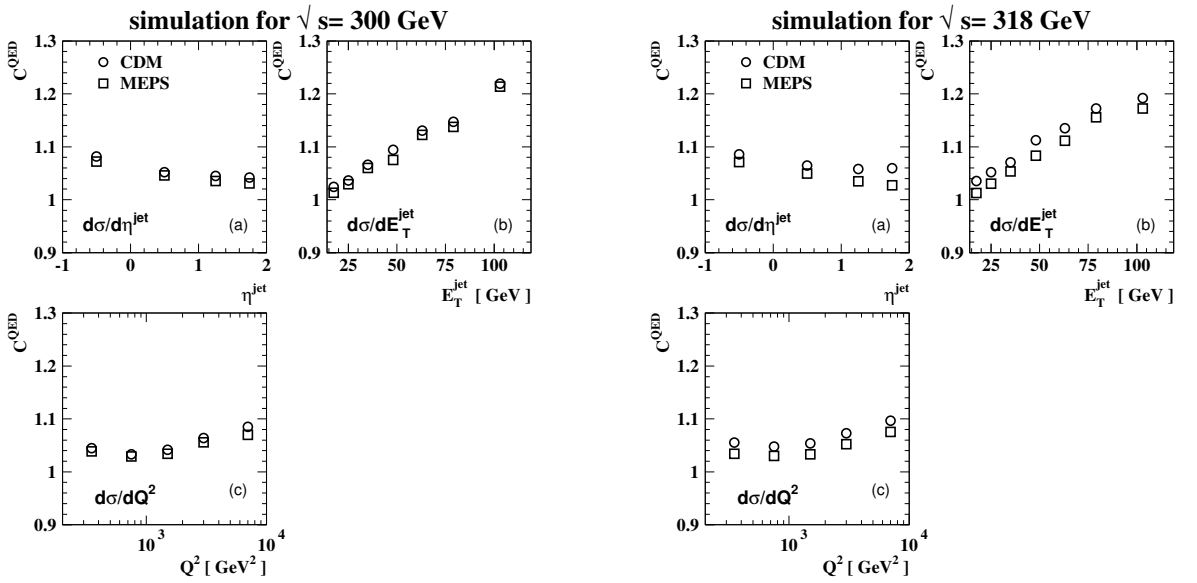
Figure 6.11 - QED correction factors for the inclusive jet cross section measurement as a function of (a) η^{jet}, (b) E_T^{jet} and (c) Q^2, as given by the CDM and MEPS MC models for the simulation with center-of-mass energy $\sqrt{300}$ GeV (left) and $\sqrt{318}$ GeV (right).
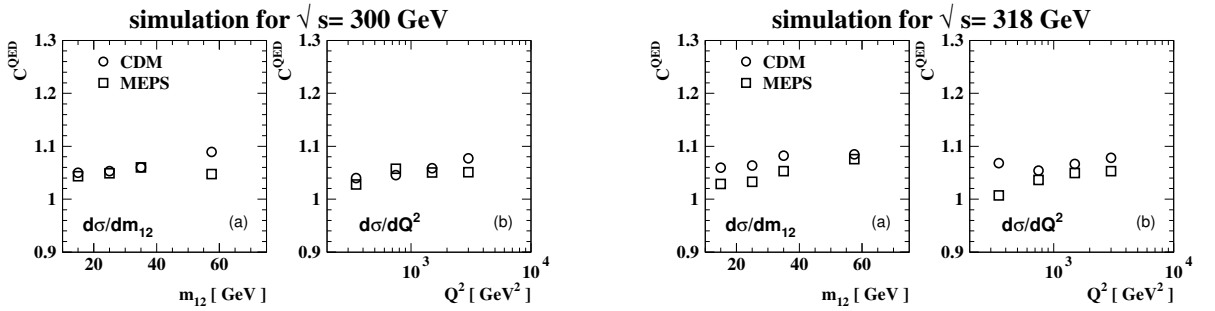
Figure 6.12 - QED correction factors for the dijet cross section measurement as a function of (a) m_{12} and (b) Q^2, as given by the CDM and MEPS MC models for the simulation with center-of-mass energy $\sqrt{300}$ GeV (left) and $\sqrt{318}$ GeV (right).

the correction factor increases as E_T^{jet} increases as much as 25%. The simulations with different center-of-mass energies give similar correction factors.

The deviation of C^{QED} from unity is negligible in the case of the subjet multiplicity.

6.3 Study of Systematic Uncertainties

The corrected observables can be systematically mismeasured due to a non-perfect understanding and simulation of the physics and of detector effects. Studies have been done in order to estimate the size of the systematic uncertainties.

One source of uncertainty is the mismeasurement of the variables on which cuts are

applied at the detector level. Therefore, the cuts at the calorimeter level are varied by 10%, which is approximately the same as the resolution of the cut variables, in both directions around the cut value and keeping the hadron level cut fixed. In the ideal case of the Monte Carlo model describing perfectly the data, such a change of a cut would not affect at all the final result. However, since this is not always true, the variations (if any) in the measured quantities would indicate a possible systematic effect.

The main signature of CC events is the presence of missing transverse momentum, $\not{p}_t$. The data were selected with a cut of $\not{p}_t > 11$ GeV which has been changed to 12 GeV or 10 GeV. This gives a variation on the cross sections of less than 5%. In the case of the subjet multiplicities the uncertainty is less than 2%. Other selection tresholds were also varied:

- $N_{track}(vertex)/N_{track}(total) > 0.2$ was changed to 0.3 or 0.1;

- $|\Delta\phi| < 1$ rad was changed to 1.1 rad or 0.9 rad;

- $|Z_{vertex}| < 50$ cm was changed to 55 cm or 45 cm;

- $\not{p}_t/E_T > 0.5$ was changed to 0.6 or 0.4 for the inclusive jet sample selection. $\not{p}_t/E_T > 0.3$ was changed to 0.4 or 0.2 for the dijet sample selection;

- $\not{p}_t^{good\ tracks}/\not{p}_t > 0.1$ was changed to 0.15 or 0.05;

- $\dfrac{\not{p}_t^{-1r}}{\not{p}_t} > 0.8$ was changed to 0.9 or 0.7;

- $E_t^{max}/E_t > 0.7$ was changed to 0.8 or 0.6.

The variation of these selection cuts gave a change typically less than 2% for all the measured observables;

Another possible source of systematic uncertainty is the difference in the results by using the CDM or MEPS samples to correct the distributions for detector effects. The central results have been obtained by correcting for detector effects using the CDM model. The differences in the results with the MEPS model is included as a systematic uncertainty. The uncertainty is typically smaller than 5% for the cross-section measurements and 2% for the measurements of the mean subjet multiplicity.

All these systematic uncertainties, i.e. the ones related to the variation of the data selection cuts and the uncertainty related to the use of MC models to correct the data for detector effects, were added in quadrature to the statistical errors and are shown as error bars in the figures.

There are sources of systematic errors which are correlated. The most important ones are:

- the integrated luminosity and

- the uncertainty in the energy scale of the calorimeter.

The uncertainty in the determination of the luminosity gives rise to an overall normalisation uncertainty of 2.0% in the measurement of cross sections, which is not included in the plots.

The uncertainty on the absolute energy scale affects the reconstruction of the transverse energy of the selected jets and of the reconstructed kinematic variables measured with the CAL. The uncertainties related to the transverse energy of the jets and the kinematic variables were estimated separately.

The uncertainty on the absolute energy scale of the jets was estimated to be $\pm 1\%$ for $E_T^{jet} > 10$ GeV and $\pm 3\%$ for lower E_T^{jet} values [Ch02c, Ch02d, Wi02]. The variation of the transverse energy of the jets by the estimated values resulted in an uncertainty of less than 5% (12 %) for the inclusive jet (dijet) cross sections and of less than 2% for the mean subjet multiplicity.

The uncertainty on the reconstructed kinematic variables was estimated by varying the energy variables measured by the CAL, like $\not{p}_t$ or E_T, by $\pm 3\%$. The uncertainty was less than 5% for all the distributions.

Both uncertanties associated with the energy scale are added in quadrature and are shown as shaded band in the plots presenting the results.

The ratio $\mathcal{O}^*/\mathcal{O}$, for all the sources of systematic uncertainty studied, is shown in figures 6.13 to 6.48 : $\mathcal{O}$ is the measured observable with the standard method and $\mathcal{O}^*$ is the value of the observable obtained upon variation of one of the aspects of the method. The shaded band in these figures shows the statistical uncertainty of the data. The systematic uncertainties in the plots are listed below:

- E_T^{jet} is varied by $\pm 1\%$ ($\pm 3\%$) for jets with $E_T^{jet} > 10$ GeV ($E_T^{jet} < 10$ GeV);

- the energy quantities measured with the CAL are varied by $\pm 3\%$;

- the cut on $\not{p}_t$ is varied by ± 1 GeV;

- the cut on $N_{track}(vertex)/N_{track}(total) > 0.2$ is changed to 0.3 or 0.1;

- the cut on $|\Delta\phi| < 1$ rad is changed to 1.1 rad or 0.9 rad;

- the cut on $|Z_{vertex}| < 50$ cm is changed to 55 cm or 45 cm;

- the cut on $\not{p}_t/E_T > 0.5$ (0.3) is changed to 0.6 (0.4) or 0.4 (0.2) for the selection of the inclusive jet (dijet) sample;

- the cut on $\not{p}_t^{good\ tracks}/\not{p}_t > 0.1$ is changed to 0.15 or 0.05;

- the cut on $\dfrac{\not{p}_t^{-1r}}{\not{p}_t} > 0.8$ is changed to 0.9 or 0.7;

- the cut on $E_t^{max}/E_t > 0.7$ is changed to 0.8 or 0.6;

- the MC MEPS is used instead of CDM to correct the data to the hadron level.

In all the observables considered in this analysis, the correlated and uncorrelated systematic uncertainties are smaller than the statistical uncertainty.
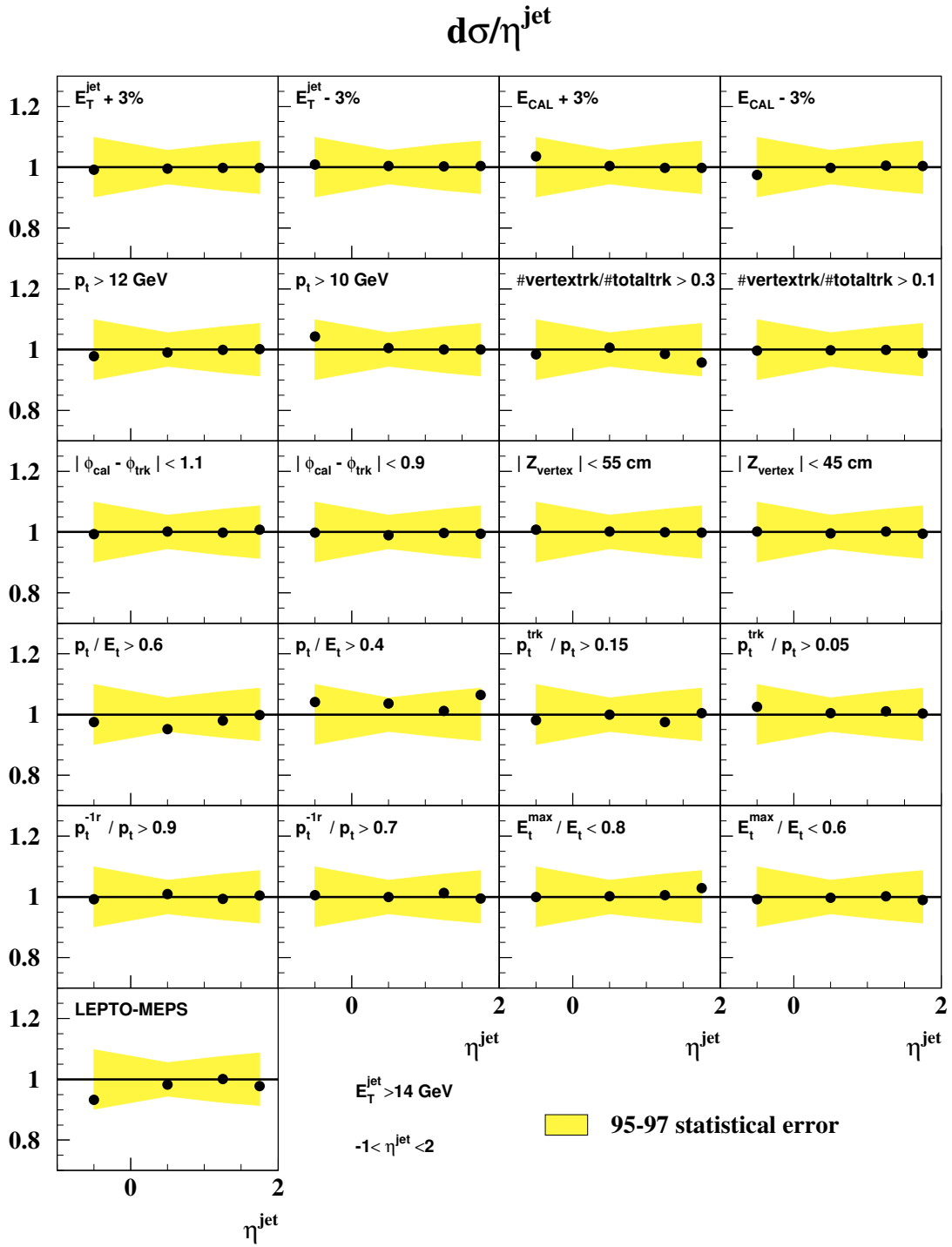
$$d\sigma/\eta^{jet}$$

Figure 6.13 - Ratio $\mathcal{O}^*/\mathcal{O}$ for the systematic variations of the measured inclusive jet cross section as a function of η^{jet} for the data taken in the years 1995-1997. The shaded band shows the statistical uncertainty of the data.
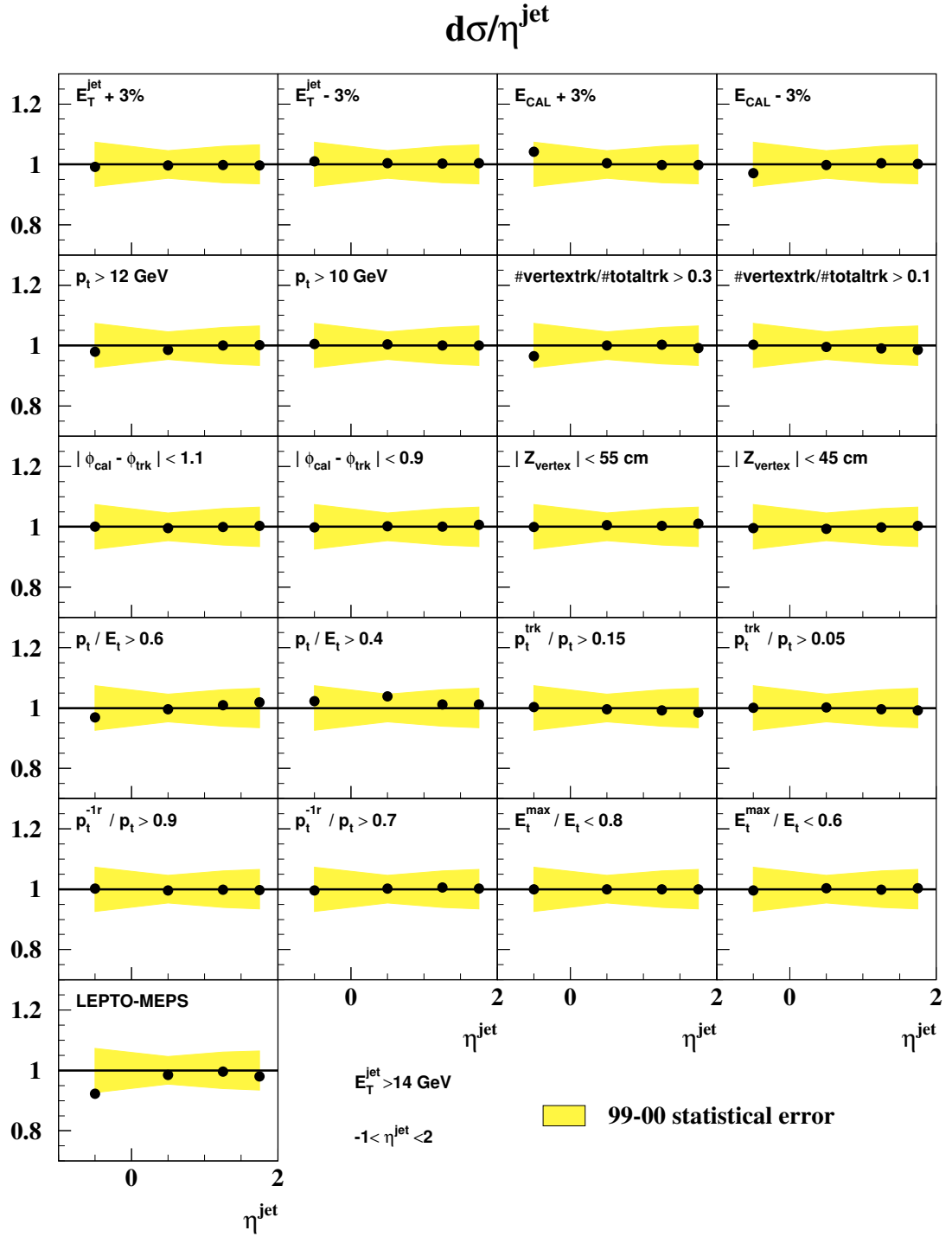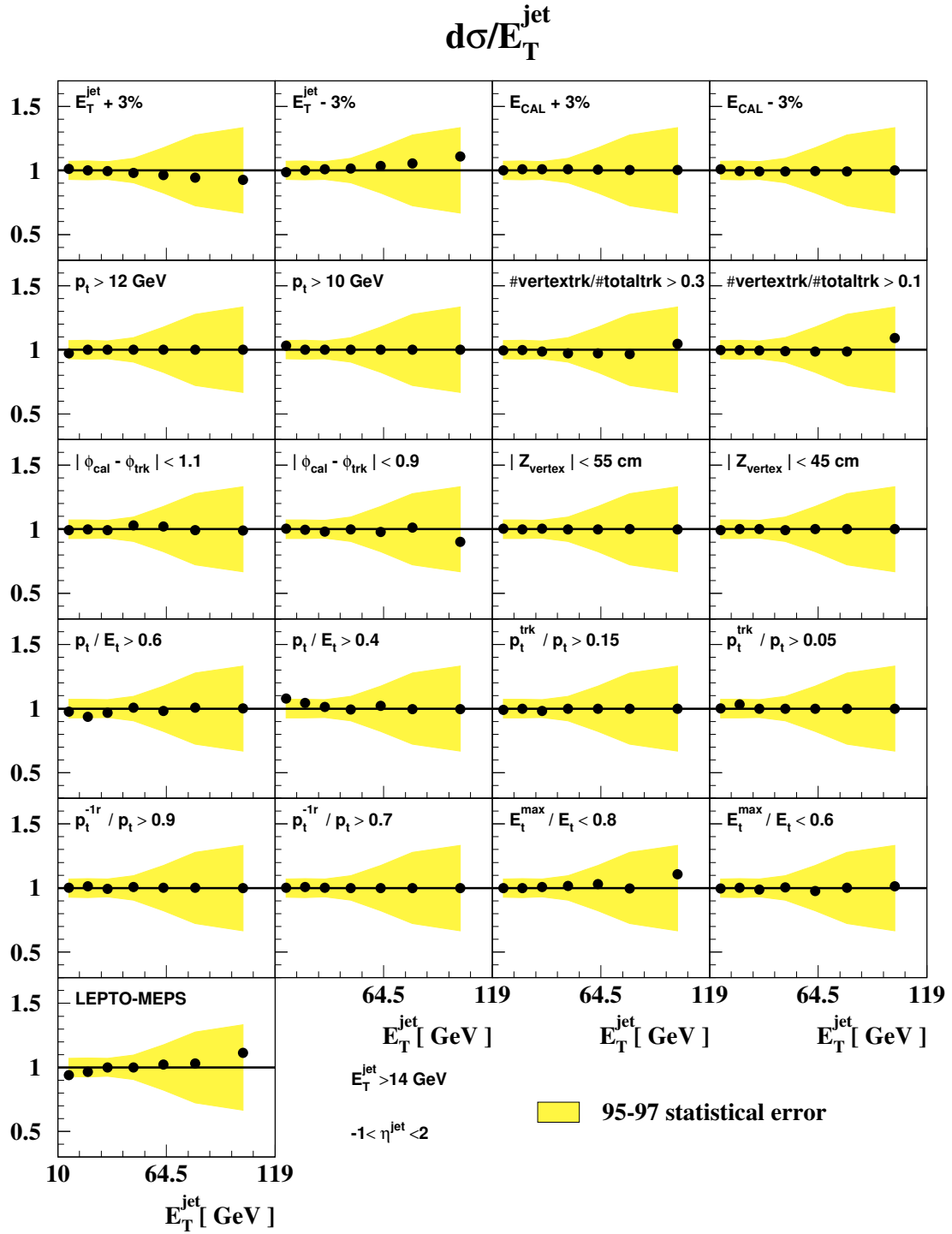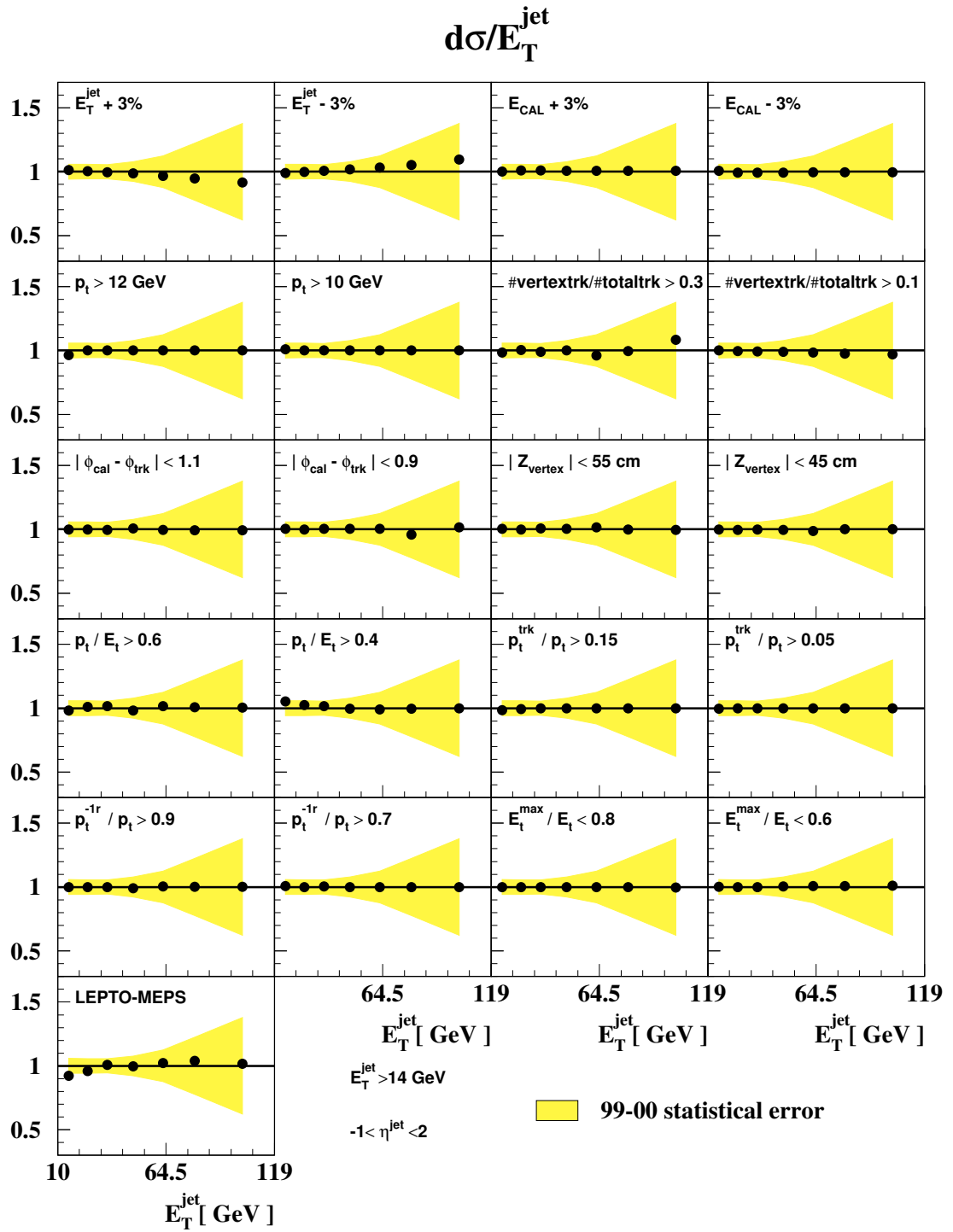
$$d\sigma/\eta^{jet}$$

Figure 6.14 - Ratio $\mathcal{O}^*/\mathcal{O}$ for the systematic variations of the measured inclusive jet cross section as a function of η^{jet} for the data taken in the years 1999-2000. The shaded band shows the statistical uncertainty of the data.

Figure 6.15 - Ratio $\mathcal{O}^*/\mathcal{O}$ for the systematic variations of the measured inclusive jet cross section as a function of E_T^{jet} for the data taken in the years 1995-1997. The shaded band shows the statistical uncertainty of the data.
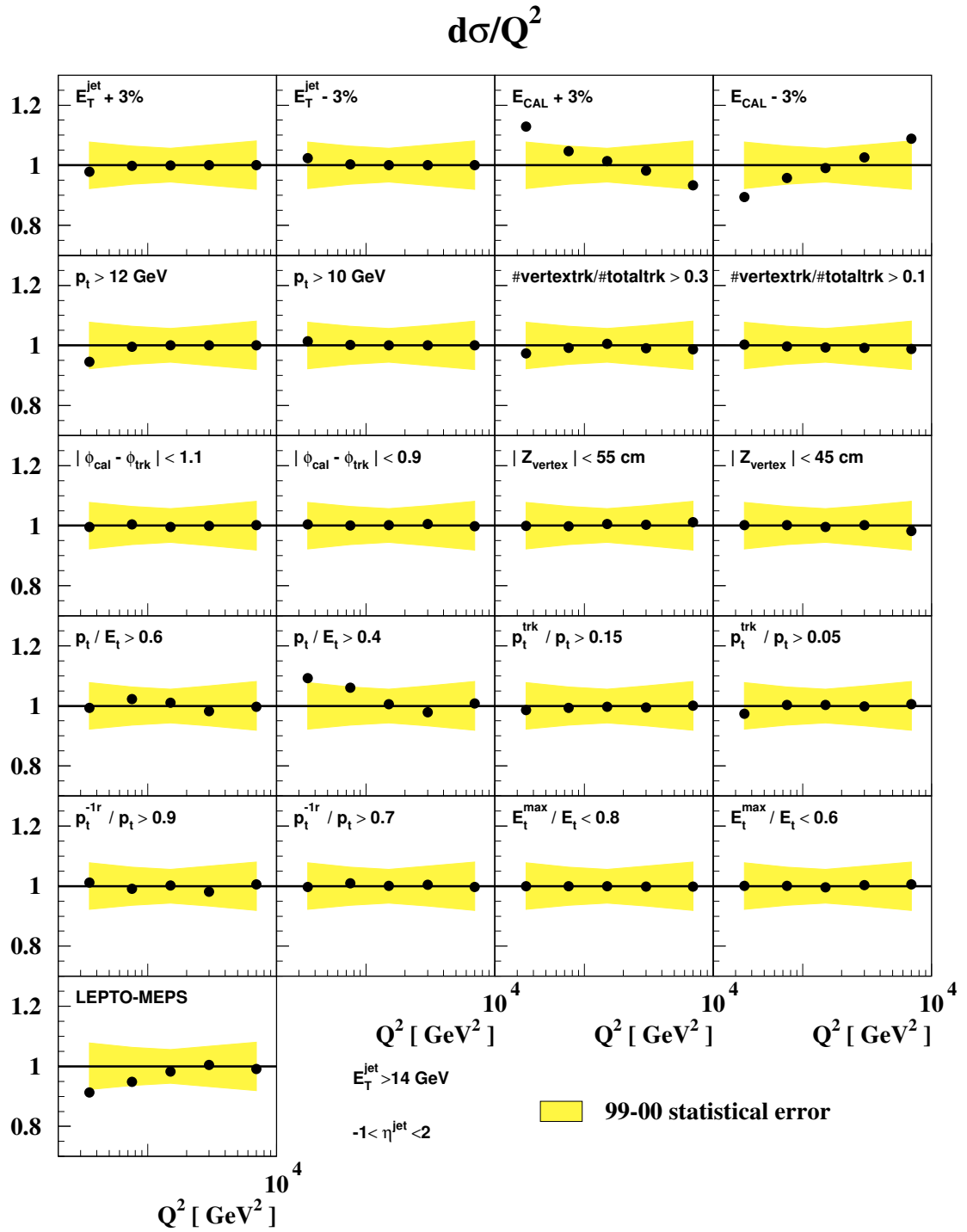
$$d\sigma/E_T^{jet}$$

Figure 6.16 - Ratio $\mathcal{O}^*/\mathcal{O}$ for the systematic variations of the measured inclusive jet cross section as a function of E_T^{jet} for the data taken in the years 1999-2000. The shaded band shows the statistical uncertainty of the data.

$$d\sigma/Q^2$$

Figure 6.17 - Ratio $\mathcal{O}^*/\mathcal{O}$ for the systematic variations of the measured inclusive jet cross section as a function of Q^2 for the data taken in the years 1995-1997. The shaded band shows the statistical uncertainty of the data.
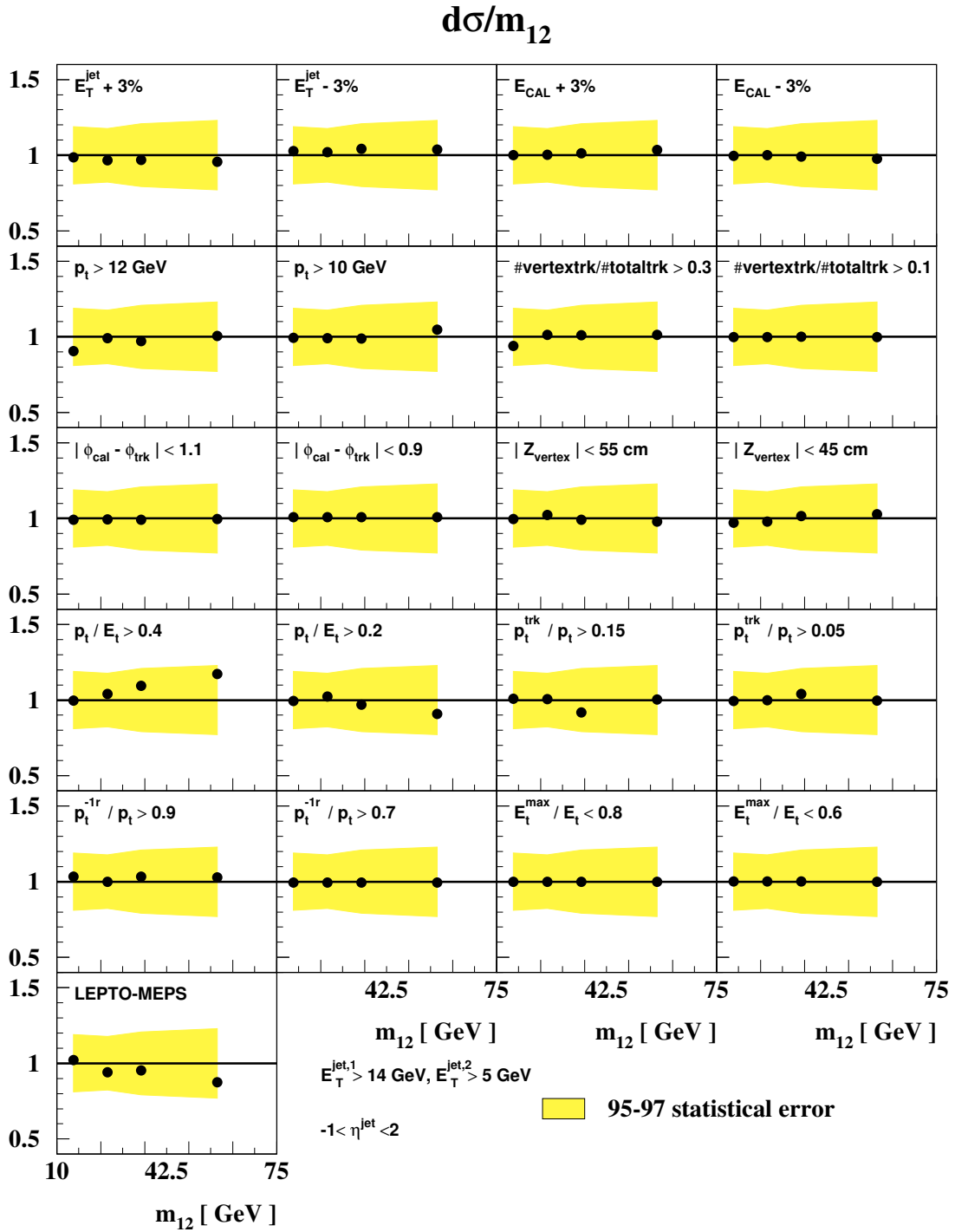
Figure 6.18 - Ratio $\mathcal{O}^*/\mathcal{O}$ for the systematic variations of the measured inclusive jet cross section as a function of Q^2 for the data taken in the years 1999-2000. The shaded band shows the statistical uncertainty of the data.

Figure 6.19 - Ratio $\mathcal{O}^*/\mathcal{O}$ for the systematic variations of the measured dijet cross section as a function of Q^2 for the data taken in the years 1995-1997. The shaded band shows the statistical uncertainty of the data.
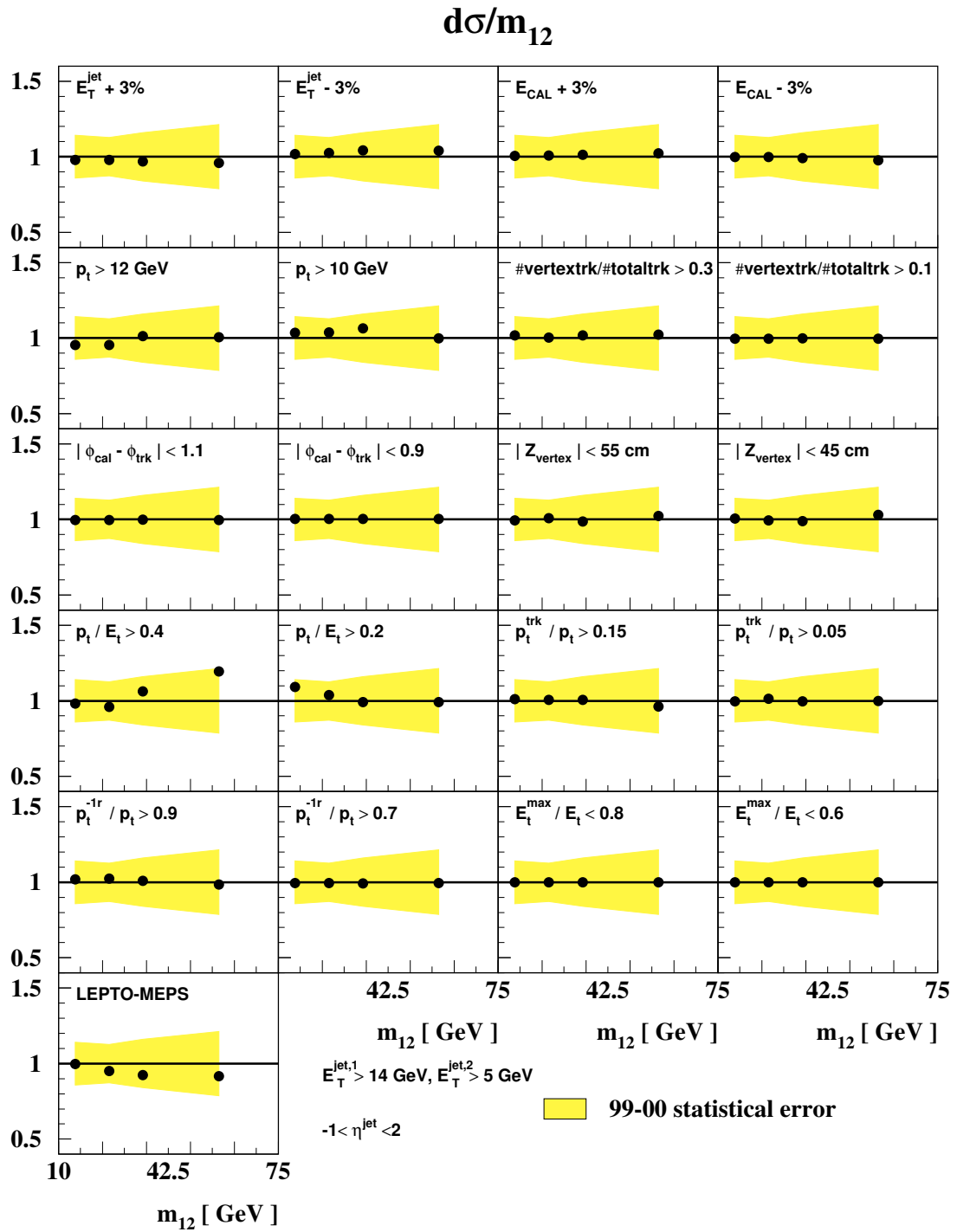
Figure 6.20 - Ratio $\mathcal{O}^*/\mathcal{O}$ for the systematic variations of the measured dijet cross section as a function of m_{12} for the data taken in the years 1999-2000. The shaded band shows the statistical uncertainty of the data.
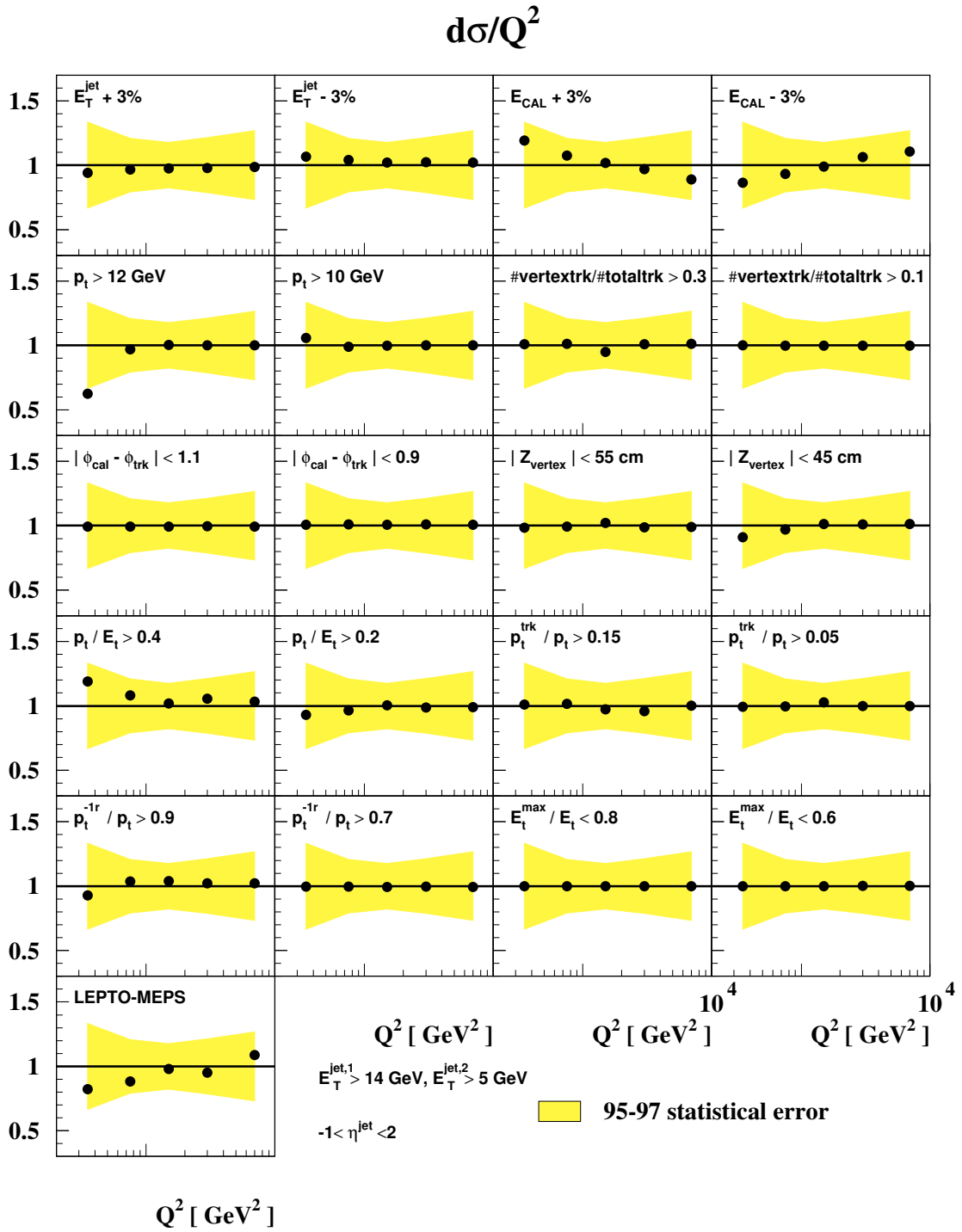
Figure 6.21 - Ratio $\mathcal{O}^*/\mathcal{O}$ for the systematic variations of the measured dijet cross section as a function of Q^2 for the data taken in the years 1995-1997. The shaded band shows the statistical uncertainty of the data.
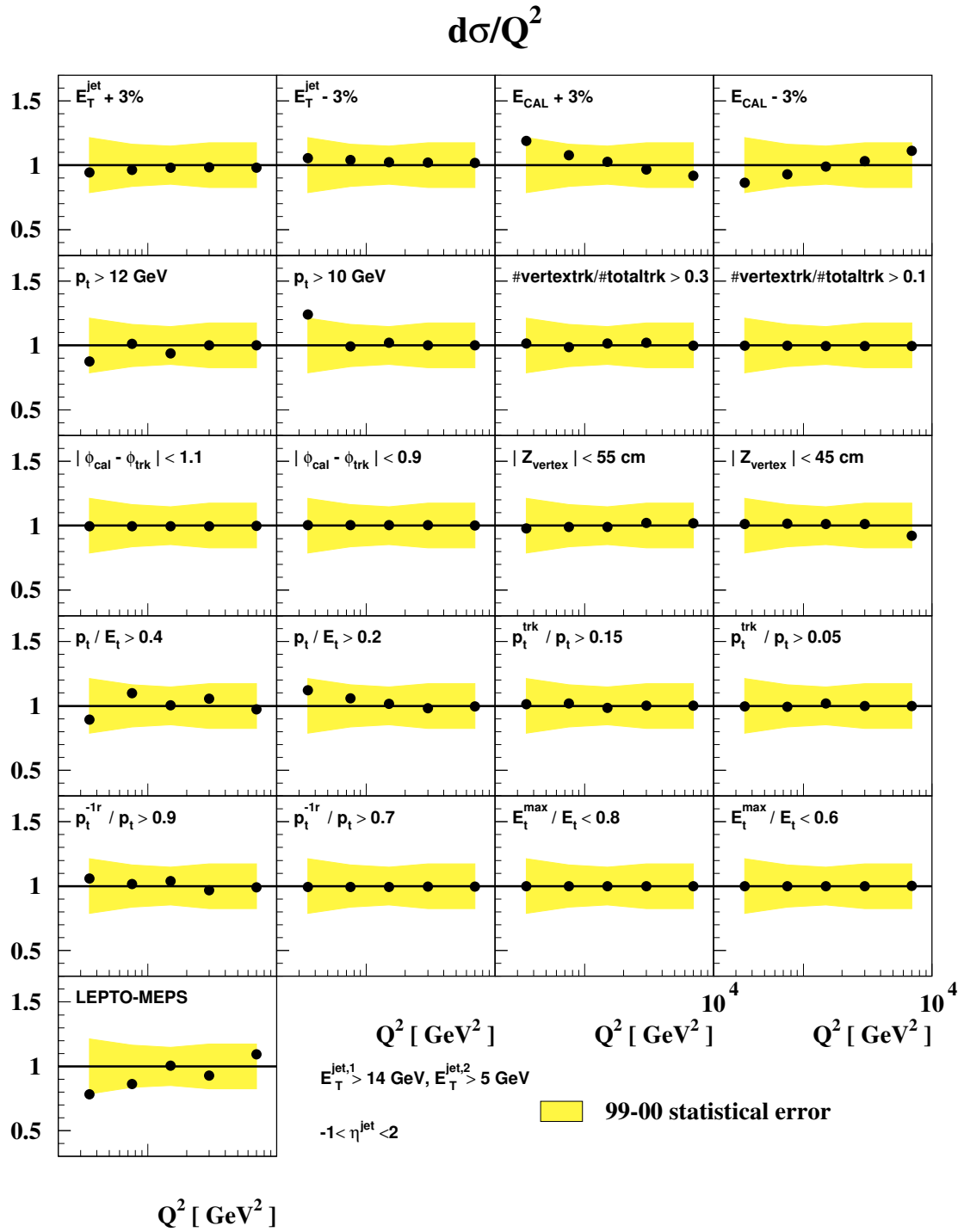
Figure 6.22 - Ratio $\mathcal{O}^*/\mathcal{O}$ for the systematic variations of the measured dijet cross section as a function of Q^2 for the data taken in the years 1999-2000. The shaded band shows the statistical uncertainty of the data.
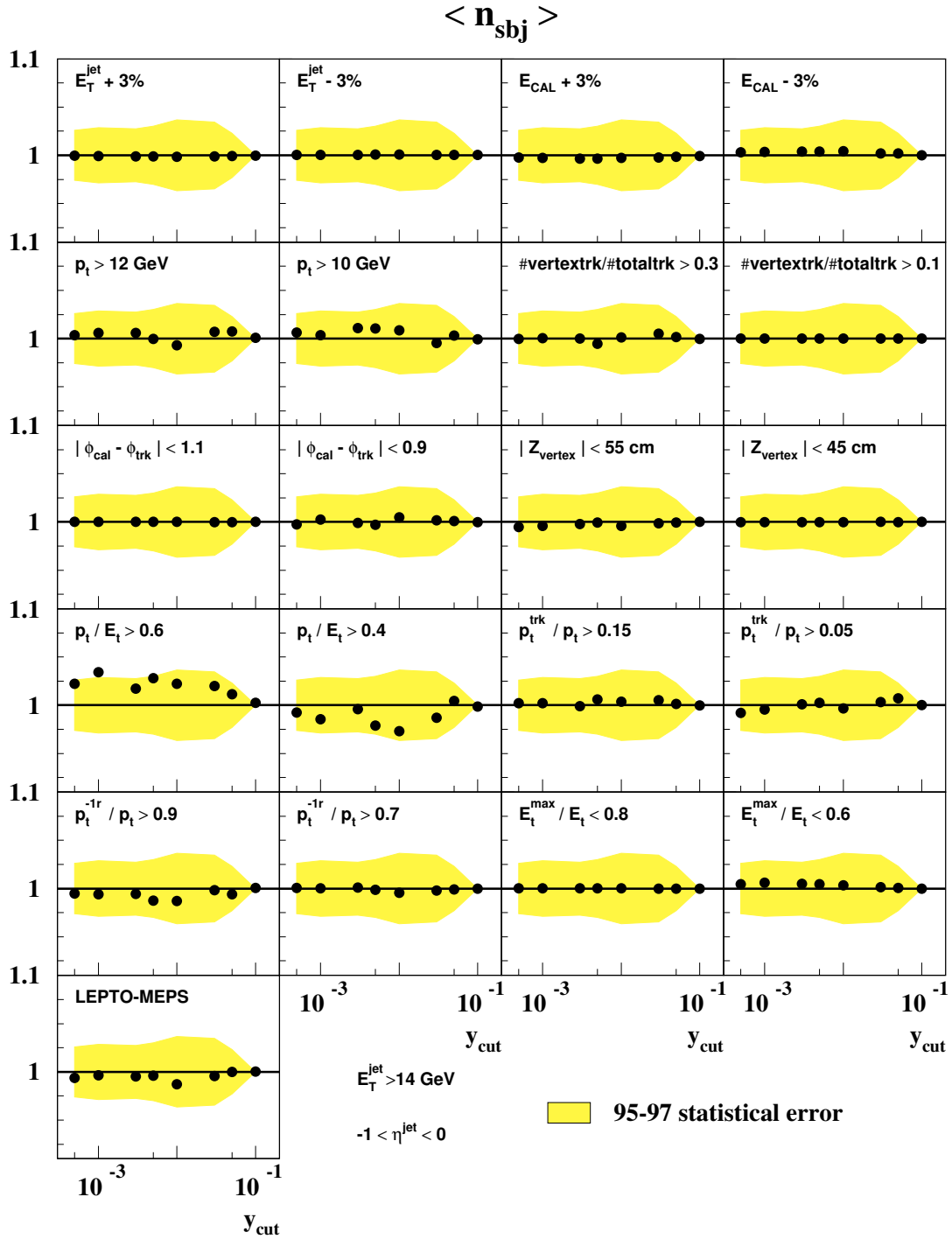
Figure 6.23 - Ratio $\mathcal{O}^*/\mathcal{O}$ for the systematic variations of the measured $\langle n_{sbj} \rangle$ as a function of y_{cut} and $-1 < \eta^{jet} < 0$ for the data taken in the years 1995-1997. The shaded band shows the statistical uncertainty of the data.
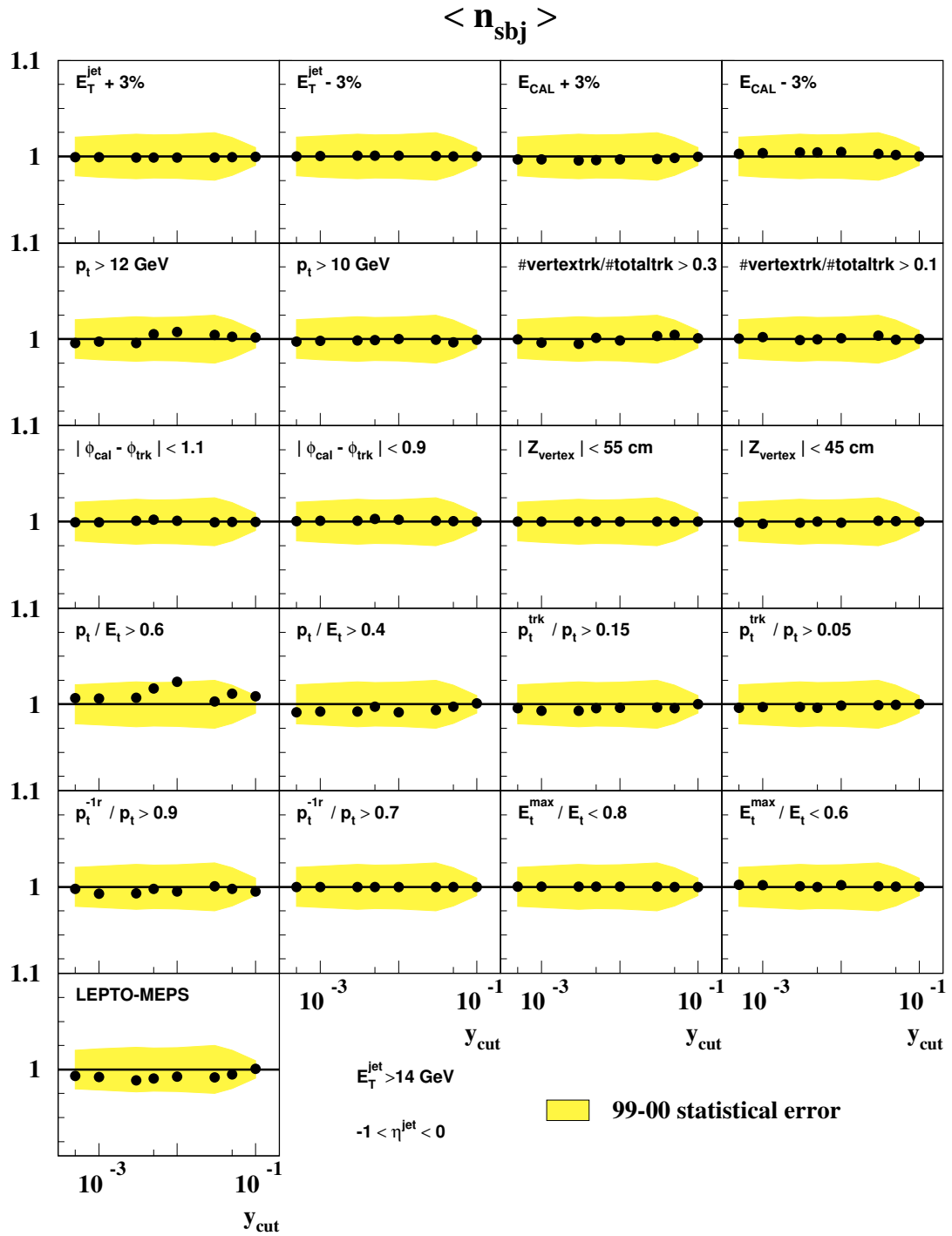
$< \mathbf{n_{sbj}} >$

Figure 6.24 - Ratio $\mathcal{O}^*/\mathcal{O}$ for the systematic variations of the measured $\langle n_{sbj} \rangle$ as a function of y_{cut} and $-1 < \eta^{jet} < 0$ for the data taken in the years 1999-2000. The shaded band shows the statistical uncertainty of the data.

Figure 6.25 - Ratio $\mathcal{O}^*/\mathcal{O}$ for the systematic variations of the measured $\langle n_{sbj} \rangle$ as a function of y_{cut} and $0 < \eta^{jet} < 1$ for the data taken in the years 1995-1997. The shaded band shows the statistical uncertainty of the data.
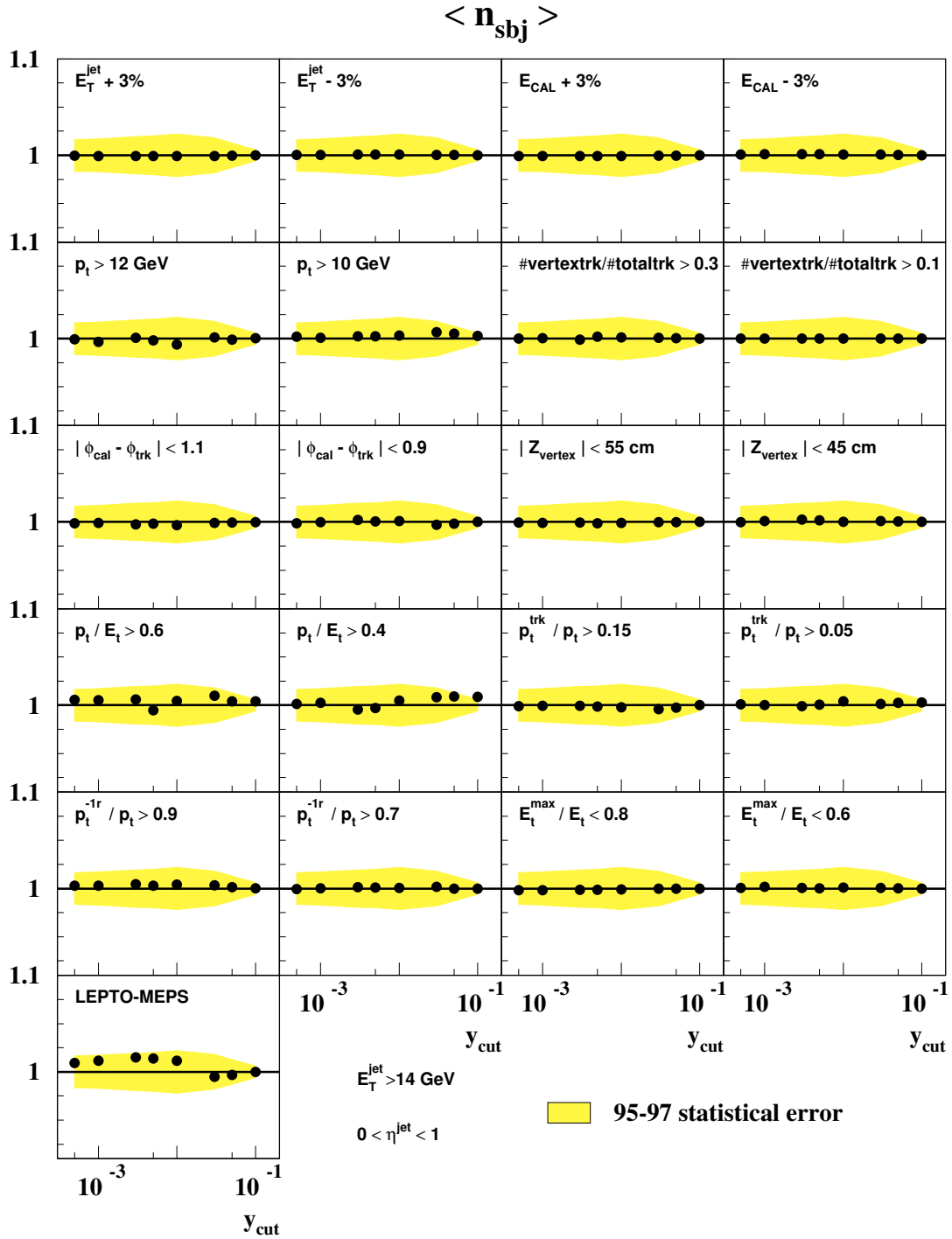
Figure 6.26 - Ratio $\mathcal{O}^*/\mathcal{O}$ for the systematic variations of the measured $\langle n_{sbj} \rangle$ as a function of y_{cut} and $0 < \eta^{jet} < 1$ for the data taken in the years 1999-2000. The shaded band shows the statistical uncertainty of the data.

Figure 6.27 - Ratio $\mathcal{O}^*/\mathcal{O}$ for the systematic variations of the measured $\langle n_{sbj} \rangle$ as a function of y_{cut} and $1 < \eta^{jet} < 1.5$ for the data taken in the years 1995-1997. The shaded band shows the statistical uncertainty of the data.
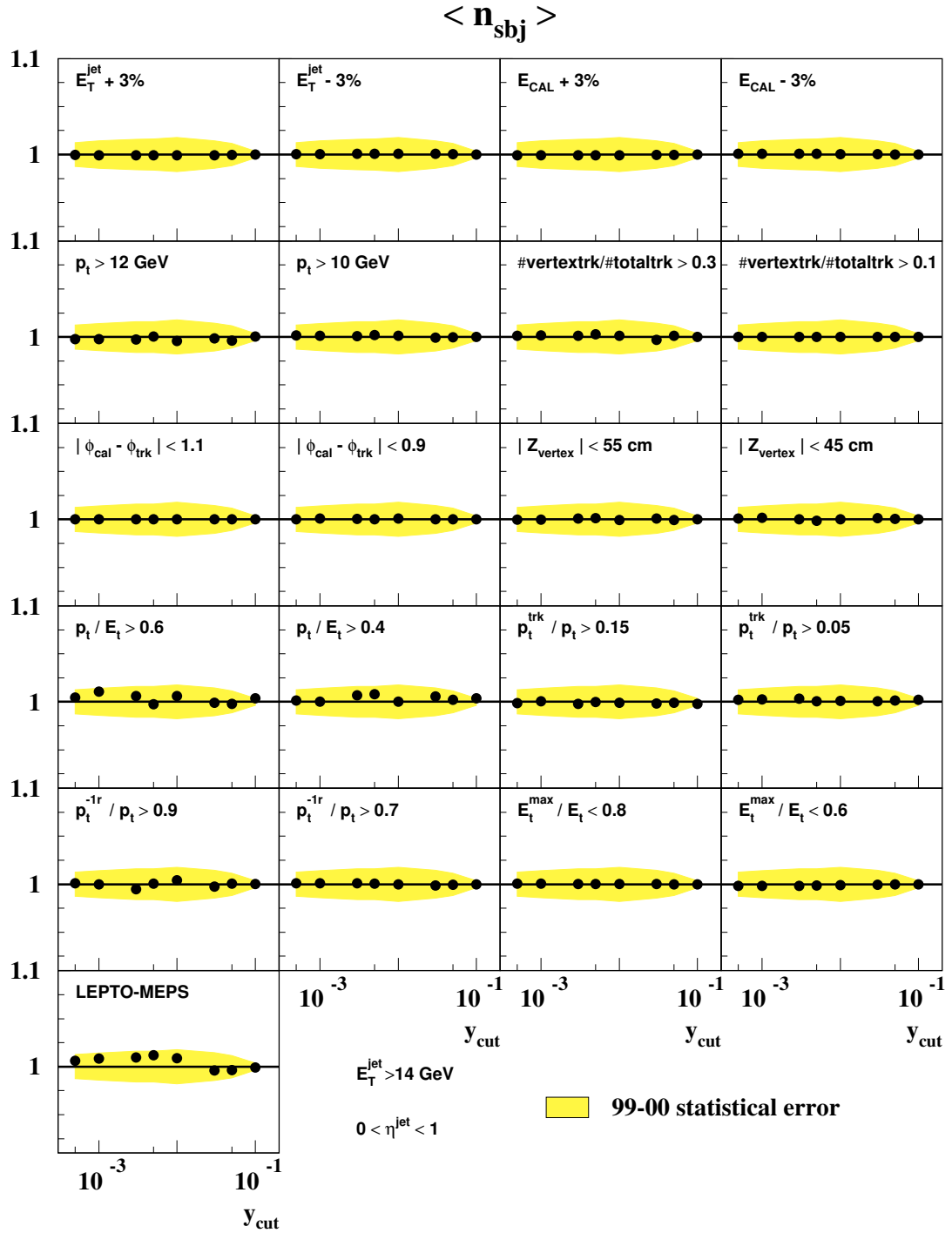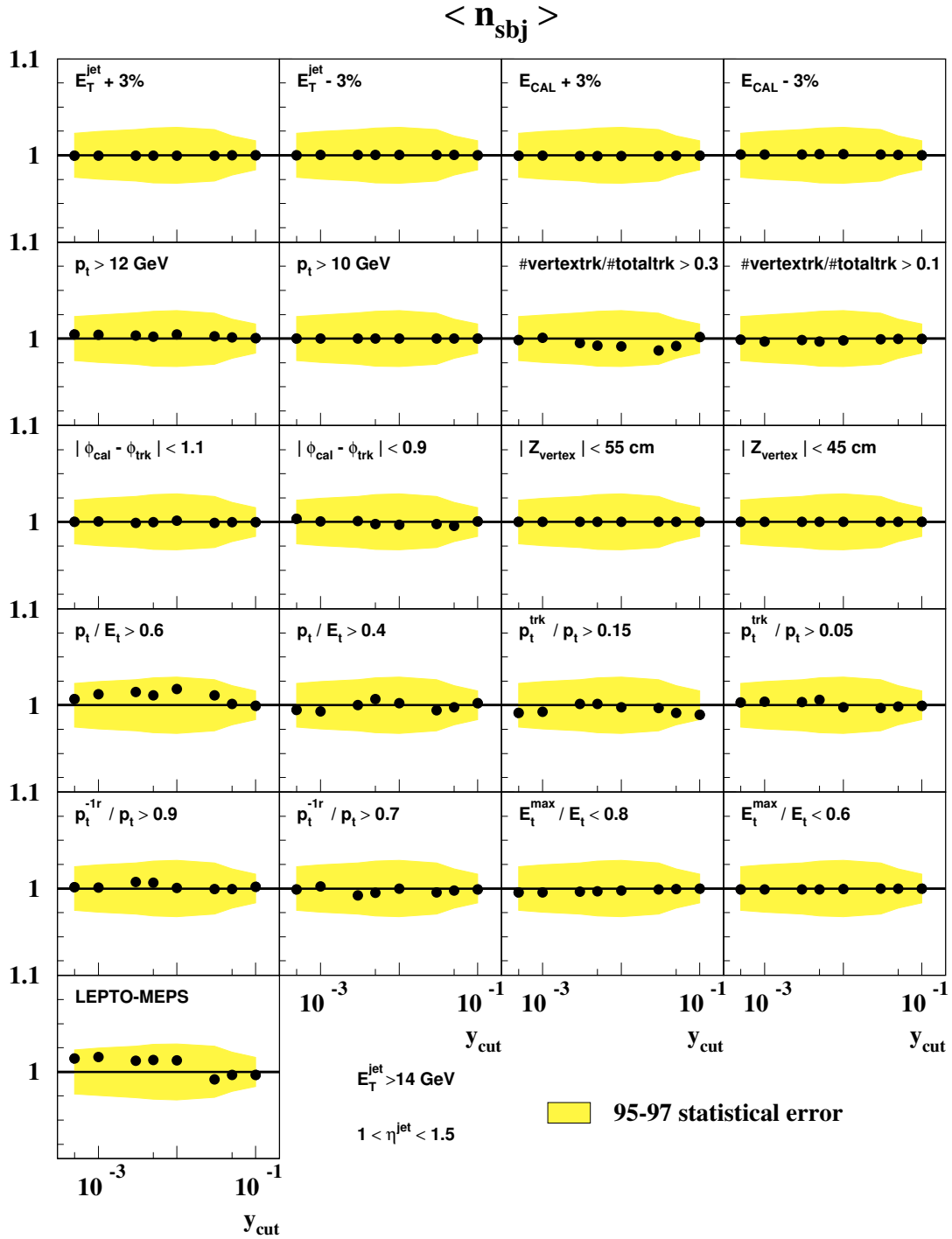
Figure 6.28 - Ratio $\mathcal{O}^*/\mathcal{O}$ for the systematic variations of the measured $\langle n_{sbj} \rangle$ as a function of y_{cut} and $1 < \eta^{jet} < 1.5$ for the data taken in the years 1999-2000. The shaded band shows the statistical uncertainty of the data.

Figure 6.29 - Ratio $\mathcal{O}^*/\mathcal{O}$ for the systematic variations of the measured $\langle n_{sbj} \rangle$ as a function of y_{cut} and $1.5 < \eta^{jet} < 2.$ for the data taken in the years 1995-1997. The shaded band shows the statistical uncertainty of the data.
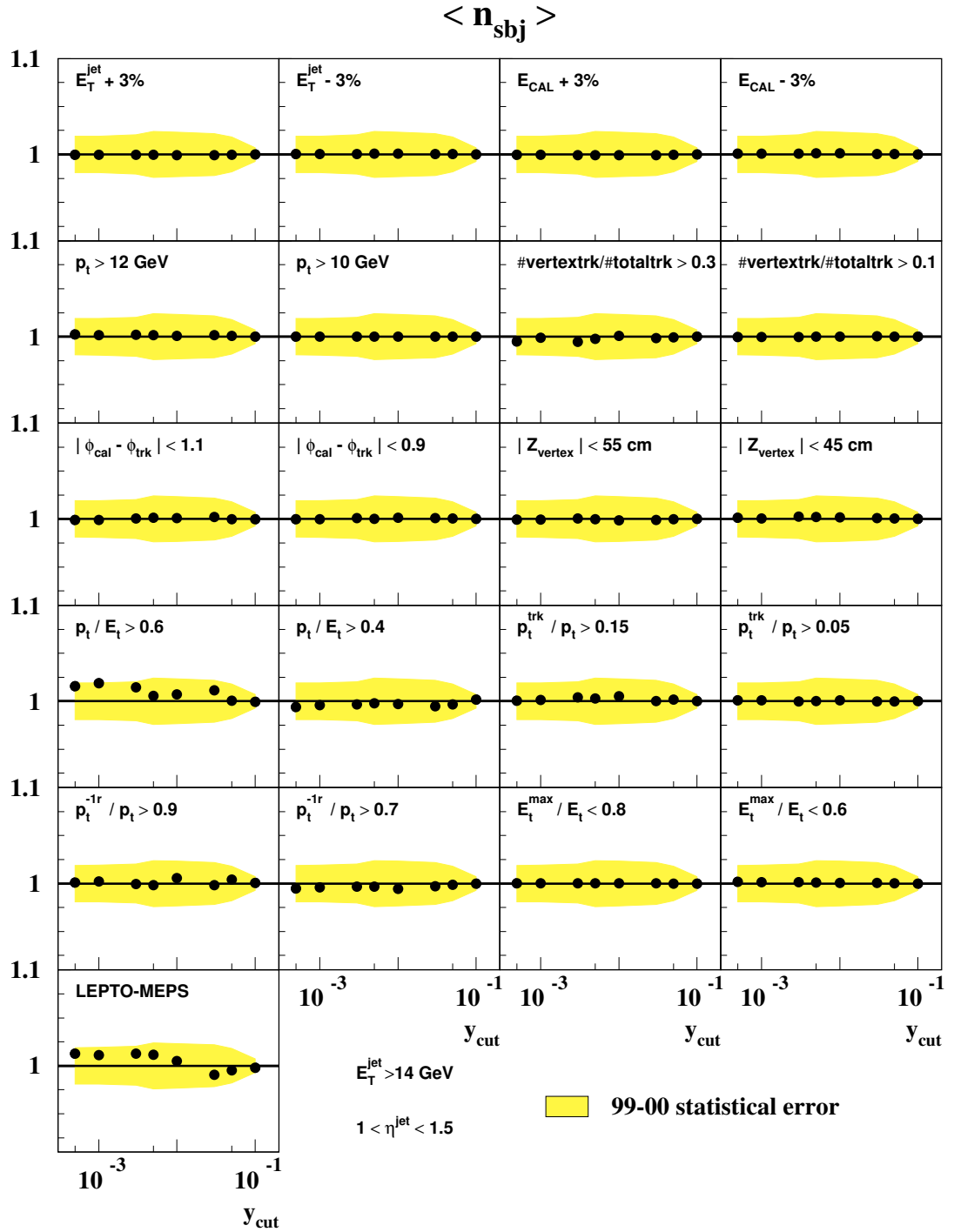
Figure 6.30 - Ratio $\mathcal{O}^*/\mathcal{O}$ for the systematic variations of the measured $\langle n_{sbj} \rangle$ as a function of y_{cut} and $1.5 < \eta^{jet} < 2$ for the data taken in the years 1999-2000. The shaded band shows the statistical uncertainty of the data.
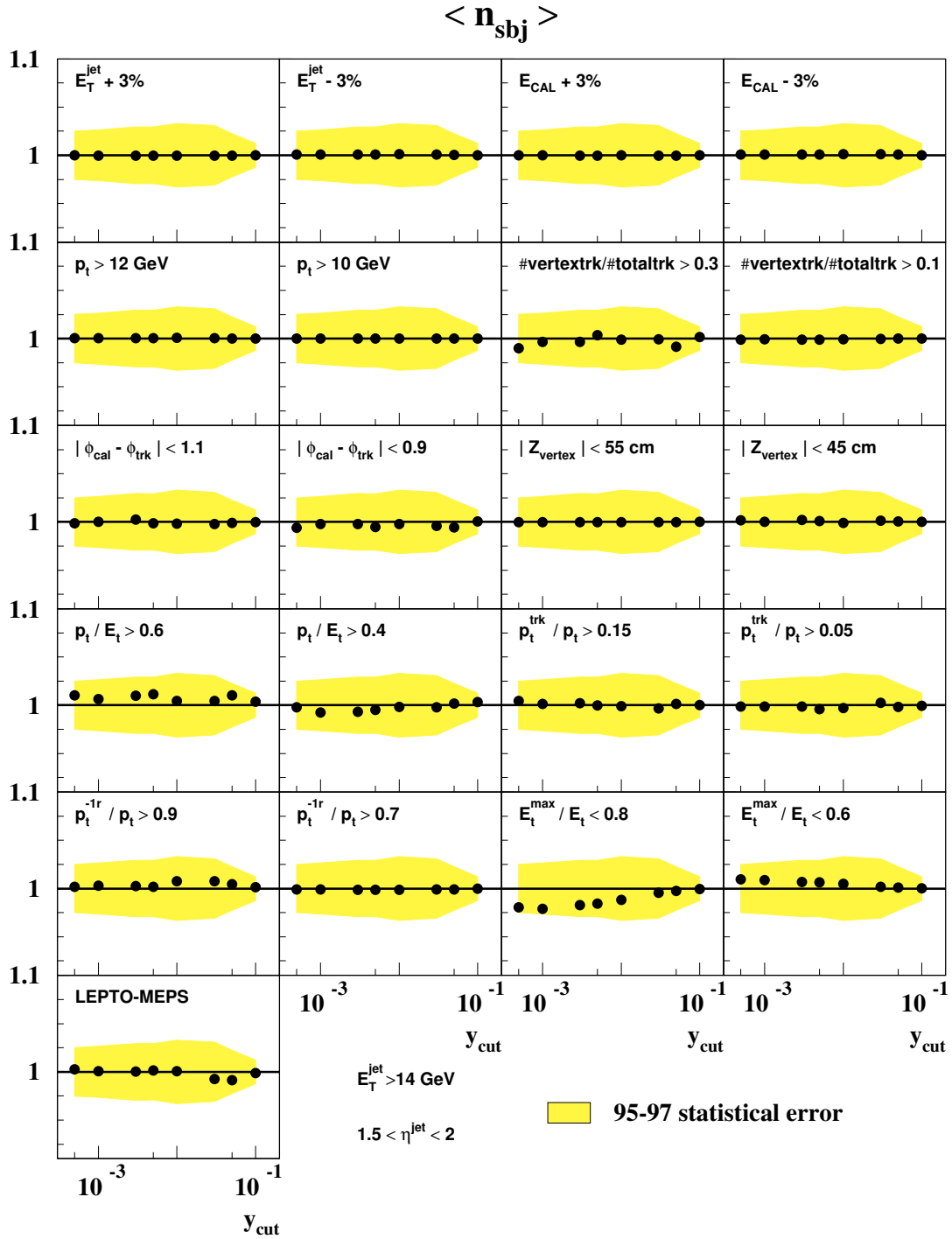
$$< n_{sbj} >$$

Figure 6.31 - Ratio $\mathcal{O}^*/\mathcal{O}$ for the systematic variations of the measured $\langle n_{sbj} \rangle$ as a function of y_{cut} and $14 < E_T^{jet} < 17$ for the data taken in the years 1995-1997. The shaded band shows the statistical uncertainty of the data.

Figure 6.32 - Ratio $\mathcal{O}^*/\mathcal{O}$ for the systematic variations of the measured $\langle n_{sbj} \rangle$ as a function of y_{cut} and $14 < E_T^{jet} < 17$ for the data taken in the years 1999-2000. The shaded band shows the statistical uncertainty of the data.

Figure 6.33 - Ratio $\mathcal{O}^*/\mathcal{O}$ for the systematic variations of the measured $\langle n_{sbj} \rangle$ as a function of y_{cut} and $17 < E_T^{jet} < 21$ for the data taken in the years 1995-1997. The shaded band shows the statistical uncertainty of the data.
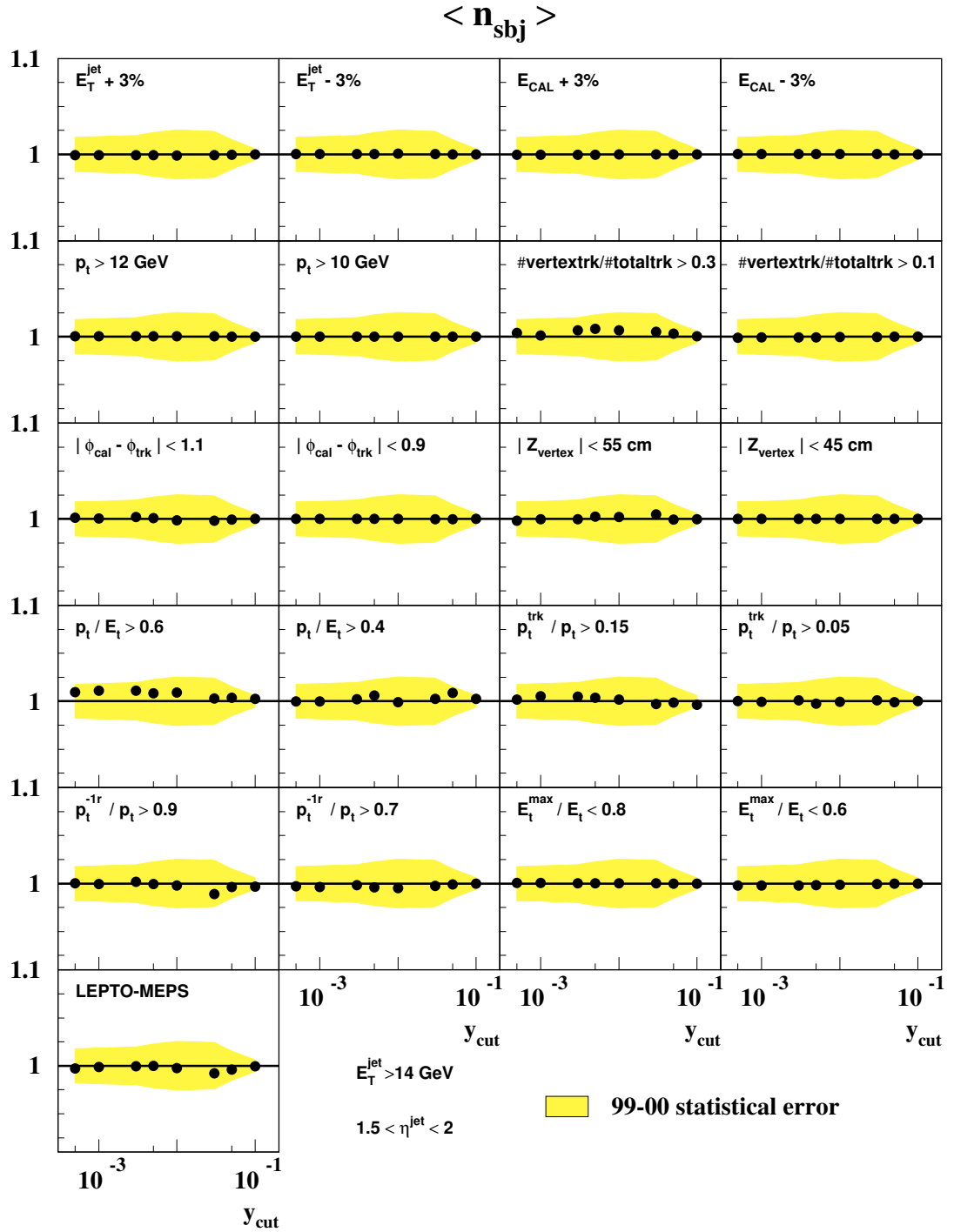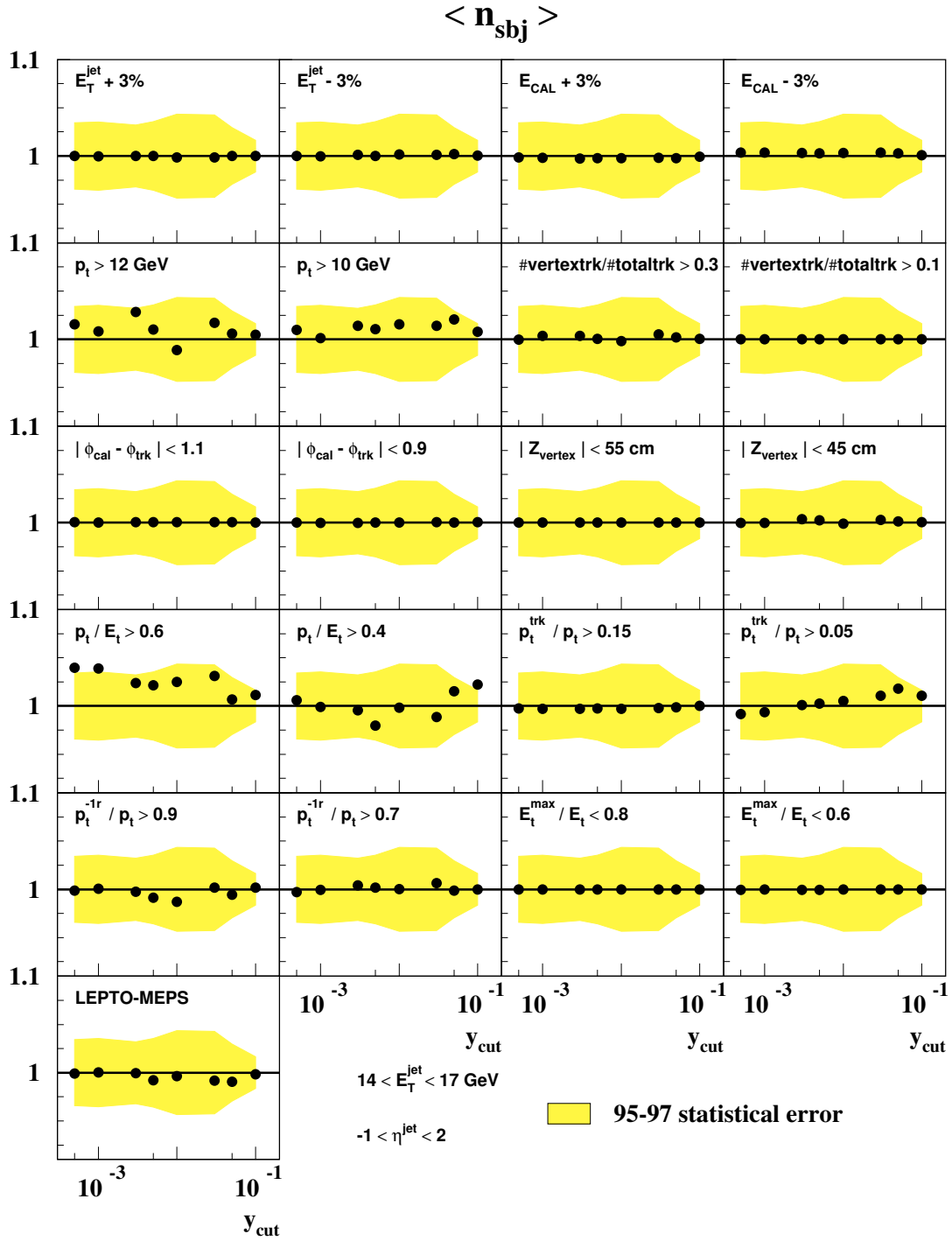
Figure 6.34 - Ratio $\mathcal{O}^*/\mathcal{O}$ for the systematic variations of the measured $\langle n_{sbj} \rangle$ as a function of y_{cut} and $17 < E_T^{jet} < 21$ for the data taken in the years 1999-2000. The shaded band shows the statistical uncertainty of the data.

$$< n_{sbj} >$$

Figure 6.35 - Ratio $\mathcal{O}^*/\mathcal{O}$ for the systematic variations of the measured $\langle n_{sbj} \rangle$ as a function of y_{cut} and $21 < E_T^{jet} < 25$ for the data taken in the years 1995-1997. The shaded band shows the statistical uncertainty of the data.
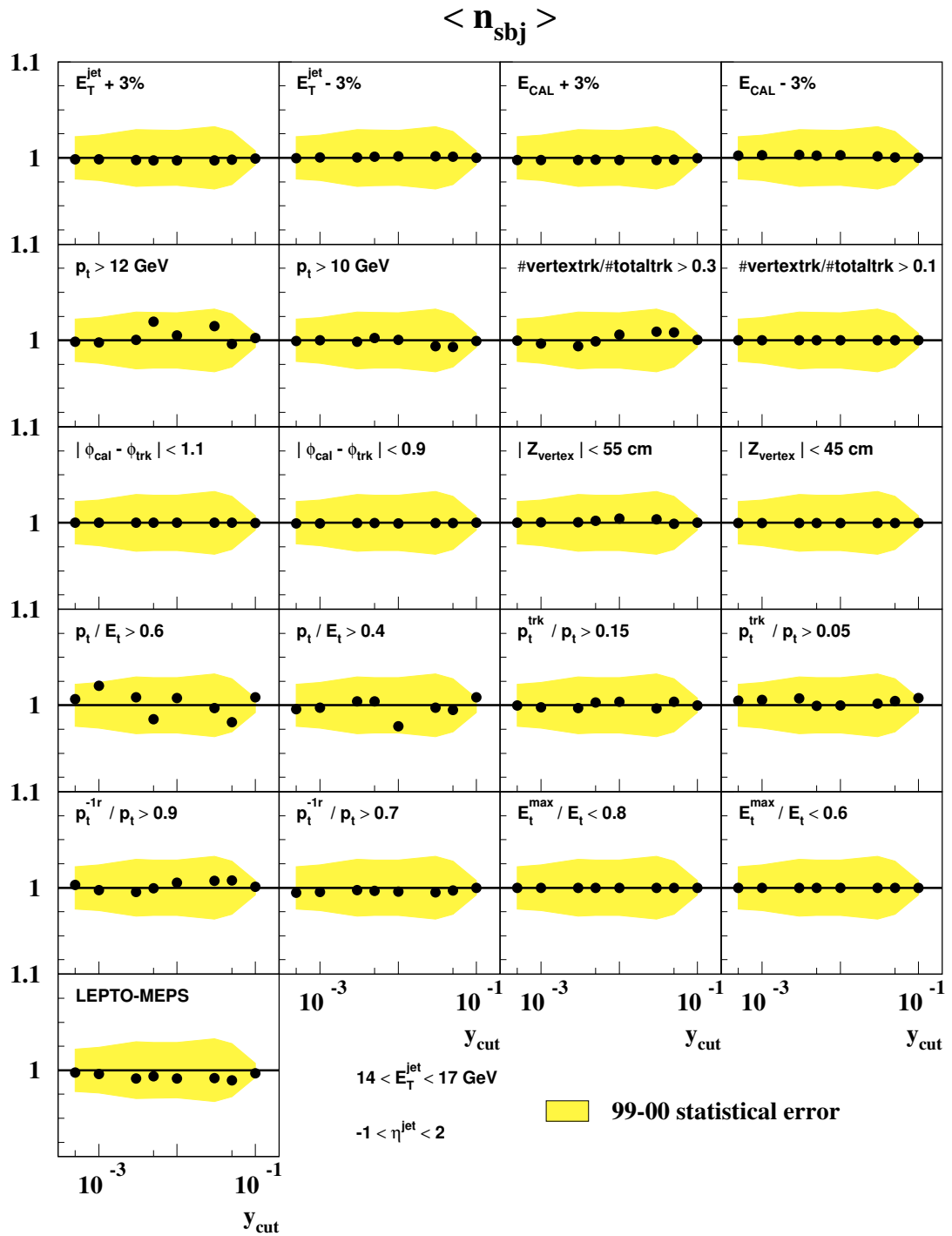
$$< n_{sbj} >$$

Figure 6.36 - Ratio $\mathcal{O}^*/\mathcal{O}$ for the systematic variations of the measured $\langle n_{sbj} \rangle$ as a function of y_{cut} and $21 < E_T^{jet} < 25$ for the data taken in the years 1999-2000. The shaded band shows the statistical uncertainty of the data.
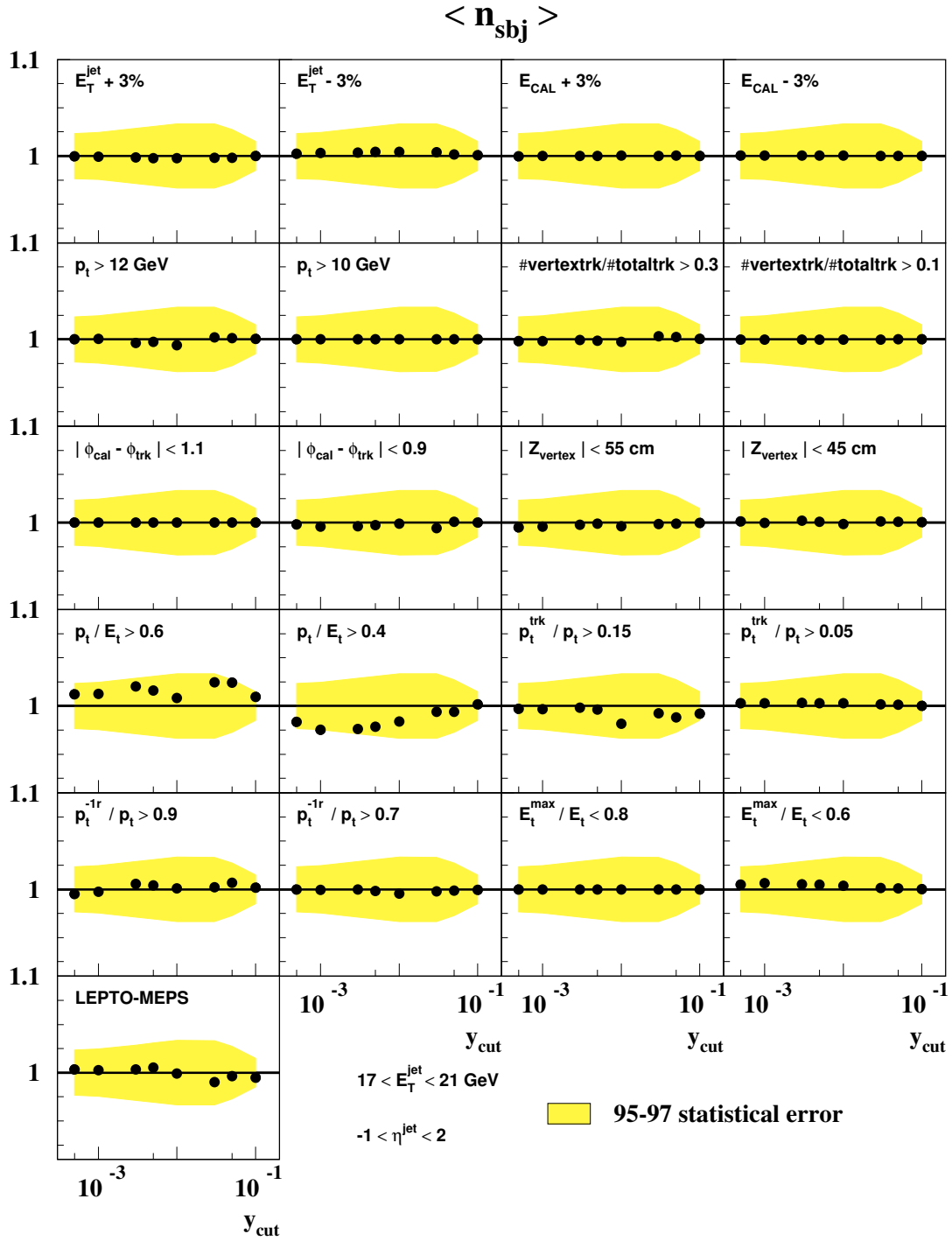
Figure 6.37 - Ratio $\mathcal{O}^*/\mathcal{O}$ for the systematic variations of the measured $\langle n_{sbj} \rangle$ as a function of y_{cut} and $25 < E_T^{jet} < 35$ for the data taken in the years 1995-1997. The shaded band shows the statistical uncertainty of the data.
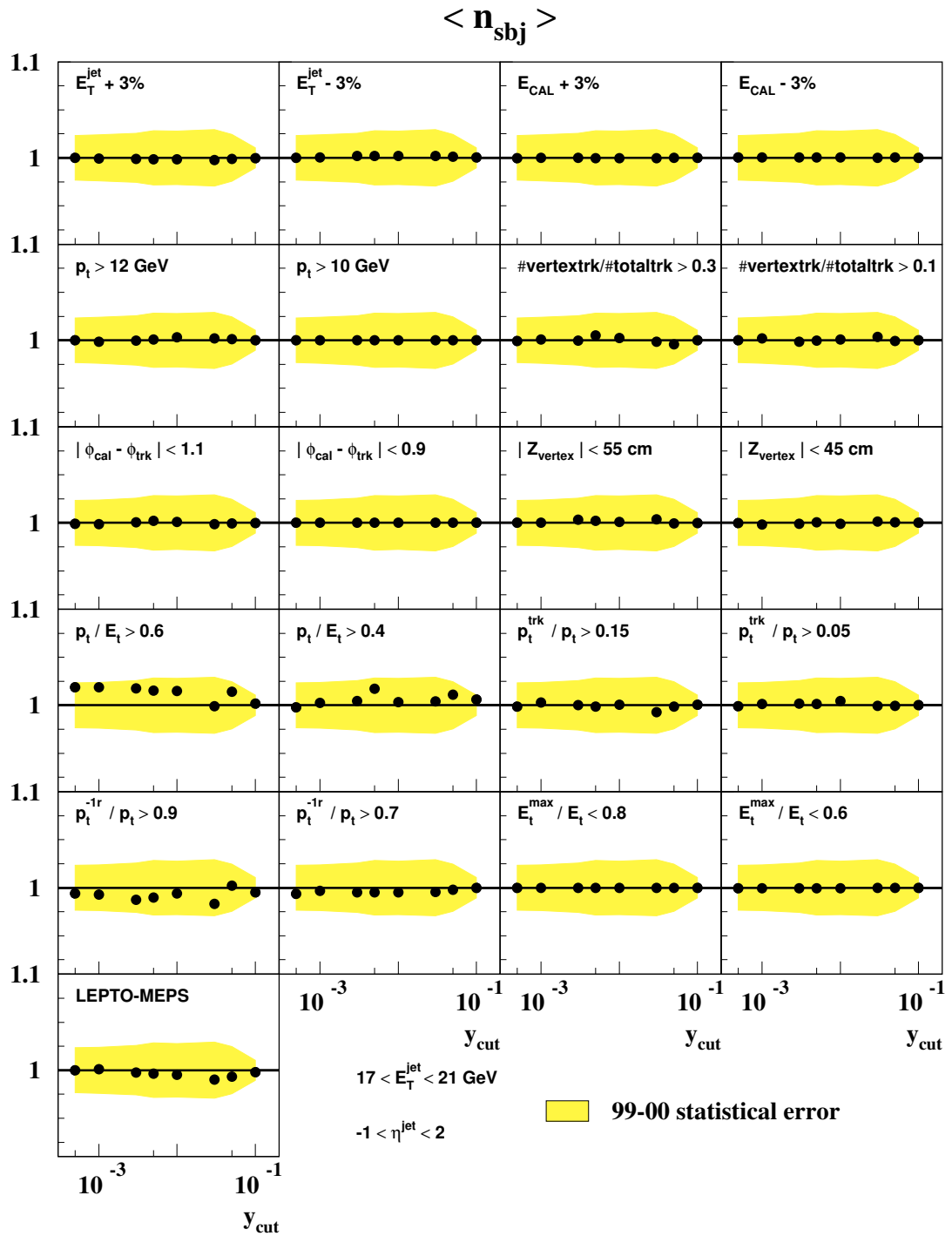
Figure 6.38 - Ratio $\mathcal{O}^*/\mathcal{O}$ for the systematic variations of the measured $\langle n_{sbj} \rangle$ as a function of y_{cut} and $25 < E_T^{jet} < 35$ for the data taken in the years 1999-2000. The shaded band shows the statistical uncertainty of the data.

$$< n_{sbj} >$$

Figure 6.39 - Ratio $\mathcal{O}^*/\mathcal{O}$ for the systematic variations of the measured $\langle n_{sbj} \rangle$ as a function of y_{cut} and $35 < E_T^{jet} < 55$ for the data taken in the years 1995-1997. The shaded band shows the statistical uncertainty of the data.
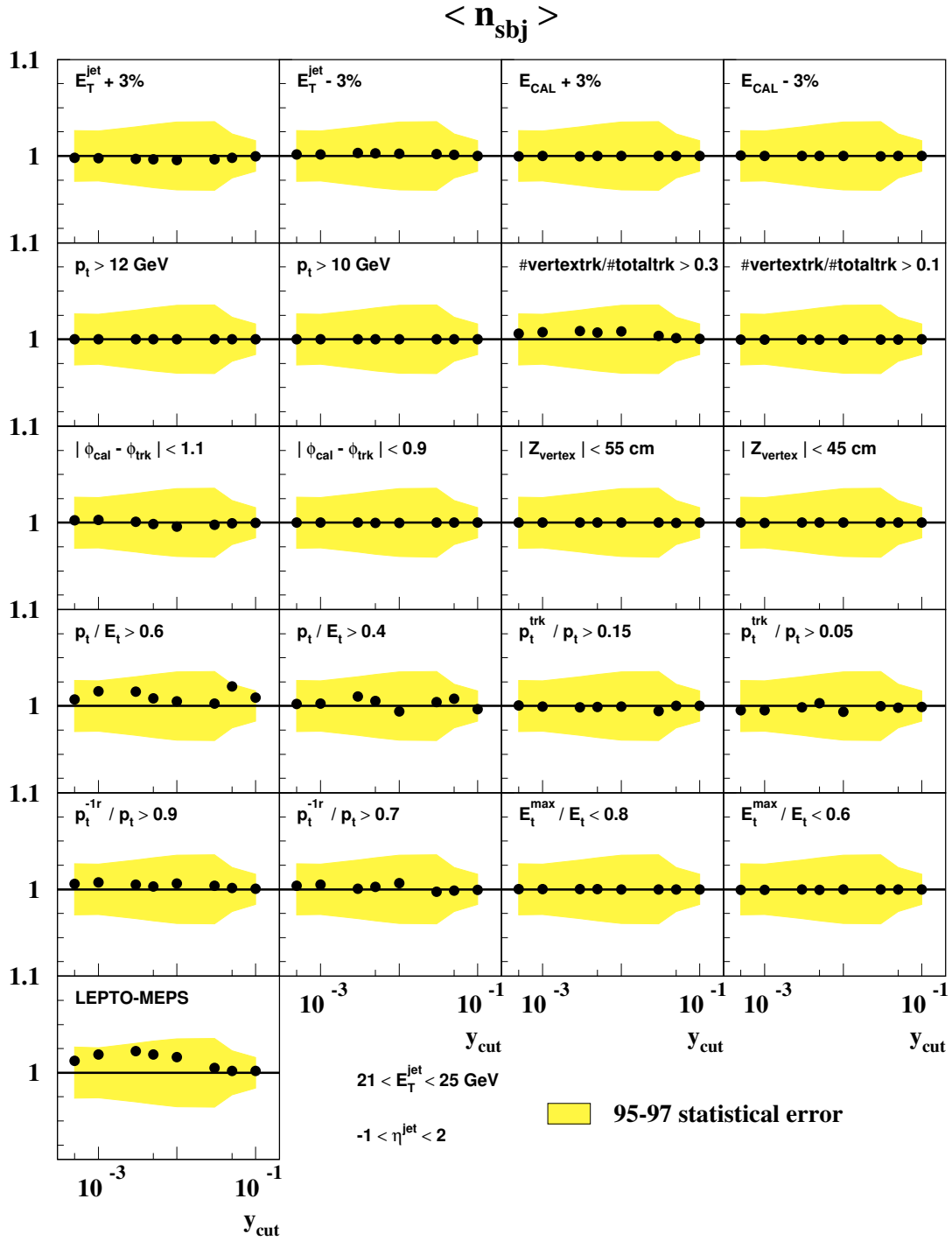
Figure 6.40 - Ratio $\mathcal{O}^*/\mathcal{O}$ for the systematic variations of the measured $\langle n_{sbj} \rangle$ as a function of y_{cut} and $35 < E_T^{jet} < 55$ for the data taken in the years 1999-2000. The shaded band shows the statistical uncertainty of the data.

Figure 6.41 - Ratio $\mathcal{O}^*/\mathcal{O}$ for the systematic variations of the measured $\langle n_{sbj} \rangle$ as a function of y_{cut} and $55 < E_T^{jet} < 119$ for the data taken in the years 1995-1997. The shaded band shows the statistical uncertainty of the data.
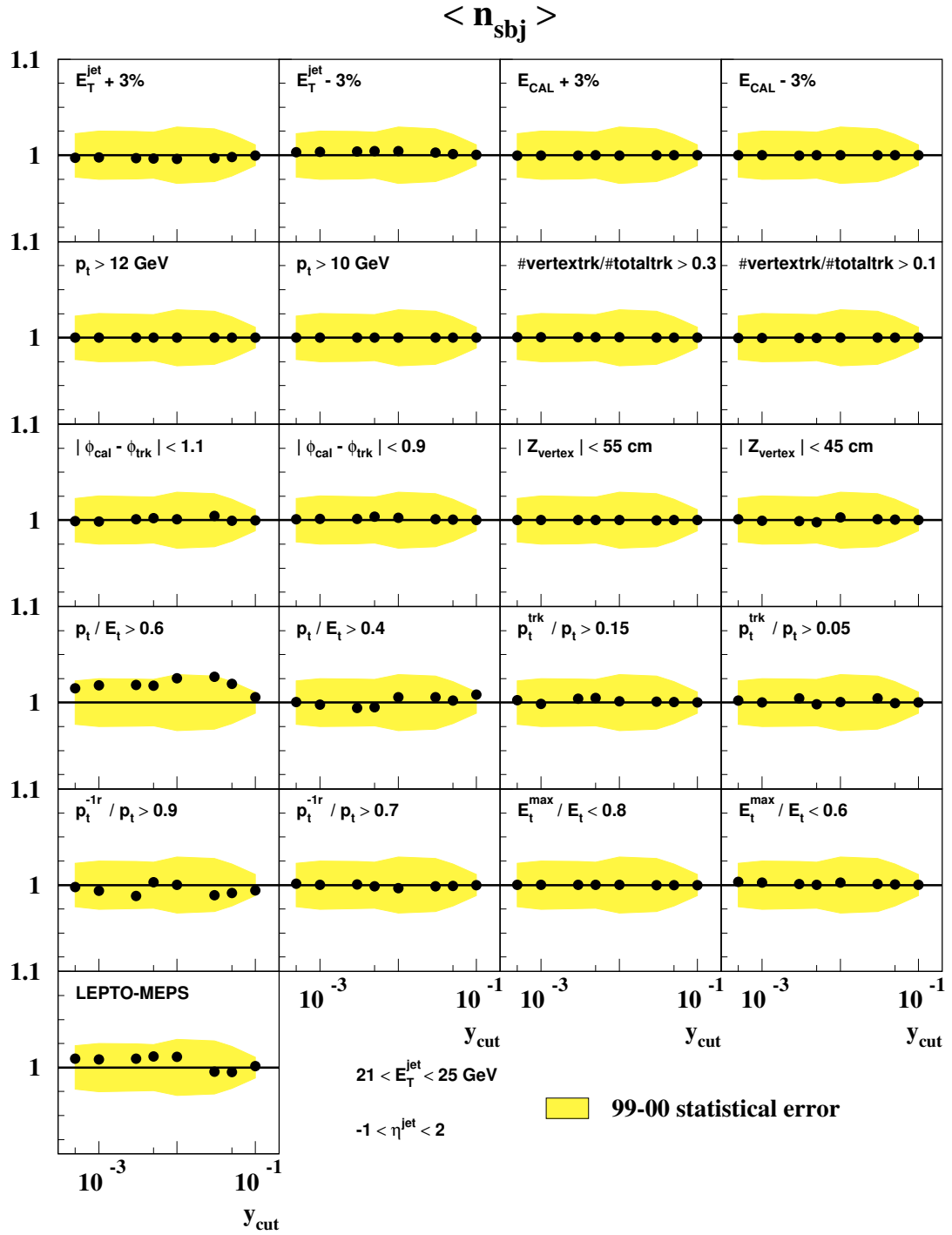
Figure 6.42 - Ratio $\mathcal{O}^*/\mathcal{O}$ for the systematic variations of the measured $\langle n_{sbj} \rangle$ as a function of y_{cut} and $55 < E_T^{jet} < 119$ for the data taken in the years 1999-2000. The shaded band shows the statistical uncertainty of the data.
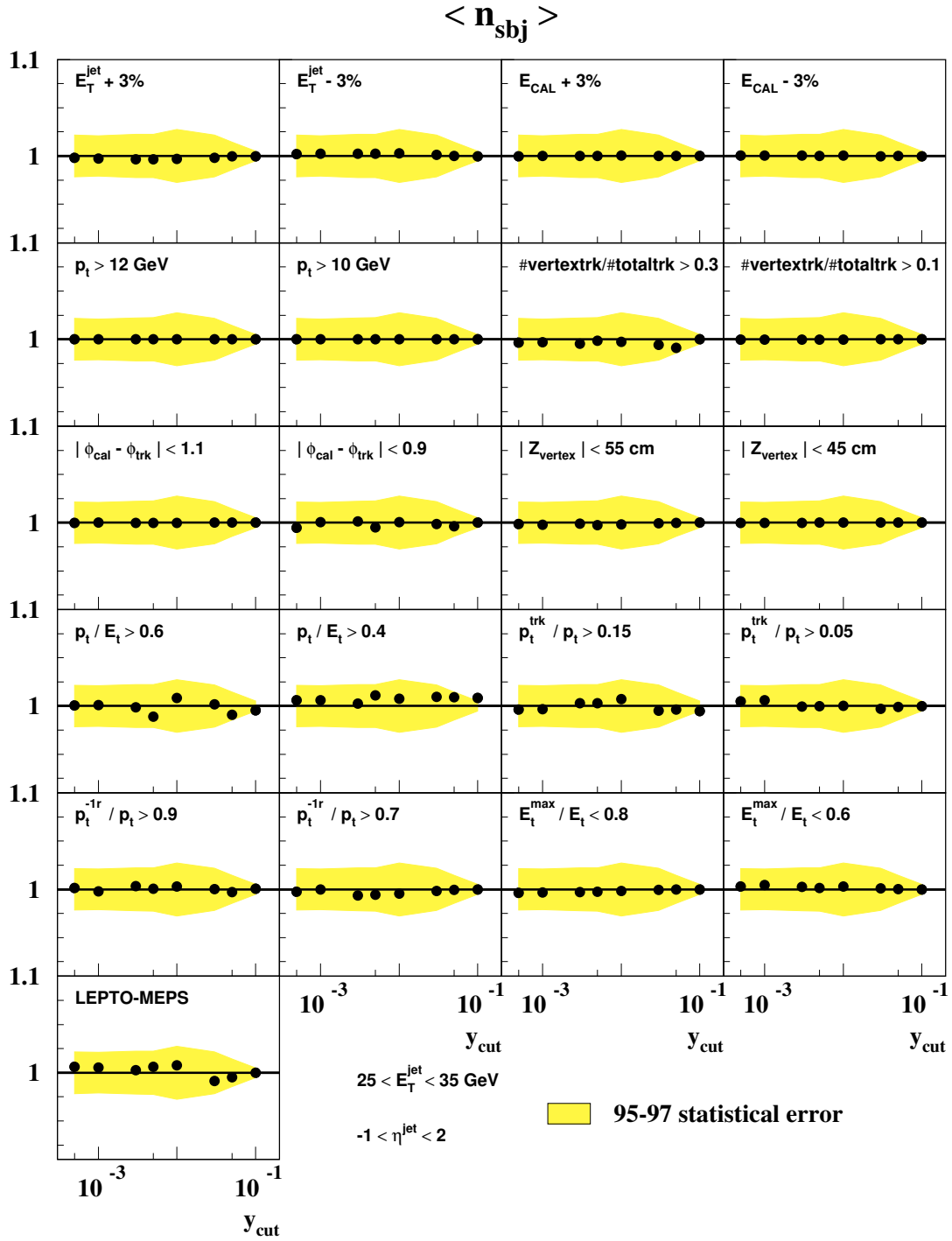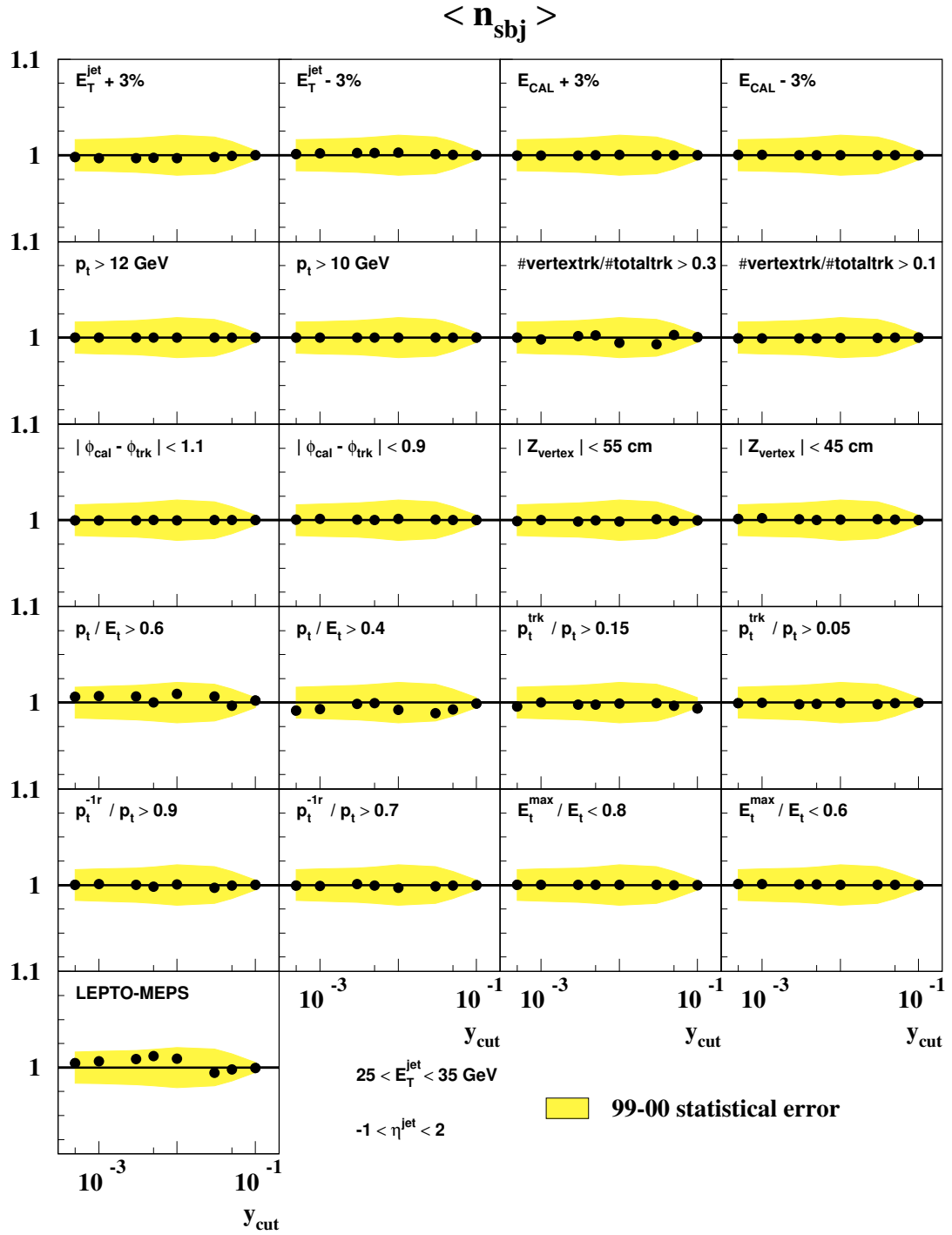
Figure 6.43 - Ratio $\mathcal{O}^*/\mathcal{O}$ for the systematic variations of the measured $\langle n_{sbj} \rangle$ as a function of E_T^{jet} for a fixed $y_{cut} = 10^{-2}$ for the data taken in the years 1995-1997. The shaded band shows the statistical uncertainty of the data.

Figure 6.44 - Ratio $\mathcal{O}^*/\mathcal{O}$ for the systematic variations of the measured $\langle n_{sbj} \rangle$ as a function of E_T^{jet} for a fixed $y_{cut} = 10^{-2}$ for the data taken in the years 1999-2000. The shaded band shows the statistical uncertainty of the data.
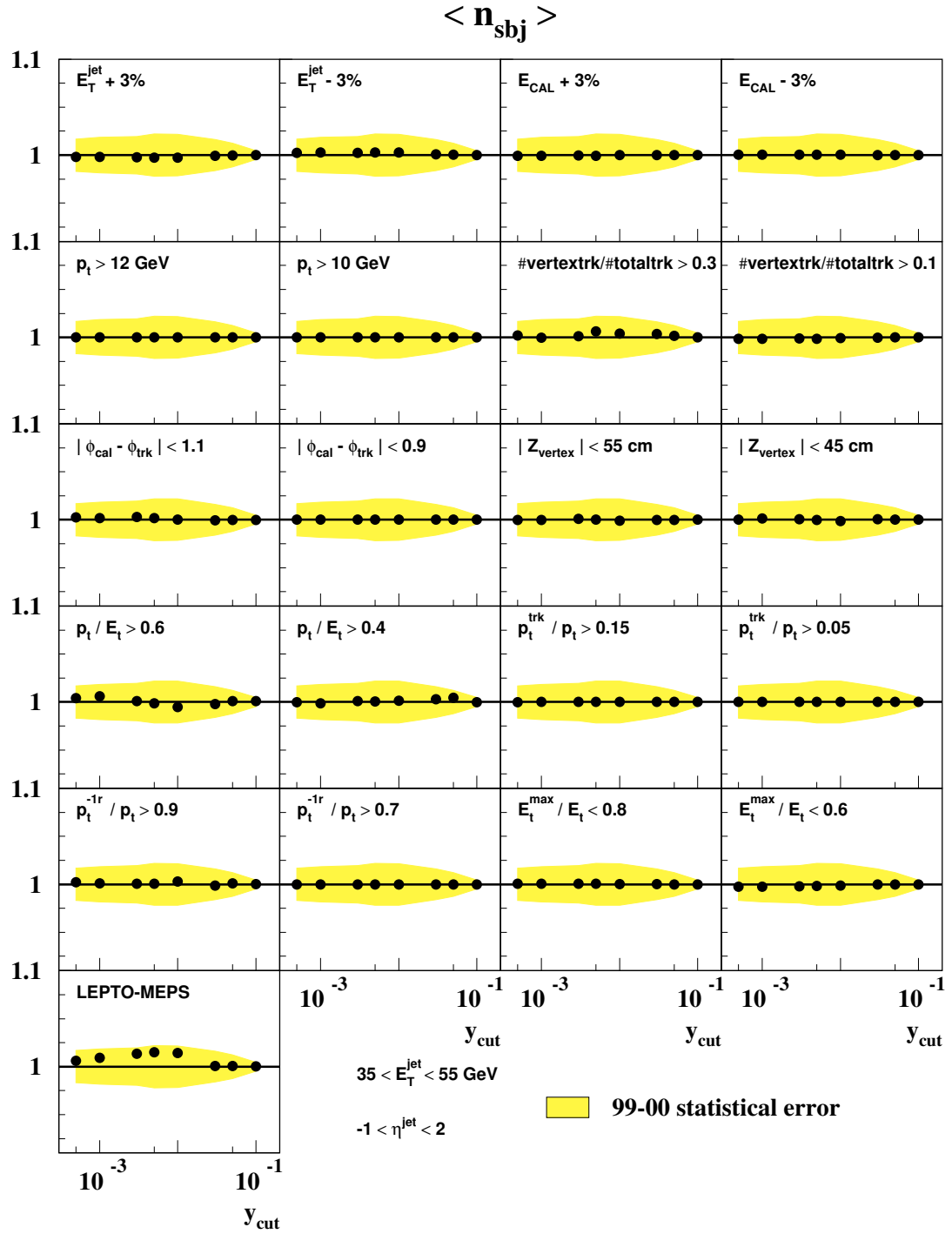
Figure 6.45 - Ratio $\mathcal{O}^*/\mathcal{O}$ for the systematic variations of the measured $\langle n_{sbj} \rangle$ as a function of η^{jet} for a fixed $y_{cut} = 10^{-2}$ for the data taken in the years 1995-1997. The shaded band shows the statistical uncertainty of the data.

Figure 6.46 - Ratio $\mathcal{O}^*/\mathcal{O}$ for the systematic variations of the measured $\langle n_{sbj} \rangle$ as a function of η^{jet} for a fixed $y_{cut} = 10^{-2}$ for the data taken in the years 1999-2000. The shaded band shows the statistical uncertainty of the data.

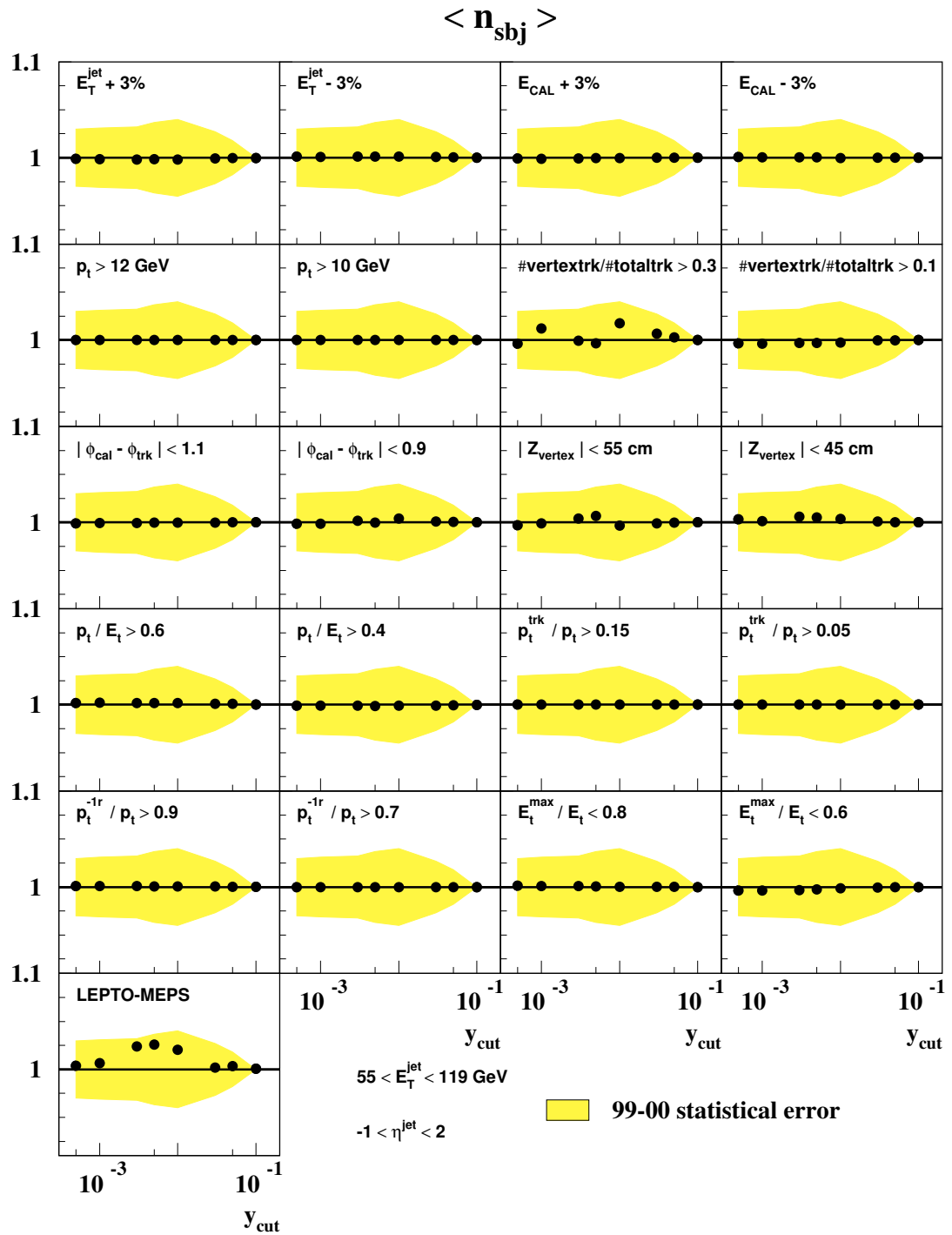**Figure 6.47** - Ratio $\mathcal{O}^*/\mathcal{O}$ for the systematic variations of the measured $\langle n_{sbj} \rangle$ as a function of Q^2 for a fixed $y_{cut} = 10^{-2}$ for the data taken in the years 1995-1997. The shaded band shows the statistical uncertainty of the data.
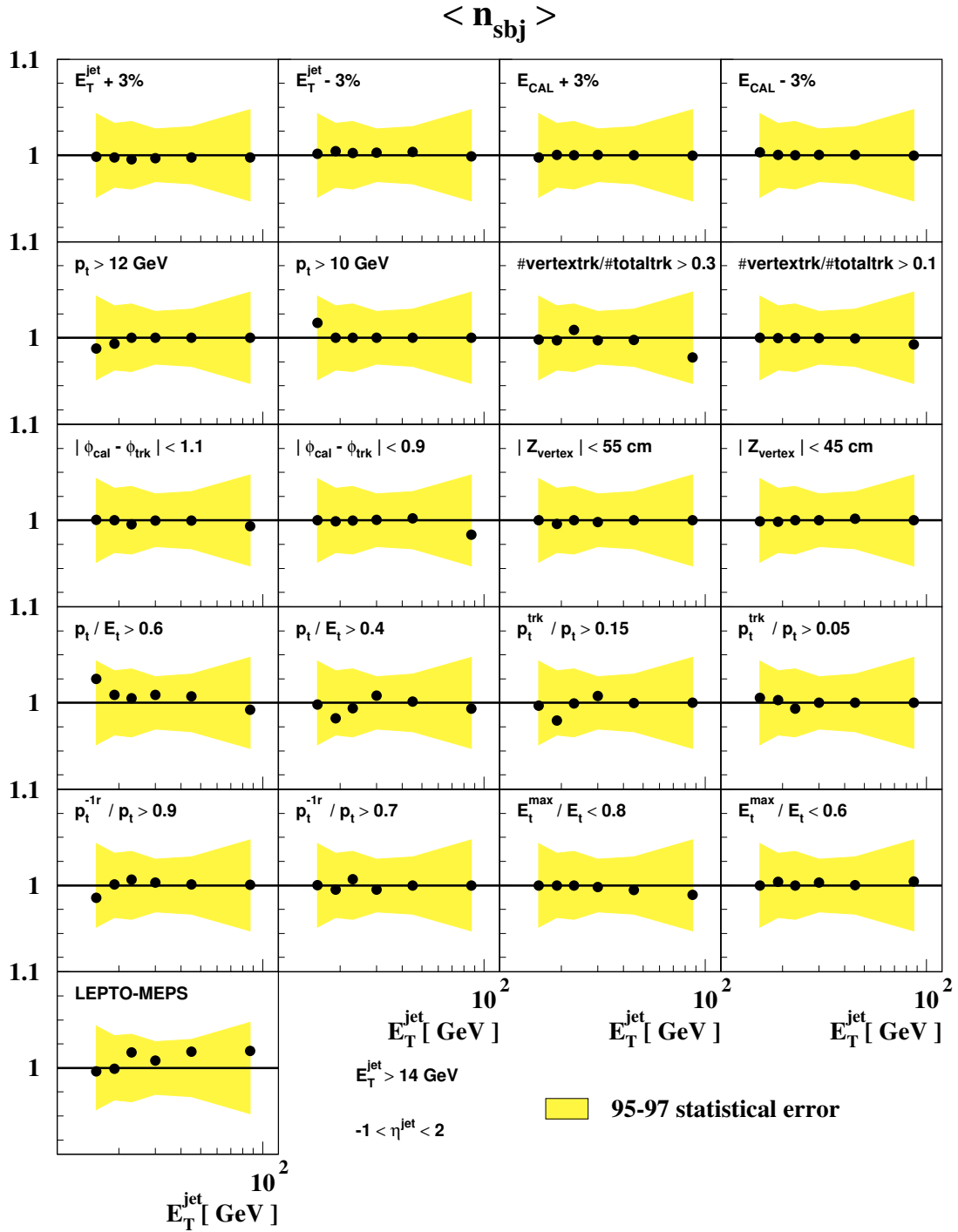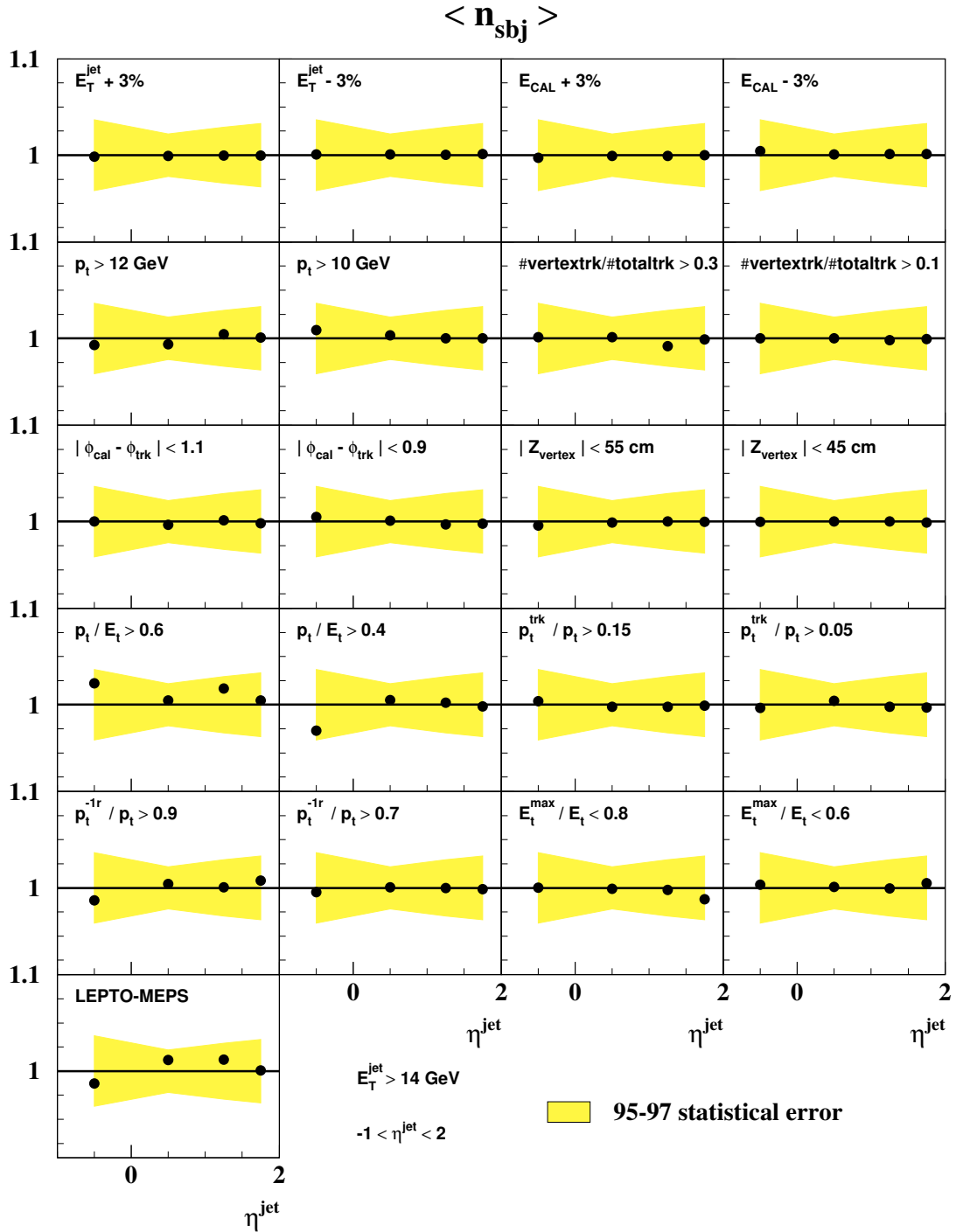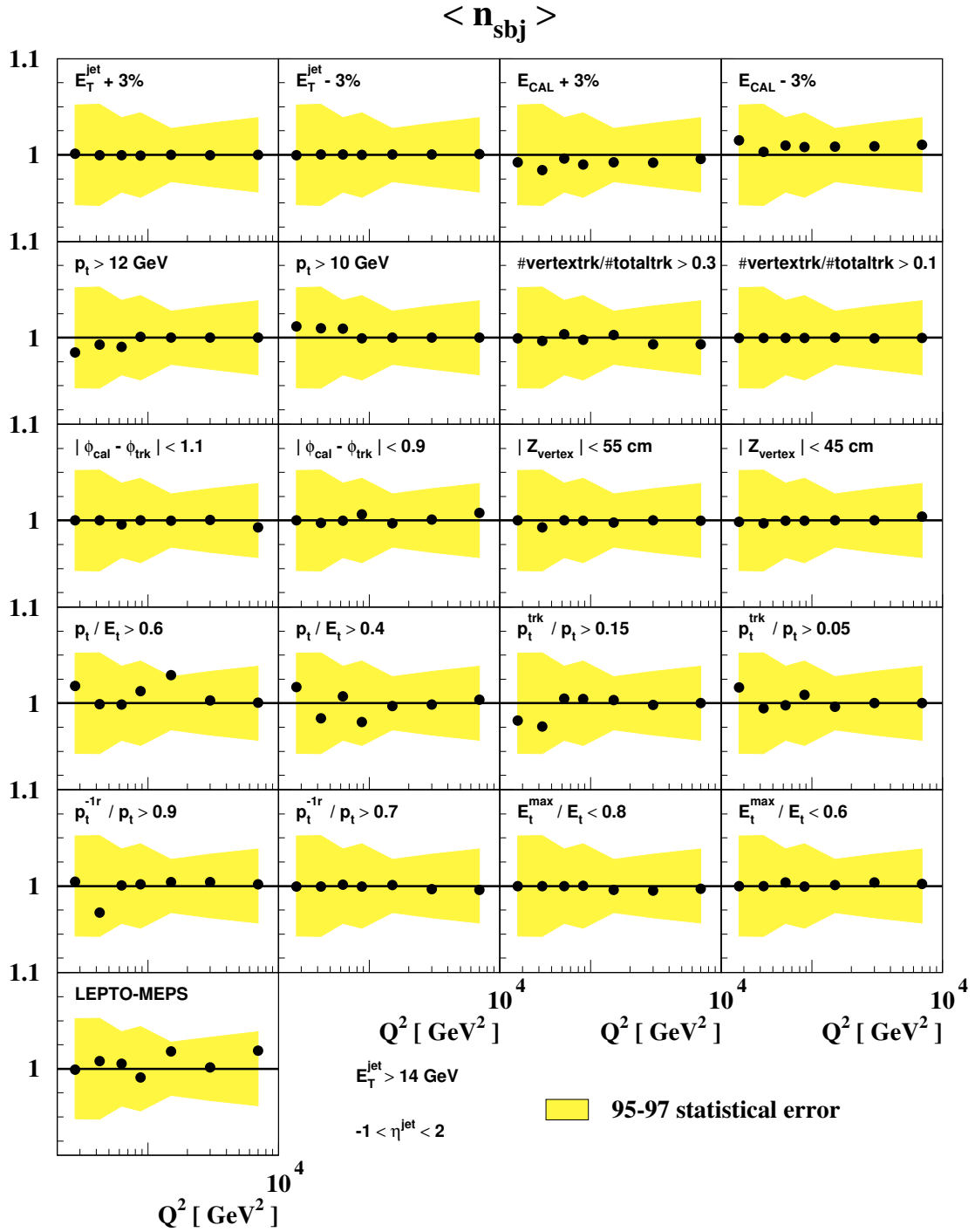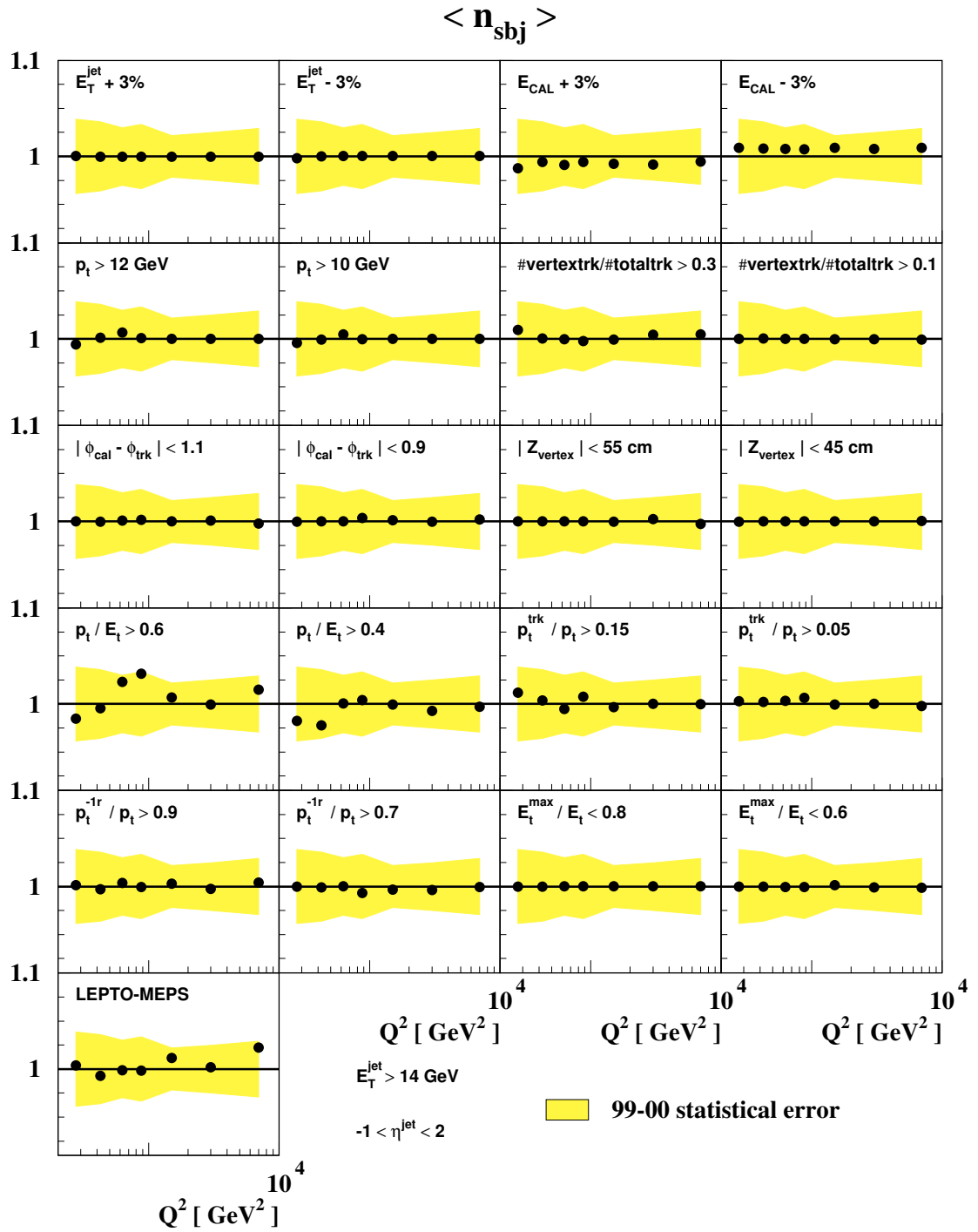
$$< n_{sbj} >$$

Figure 6.48 - Ratio $\mathcal{O}^*/\mathcal{O}$ for the systematic variations of the measured $\langle n_{sbj} \rangle$ as a function of Q^2 for a fixed $y_{cut} = 10^{-2}$ for the data taken in the years 1999-2000. The shaded band shows the statistical uncertainty of the data.

Chapter 7

Discussion of the results

7.1   NLO QCD predictions for jet production

One of the features of the hadronic final states is the appearance of jets of hadrons. By use of a suitable experimental jet algorithm (see Sect. 3), the hadronic data may be organized into final states containing a definite number of jets. This defines the topological structure of the event for a given jet algorithm. Different jet algorithms or jet defining cuts can lead to different number of jets being reconstructed in a given event. Thus jet cross sections depend on the procedure used to define an experimental jet.

From the theoretical point of view, the jet algorithm plays an important role in the selection of high momentum transfer events in which the soft radiation is removed by a cut on the minimal transverse energy of a jet. At the same time, the behavior of individual hadrons is averaged out by replacing all hadrons belonging to a jet by a single jet axis and jet (transverse) energy. As the hadronic information is averaged out, the hadronic jet axis and energy experimentally observed can be related to the jet axis and energy constructed from a parton shower calculated within perturbative QCD. As hadronisation effects cannot be predicted by perturbative QCD, suitable jet algorithms must be chosen to minimize these effects so as to allow a more direct comparison between theory and experiment.

Precise theoretical determinations of jet cross sections are important since physics beyond the Standard Model is often evident in events containing a specific number of jets. The corresponding QCD background is then the exclusive jet cross section containing the same number of jets. At present, perturbative QCD predictions for jet production in CC DIS are available to second order in α_s, referred to as next-to-leading order (NLO) predictions. These calculations are only available for a jet of partons. Parton-to-hadron correction factors have been obtained (see section 7.1.4) from the Monte-Carlo models to compare the calculations with the data at the hadron level.

The jet cross sections are obtained by a Monte Carlo integration over the phase space of the final state partons. This approach allows any experimental jet algorithm and acceptance corrections to be applied, and any distribution depending on the jet observables to be studied. At leading order in the perturbative QCD calculation, the

113

jet is modelled by a single parton, the jet defining cuts are applied to this lone parton and the parton's direction and energy describe the jet's axis and energy.

Comparisons of lowest order QCD predictions of jet distributions with experimental data have been seen to be reasonable. Generally, the shapes of infrared-safe observables are well determined while the overall normalisation is uncertain, due to the dependence on the renormalisation and factorisation scales μ_R and μ_F, respectively.

The addition of NLO effects produces important improvements over a leading order calculation:

- the dependence on the scales μ_R and μ_F are reduced, so that the normalisation is more precise;

- the parton shower is better reconstructed as two partons may be combined to form a single jet. In this way, the jet cross sections are able to reproduce the details of the jet finding algorithm like the method used to combine the hadrons;

- the calculation is able to reproduce to detector limitations such as the radiation outside the detector.

The general structure of the n-jet cross section in DIS is given by [Mi96]

$$d\sigma^{had}[n-\text{jet}] = \sum_a \int dx f_a(x, \mu_F^2) \, d\widehat{\sigma}^a(p = xP, \alpha_s(\mu_R^2), \mu_R^2, \mu_F^2) \qquad (7.1)$$

where the sum runs over the incident partons $a = q, \overline{q}, g$ which carry a fraction x of the proton momentum. $\widehat{\sigma}^a$ denotes the partonic cross section from which the collinear initial-state singularities have been factorised out at a scale μ_F and have been implicitly included in the scale dependent parton densities $f_a(x, \mu_F^2)$.

At NLO $\widehat{\sigma}^a$ receives contributions from the *virtual corrections* to n-parton production, and from *real corrections* in the form of $(n+1)$-parton final states. Both contributions are divergent. The matrix elements of the virtual diagrams are infrared-divergent while the matrix elements for real corrections are well defined. However when the $(n+1)$-parton matrix elements are integrated over the allowed regions of phase-space an infrared-divergent cross section is obtained. This comes from the fact that the jet algorithm allows one of the partons to be soft or for two partons within a jet to be collinear. Infrared as well as collinear divergencies associated with the final state partons are cancelled against the corresponding divergencies of the virtual contributions. The ultraviolet divergencies of the virtual corrections are removed by the renormalisation procedure which introduces a dependence on μ_R and depends on the renormalisation scheme adopted. The remaining initial-state divergencies are factorized into the bare parton densities introducing the dependence on μ_F. There are two different ways to achieve the separation of the divergent and finite contributions: the subtraction method and the phase-space-slicing method.

The *subtraction method* cancels the infrared singularities point-by-point in phase space. The subtraction terms have a simple form after applying the factorisation theorems of perturbative QCD. The difficulty of the method is to arrange the subtractions in such a way that in a numerical evaluation no spurious singularity appears.

The *phase-space-slicing method* relies on the separation of singular phase-space regions from non-singular ones by means of a small slicing parameter $s_{min} \to 0$. Soft and collinear approximations are used in the regions where at least one pair of partons, including the initial ones, has $s_{ij} = 2p_i \cdot p_j < s_{min}$ and the soft and/or collinear final state parton is integrated over analytically. Adding this soft and collinear part to the virtual contribtions give a finite result for n-parton final states. This n-parton contribution is negative and grows logarithmically in magnitude as s_{min} is decreased. This logarithm growth is exactly cancelled by the increase in the $(n+1)$-parton cross section, once s_{min} is small enough for the approximations to be valid. The integration over the $(n + 1)$-parton phase space with $s_{ij} > s_{min}$ is done by Monte Carlo techniques.

To make use of the crossing properties of the matrix elements the next-to-leading hadronic cross section is defined as [Gi61]

$$d\sigma^{had}[n - jet] = \sum_a \int dx \mathcal{F}_a(x)\ d\sigma_a^{NLO}(x), \tag{7.2}$$

where $\mathcal{F}_a$ is an "effective" NLO structure function and $d\sigma_a^{NLO}$ is the "crossed" partonic cross section. $d\sigma_a^{NLO}$ can be expanded as a series in the coupling constant α_s

$$d\sigma_a^{NLO} = d\sigma_a^{LO} + \alpha_s d\delta\sigma_a^{NLO} + \mathcal{O}(\alpha_s^2), \tag{7.3}$$

where α_s is evaluated at μ_R. After mass factorisation, the effective structure function $\mathcal{F}_a$ may be written as [Gi61]

$$\mathcal{F}_a(x) = f_a(x, \mu_F) + \alpha_s C_a(x, \mu_f) + \mathcal{O}(\alpha_s^2), \tag{7.4}$$

where $C_a(x, \mu_f)$ are the crossing functions. These functions contain the convolution of the parton distribution functions with Altarelli-Parisi splitting functions [Al77] and in addition take into account the crossing of a final state cluster to the initial state, within the s_{min} cone.

7.1.1   The program MEPJET

The measurements have been compared with NLO QCD calculations using the program MEPJET [Mi96]. At present MEPJET is the only NLO program for deep inelastic scattering which includes W exchange.

MEPJET employs the *phase-space slicing method* with an invariant cut-off parameter s_{min}. The program uses the minimal subtraction method, $\overline{MS}$, as renormalisation and factorisation schemes. The number of flavours is fixed to $n_f = 5$, that is gluons are allowed to split into five flavours of quarks. To make use of the crossing properties of the matrix elements, the program uses crossing functions to obtain the NLO QCD predictions.

MEPJET provides the kinematical information (momenta) of the final state partons. The same jet algorithm used for the experimental data was applied to these partons to obtain predictions of the measured distributions at the parton level.

7.1.2 Theoretical predictions

The NLO QCD predictions of differential jet cross sections and subjet multiplicities were obtained with the program MEPJET, using the default value of the slicing parameter $s_{min} = 0.1$ GeV^2. The CTEQ4M [La97] parametrisations of the proton PDFs were used and the appropiate crossing functions were obtained and used in the calculations. The factorisation and renormalisation scales were set to Q^2.

The differential jet cross-section predictions up to next-to-leading order can be parametrised as a perturbative series in α_s

$$\sigma_{jets} = C_0 + C_1 \alpha_s + C_2 \alpha_s^2. \tag{7.5}$$

All the diagrams needed to compute the three terms for CC interactions are at present available and included in MEPJET.

Figure 7.1 shows the LO and NLO QCD predictions for the differential jet cross section $d\sigma/dQ^2$ as a function of Q^2 for the inclusive and dijet cross sections, which are consistent with a massive propagator. The K$-$factors, defined as the ratio of the NLO over the LO cross sections, are also shown. The NLO QCD corrections are $\sim 10\%$ for inclusive jet and dijet production.

The mean subjet multiplicity at a fixed order in the perturbative QCD expansion depends on the number of partons inside a jet. At lowest order the jet is only formed by one parton and $\langle n_{sbj} \rangle$ is exactly unity, independently of the resolution scale. This order is referred to as the trivial order.

If two partons are inside a jet, it will be possible to find 1 or 2 subjets depending on the resolution scale. The contributions in which a jet contains two subjets constitutes the first non-trivial contribution to $\langle n_{sbj} \rangle$. This order is referred to as the leading order.

The LO contribution to $\langle n_{sbj} \rangle$ is obtained as the ratio of the prediction of the number of jets containing two subjets at a given resolution scale, over the prediction of the number of jets

$$\langle n_{sbj} \rangle = 1 + \frac{N_{jets}(sbj = 2)}{N_{jets}} = 1 + A_1 \alpha_s \tag{7.6}$$

where both numerator and denominator are calculated to the first non-trivial order.

The NLO contribution to $\langle n_{sbj} \rangle - 1$ is obtained as the ratio of the cross section to produce jets containing a given number of subjets greater than 1 at a given resolution scale over the prediction of the cross section to produce jets

$$\langle n_{sbj} \rangle - 1 = \frac{\sum\limits_{jets} n_{sbj}^{jet} - 1}{\sum\limits_{jets} 1} = \frac{a_1 \alpha_s + a_2 \alpha_s^2}{b_0 + b_1 \alpha_s}. \tag{7.7}$$

The final prediction of $\langle n_{sbj} \rangle$ is obtained by adding unity to the calculation in Eq. 7.7.

Figure 7.2 shows the LO and NLO QCD predictions of $\langle n_{sbj} \rangle$ as a function of E_T^{jet} for a fixed value of $y_{cut} = 10^{-2}$, which decreases as E_T^{jet} increases. The NLO QCD calculation predicts larger multiplicities than the LO QCD calculation and the K$-$factor is $\sim 10\%$.
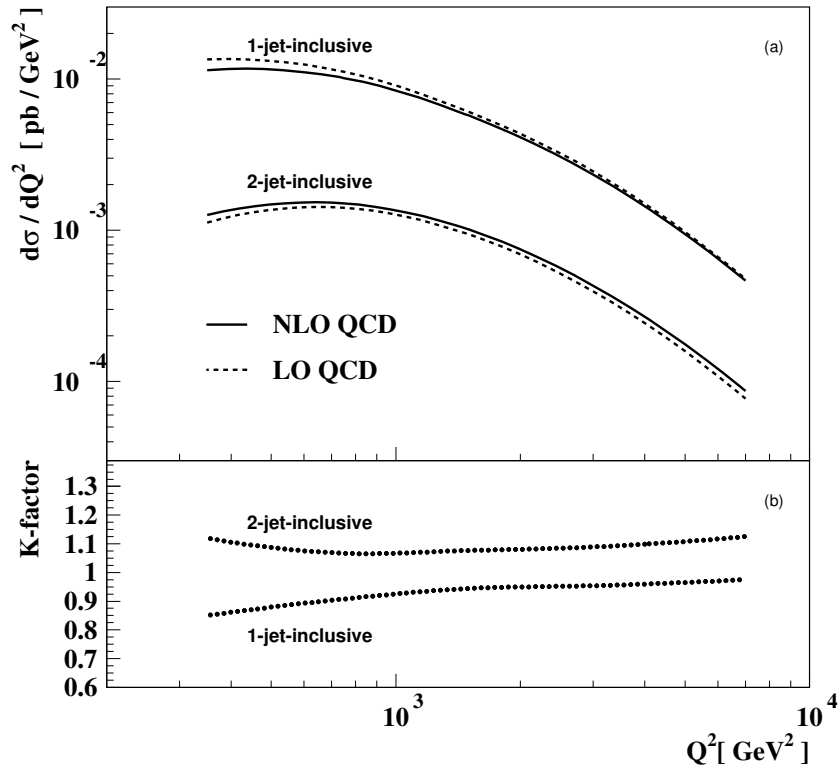
Figure 7.1 - (a) LO and NLO QCD predictions for $d\sigma/dQ^2$ for inclusive jet and dijet production. (b) K−factor for the inclusive jet and dijet cross section $d\sigma/dQ^2$.
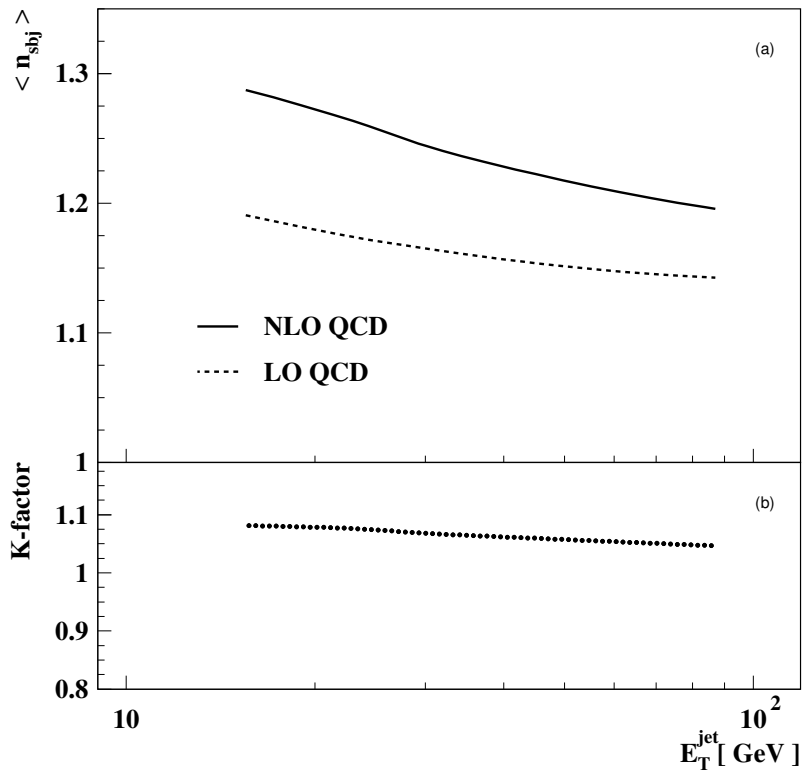

Figure 7.2 - (a) LO and NLO QCD predictions for $\langle n_{sbj} \rangle$ as a function of E_T^{jet} for a fixed value of $y_{cut} = 10^{-2}$. (b) K−factor of $\langle n_{sbj} \rangle$.

7.1.3 Estimation of the theoretical uncertainties

The theoretical calculations have uncertainties related to the

- parameter space;

- numerical integration;

- missing higher orders in the perturbative series;

- uncertainties of the proton PDFs.

To estimate the theoretical uncertainties of the calculations the following contributions have been considered:

- the uncertainty in the calculations due to the uncertainty in the proton PDFs was estimated by using the CTEQ5M [La00] and MRST [Ma98] sets instead of CTEQ4M [La97]. The uncertainty of the cross sections was typically $\sim 2\%$ (see Figs. 7.3, 7.4) and was negligible for the mean subjet multiplicity (see Fig. 7.11a and 7.11b);

- the uncertainty in the calculations due to the uncertainty in the proton PDFs was also estimated by repeating the calculations with a larger d/u quark ratio at large Bjorken x as assumed in one of the MRST PDF sets. This paramesitation has been seen describe better the inclusive charged current cross section at high x [Ya99]. The uncertainty of the cross sections was less than $\sim 4\%$ for the inclusive jet cross section except at high E_T^{jet} where it reaches $\sim 20\%$ (see Fig. 7.5) and less than $\sim 10\%$ for the dijet cross sections (see Fig. 7.6) This uncertainty was negligible for the mean subjet multiplicity;

- the uncertainty in the calculations due to that in $\alpha_s(M_Z)$ was estimated by repeating the calculations using two additional sets of proton PDFs, CTEQ4A2 and CTEQ4A4, which assume $\alpha_s(M_Z)$= 0.113 and 0.119, respectively. The uncertainty of the cross sections was typically $\sim 2\%$ (see Figs. 7.7 and 7.8) and $\sim 1\%$ for the mean subjet multiplicity (see Fig. 7.11);

- the uncertainty in the NLO QCD calculations due to terms beyond NLO was estimated by varying μ_R between Q/2 and 2Q, keeping μ_F fixed at Q. The uncertainty of the cross sections was less than 5% (see Figs. 7.9 and 7.10). The uncertainty on the mean subjet multiplicity was $\sim 3\%$ for $y_{cut} = 10^{-2}$ (see Fig. 7.11);

- The variance of the hadronisation corrections as predicted by CDM and MEPS was taken as the uncertainty in the correction; it typically amounted to less than 1% (3%) for inclusive jet (dijet) cross sections. For the subjet multiplicities the uncertainty was less than 3% for $y_{cut} = 10^{-2}$.

- the uncertainty in the NLO QCD calculations due to the cut-off parameter s_{min} was estimated by varying s_{min} from the default value of 0.1 GeV^2 to 0.05 GeV^2 and 0.01 GeV^2. This uncertainty was less than 1% in all the calculations and was neglected in the estimation of the total theoretical uncertainty.
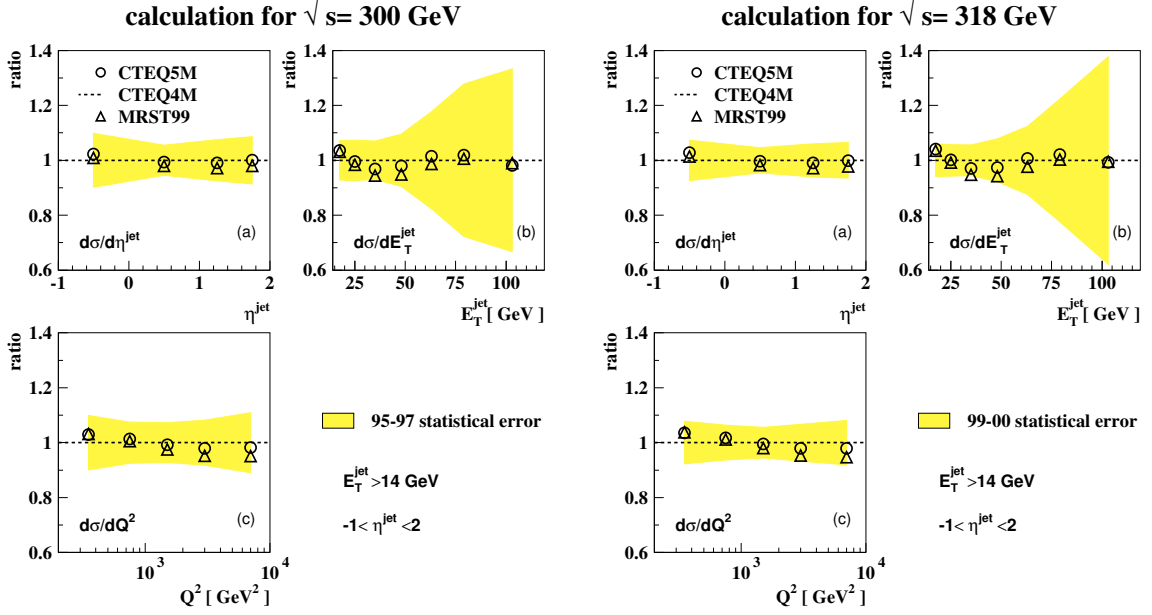
Figure 7.3 - Ratio of the predictions by MEPJET for the inclusive jet cross section obtained with CTEQ5M and MRST proton PDFs with the one obtained with CTEQ4M as a function of (a) η^{jet}, (b) E_T^{jet} and (c) Q^2, for the calculation with center-of-mass energy $\sqrt{300}$ GeV (left) and $\sqrt{318}$ GeV (right).

The total theoretical uncertainty was obtained by adding in quadrature the individual uncertainties listed above and is shown as the hatched bands in the figures presenting the results.
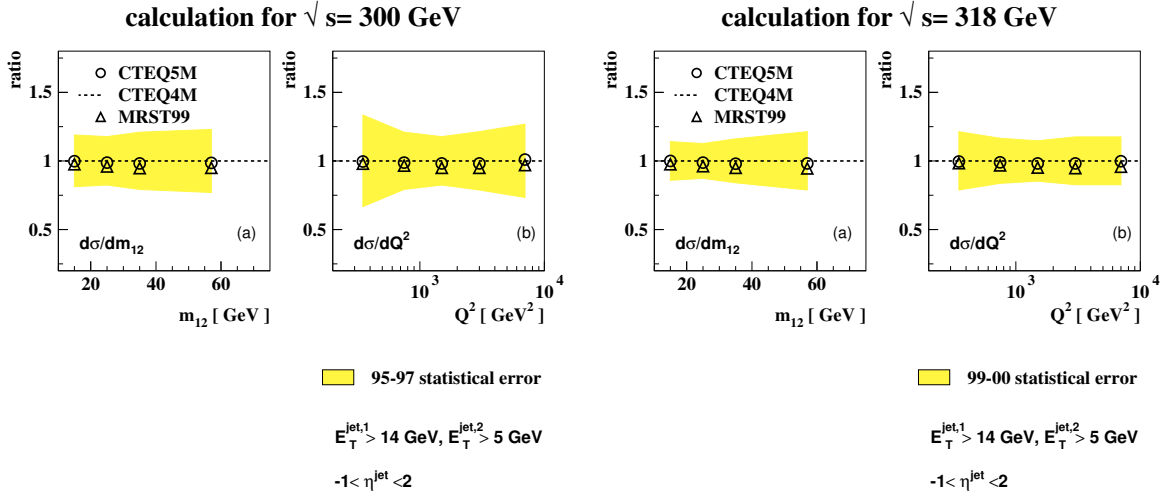

Figure 7.4 - Ratio of the predictions by MEPJET for the inclusive jet cross section obtained with CTEQ5M and MRST proton PDFs with the one obtained with CTEQ4M as a function of (a) m_{12} and (b) Q^2, for the calculation with center-of-mass energy $\sqrt{300}$ GeV (left) and $\sqrt{318}$ GeV (right).
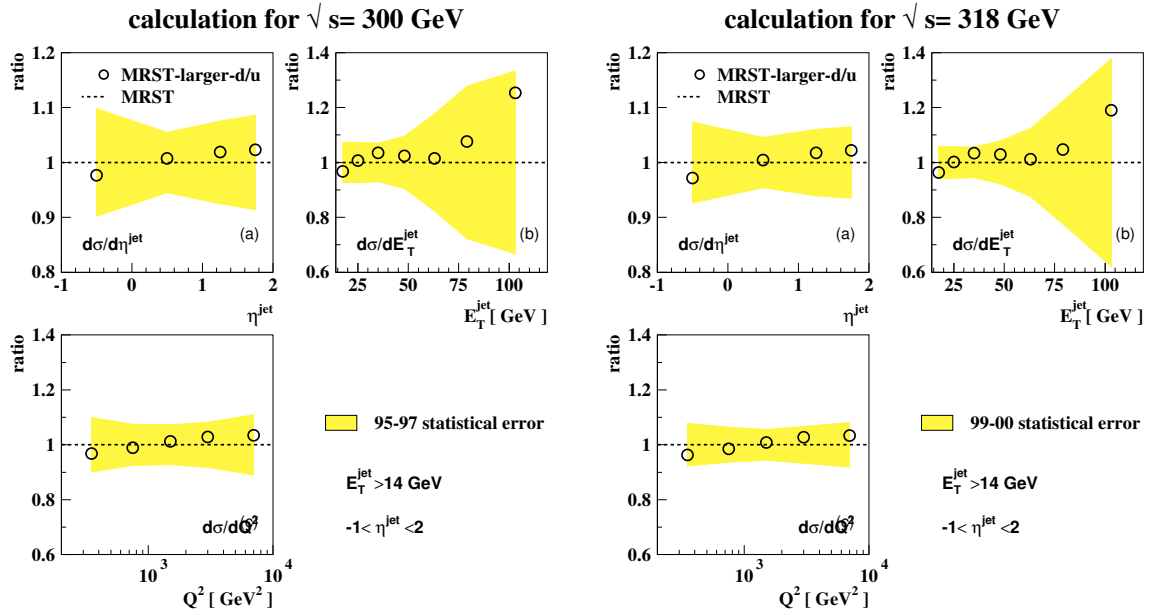
Figure 7.5 - Ratio of the prediction for the inclusive jet cross section obtained with a proton PDF with larger d/u quark ratio at large Bjorken x from the MRST set with the central MRST PDF as a function of (a) η^{jet}, (b) E_T^{jet} and (c) Q^2, for the calculation with center-of-mass energy $\sqrt{300}$ GeV (left) and $\sqrt{318}$ GeV (right).
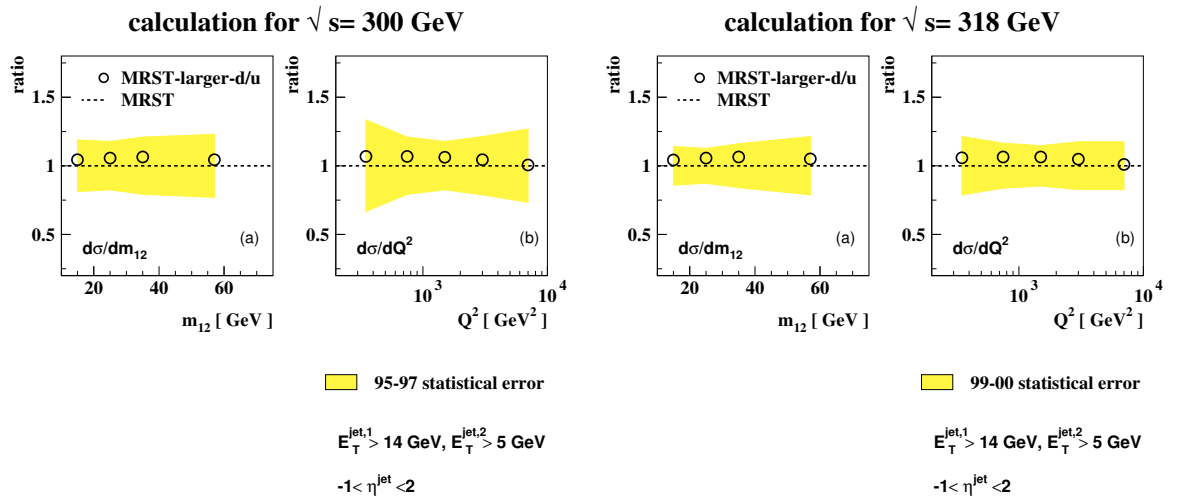

Figure 7.6 - Ratio of the prediction for the dijet cross section obtained with a proton PDF with larger d/u quark ratio at large Bjorken x from the MRST set with the central MRST PDF as a function of (a) m_{12} and (b) Q^2, for the calculation with center-of-mass energy $\sqrt{300}$ GeV (left) and $\sqrt{318}$ GeV (right).
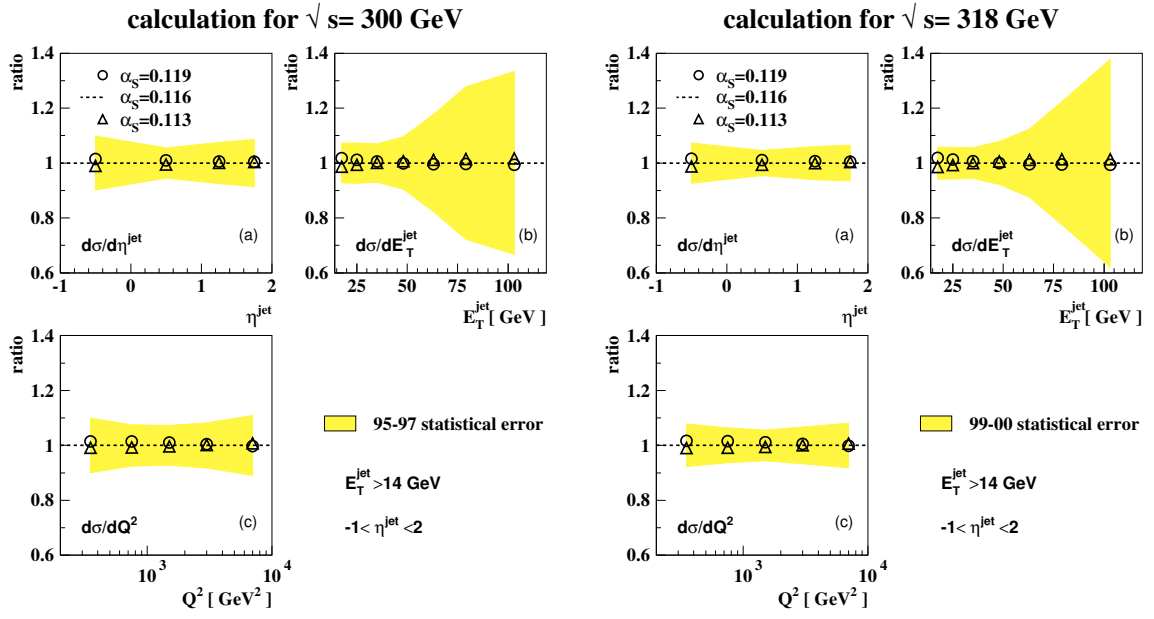
Figure 7.7 - Ratio of the predictions by MEPJET for the inclusive jet cross section obtained with $\alpha_s(M_Z) = 0.119$ and $\alpha_s(M_Z) = 0.113$ with the one obtained with $\alpha_s(M_Z) = 0.116$ as a function of (a) η^{jet}, (b) E_T^{jet} and (c) Q^2, for the calculation with center-of-mass energy $\sqrt{300}$ GeV (left) and $\sqrt{318}$ GeV (right).
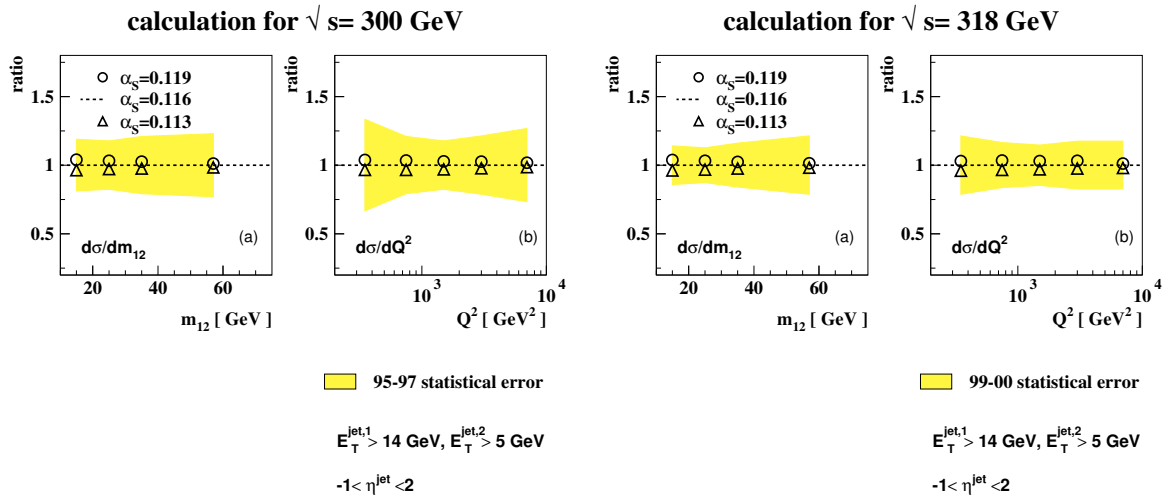

Figure 7.8 - Ratio of the predictions by MEPJET for the dijet cross section obtained with $\alpha_s(M_Z) = 0.119$ and $\alpha_s(M_Z) = 0.113$ with the one obtained with $\alpha_s(M_Z) = 0.116$ as a function of (a) m_{12} and (b) Q^2, for the calculation with center-of-mass energy $\sqrt{300}$ GeV (left) and $\sqrt{318}$ GeV (right).

Figure 7.9 - Ratio of the predictions by MEPJET for the inclusive jet cross section obtained with the renormalisation scale, μ_R, fixed to $\mu_R = 2Q$ and $\mu_R = Q/2$ with the one obtained with $\mu_R = Q$ as a function of (a) η^{jet}, (b) E_T^{jet} and (c) Q^2, for the calculation with center-of-mass energy $\sqrt{300}$ GeV (left) and $\sqrt{318}$ GeV (right).

Figure 7.10 - Ratio of the predictions by MEPJET for the dijet cross section obtained with the renormalisation scale, μ_R, fixed to $\mu_R = 2Q$ and $\mu_R = Q/2$ with the one obtained with $\mu_R = Q$ as a function of (a) m_{12} and (b) Q^2, for the calculation with center-of-mass energy $\sqrt{300}$ GeV (left) and $\sqrt{318}$ GeV (right).
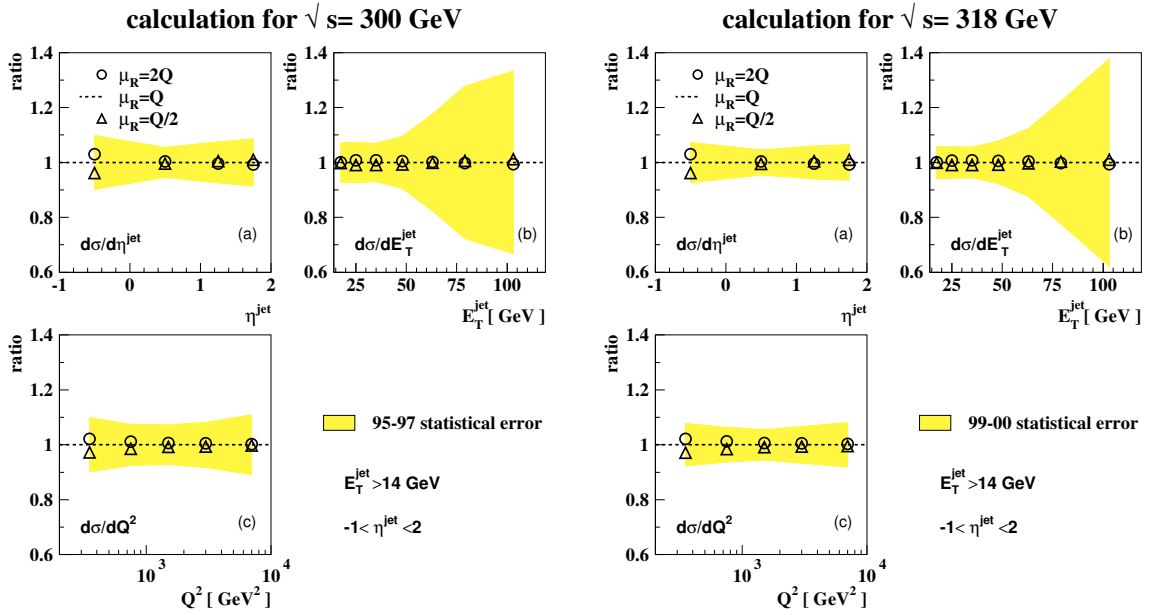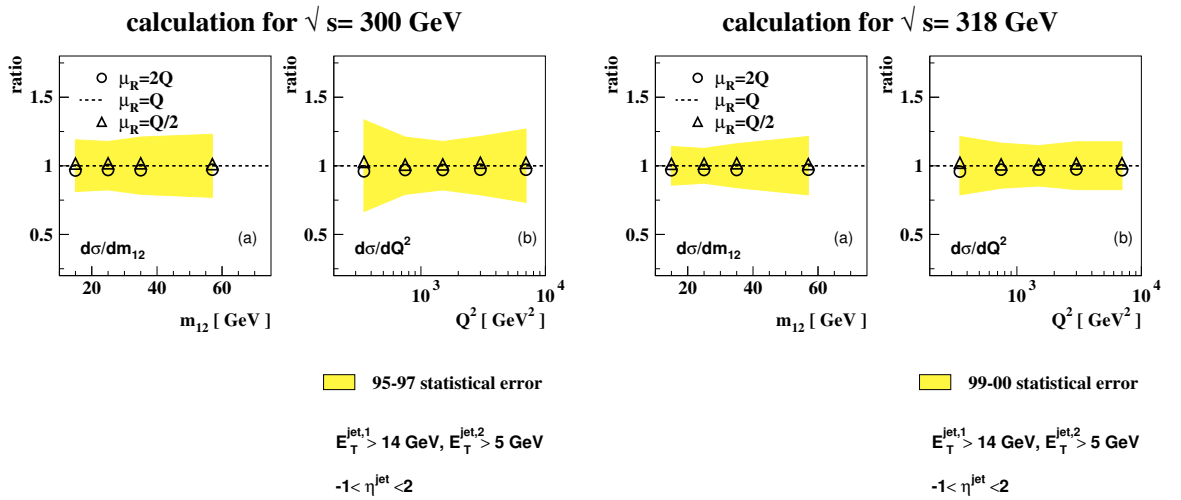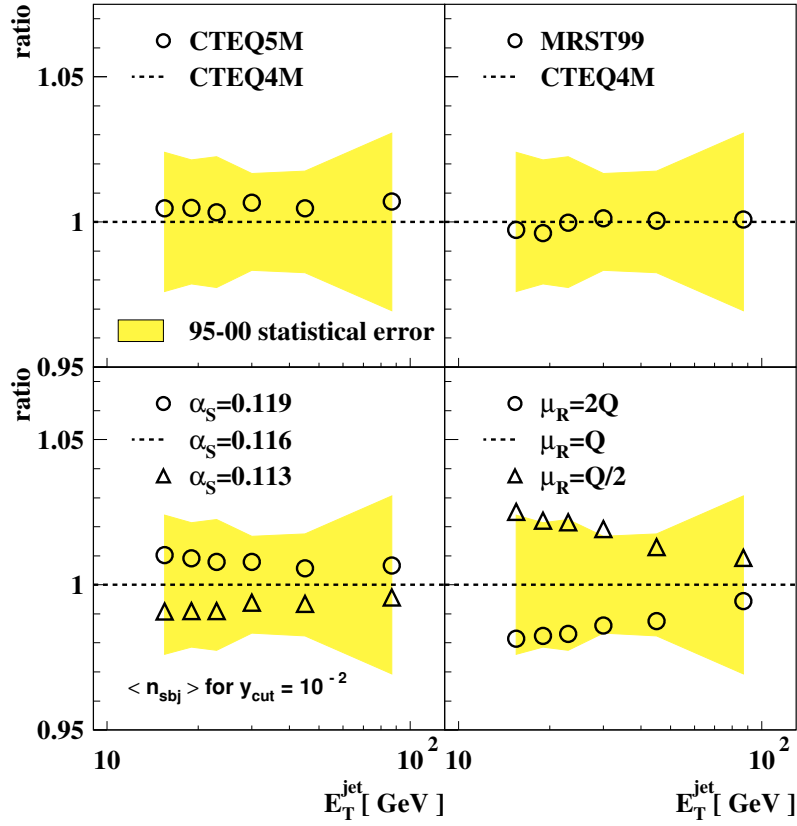
Figure 7.11 - Ratio of the predictions by MEPJET of $\langle n_{sbj} \rangle$ with different (a),(b) PDF, (c) value of $\alpha_s(M_Z)$, and (d) renormalisation scale, as a function of E_T^{jet} for a fixed value of $y_{cut} = 10^{-2}$.

7.1.4 Parton-to-hadron corrections

Since the measurements refer to jets of hadrons wheras the NLO QCD calculations refer to partons, the predictions have been corrected to the hadron level using the MC models. The multiplicative correction factor (C_{had}) is defined as the ratio of the cross section, or mean subjet multiplicity, for jets of hadrons over the same quantity for jets of partons. It was estimated by using the MC programs described in Section 5.1. The mean of the ratios obtained with the CDM and MEPS models was taken as the value of C_{had} since both predictions were in good agreement.

The value of C_{had} is ~ 1.0 (~ 0.9) for the inclusive jet (dijet) cross sections (see Figs. 7.12 and 7.13). For the mean subjet multiplicity, C_{had} is 2.13 at $y_{cut} = 5 \cdot 10^{-4}$ and decreases as E_T^{jet} increases. Figure 7.14 shows the values of C_{had} for $\langle n_{sbj} \rangle$ for a fixed value of $y_{cut} = 10^{-2}$ as a function of (a) η^{jet}, (b) E_T^{jet} and (c) Q^2, which are smaller than 1.3%. The QCD analysis leading to the extraction of α_s was performed by using the measurements of the mean subjet multiplicity at $y_{cut} = 10^{-2}$ for jets with $E_T^{jet} > 25$ GeV, a region in which the value of C_{had} differs from unity by less than 10%.
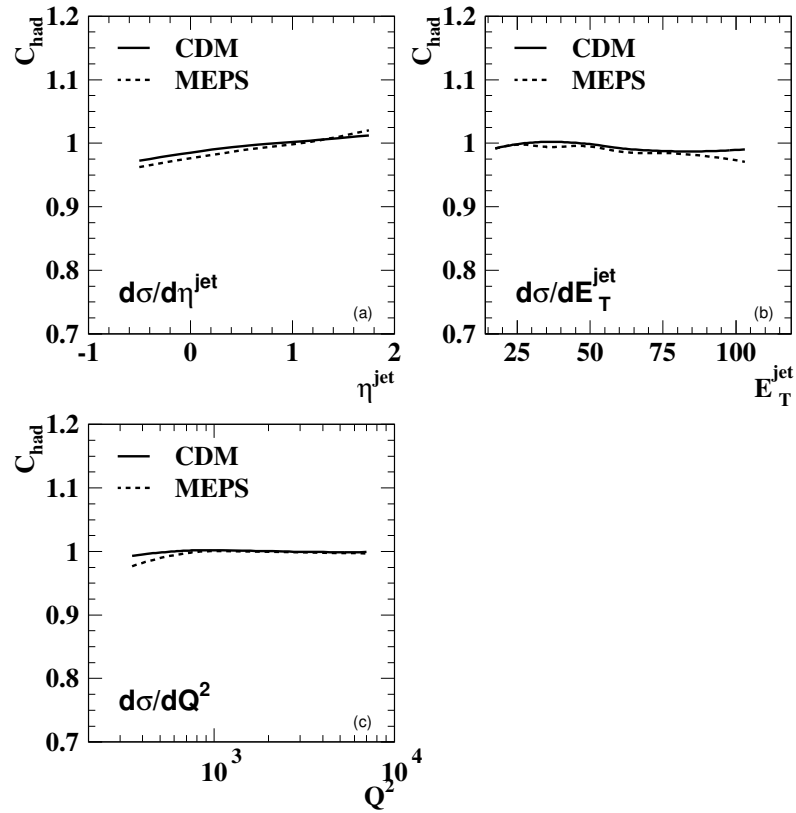
Figure 7.12 - C_{had} for the inclusive jet cross section as a function of (a) η^{jet}, (b) E_T^{jet} and (c) Q^2, given by the CDM and MEPS models.
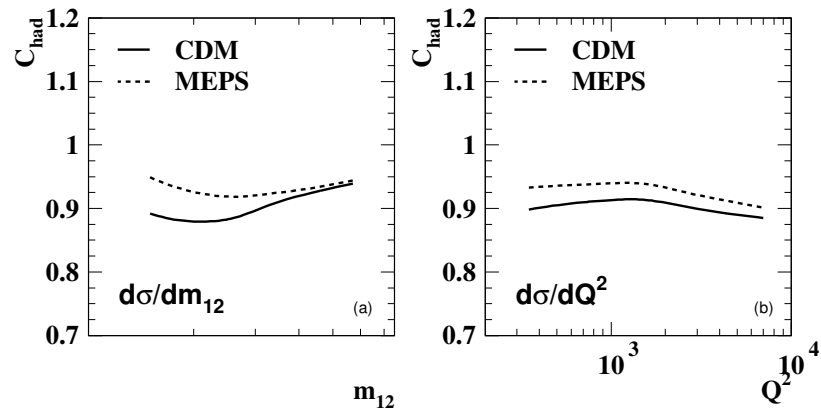
Figure 7.13 - C^{had} for the dijet cross section as a function of (a) m_{12} and (b) Q^2, given by the CDM and MEPS models.

Figure 7.14 - C_{had} for the $\langle n_{sbj} \rangle$ as a function of y_{cut} in different η^{jet} (left) and E_T^{jet} (right) regions.

Figure 7.15 - C_{had} for $\langle n_{sbj} \rangle$ as a function of (a) η^{jet}, (b) E_T^{jet} and (c) Q^2 for a fixed value of $y_{cut} = 10^{-2}$.

7.2 Differential jet cross section measurements

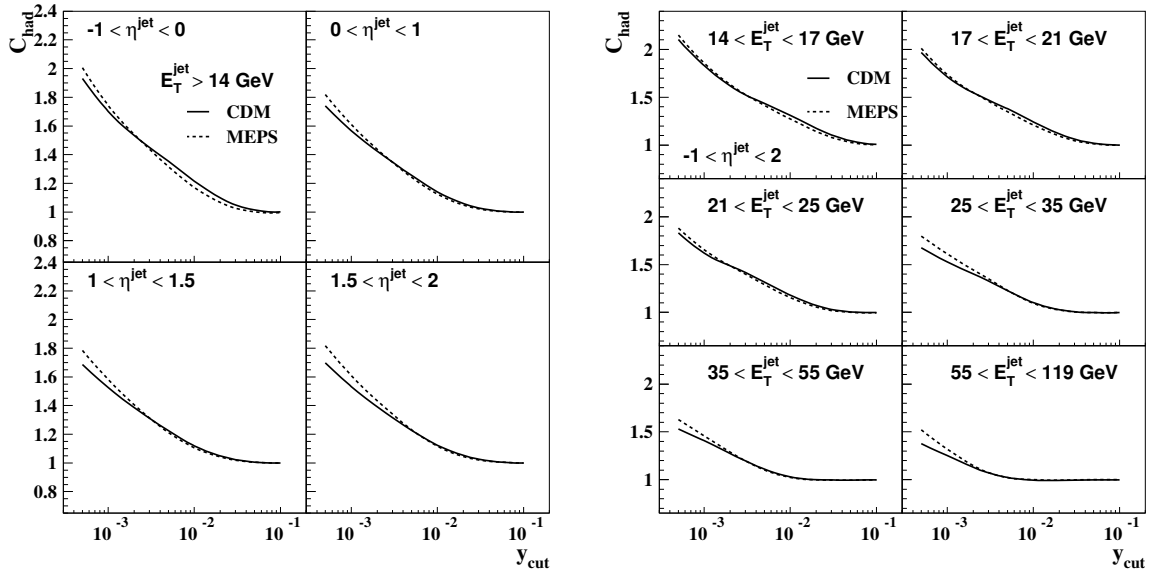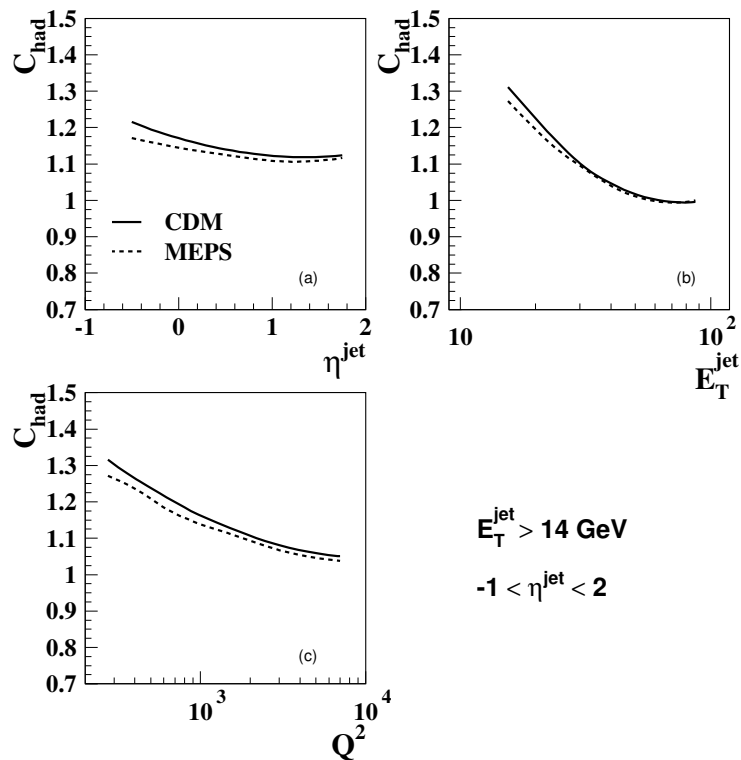The hadronic final state in charged current DIS can be characterized in terms of the production rate of jets, that is jet cross sections.

The data used for the jet cross sections was collected with the ZEUS detector at HERA during the 1995-1997 and 1999-2000 periods and correspond to an integrated luminosity of 110.5 pb^{-1}. During the running periods 1995-1997 (1999-2000) HERA operated with protons of energy $E_p = 820$ GeV (920 GeV) and positrons of energy $E_e = 27.5$ GeV, yielding a centre-of-mass energy of 300 GeV (318 GeV).

Due to the different center-of-mass energy of the two data sets, the measurements based on each set are presented separately in Sections 7.2.1 and 7.2.2. In Section 7.2.3 a combination method for both data sets will be discussed and combined measurements is presented.

7.2.1 Inclusive differential jet cross sections

Using the selected data sample, the differential inclusive jet cross sections were measured in the kinematic region defined by $Q^2 > 200$ GeV ^{2} and $y < 0.9$. These cross sections refer to all jets of hadrons an event with $E_T^{jet} > 14$ GeV and $-1 < \eta^{jet} < 2$.

The measurements of the differential inclusive jet cross section as a function of Q^2, η^{jet} and E_T^{jet} are shown in Figures 7.16 to 7.18. The measured $d\sigma/dQ^2$ ($d\sigma/E_T^{jet}$) exhibits a fall-off by two (three) orders of magnitude in the Q^2 (E_T^{jet}) range considered. $d\sigma/dQ^2$ is almost flat for small values of Q^2 which can be interpreted as due to the presence of a masive propagator in CC interactions. The $d\sigma/d\eta^{jet}$ distribution has a maximum at $\eta^{jet} \sim 1$.

In each plot, the measurements for the two different e^+p scattering data sets, are shown. The shapes of the measured cross sections of both data sets are similar. The cross sections measured with the data taken in 1999-2000 are larger than the ones obtained with the data taken in 1995-1997, as expected from the larger center-of-mass energy in 1999-2000.

The LO MC predictions given by CDM and the NLO QCD calculations given by MEPJET are compared to the data. Both CDM and MEPJET give a very good description of the shape and normalisation of all the differential inclusive jet cross sections measured.

7.2.2 Dijet differential cross sections

Using the selected dijet data, the differential inclusive jet cross sections were measured in the kinematic region defined by $Q^2 > 200$ GeV^2 and $y < 0.9$. These cross sections refer to the two jets of hadrons with highest transverse energy in an event, with $E_T^{jet,1} > 14$ GeV, $E_T^{jet,2} > 5$ GeV and $-1 < \eta^{jet} < 2$.

The differential dijet cross section as a function of Q^2 is presented in Fig. 7.19. The

value of $\mathrm{d}\sigma/\mathrm{d}Q^2$ falls by almost two orders of magnitude in the Q^2 range considered. Figure 7.20 shows the invariant-mass spectrum of the two-highest E_T jets.

Calculations from NLO QCD are compared to the measurements. The shape and the normalisation of the differential dijet cross sections measured are well described.
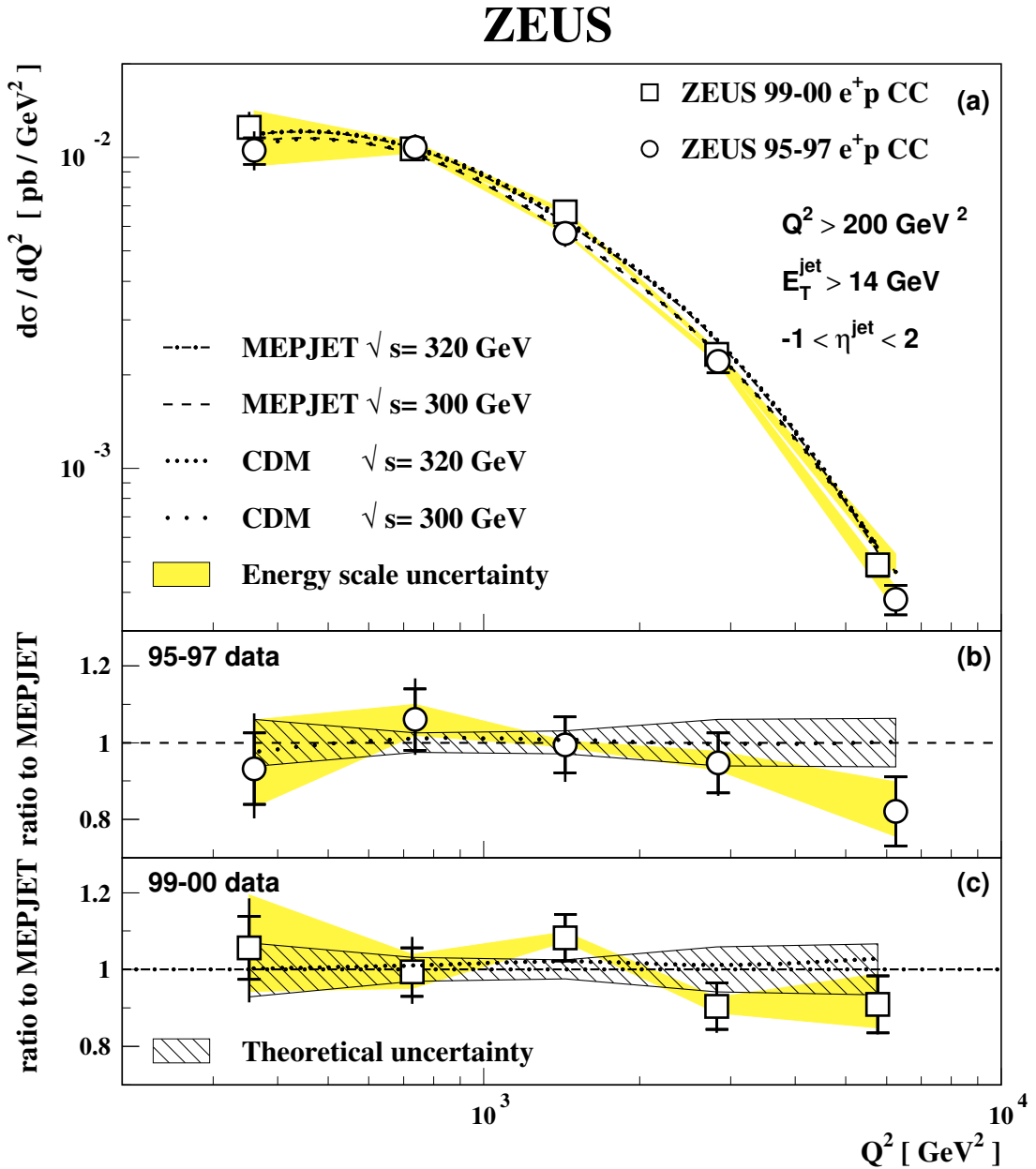
ZEUS

Figure 7.16 - (a) The differential cross section $d\sigma/dQ^2$ for inclusive jet production with $E_T^{jet} > 14$ GeV and $-1 < \eta^{jet} < 2$ in the kinematic region $Q^2 > 200$ GeV^2 and $y < 0.9$ for the **95-97** (open circles) and **99-00** (open squares) data sets. The inner error bars represent the statistical uncertainty of the data, and the outer error errors bars show the statistical and the systematic uncertainties (not associated with the uncertainty in the absolute energy scale of the CAL) added in quadrature. The shaded band displays the uncertainty due to the absolute energy scale of the CAL. The parton shower Monte Carlo prediction given by CDM for $\sqrt{s} = 300$ GeV (sparse-dotted) and for $\sqrt{s} = 318$ GeV (dotted) and the next-to-leading-order prediction obtained with MEPJET for $\sqrt{s} = 300$ GeV (dashed) and for $\sqrt{s} = 318$ GeV (dot-dashed) are shown. The ratio of the measured $d\sigma/dQ^2$ to the next-to-leading calculation for the (b) **95-97** (c) **99-00** e^+p data sets. The theoretical uncertainty is indicated by the hatched band.
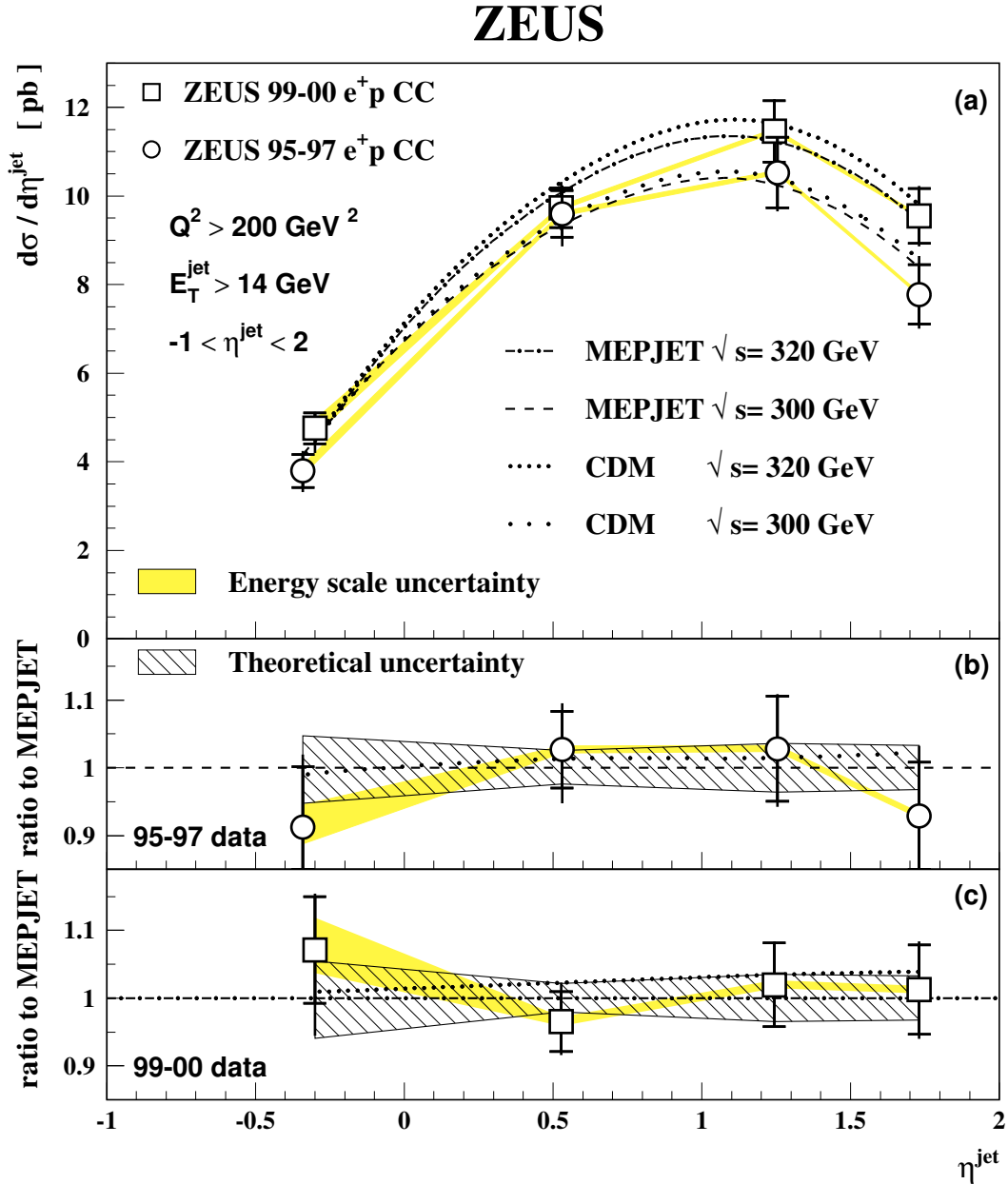
Figure 7.17 - The differential cross section $d\sigma/d\eta^{jet}$ for inclusive jet production with $E_T^{jet} > 14$ GeV and $-1 < \eta^{jet} < 2$ in the kinematic region $Q^2 > 200$ GeV ^{2} and $y < 0.9$. Other details are as given in figure 7.16.
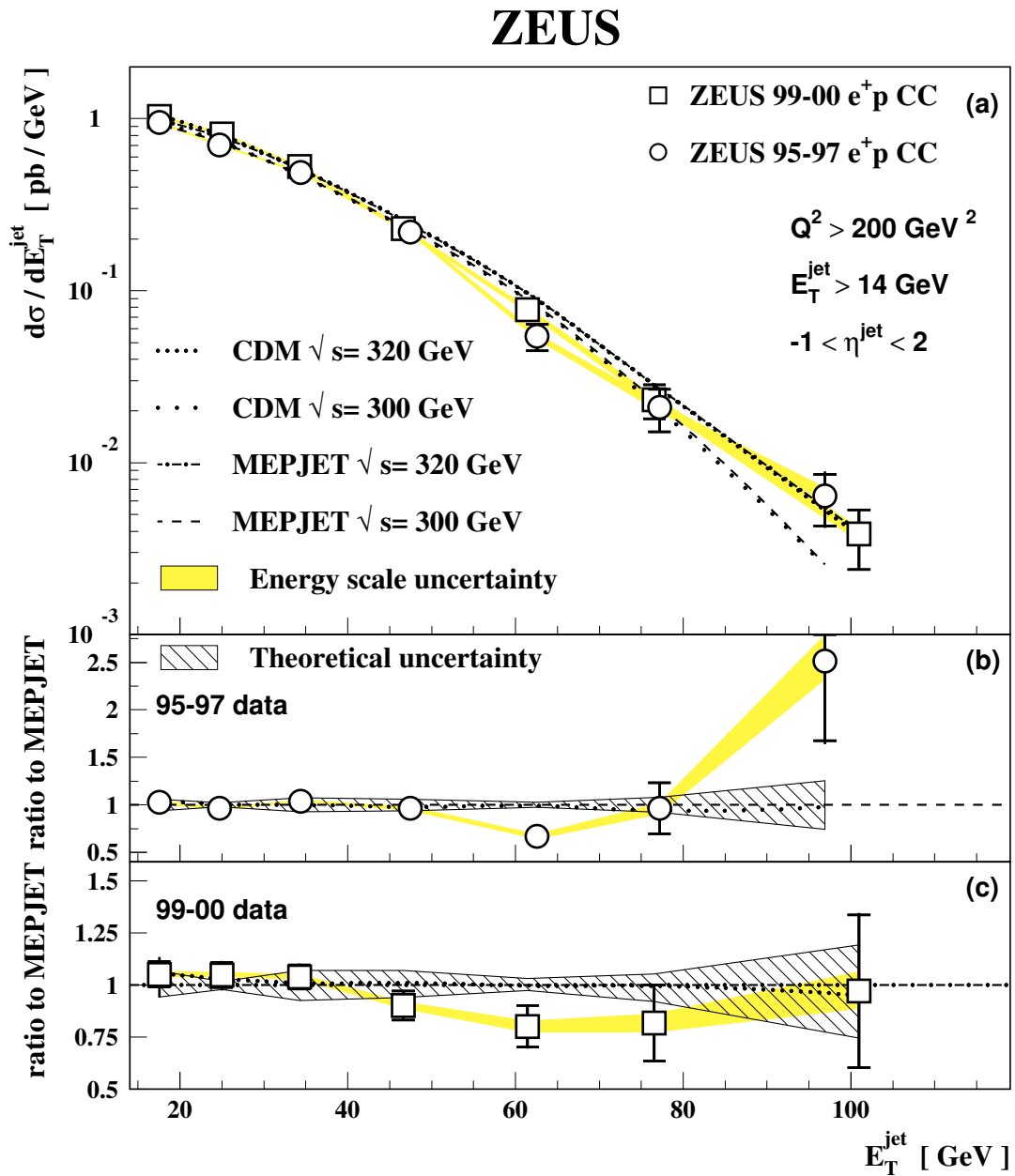
Figure 7.18 - The differential cross section $d\sigma/dE_T^{jet}$ for inclusive jet production with $E_T^{jet} > 14$ GeV and $-1 < \eta^{jet} < 2$ in the kinematic region $Q^2 > 200$ GeV^2 and $y < 0.9$. Other details are as given in figure 7.16.
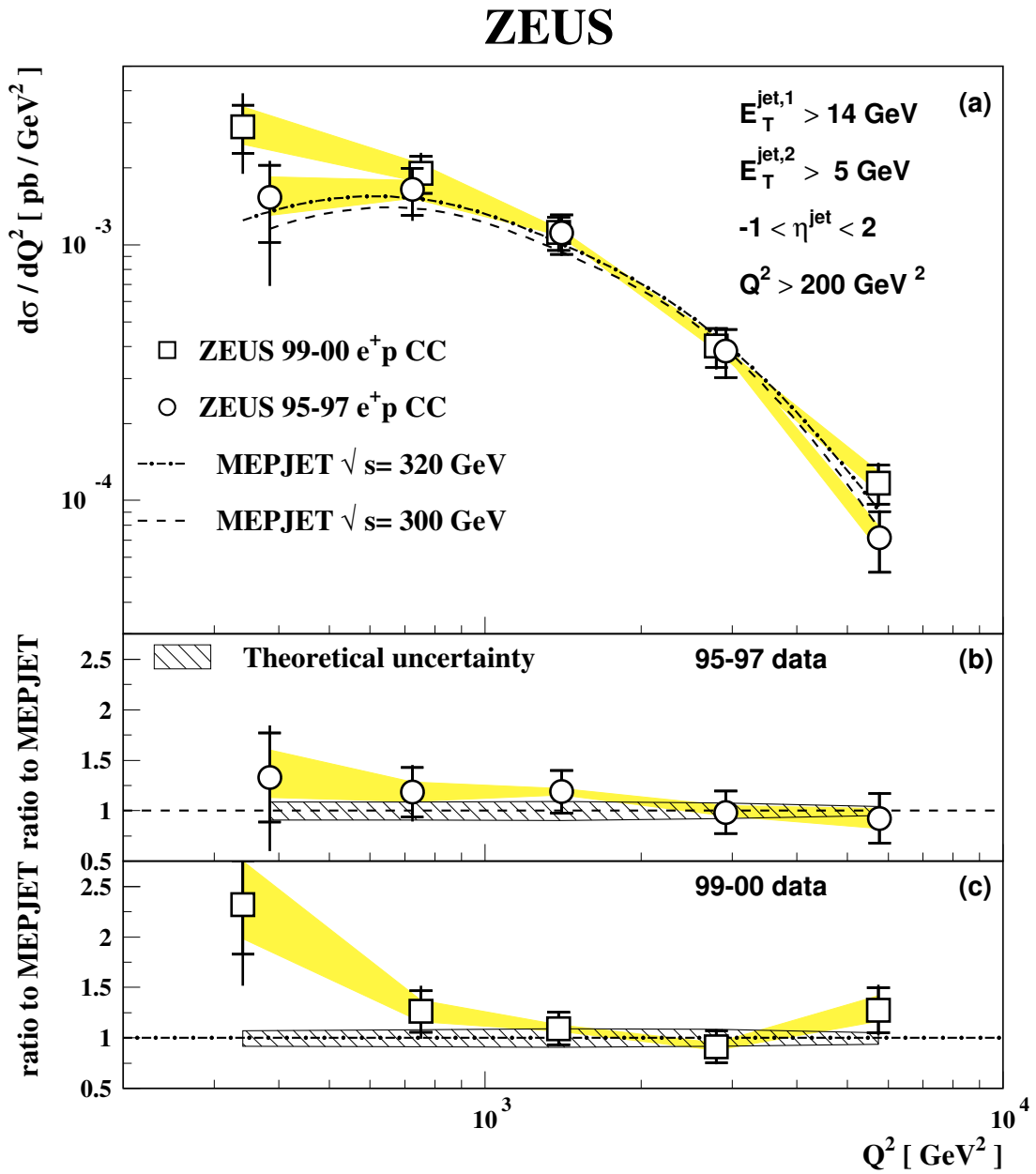
Figure 7.19 - (a) The differential cross-section $d\sigma/dQ^2$ for dijet production with $E_T^{jet,1} > 14$ **GeV**, $E_T^{jet,2} > 5$ **GeV** and $-1 < \eta^{jet} < 2$ **in the kinematic region** $Q^2 > 200$ **GeV** ^{2} **and** $y < 0.9$. **Other details are as given in the caption to Fig. 7.16.**

Figure 7.20 - (a) The differential cross-section $d\sigma/dm_{12}$ for dijet production with $E_T^{jet,1} > 14$ GeV, $E_T^{jet,2} > 5$ GeV and $-1 < \eta^{jet} < 2$ in the kinematic region $Q^2 > 200$ GeV ^{2} and $y < 0.9$. Other details are as given in the caption to Fig. 7.16.
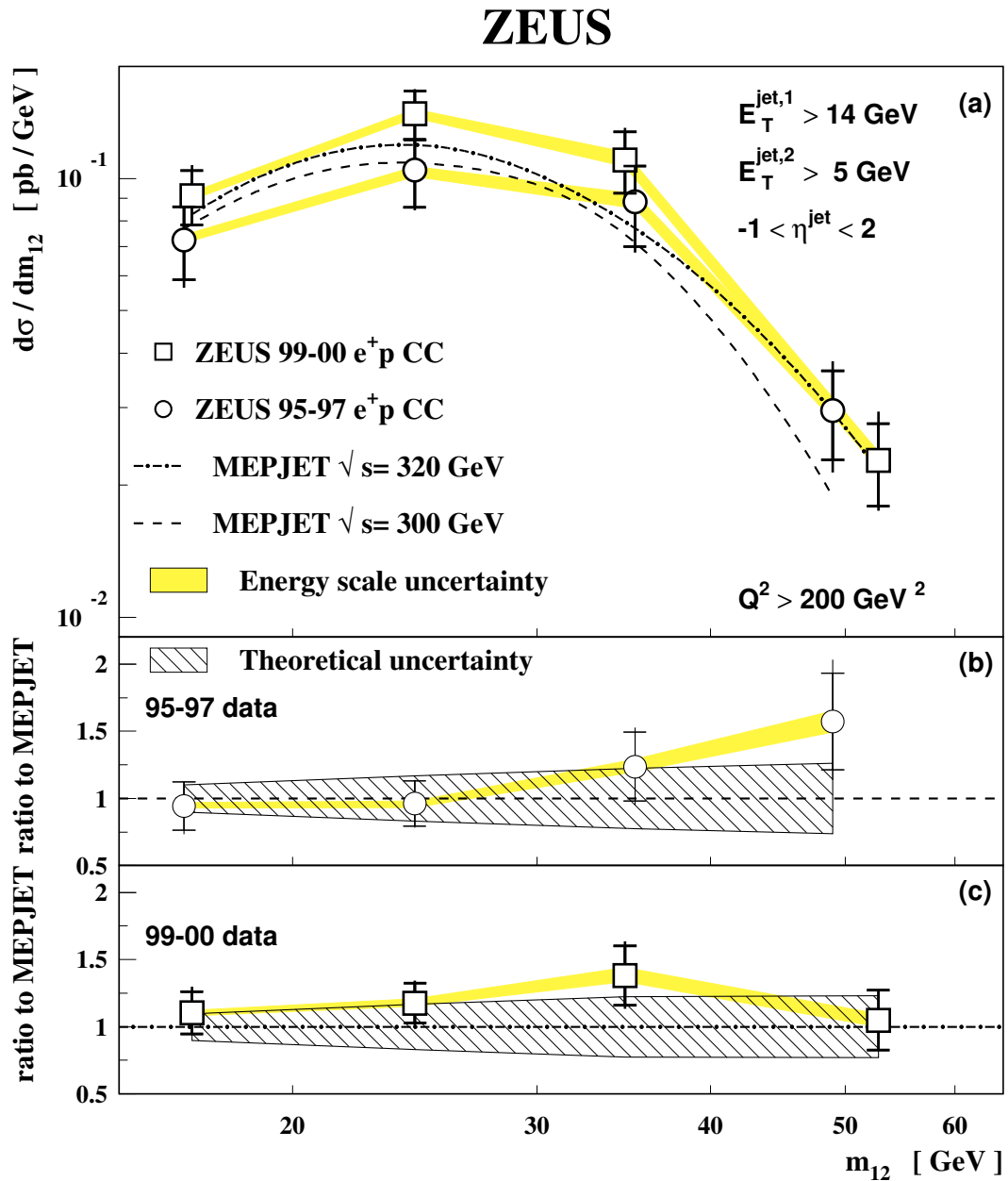
7.2.3 Combination of cross sections at different center-of-mass energies

Differential jet cross sections have been measured at two different center-of-mass energies $\sqrt{s} = 300$ and 318 GeV: $\sigma_{300} \pm \Delta_{300}$ (1995-1997) and $\sigma_{318} \pm \Delta_{318}$ (1999-2000), where $\sigma_{\sqrt{s}}$ is the measured cross section already corrected for detector effects and $\Delta_{\sqrt{s}}$ is the statistical error of the measurement.

A possible way to combine both measurements is to obtain a theoretical correction factor to account for the differences associated with the different center-of-mass energy and to apply this factor to one of the data sets. In this analysis, the measured cross sections at $\sqrt{s} = 300$ GeV have been "corrected" to an effective $\sqrt{s} = 318$ GeV using a bin-by-bin theoretical correction factor, $\mathcal{F}$:

$$\widetilde{\sigma}_{300} = \sigma_{300} \cdot \frac{\sigma_{318}^{\text{th}}}{\sigma_{300}^{\text{th}}} = \sigma_{300} \cdot \mathcal{F}, \tag{7.8}$$

where $\widetilde{\sigma}_{300}$ refers to the corrected quantity.

Then the cross sections can be combined according to the following formula:

$$\sigma_{\text{comb}} = \frac{\widetilde{\sigma}_{300} \cdot \frac{1}{\widetilde{\Delta}_{300}^2} + \sigma_{318} \cdot \frac{1}{\Delta_{318}^2}}{\frac{1}{\widetilde{\Delta}_{300}^2} + \frac{1}{\Delta_{318}^2}} = \frac{(\sigma_{300} \cdot \mathcal{F}) \cdot \frac{1}{\Delta_{300}^2 \cdot \mathcal{F}^2} + \sigma_{318} \cdot \frac{1}{\Delta_{318}^2}}{\frac{1}{\Delta_{300}^2 \cdot \mathcal{F}^2} + \frac{1}{\Delta_{318}^2}}. \tag{7.9}$$

This method of combination is referred to as the *"statistical-weighted method"*.

As the measured cross sections have sufficient statistics in all the bins, the measured number of events can be related to the luminosity by the relation

$$N_{\sqrt{s}} \simeq \mathcal{L}_{\sqrt{s}} \cdot \sigma_{\sqrt{s}}^{\text{th}}. \tag{7.10}$$

The statistical error of the measurents can then be expressed as

$$\Delta_{\sqrt{s}}^2 = \frac{N_{\sqrt{s}}}{(\mathcal{L}_{\sqrt{s}})^2} \simeq \frac{\mathcal{L}_{\sqrt{s}} \cdot \sigma_{\sqrt{s}}^{\text{th}}}{(\mathcal{L}_{\sqrt{s}})^2} = \frac{\sigma_{\sqrt{s}}^{\text{th}}}{\mathcal{L}_{\sqrt{s}}}. \tag{7.11}$$

The substitution of Equation 7.11 in Equation 7.9 leads to:

$$\sigma_{\text{comb}} = \frac{\sigma_{300} \cdot \mathcal{L}_{300} + \sigma_{318} \cdot \mathcal{L}_{318}}{\mathcal{L}_{300} \cdot \frac{\sigma_{300}^{\text{th}}}{\sigma_{318}^{\text{th}}} + \mathcal{L}_{318}} = \frac{\sigma_{300} \cdot \mathcal{L}_{300} + \sigma_{318} \cdot \mathcal{L}_{318}}{\mathcal{L}_{300} \cdot \frac{1}{\mathcal{F}} + \mathcal{L}_{318}}. \tag{7.12}$$

This method of combination is referred to as the *"luminosity-weighted method"*.

The combined cross sections using the "statistical-weighted method" and the "luminosity-weighted method" agree well in the regions where the data are precise. In the regions where the statistical uncertainty is large, the "luminosity-weighted method" is less sensitive to statistical fluctuations.

The "luminosity-weighted method" has been used in the presentation of the results. The statistical error of the combined data is given by:

$$\Delta_{\text{comb}}(\text{stat}) = \frac{\sqrt{\Delta_{300}^2 \cdot \mathcal{L}_{300}^2 + \Delta_{318}^2 \cdot \mathcal{L}_{318}^2}}{\mathcal{L}_{300} \cdot \frac{1}{\mathcal{F}} + \mathcal{L}_{318}} \tag{7.13}$$

The systematic error is asumed to be fully correlated between the two measurements. For each systematic check the combined quantity is evaluated

$$\widehat{\sigma}_{comb} = \frac{\widehat{\sigma}_{300} \cdot \mathcal{L}_{300} + \widehat{\sigma}_{318} \cdot \mathcal{L}_{318}}{\mathcal{L}_{300} \cdot \frac{1}{\mathcal{F}} + \mathcal{L}_{318}} \quad ; \quad \Delta_{comb}(syst) = \widehat{\sigma}_{comb} - \sigma_{comb}, \qquad (7.14)$$

where $\widehat{\sigma}_{\sqrt{s}}$ is the cross section evaluated for each systematic check. Finally all the systematic uncertainties are added in quadrature.

The data combination method relies on the theoretical factor $\mathcal{F}$. Future improvements in the theoretical calculations could change the value of $\mathcal{F}$ which would change the combined data. For this reason the uncombined data are also presented so that improved combination methods could be applied in the future.

Figures 7.21a- 7.25a show the theoretical predictions given by MEPJET of the measured differential jet cross sections for $\sqrt{s} = 300$ and 318 GeV. Figures 7.21b- 7.25b show the prediction for $\mathcal{F}$ given by MEPJET, CDM and MEPS. Figures 7.21c- 7.25c show the ratio of $\mathcal{F}$ given by either CDM or MEPS over the one predicted by MEP-JET. The values of $\mathcal{F}$ predicted by MEPJET and CDM are very similar for all cross sections. The factor $\mathcal{F}$ given by MEPJET has been used to combine the measured differential jet cross sections.

The combined differential jet cross sections are shown in Figures 7.26- 7.30.
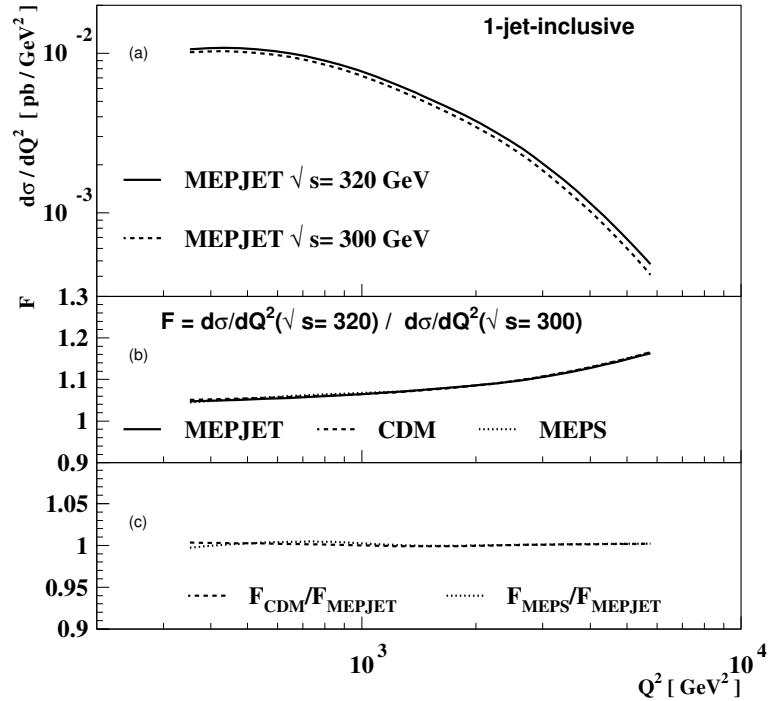
Figure 7.21 - (a) Predictions given by MEPJET for the inclusive jet cross-section $d\sigma/dQ^2$ for $\sqrt{s} = 300$ GeV (dashed) and for $\sqrt{s} = 318$ GeV (solid). (b) Theoretical correction factor to combine the measured cross sections $d\sigma/dQ^2$ for inclusive jet production at two different center-of-mass energies given by MEPJET (solid), CDM(dashed) and MEPS (dotted). (c) Ratio of the theoretical correction factors with the one predicted by MEPJET.

Figure 7.22 - Theoretical correction factor to combine the measured $d\sigma/d\eta^{jet}$ inclusive jet cross sections. Other details as given in the caption of figure 7.21.

Figure 7.23 - Theoretical correction factor to combine the measured $d\sigma/dE_T^{jet}$ inclusive jet cross sections. Other details as given in the caption of figure 7.21.

Figure 7.24 - Theoretical correction factor to combine the measured $d\sigma/dQ^2$ dijet cross sections. Other details as given in the caption of figure 7.21.
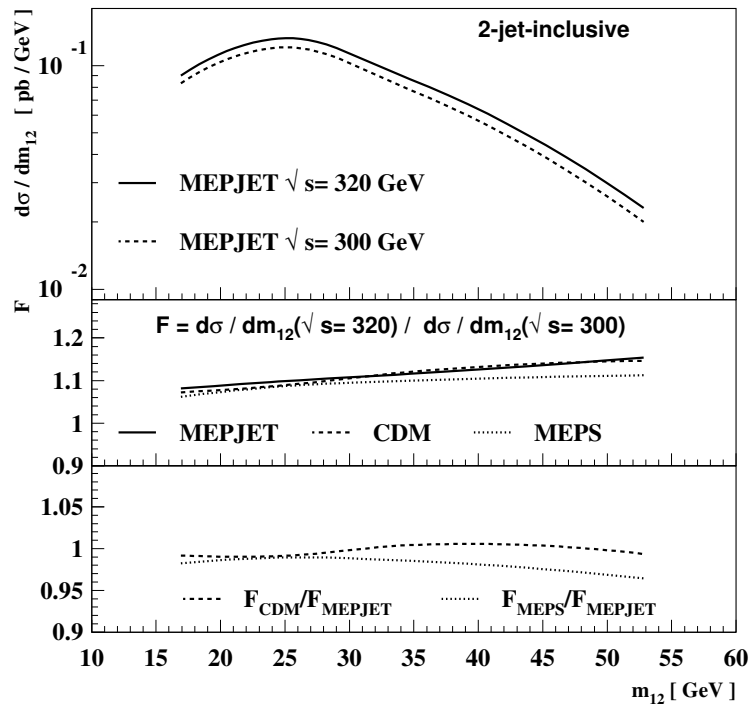
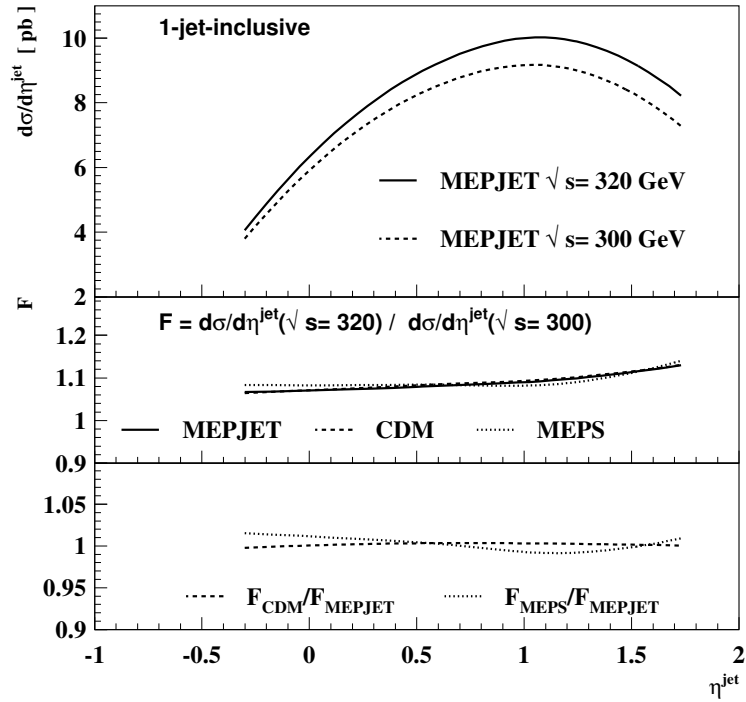**Figure 7.25** - Theoretical correction factor to combine the measured $d\sigma/dm_{12}$ dijet cross sections. Other details as given in the caption of figure 7.21.

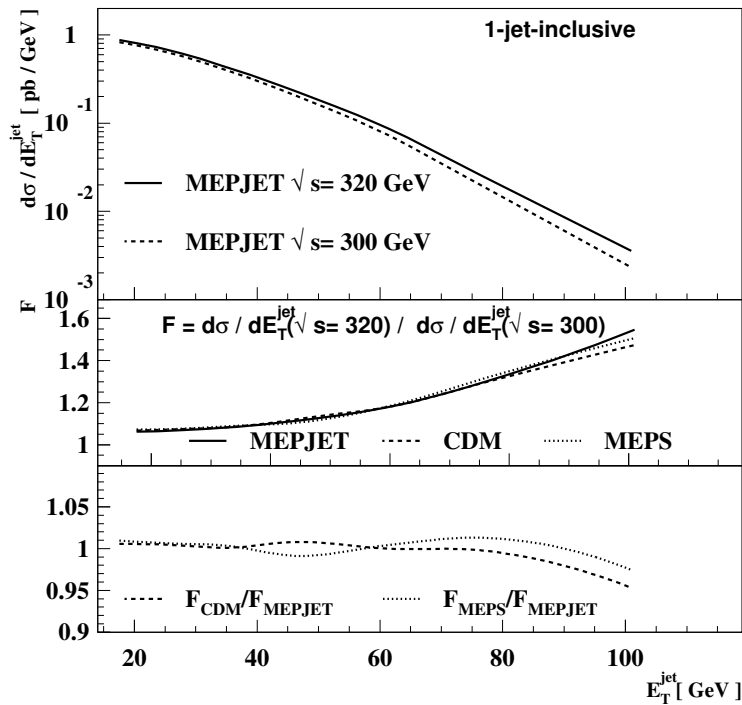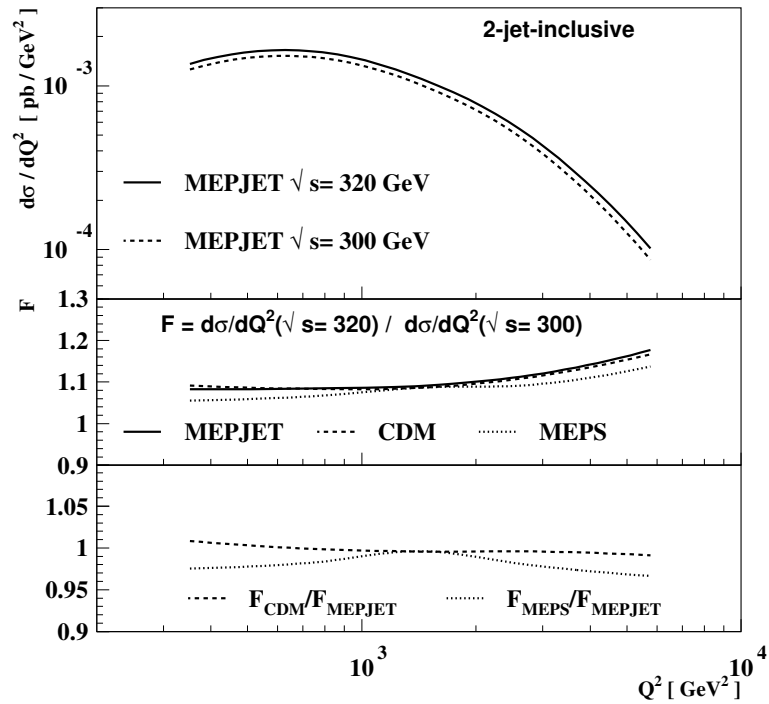**Figure 7.26 -** (a) The combined differential cross section $d\sigma/dQ^2$ for inclusive jet production with $E_T^{jet} > 14$ GeV and $-1 < \eta^{jet} < 2$ in the kinematic region $Q^2 > 200$ GeV ^{2} and $y < 0.9$ (black dots). The inner error bars represent the statistical uncertainty of the data, and the outer error errors bars show the statistical and the systematic uncertainties (not associated with the uncertainty in the absolute energy scale of the CAL) added in quadrature. The shaded band displays the uncertainty due to the absolute energy scale of the CAL. The parton shower Monte Carlo prediction given by CDM for $\sqrt{s} = 318$ GeV (dashed line) and the next-to-leading-order prediction obtained with MEPJET for $\sqrt{s} = 318$ GeV (solid line) are shown. (b) The ratio of the measured $d\sigma/dQ^2$ to the next-to-leading calculation. The theoretical uncertainty is indicated by the hatched band.

ZEUS

Figure 7.27 - The differential cross section $d\sigma/d\eta^{jet}$ for inclusive jet production with $E_T^{jet} > 14$ GeV and $-1 < \eta^{jet} < 2$ in the kinematic region $Q^2 > 200$ GeV ^{2} and $y < 0.9$. Other details are as given in figure 7.26.
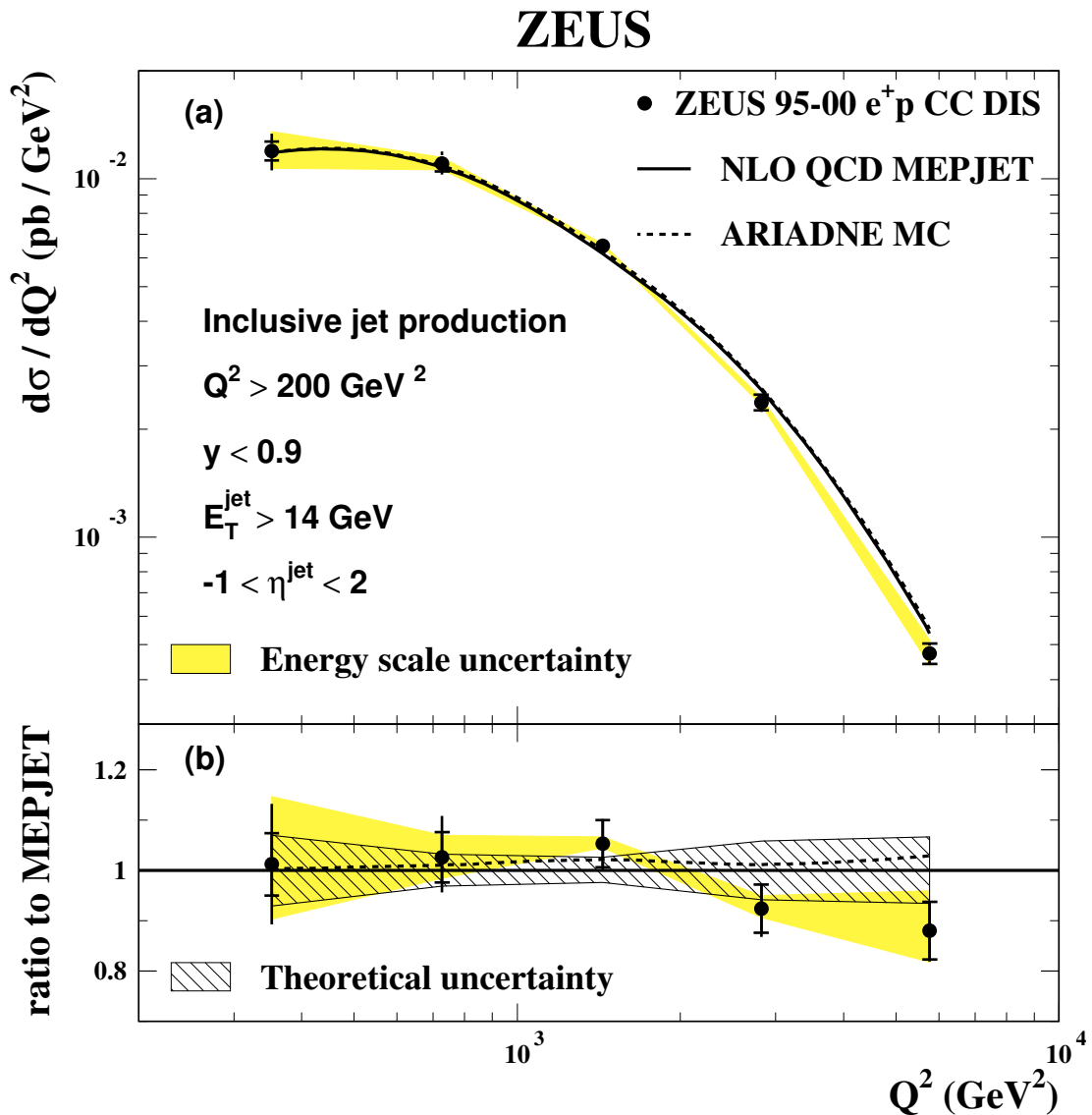
Figure 7.28 - The combined differential cross section $d\sigma/dE_T^{jet}$ for inclusive jet production with $E_T^{jet} > 14$ GeV and $-1 < \eta^{jet} < 2$ in the kinematic region $Q^2 > 200$ GeV ^{2} and $y < 0.9$. Other details are as given in figure 7.26.

Figure 7.29 - (a) The combined differential cross-section $d\sigma/dQ^2$ for dijet production with $E_T^{jet,1} > 14$ GeV, $E_T^{jet,2} > 5$ GeV and $-1 < \eta^{jet} < 2$ in the kinematic region $Q^2 > 200$ GeV ^{2} and $y < 0.9$. Other details are as given in the caption to Fig. 7.26.

Figure 7.30 - (a) The combined differential cross-section $d\sigma/dm_{12}$ for dijet production with $E_T^{jet,1} > 14$ GeV, $E_T^{jet,2} > 5$ GeV and $-1 < \eta^{jet} < 2$ in the kinematic region $Q^2 > 200$ GeV ^{2} and $y < 0.9$. Other details are as given in the caption to Fig. 7.26.

7.3   Measurement of the mass of W gauge boson

The absolute magnitude of the CC cross-section prediction is determined by the Weinberg angle ($\sin^2\theta_W$) and the PDF's. The Q^2 dependence of the CC cross section includes the propagator term $[1/(M_W^2 + Q^2)]^2$. The sensitivity of the measured inclusive jet differential cross section as a function of E_T^{jet} to the mass of the W gauge boson, M_W, is illustrated in Fig. 7.31. The measured $d\sigma/E_T^{jet}$, corrected for QED radiative effects, was used to determine M_W. The procedure used to calculate LO MC predictions of $d\sigma/E_T^{jet}$ for different values of M_W keeping $\sin^2\theta_W$ fixed, were calculated. For each E_T^{jet} bin, i, the LO predictions were used to parametrize the M_W dependence of $d\sigma/E_T^{jet}$ (see Fig. 7.32) according to the functional form

$$\left[\frac{d\sigma}{dE_T^{jet}} (M_W) \right]_i = C_0^i + C_1^i \cdot M_W + C_2^i \cdot M_W^2. \qquad (7.15)$$

This parametrisation was used to extract a value of M_W in each E_T^{jet} bin. A combined value of M_W was then determined by a χ^2-fit to the measured $d\sigma/E_T^{jet}$ for all E_T^{jet} bins. In addition, a combined value of M_W was obtained by repeating the previous procedure normalising all the LO MC predictions to the measured data, to avoid the dependence on the value of $\sin^2\theta_W$. The predictions were normalised to the first bin of the measured $d\sigma/E_T^{jet}$. The values for M_W obtained from the measurement of $d\sigma/E_T^{jet}$ for various E_T^{jet} regions are shown in Fig. 7.33. All the values are in good agreement with each other. The values of M_W obtained from a χ^2-fit to the measured $d\sigma/E_T^{jet}$ combining all E_T^{jet} bins are:

$$M_W = 80.1 \pm 0.9 \text{ (stat)} {}^{+1.5}_{-1.4} \text{ (syst.)} \pm 0.7 \text{ (th.)} \text{ GeV}; \sin^2\theta_W \text{ fixed}, \qquad (7.16)$$

$$M_W = 78.0 \pm 4.7 \text{ (stat)} {}^{+12.2}_{-11.0} \text{ (syst.)} {}^{+3.8}_{-6.8} \text{ (th.)} \text{ GeV}; \text{ norm. fixed}. \qquad (7.17)$$

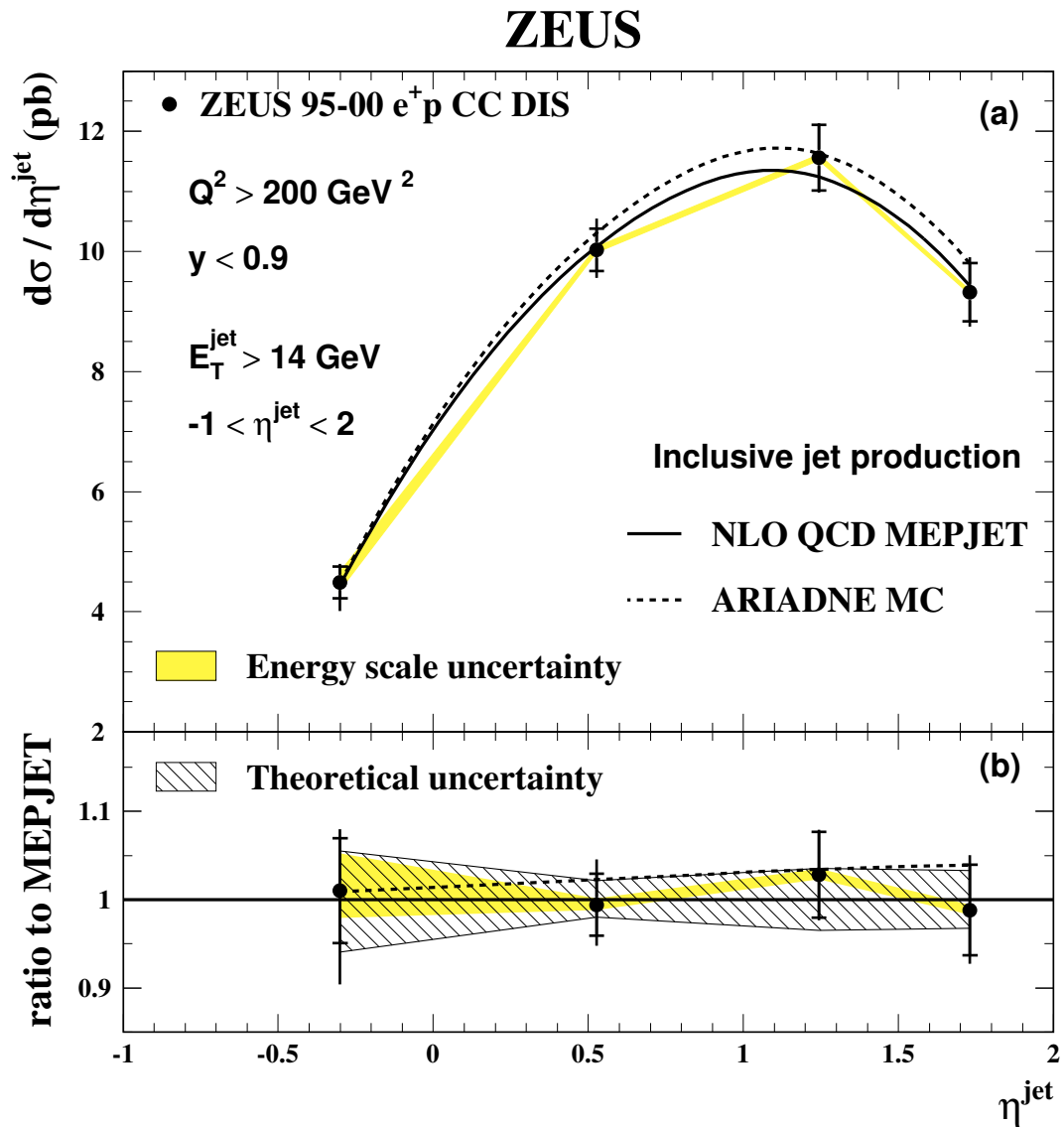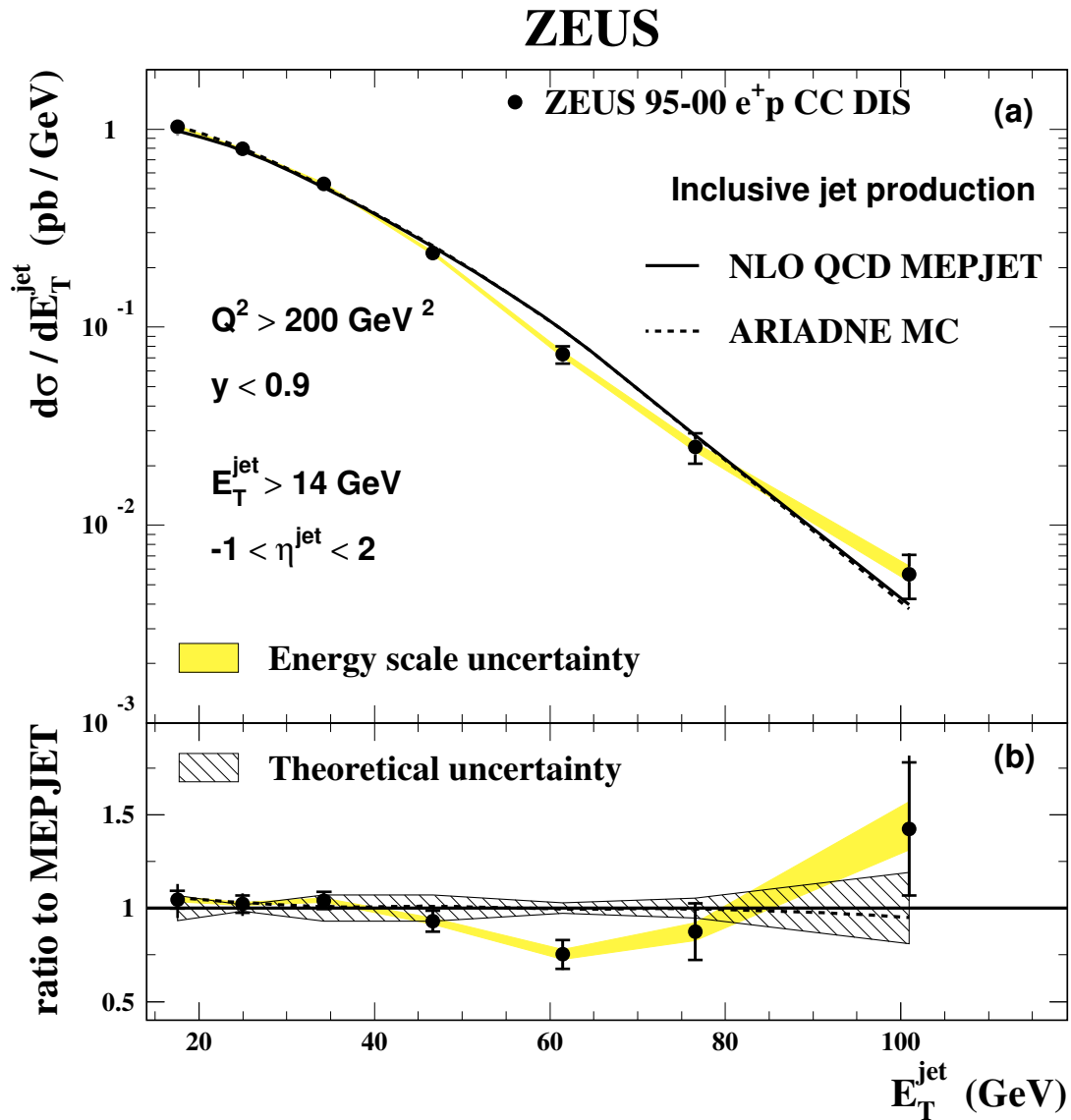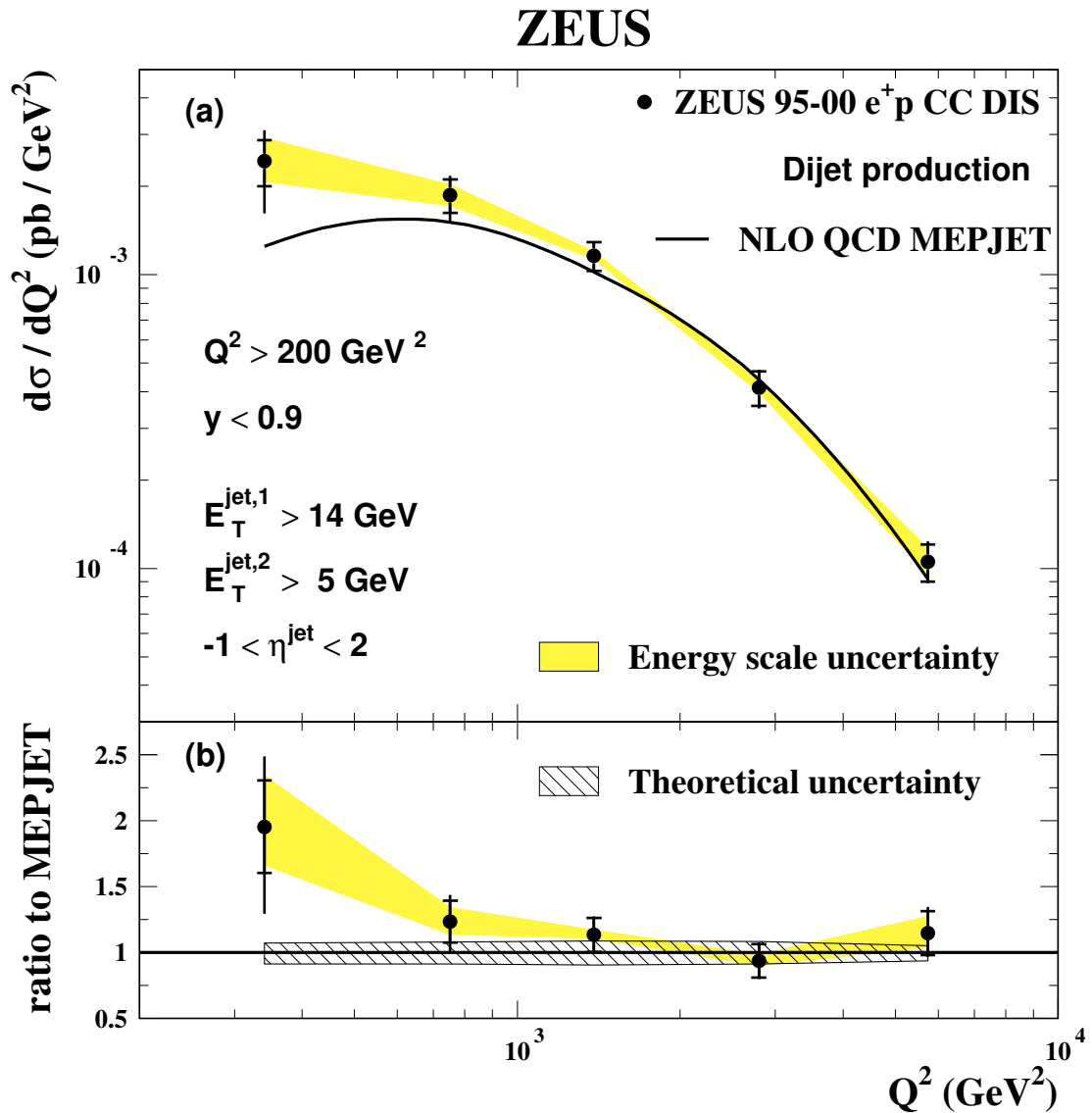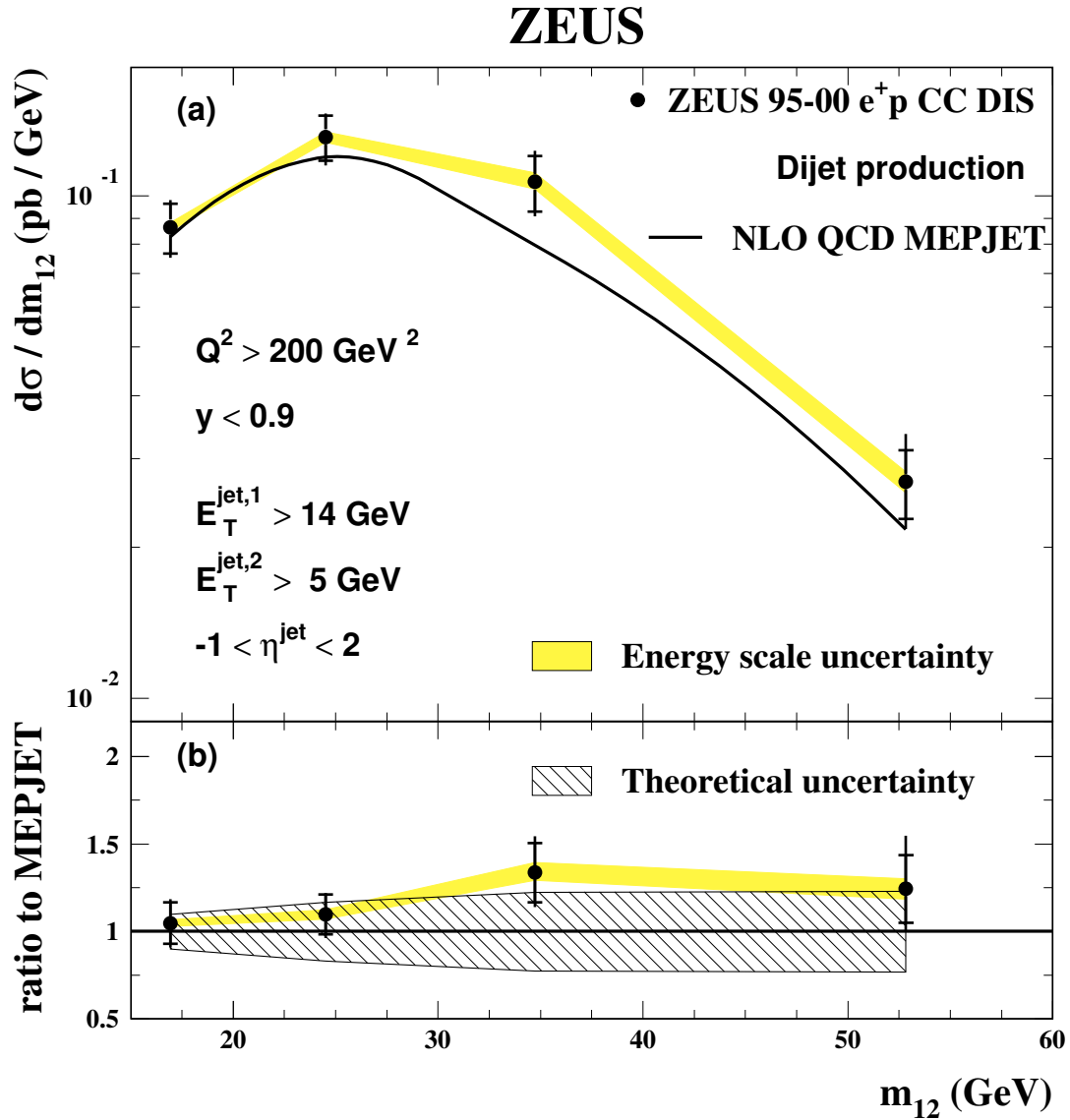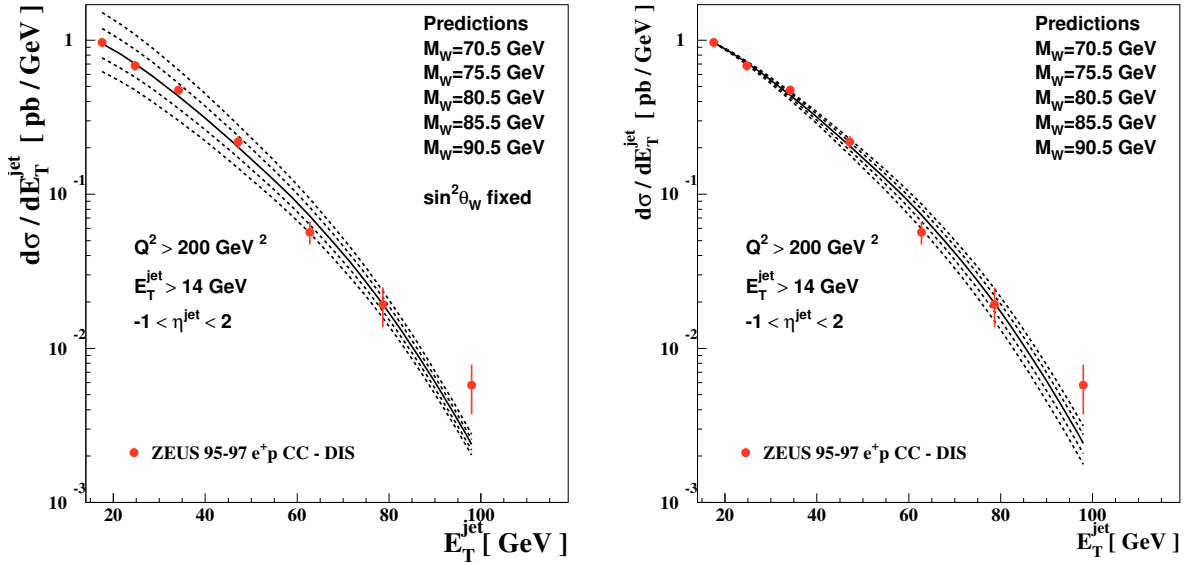**Figure 7.31 -** The differential cross section $d\sigma/dE_T^{jet}$ for inclusive jet production with $E_T^{jet} > 14$ GeV and $-1 < \eta^{jet} < 2$ in the kinematic region $Q^2 > 200$ GeV ^{2} and $y < 0.9$. LO Monte Carlo predictions assuming different values of M_W are shown.
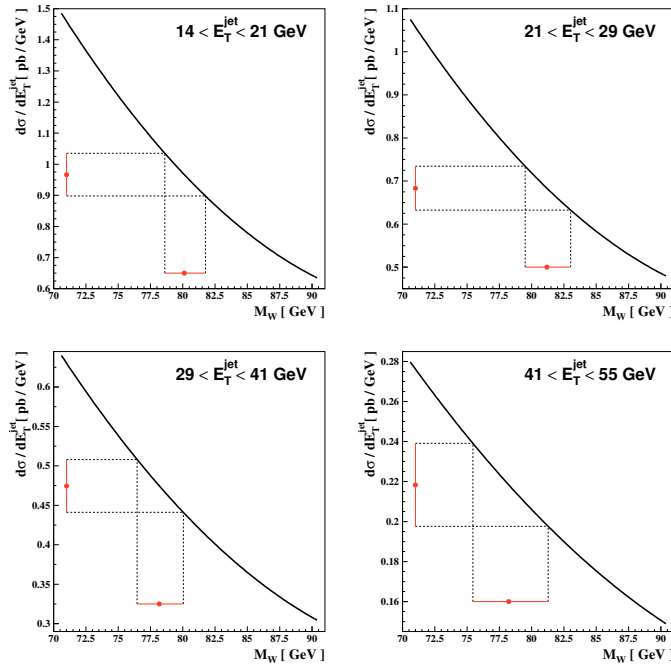
Figure 7.32 - Parametrisations of the M_W dependence of the differential cross section $d\sigma/dE_T^{jet}$ calculations in different E_T^{jet} regions.
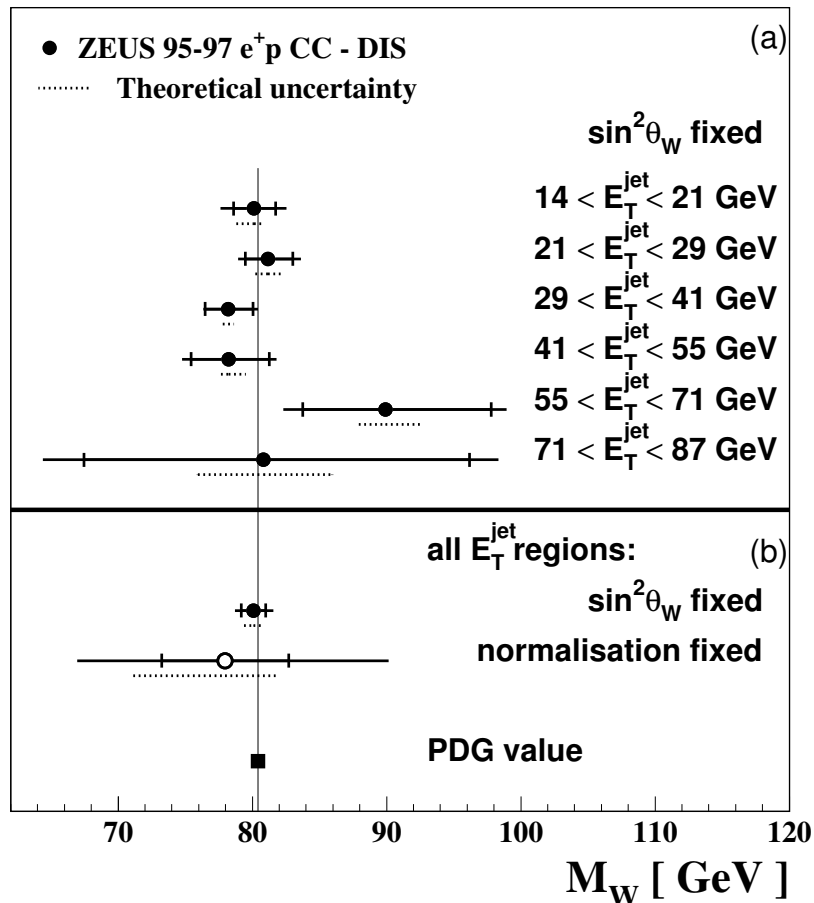
Figure 7.33 - (a) The M_W values determined form a fit to the measured inclusive jet differential cross section $d\sigma/E_T^{jet}$ in different E_T^{jet} regions keeping $\sin^2\theta_W$ fixed. (b) The combined value of M_W obtained using all the E_T^{jet} regions keeping either $\sin^2\theta_W$ fixed (black dot) or the normalisation fixed (open circle). The inner error bars represent the statistical uncertainty of the data and the outer error bars show the statistical and the systematic uncertainties added in quadrature. The dotted line below each point indicates the theoretical uncertainty.

7.3.1 Uncertainties in the extraction of M_W

The systematic and theoretical uncertainties in the measurement of M_W have been estimated. The systematic uncertainties have been estimated by repeating the M_W extraction procedure explained in 7.3 with all the systematic checks that have been performed in the data. The main contributions come from the use of MEPS instead of CDM to correct the data and the p_t/E_t cut. Three sources of theoretical uncertainty are considered

- the uncertainty due to the proton PDF was estimated using CTEQ5M and MRST instead of CTEQ4M in the predictions;

- the uncertainty due to that on $\alpha_S(M_Z)$ was estimated by repeating the calculations using CTEQ4A1 and CTEQ4A5, which were determined assuming $\alpha_S(M_Z)$= 0.110 and 0.122, respectively. The differences between the calculations an those based on CTEQ4M, $\alpha_S(M_Z)$=0.116, were taken as the uncertainty;

- the uncertainty on the model of the QCD cascade was estimated using MEPS instead of CDM to parametrize the dependence of the cross section with the value of M_W.

Figure 7.34 shows the uncertainties in the case of the extraction of M_W as a best χ^2-fit to all E_T^{jet} regions keeping $\sin^2\theta$ fixed.
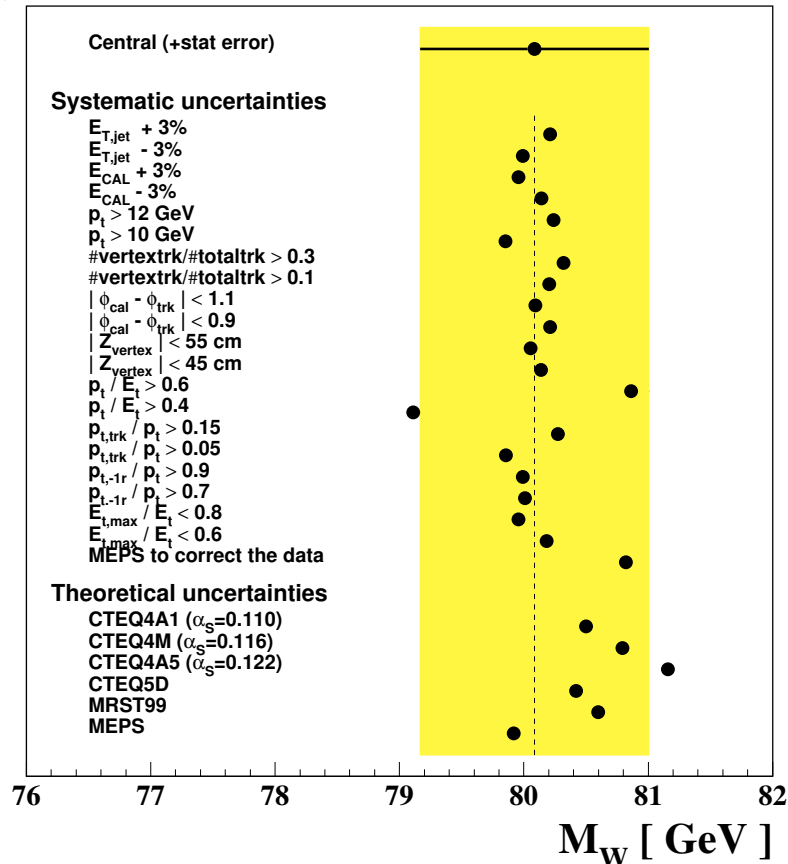
Figure 7.34 - Systematic and theoretical uncertainties in the extraction of M_W as a best χ^2 fit to all E_T^{jet} regions and keeping $\sin^2\theta$ fixed.

7.4 Subjet multiplicity measurements

The mean subjet multiplicity, $\langle n_{sbj} \rangle$, has been determined using the inclusive sample of jets in the kinematic region defined by $Q^2 > 200$ GeV^2 and $y < 0.9$. The $\langle n_{sbj} \rangle$ values were obtained with every jet of hadrons in the event with $E_T^{jet} > 14$ GeV and $-1 < \eta^{jet} < 2$. The dependence of the mean subjet multiplicity was estimated to be negligible on the center-of-mass energy and, thus, the measurements of the mean subjet multiplicity have been obtained using the whole e^+p data sample, that is the data taken in 1995-2000.

The results are shown as a function of y_{cut} in different η^{jet} and E_T^{jet} regions in Figs. 7.35 and 7.36, respectively. The values of $\langle n_{sbj} \rangle$ at $y_{cut} = 0.01$ as a function of η^{jet} and E_T^{jet} are shown in Fig. 7.37. The measured $\langle n_{sbj} \rangle$ exhibit no significant dependence on η^{jet}, but decrease as E_T^{jet} increases.

The NLO QCD calculations based on MEPJET are compared to the data. The data are reasonably described by the NLO QCD calculation.
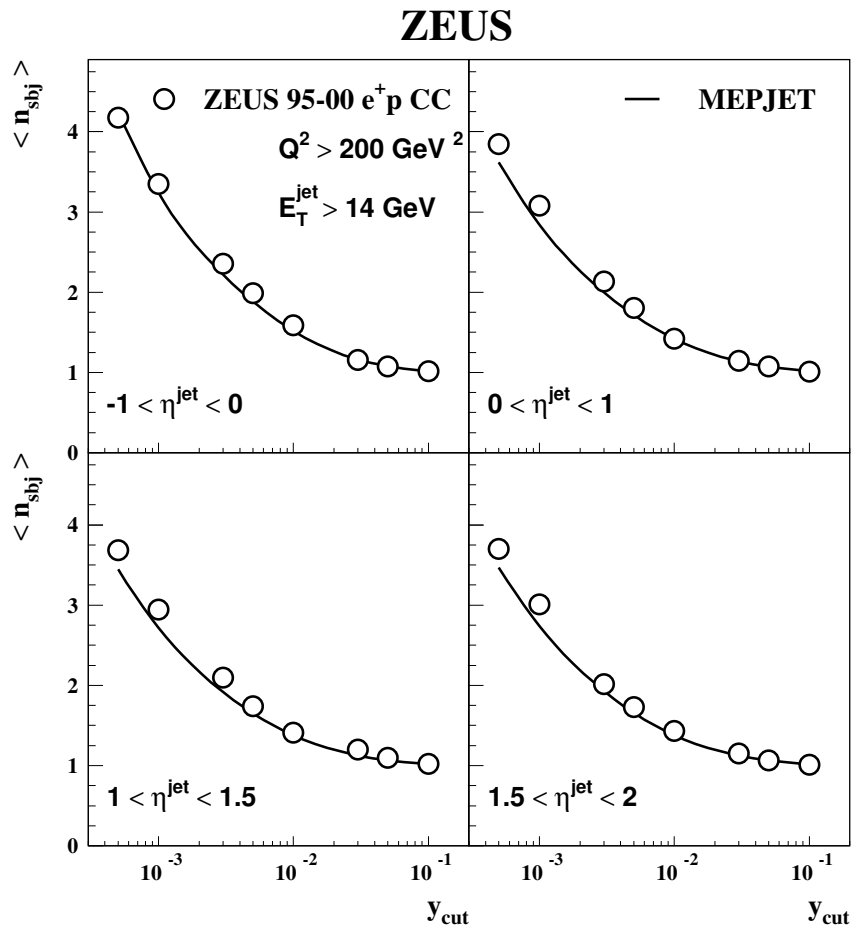
Figure 7.35 - Mean subjet multiplicity, $\langle n_{sbj} \rangle$, as a function of y_{cut}, for inclusive jet production with $E_T^{jet} > 14$ GeV in different η^{jet} regions. The next-to-leading-order prediction based on MEPJET (solid line) is shown.

ZEUS

Figure 7.36 - $\langle n_{sbj} \rangle$ as a function of y_{cut} for inclusive jet production with $-1 < \eta^{jet} < 2$ in different E_T^{jet} regions.

Figure 7.37 - $\langle n_{sbj} \rangle$ for inclusive jet production with $E_T^{jet} > 14$ GeV and $-1 < \eta^{jet} < 2$ as function of (a) η^{jet} and (b) E_T^{jet} for a fixed value of $y_{cut} = 10^{-2}$.

7.4.1 Measurement of α_s

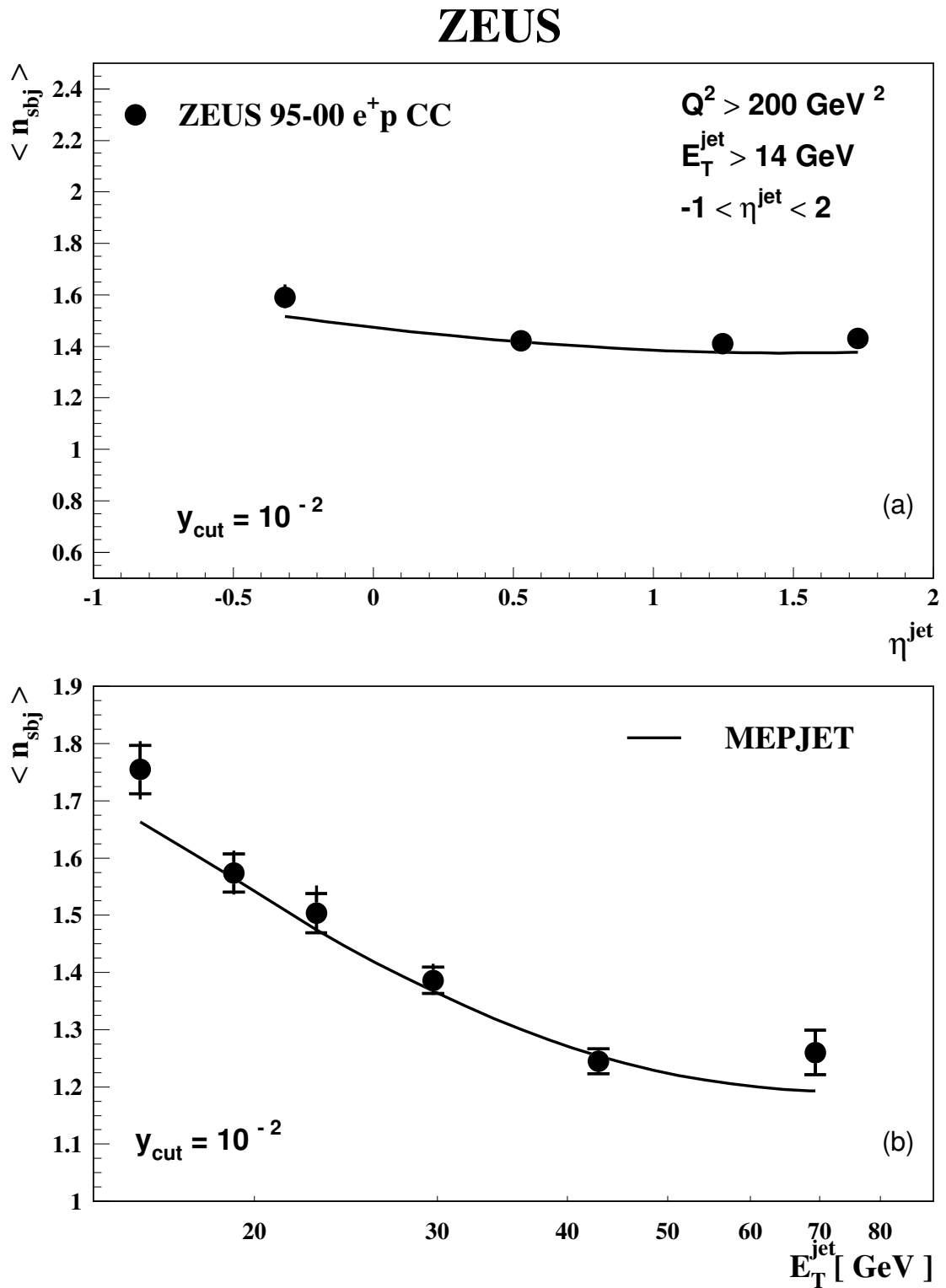The sensitivity of the subjet multiplicity to the value of $\alpha_s(M_Z)$ is illustrated in Fig. 7.38, which compares the measured $\langle n_{sbj} \rangle$ at $y_{cut} = 10^{-2}$ as a function of E_T^{jet} with NLO QCD calculations obtained with different values of $\alpha_s(M_Z)$.

The measured $\langle n_{sbj} \rangle$ at $y_{cut} = 10^{-2}$ as a function of E_T^{jet} was used to determine $\alpha_s(M_Z)$. The following procedure was used:

- NLO QCD calculations of $\langle n_{sbj} \rangle$ were performed for the five sets of the CTEQ4 "A-series". The value of $\alpha_s(M_Z)$ used in each calculation was that associated with the correspondig set of PDFs;

- for each bin, i in E_T^{jet}, the NLO QCD calculations, corrected for hadronisation effects, were used to parametrise the $\alpha_s(M_Z)$ dependence of $\langle n_{sbj} \rangle$ (see Fig. 7.39) according to

$$[\langle n_{sbj} \rangle \, (\alpha_s(M_Z))\,]_i = 1 + \; C_1^i \cdot \alpha_s(M_Z) \; + \; C_2^i \cdot \alpha_s(M_Z)^2. \tag{7.18}$$

  The coefficients C_1^i and C_2^i were determined by performing a χ^2-fit to the NLO QCD predictions. This simple parametrisation gives a good description of the $\alpha_s(M_Z)$ dependence of $\langle n_{sbj} \rangle$ over the entire range spanned by the CTEQ4 "A-series";

- this parametrisation was used to extract a value of $\alpha_s(M_Z)$ in each bin;

- in addition, a combined value of $\alpha_s(M_Z)$ was determined by a χ^2-fit of Eq.(7.18) to the measured $\langle n_{sbj} \rangle$ values for all bins.

This procedure correctly handles the complete α_s-dependence of the calculations (the explicit dependence coming from the partonic cross sections as well as the implicit one coming form the PDFs) in the fit, while preserving the correlation between α_s and the PDFs.

The uncertainty in the extracted values of $\alpha_s(M_Z)$ due to the experimental systematic uncertainties was evaluated by repeating the above analysis for each systematic check. The largest contribution to the experimental uncertainty was that due to the simulation of the hadronic final state.

The theoretical uncertainties, evaluated as described in section 7.1.3, arising from terms beyond NLO and uncertainties in the hadronisation correction were considered. These resulted in uncertainties in $\alpha_s(M_Z)$ of $\Delta\alpha_s(M_Z) = {}^{+0.0064}_{-0.0051}$ and $\Delta\alpha_s(M_Z) = \pm 0.0014$, respectively. The total theoretical uncertainty was obtained by adding these uncertainties in quadrature. Other uncertainties described in section 7.1.3 were small and have been neglected. As a cross check, a linear parametrisation of the $\alpha_s(M_Z)$ dependence of $\langle n_{sbj} \rangle$ was considered, and the extracted value of $\alpha_s(M_Z)$ changed by less than 0.00001.

The values of $\alpha_s(M_Z)$ obtained from the measurement of $\langle n_{sbj} \rangle$ in each region of E_T^{jet}, shown in Fig. 7.40, are in good agreement with each other. The value of $\alpha_s(M_Z)$ obtained from the measurements of $\langle n_{sbj} \rangle$ at $y_{cut} = 10^{-2}$ for $25 < E_T^{jet} < 119$ GeV, a

region where the parton-to-hadron correction was less than 10%, is

$$\alpha_s(M_Z) = 0.1202 \pm 0.0052 \text{ (stat)} \, ^{+0.0060}_{-0.0019} \text{ (syst.)} \, ^{+0.0065}_{-0.0053} \text{ (th.)}.$$

This result is consistent with other recent determinations at HERA using measurements of inclusive jet cross sections [Ch02b, Ad01b], dijet cross sections [Br01] as well as $\langle n_{sbj} \rangle$ [ZE01b] in NC DIS and with the PDG value, $\alpha_s(M_Z) = 0.1172 \pm 0.0020$ [Ha02].
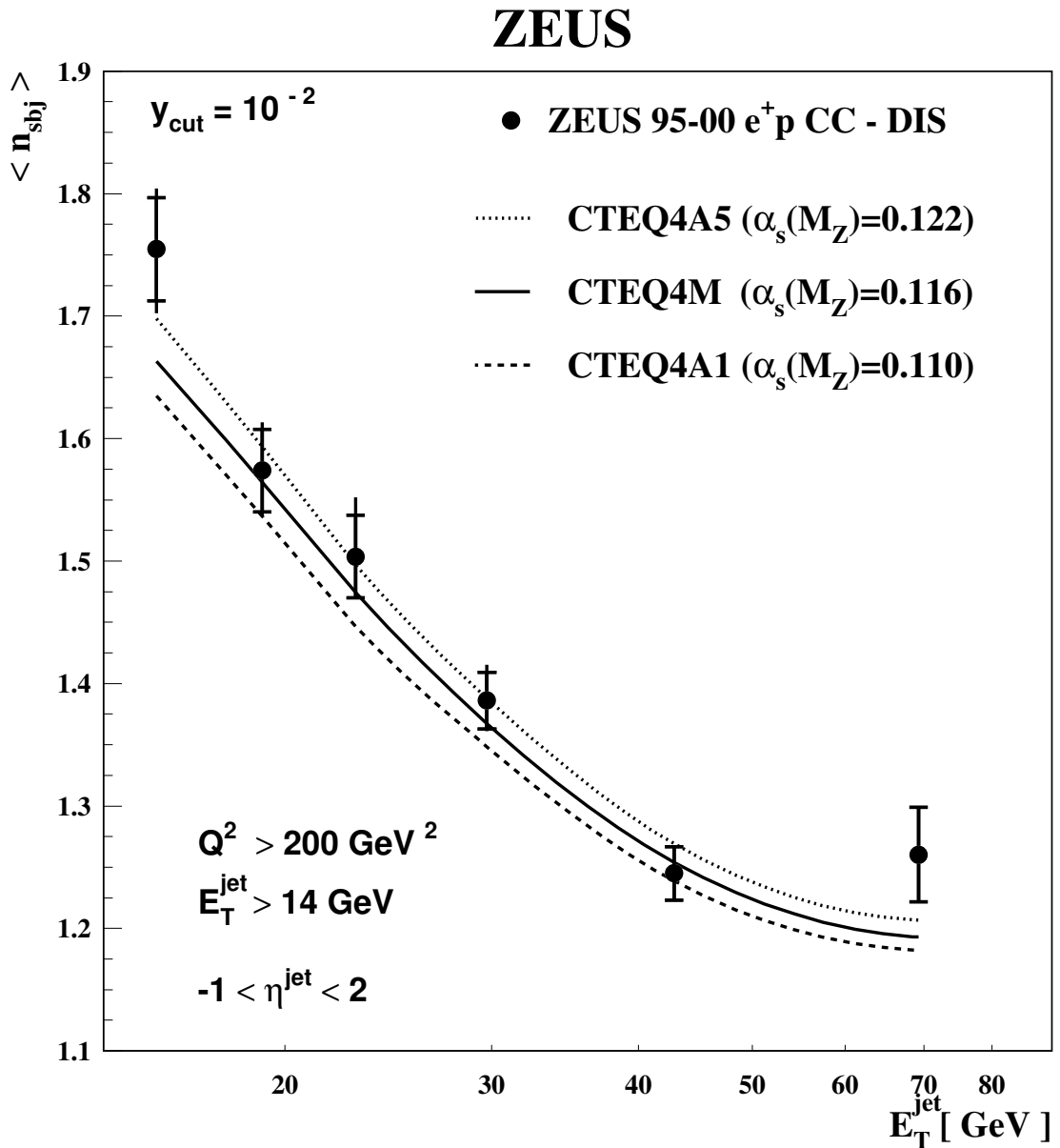
Figure 7.38 - Mean subjet multiplicity, $\langle n_{sbj} \rangle$, at $y_{cut} = 10^{-2}$ as a function E_T^{jet}, for inclusive jet production with $-1 < \eta^{jet} < 2$. The inner error bars represent the statistical uncertainty of the data and the outer error bars show the statistical and systematic uncertainties added in quadrature. The NLO QCD predictions obtained with MEPJET using the CTEQ4 sets of proton PDFs are shown.
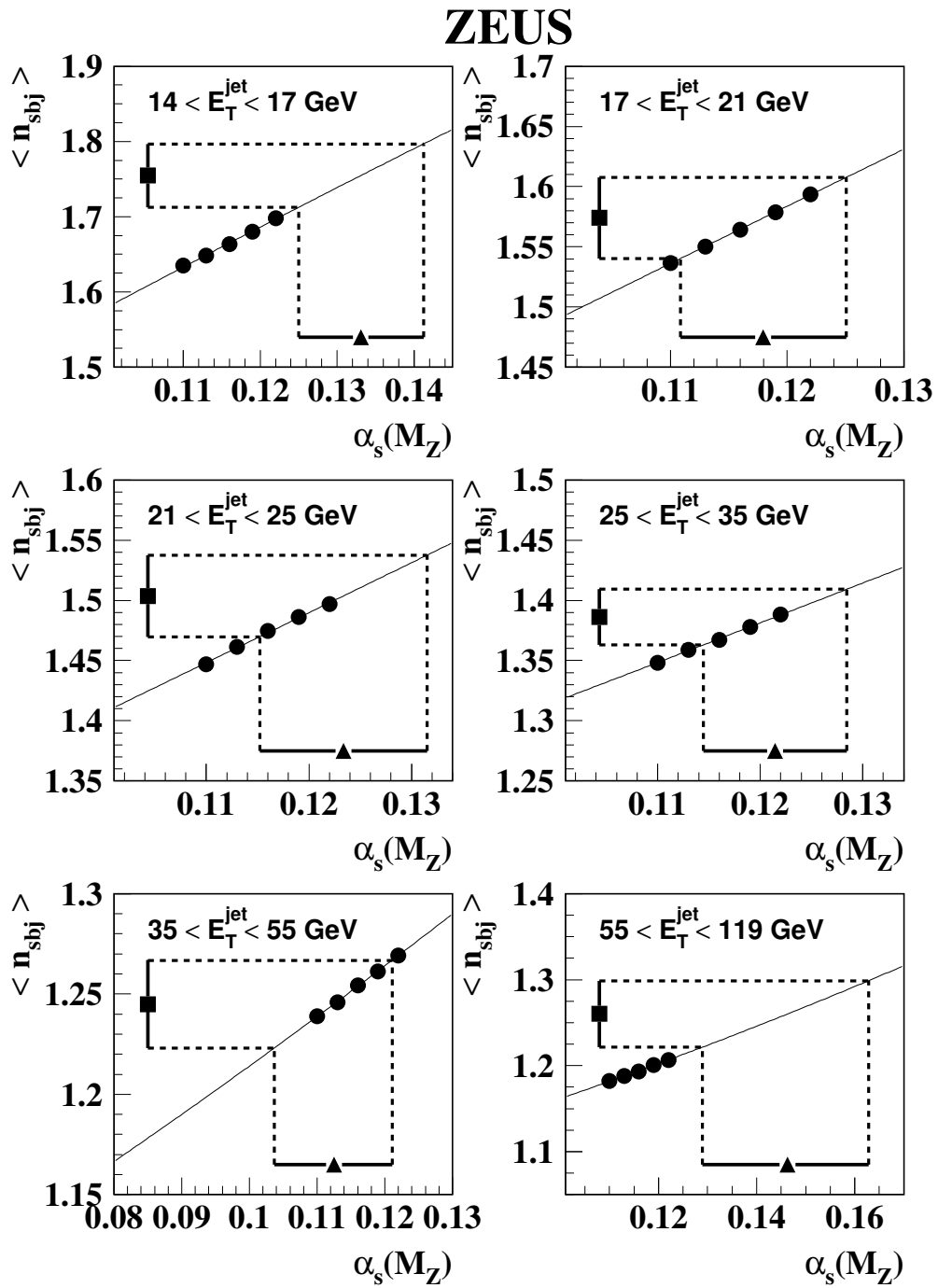
Figure 7.39 - Parametrisation of the α_s dependence of the calculations of $\langle n_{sbj} \rangle$ for inclusive jet production with $-1 < \eta^{jet} < 2$ in different E_T^{jet} regions.
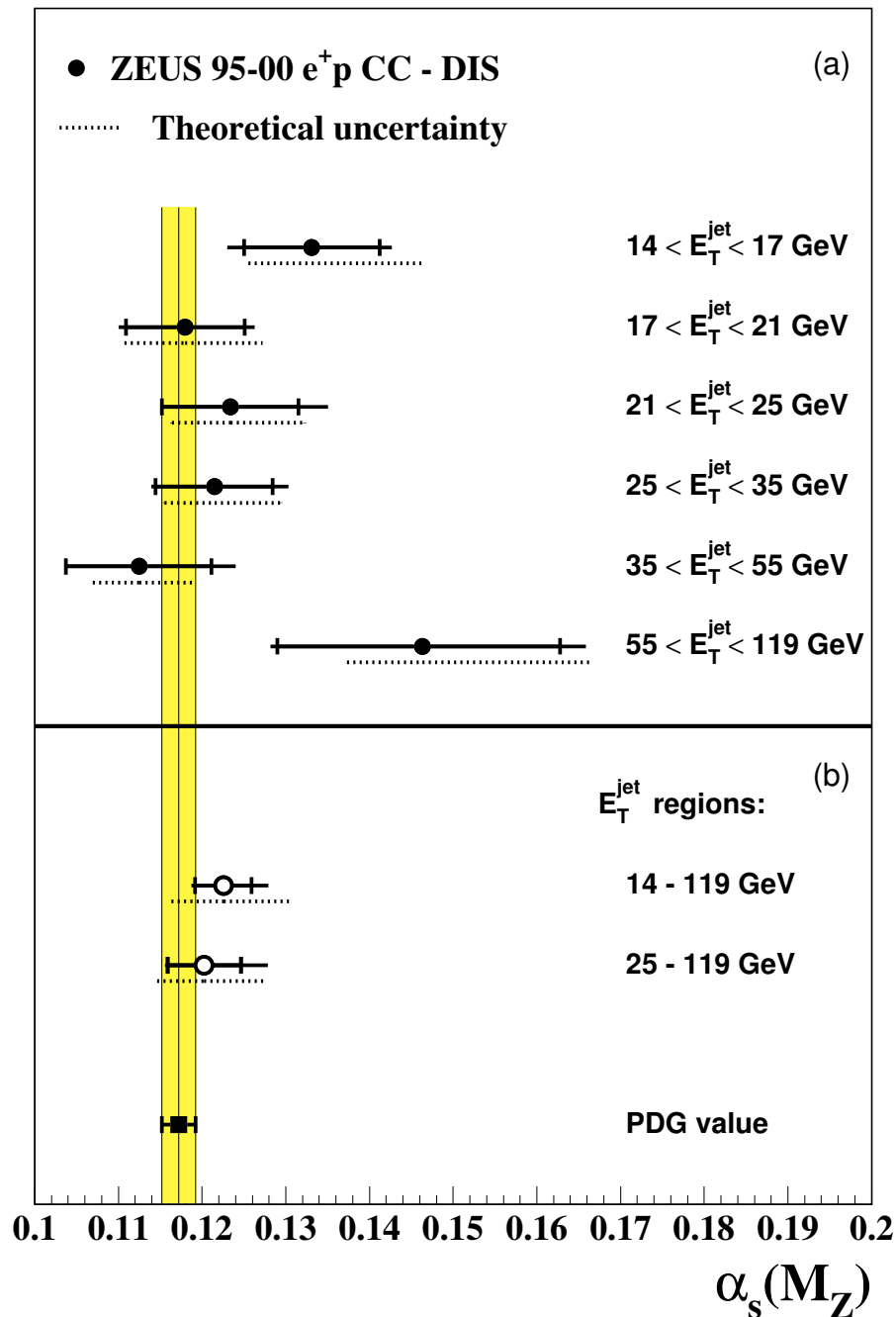
Figure 7.40 - (a) The $\alpha_s(M_Z)$ values determined form a fit to the measured subjet multiplicity $\langle n_{sbj} \rangle$ at $y_{cut} = 10^{-2}$ as a function of E_T^{jet} in different E_T^{jet} regions (black dots). (b) The combined value of $\alpha_s(M_Z)$ obtained using either all the E_T^{jet} regions or just the region $25 < E_T^{jet} < 119$ GeV (open circles). The inner error bars represent the statistical uncertainty of the data, and the outer error bars show the statistical and the systematic uncertainties added in quadrature. The dotted line below each point indicates the theoretical uncertainty. For comparison, the PDG value and its uncertainty are shown.

7.4.2 Comparison of subjet multiplicities in CC and NC DIS

The measurements of subjet multiplicities in CC interactions presented here are compared to similar measurements NC DIS [ZE01b, Go02]. The NC data was re-analysed in the same kinematic region as that of the CC analysis. The jet substructure is expected to depend mainly on E_T^{jet} and to a lesser extent on the hard scattering process.

The measurements of $\langle n_{sbj} \rangle$ at $y_{cut} = 10^{-2}$ as a function of E_T^{jet} in CC and NC DIS are compared in Fig. 7.43a. The $\langle n_{sbj} \rangle$ is slightly larger for jets in NC DIS than for CC DIS for a given jet transverse energy. The measurements of $\langle n_{sbj} \rangle$ at $y_{cut} = 10^{-2}$ as a function of Q^2 in CC and NC DIS are compared in Fig. 7.43b. The values of $\langle n_{sbj} \rangle$ as a function of Q^2 in NC and CC DIS are similar. Both sets of measurements are in agreement with the NLO predictions.

The LO and NLO QCD predictions show the same differences as those observed in the data, that is, $\langle n_{sbj} \rangle$ is slightly larger for jets in NC DIS than in CC DIS for a given jet transverse energy and are similar as a function of Q^2(see Fig. 7.41).

In Fig. 7.42 the comparison of the Q^2 spectra in different regions of E_T^{jet} and the E_T^{jet} spectra in different regions of Q^2 for NC and CC processes are shown. For a fixed value of E_T^{jet} the Q^2 spectra in NC and CC DIS are different whilst for a fixed value of Q^2 the E_T^{jet} spectra are very similar. The differences observed in the subjet multiplicity as function of E_T^{jet} can be, therefore, attributed to the differences in the Q^2 spectra of the two processes.

MEPJET predictions	Phase space
—— CC NLO	$E_T^{jet} > 14$ GeV
····· NC NLO	$-1 < \eta^{jet} < 2$
······· CC LO	$Q^2 > 200$ GeV^2
···· NC LO	$y < 0.9$
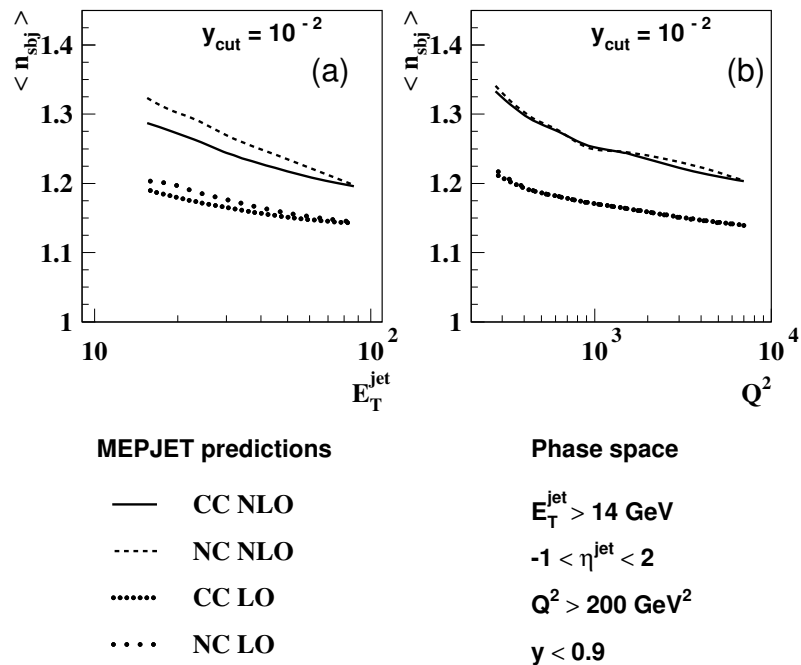
Figure 7.41 - LO and NLO QCD predictions of $\langle n_{sbj} \rangle$ for inclusive jet production in CC DIS and NC DIS as a function of (a) E_T^{jet} and (b) Q^2. The predictions have not been corrected for hadronization.
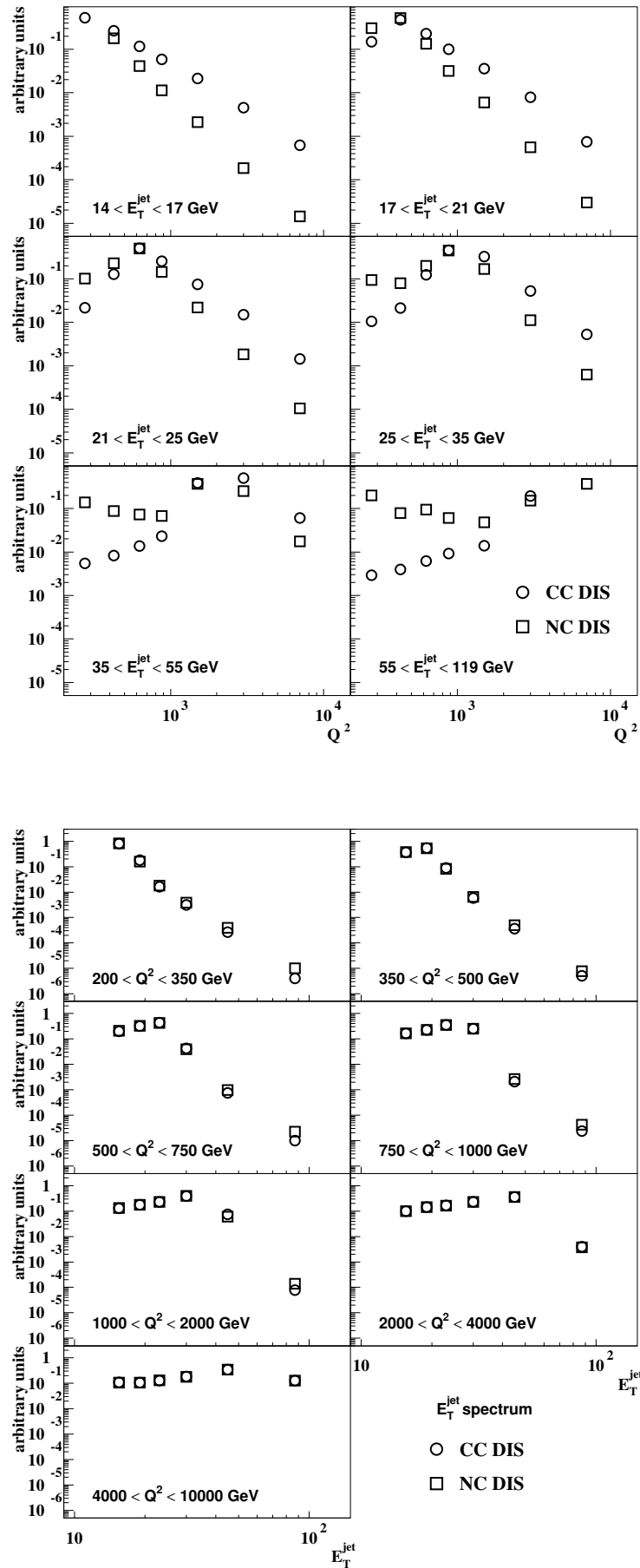
Figure 7.42 - Comparison of the Q^2 spectra in NC and CD DIS for different regions in E_T^{jet} (top) and of the E_T^{jet} spectra for different regions in Q^2 (bottom). The normalisation is arbitrary.
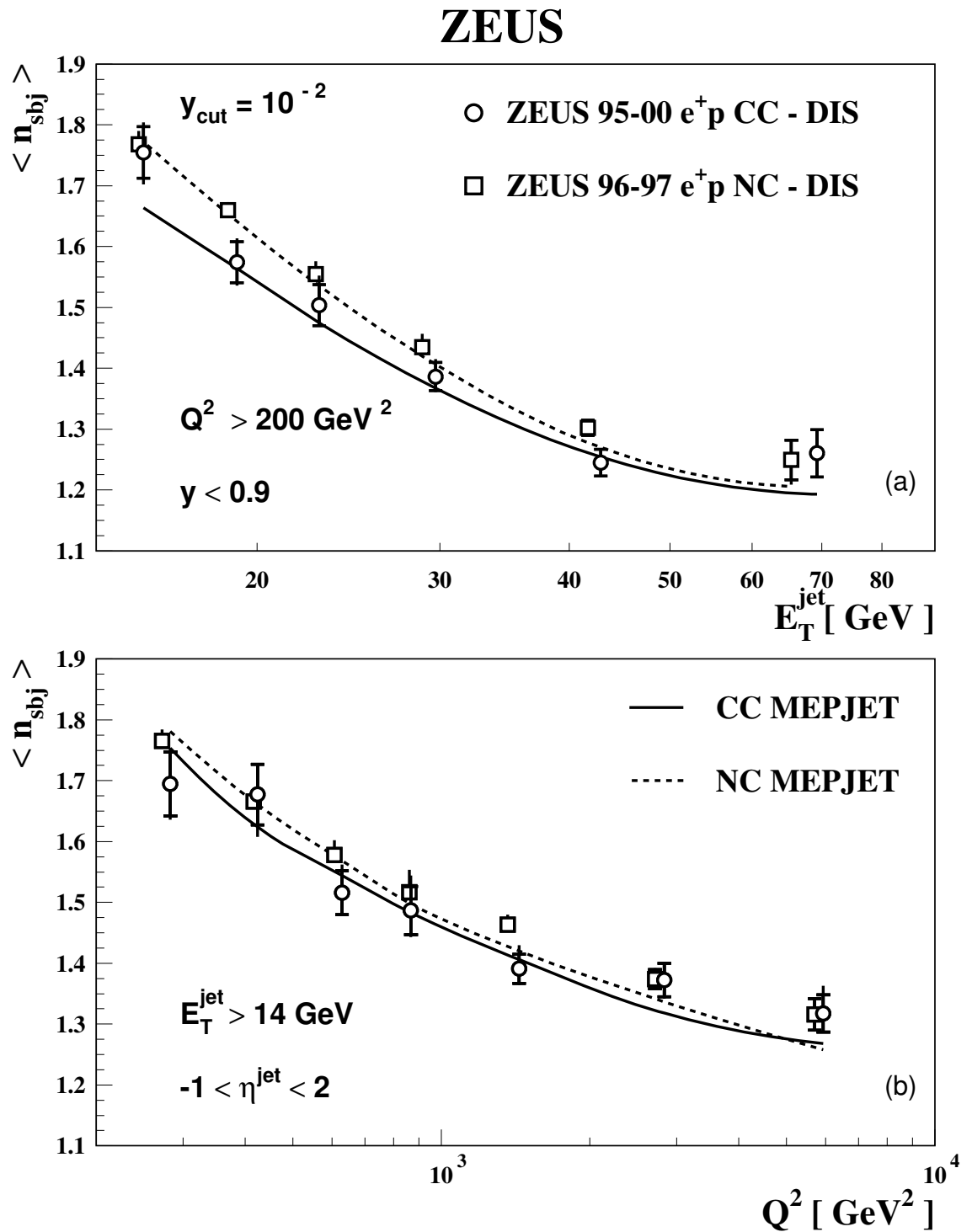
Figure 7.43 - $\langle n_{sbj} \rangle$ for inclusive jet production in charged current DIS (open circles) and neutral current DIS (open squares) as a function of (a) E_T^{jet} and (b) Q^2.

Chapter 8

Conclusions

The hadronic final state in charged current deep inelastic scattering in the kinematic range $Q^2 > 200$ GeV^2 and $y < 0.9$ has been studied by measuring the reaction $e^+p \rightarrow \overline{\nu_e} + +\text{jet(s)} + X$ with the ZEUS detector at HERA using an integrated luminosity of 110.5 pb^{-1}. Events having one or more jets with transverse energies $E_T^{\text{jet}} > 14$ GeV in the final state have been selected using the longitudinally invariant k_T algorithm in the laboratory frame. Measurements of differential cross sections for inclusive jet and dijet production have been presented.

The data have been compared with the predictions of parton-shower Monte Carlo calculations using the CTEQ4D parametrisations of the proton parton density functions. The measurements have also been compared to next-to-leading-order QCD calculations using the CTEQ4M parametrisations of the proton parton density functions.

The predictions of the colour-dipole-model give a reasonable description of the inclusive jet differential cross section measurements. A fit to the measured inclusive jet differential cross section to $d\sigma/E_T^{\text{jet}}$ yielded

$$M_W = 80.1 \pm 0.9 \text{ (stat.)} {}^{+1.5}_{-1.4} \text{ (syst.)} \pm 0.7 \text{ (th.)} \text{ GeV.}$$

The value of M_W obtained in this analysis is consistent with the current PDG world average obtained with direct measurements $M_W = 80.41 \pm 0.10$ GeV [Ha02]. Since CC DIS represents a space-like exchange, the result obtained is complementary to the measurements obtained with time-like production of the W boson and constitutes and important check of SM consistency.

NLO QCD calculations provide a reasonable description of the shape and normalisation of the measured inclusive jet and dijet cross sections.

The internal structure of the inclusive jet sample has been studied in terms of the mean subjet multiplicity. The average number of subjets decreases as E_T^{jet} increases. The NLO QCD calculations agree well with the measurements. The measurements of the mean subjet multiplicity in CC and NC DIS as a function of Q^2 are found to be similar. The measured $\langle n_{sbj} \rangle$ at a given E_T^{jet} is somewhat smaller in CC DIS than in NC DIS, which can be attributed to the different Q^2 spectra of the two processes.

A fit to the measured $\langle n_{sbj} \rangle$ as a function of E_T^{jet} at $y_{\text{cut}} = 10^{-2}$ provides a determina-

tion of the strong coupling constant. The value of $\alpha_s(M_Z)$ determined by fitting the NLO QCD calculations to the measured $\langle n_{sbj} \rangle$ at $y_{cut} = 10^{-2}$ for $E_T^{jet} > 25$ GeV is

$$\alpha_s(M_Z) \;=\; 0.1202 \pm 0.0052 \,\text{(stat.)} \, {}^{+0.0060}_{-0.0019} \; \text{(syst.)} \, {}^{+0.0065}_{-0.0053} \, \text{(th.).}$$

Chapter 9

Conclusiones en castellano

El estado hadrónico final en en colisiones e^+p profundamente inelásticas (DIS) mediadas por interacciones débiles cargadas (CC) ha sido estudiado mediante la reacción $e^+p \rightarrow \overline{\nu_e} + +\text{jet(s)} + X$ con el detector ZEUS en HERA usando una luminosidad integrada de 110.5 pb^{-1}. Los sucesos con uno o más "jets" con energías transversas $E_T^{jet} > 14$ GeV en el estado final han sido seleccionadas usando el algoritmo k_T en el sistema de referencia del laboratorio. Las medidas de secciones eficaces diferenciales para producción inclusiva de "jets" y de producción de dos o más "jets" han sido presentados. Los datos han sido comparados a predicciones de Monte Carlo con cascada partónicas realizadas con las parametrizaciones CTEQ4D de las funciones de densidad partónicas del protón. Las medidas también han sido comparadas con cálculos de QCD a segundo orden (NLO) con las parametrizaciones CTEQ4M de las funciones de densidad partónicas del protón.

Las predicciones del modelo del "dipolo de color" describen de manera razonable las medidas de secciones eficaces inclusivas. Un ajuste a las medidas diferenciales inclusivas de $d\sigma/E_T^{jet}$ proporcionaron un valor para la masa del bosón gauge W

$$M_W = 80.1 \pm 0.9 \text{ (estad.)} {}^{+1.5}_{-1.4} \text{ (sist.)} \pm 0.7 \text{ (teor.)} \text{ GeV}.$$

El valor de M_W que se obtiene en este análisis es consistente con la medidas directas de la masa $M_W = 80.41 \pm 0.10$ GeV. Como en CC DIS hay una producción virtual del bosón gauge W, este resultado es complementario con las medidas de producción directa (real) de bosón W y constituye un test importante de consistencia dentro del modelo estándar.

Los cálculos NLO proporcionan una descripción razonable de la forma y normalización de las medidas inclusivas de "jets" y de la producción de dos o más "jets".

La estructura interna de la muestra inclusiva de "jets" ha sido estudiada en términos de la multiplicidad media de "subjets". El valor medio de "subjets" disminuye al aumentar E_T^{jet}. Los cálculos NLO están en buen acuerdo con las medidas. Las medidas de la multiplicidad media en interacciones débiles cargadas y neutras (NC) como función de Q^2 son similares. Las medidas de $\langle n_{sbj} \rangle$ para un valor dado de E_T^{jet} es algo inferior en CC DIS que en NC DIS, que se puede atribuir a las diferencias en el espectro en Q^2 en ambos procesos.

Un ajuste a las medida de $\langle n_{sbj} \rangle$ como función de E_T^{jet} para un valor fijo de $y_{cut} = 10^{-2}$

proporciona una determinación de la constante de acoplo fuerte $\alpha_s(M_Z)$. El valor de $\alpha_s(M_Z)$ obtenido como un ajuste a las medidas en la región $E_T^{\text{jet}} > 25$ GeV es

$$\alpha_s(M_Z) \;=\; 0.1202 \,\pm\, 0.0052 \,\text{(estad.)} \;{}^{+0.0060}_{-0.0019}\; \text{(sist.)} \;{}^{+0.0065}_{-0.0053}\; \text{(teor.)}.$$

Bibliography

[Ab95]   H. Abramowitz, A. Caldwell and R. Sinkus, Nucl. Inst. Meth. **A 365**, 508
          (1995);
          R. Sinkus and T. Voss, Nucl. Inst. Meth. **A 391** 360 (1997).

[Ad01]   H1 Collaboration, C. Adloff et al. *Dijet Production in Charged and Neu-
          tral Current* e^+p *Interactions at High* Q^2, Eur. Phys. J. **C 19** 429 (2001).

[Ad01b]   H1 Collaboration, C. Adloff et al., *Measurement and QCD analysis of
          jet cross sections in deep-inelastic positron proton collisions at s**(1/2)
          of 300-GeV* Eur. Phys. J. **C 19** 289 (2001).

[Ad01c]   H1 Collaboration, C. Adloff et al., *Measurement of Charged and Neutral
          Current Cross Sections in Electron–Proton Collisions at High* Q^2 Eur.
          Phys. J. **C 19** 269 (2001).

[Ah94]   H1 Collaboration, T. Ahmed et al., *First Measurement of the Charged
          Current Cross Section at HERA*, Phys. Lett. **B 324** 241 (1994).

[Ah00]   SNO Collaboration, Q. R. Ahmad et al., *Direct evidence for neutrino
          flavor transformation from neutral-current interactions in the Sudbury
          Neutrino Observatory*, Phys. Rev. Lett. **89** 011301 (2002) and *Measure-
          ment of day and night neutrino energy spectra at SNO and constraints
          on neutrino mixing parameters*, Phys. Rev. Lett. **89**, 011302 (2002).

[Ai95]   H1 Collaboration, S. Aid et al., *Measurement of the* e^+ *and* e^- *Induced
          Charged Current Cross Sections at HERA*, Z. Phys. **C 67** 565 (1995).

[Ai96]   H1 Collaboration, S. Aid et al., *Measurement of the* Q^2 *Dependence of
          the Charged and Neutral Current Cross Sections in* $e^{\pm}p$ *Scattering at
          HERA*, Phys. Lett. **B 379** 319 (1996).

[Al77]   G. Altarelli and G. Parisi, Nucl. Phys. **B126** 298 (1977);
          V.N. Gribov and L.N. Lipatov, Sov. J. Nucl Phys. **15** 438 (1972);
          L.N. Lipatov, Sov. J. Nucl. Phys. **20** 96 (1975);
          Y.L. Dokshitzer, Sov. Phys. JETP. **46** 641 (1977).

[An92]   J. Andruskow et al., DESY 92-066 (1992);
          K. Piotrzkowski, DESY F35D-93-06 (1993).

[Ba95]   L.A.T. Bauerdick et al., DESY-95-236 (1995).

[Be34]   H. Bethe and W. Heitler, Proc. Roy. Soc. **A 146** 83 (1934).

[Bl69]   E.D. Bloom et al. Phys. Rev. Lett. **23** 930 (1969);
           W. K. Panofsky, *Proceedings of the International Conference in High Energy Physics* Viena, Austria (1968).

[Br87]   R. Brun et al., *Geant3.13*, CERN DD/EE/84-1 (1987).

[Br99]   ZEUS Collaboration, J. Breitweg et al., *Measurement of Jet Shapes in High-Q^2 Deep Inelastic Scattering at HERA*, Eur. Phys. J. **C 8** 367 (1999).

[Br00]   ZEUS Collaboration, J. Breitweg et al., *Measurement of High-Q^2 Charged-Current e^+p Deep Inelastic Scattering Cross Sections at HERA*, Eur. Phys. J. **C 12** 411 (2000);
           K. Nagano, *Measurement of Charged-Current e+p Deep Inelastic Scattering Cross Sections at sqrt(s)=300 GeV*. PhD Thesis, University of Tokyo, KEK report 99-11 (1998).

[Br01]   ZEUS Collaboration, J. Breitweg et al., *Measurement of Dijet Production in Neutral Current Deep Inelastic Scattering at High Q^2 and Determination of α_s*, Phys. Lett. **B 507** 70 (2001).

[Ca63]   N. Cabibbo, Phys. Rev. Lett. **10** 531 (1963).

[Ca69]   C.G. Callan and D. Gross, Phys. Rev. Lett. **22** 156 (1969).

[Ca92]   S. Catani et al., Nucl. Phys. **B 377** 445 (1992);
           S. Catani et al., Nucl. Phys. **383** 419 (1992);
           M.H. Seymour, Nucl. Phys. **B 421** 545 (1994);
           M.H. Seymour, Phys. Lett. **B 378** 279 (1996).

[Ca93]   S. Catani et al., *Nucl. Phys.* **B406** 187 (1993).

[Ch02]   ZEUS Collaboration, S. Chekanov et al., *Measurement of high-Q**2 charged current cross sections in e- p deep inelastic scattering at HERA*, Phys. Lett. **B 539** 197 (2002).

[Ch02b]   ZEUS Collaboration, S. Chekanov et al., *Inclusive jet cross sections in the Breit frame in neutral current deep inelastic scattering at HERA and determination of α_s*, DESY-02-112, Accepted by Phys. Lett. B. (2002).

[Ch02c]   ZEUS Collaboration, S. Chekanov et al., Phys. Lett. **B 531** 428 (2002).

[Ch02d]   ZEUS Collaboration, S. Chekanov et al., Eur. Phys. J. **C 23** 615 (2002).

[Ci88]   M. Ciafaloni, *Nucl. Phys.* B **296** 49 (1988);
           S. Catani, F. Fiorani and G. Marchesini, Phys. Lett. **B 234** 339 (1990) and *Nucl. Phys.* B **336** 18 (1990).

[Co85]   J.C.D. Collins, D.E. Soper and G. Sterman, Nucl. Phys. **B 261** 104 (1985).

[De91]   M. Derrick et al., Nucl. Instr. and Meth. **A 309** 77 (1991);
           A. Andresen et al., Nucl. Instr. and Meth. **A 309** 101 (1991);
           B. Bernstein et al., Nucl. Instr. and Meth. **A 336** 23 (1993).

[DE94]   DESY, *Annual report* (1994).

[De95]   ZEUS Collaboration, M. Derrick et al., *Measurement of Charged and
           Neutral Current* e^-p *Deep Inelastic Scattering Cross Sections at High*
           Q^2, Phys. Rev. Lett. **75** 1006 (1995).

[De96]   ZEUS Collaboration, M. Derrick et al., *Study of Charged-Current* ep
           Interactions at $Q^2 > 200$GeV^2 *with the ZEUS Detector at HERA*, Z.
           Phys. **C 72** 399 (1996);
           M. Martínez Pérez, *Study of high-*Q^2 *DIS processes at HERA*, PhD
           Thesis, Universidad Autónoma de Madrid (1998).

[El92]   S.D. Ellis, Z. Kunszt and D.E. Soper, Phys. Rev. Lett. **69** 3615 (1992).

[El93]   S.D. Ellis and D.E. Soper. Phys. Rev. **D 48** 3160 (1993).

[El96]   R.K. Ellis, W.J. Stirling and B.R. Webber, *QCD and Collider Physics*.
           Cambridge Unversity Press (1996).

[Fe69]   R.P. Feynman, Phys. Rev. Lett. **23** 1415 (1969).

[Fi93]   S.M. Fisher et al., ADAMO: User's guide, CERN (1993).

[Fo93]   B. Foster et al., Nucl. Instr. and Meth. **A 338**, 254 (1993).

[Fu98]   Super-Kamiokande Collaboration, Y. Fukuda et al., *Study of the atmo-
           spheric neutrino flux in the multi-GeV energy range*, Phys. Lett. B **436**
           33 (1998).

[Ge53]   M. Gell-Mann, Phys. Rev. **92**, 833-834 (1953).

[Ge64]   M. Gell-Mann, Phys. Lett. **8** 214 (1964);
           G. Zweig, CERN-8192/TH 401 (1964);
           G. Zweig, CERN-8419/TH 402 (1964).

[Gl61]   S.L. Glashow, Nucl. Phys. **22** 579 (1961);
           A. Salam, Proceedings of The Nobel Symposium, Lerum, Sweden
           (1968);
           S. Weinberg, Phys. Rev. Lett. **19** 1264 (1967).

[Gi61]   W. T. Giele, E. W. Glover and D. A. Kosower, Nucl. Phys. **B 403**, 633
           (1993).

[Go02]   Oscar González. *Precise determinations of the strong couplin con-
           stant at HERA*. PhD Thesis, Universidad Autónoma de Madrid, DESY-
           THESIS-2002-020 (2002).

[H101]   H1 Collaboration, C. Adloff et al., *Dijet Production in Charged and Neu-
           tral Current* e^+p *Interactions at High* Q^2 Eur. Phys. J. **C 19**, 429 (2001).

[Ha84]   F. Halzen and A.D. Martin, *Quarks and Leptons*, John Wiley Sons Inc., New York (1984).

[Ha02]   Particle Data Group, K. Hagiwara et al., *Particles and fields*, Phys. Rev. **D 66** (2002).

[HB94]   HERA-B Collaboration, *Technical Design Report*, DESY-PRC 95/01 (1995).

[HE93]   HERMES Collaboration, *Technical Design Report* (1993).

[He98]   M. Herrero, *The standard model*, arXiv:hep-ph/9812242 (1998).

[Hi53]   P. W. Higgs, Phys. Lett. **12** 132 (1964), Phys. Rev. Lett. **13** 508 (1964) and Phys. Rev. **145** 1156 (1966).
F. Englert and R. Brout, Phys. Rev. Lett. **13** 321 (1964).

[Ho53]   R. Hofstadter et al., Phys. Rev. **91** 422 (1953);
R. Hofstadter and R.W. McAllister, Phys. Rev. **98** 217 (1955);
R. Hofstadter, Ann. Rev. Nucl. Part. Sci. **7** 458 (1957).

[Hu90]   J.E. Huth et al., *Proc. of the 1990 DPF Summer Study on High Energy Physics, Colorado, edited by E.L. Berger*, (World Scientific, Singapore, 1992) 134.

[In97]   G. Ingelman, A. Edin and J. Rathsman, Comput. Phys. Commun. **101** 108 (1997).

[Ja79]   M.Krawczyk et al., *Proc. of the study for an ep facility for Europe*, DESY79-48 391 (1979).

[Ka02]   KamLAND Collaboration, *First Results from KamLAND: Evidence for Reactor Anti-Neutrino Disappearance*, arXiv:hep-ex/0212021 (2002).

[Ko73]   M. Kobayashi and T. Maskawa, Prog. Theor. Phys. **49** 652 (1973).

[Kr98]   A.Kruse and A.v. Sighem, *MUFFINCUP - A Wrapper for MUFFIN*, ZEUS-NOTE 98-025 (1998).

[Ku76]   E.A. Kuraev, L.N. Lipatov and V.S. Fadin, Sov. Phys. JETP **44** 443 (1976);
E.A. Kuraev, L.N. Lipatov and V.S. Fadin, Sov. Phys. JETP **45** 199 (1977);
Y.Y. Balitzki and L.N. Lipatov, Sov. J. Nucl. Phys. **28** 822 (1978).

[Kw92]   A. Kwiatkowski, H. Spiesberger and H. J. Mohring, Comput. Phys. Commun. **69** 155 (1992).

[La00]   H.L. Lai et al., Eur. Phys. J. C **12** 375 (2000).

[La97]   H.L. Lai et al., Phys. Rev. D **55** 1280 (1997).

[LE00]   The LEP Higgs Working Group, *A Hint of the Standard Model Higgs Boson at LEP* (2000).

[Lo92]   E. Lohrmann, *Hochenergiephysik* (1992).

[lö02]   L.Lönnblad, Comput. Phys. Commun. **71** 15 (1992).

[Ma98]   A. D. Martin, R. G. Roberts, W. J. Stirling and R. S. Thorne, Eur. Phys. J. **C 4** 463 (1998) and Eur. Phys. J. C **14** 133 (2000).

[Mi96]   E. Mirkes and D. Zeppenfeld, Phys. Lett. **B 380** 205 (1996); E. Mirkes, S. Willfahrt and D. Zeppenfeld, hep-ph/9711366.

[Na60]   Y. Nambu, Phys. Rev. Lett. **4** 380 (1960); J. Goldstone, Nuovo Cim. **19** 154 (1961).

[Ni53]   K. Nishijima and T. Nagano, Progr. Theor. Phys. **10** 581 (1953).

[Pl93]   H. Plothow-Besch, Computer Phys. Commun. **75** 396 (1993).

[Sa98]   A. Savin, *Study of Calorimeter Noise in the 1996 Data*, ZEUS-Note 98-07.

[Sc91]   G. A. Schuler and H. Spiesberger, In Hamburg 1991, Proceedings, Physics at HERA, vol. 3, 1419 (1991).

[Se95]   M.H. Seymour, hep-ph/9506421, CERN-TH/95-176 (1995).

[Sj94]   T. Sjöstrand, Computer Phys. Commun. **82** 74 (1994).

[Sm84]   W.H. Smith et al., *The ZEUS Trigger System*, ZEUS-note 89-084.

[Ui92]   H. Uijterwaal, *The Global Second Level Trigger for ZEUS*, PhD Thesis , University of Amsterdam (1992).

[Wi02]   M. Wing (on behalf of the ZEUS Collab.), hep-ex/0206036 (2002).

[Ya99]   U.K. Yang and A. Bodek, Phys. Rev. Lett. **82**, 2467 (1999).

[Yo92]   C. Youngman, *The ZEUS Data Acquistion System*, DESY 92-150A.

[ZE93]   ZEUS Collaboration, U. Holmet et al., *The ZEUS Detector*, Status Report (unpublished), DESY (1993).

[ZE01]   ZEUS Collaboration, *Measurement of jet cross sections and jet substructure in charged current deep inelastic scattering at HERA* . Contributed paper to the International Europhysics Conference on High Energy Physics, Budapest, Hungary (2001). Abstract 646.

[ZE01b]   ZEUS Collaboration, *Measurements of jet substructure in neutral current deep inelastic scattering and determination of α_S at HERA*. Contributed paper to the International Europhysics Conference on High Energy Physics, Budapest, Hungary (2001). Abstract 641.

[ZE02]   ZEUS Collaboration *Jet production in charged current deep inelastic e^+p scattering at HERA*. Contributed paper to the XXXIst International Conference on High Energy Physics, Amsterdam, The Netherlands (2002). Abstract 845.

Acknowledgements